Development of High Solute Aluminium Alloys in Net Shape through Additive Manufacturing

Abirami Babu

M. Eng. (Aerospace materials)

University of Sheffield, United Kingdom.

A thesis submitted for the degree of Doctor of Philosophy

Department of Materials Science and Engineering

Monash University

Victoria, Australia

May 2021

Copyright notice

To Daddy, Maa, Vidya and Karthik

Acknowledgements

Throughout the course of my research, I have received a great deal of assistance and support from a number of people.

First and foremost, I am deeply indebted to my supervisor, Prof. Nick Birbilis for his constant support and motivation, not only in expanding my scientific acumen, but in all aspects of life through his guidance in difficult times to bring out the best in me. This work would not be possible without his expert advice and big smile, and I also thank him for showing endless faith and patience throughout my tenure. The wisdom he has imparted will always be my source of inspiration throughout the journey of life.

I also thank my co-supervisor, A/Prof. Aijun Huang for providing me an opportunity to be a part of Monash centre for additive manufacturing. His advice both on my research and career have been invaluable.

I acknowledge the use of electron microscopy facilities at the Monash Centre for Electron Microscopy (MCEM) and this research used equipment funded by the Australian Research Council grant (LE110100223). I also extend my gratitude to Dr. Tim Williams for his valuable contribution and support over the course of my research.

This research also used the facilities at Monash X-ray Platform (MXP) and I would like to thank Mr. James Griffith and Dr. Jisheng Ma for supporting and nourishing my knowledge on several X-ray analysis techniques.

I would also like to extend my gratitude to Dr. Shravan Kairy, Dr. Oumaïma Gharbi, Dr. Yuman Zhu and Dr. Marcus Lam for helping me at various stages of my research. A big thank you to Prof. Xinhua Wu and Prof. Ian Polmear for taking time to support me on my research journey with their expertise in the field.

I express my sincere gratitude to the Department of Materials Engineering, Monash university for funding my PhD through the Monash co-funded graduate scholarship and Faculty of engineering international postgraduate research scholarship (FEIPRS), and giving me a platform to grow in the scientific world.

The past few years would not be loaded with great memories if not for my amazing colleagues, Lee Djumas, Paula Magalhaes, Guilherme Sander, Victor Cruz, Sanjay Choudhary, Qing Cao, Darren Feenstra and Timothy Murray who have supported every step of my journey. I also thank all my fellow PhD students at MCAM for their kind gesture at work and making my PhD path an enriching experience.

Lastly but majorly, I thank my family and friends who have been the strongest pillars throughout my life and for never failing to put a smile on my face. Through the tough times where we are unable to meet each other, thanks for the regular video calls and constant words of motivation from thousands of miles away.

Abstract

High strength aluminium (Al) alloys are primarily strengthened through careful alloying additions and subsequent heat treatment, in order to promote the formation of nano-sized precipitates. In the case of the 7xxx series (Al-Zn-Mg) alloy system, precipitates are rich in Mg and Zn. Typically, increasing the number density and volume fraction of such precipitates has been directly associated with enhanced mechanical properties (namely yield strength and ultimate tensile strength). However, the extent of solute (Mg and Zn) that may be conventionally alloyed with aluminium has been hampered by the limited solidification rates in conventional processing, that results in macrosegregation, cracking and grain coarsening – all of which are detrimental to properties. Recently, laser powder bed fusion (LPBF), a form of additive manufacturing, has been demonstrated as capable of exploiting the metallurgical solubility limits, owing to high local heating and subsequent rapid solidification in the LPBF process, revealing the prospect of producing Al-alloys with solute supersaturation. However, LPBF of Al-alloys to date, has been notionally restricted to a small number of alloy compositions.

The objective of the present research was to design and fabricate unique high solute Al-alloy compositions with excess Mg and Zn by exploiting the rapid solidification achieved through LPBF process. Furthermore, this work also aims at understanding the microstructural evolution, mechanical properties and corrosion behaviour. Meanwhile, the project also seeks to answer the fundamental question, ‘can there be too much solute?’, in the context of developing high strength and high solute Al-alloys through additive manufacturing.

The selection of high solute Al-alloy compositions studied herein was rationalised based on solidification modelling of a range of Al-Zn-Mg alloys with varying Zn:Mg ratio using a

CALPHAD based approach (Thermocalc®). The Scheil solidification model and Rappaz's hot cracking criterion were used to identify compositions with low hot cracking susceptibility and high volume fraction of second phase particles. Herein, research on high solute Al-Zn-Mg alloys was categorised into four phases – 1) Production of high solute Al-Zn-Mg alloys through LPBF, 2) Heat treatment and mechanical properties evaluation of the high solute Al-Zn-Mg alloys, 3) Assessment of corrosion behaviour, and 4) Elucidating the influence of second phase particles on the mechanical properties of high solute Al-Zn-Mg alloys.

LPBF prepared Al-Zn-Mg alloys were successfully fabricated and in-depth characterisation revealed the presence of previously unidentified, icosahedral quasicrystalline phase, which was named P-phase. Furthermore, the results aided in selecting a potential high solute alloy with the composition of Al-14Zn-3Mg (in wt. %) for heat treatment. The heat treatment of Al-14Zn-3Mg revealed the presence of high volume fraction of η' and η-$Mg(Zn, Al)_2$ precipitates accompanied by an improvement in mechanical properties from the as-LPBF condition. The results also demonstrate the critical solute limits in Al-alloys where excess area fraction of second phase particles > 50% results in the loss of a mechanical properties. However, electrochemical studies on Al-14Zn-3Mg demonstrated that the annihilation of intermetallic particles through rapid solidification led to reduced cathodic kinetics relative to the wrought Al-Zn-Mg alloy, AA7075-T6 (which was used a benchmark). Results also revealed that Al-14Zn-3Mg demonstrated superior polarisation resistance when compared to the wrought benchmark. *In-situ* characterisation studies were also performed on Al-14Zn-3Mg, in a manner coupled with CALPHAD predictions. The results revealed the phase transformations occurring during heat treatment, which highlighted several microstructural factors (such as the formation of T-phase) that influence the mechanical properties in high solute Al-alloys.

Publications and Awards

Published journal articles:

A.P. Babu, S.K. Kairy, A. Huang, N. Birbilis, Laser powder bed fusion of high solute Al-Zn-Mg alloys : Processing , characterisation and properties, Materials Design, 196 (2020) 109183. https://doi.org/10.1016/j.matdes.2020.109183 (Chapter 4)

A.P. Babu, A. Huang, N. Birbilis, On the heat treatment and mechanical properties of a high solute Al–Zn–Mg alloy processed through laser powder bed fusion process, Materials Science and Engineering A, 807 (2021). https://doi.org/10.1016/j.msea.2021.140857 (Chapter 5)

A.P. Babu, S. Choudhary, J.C. Griffith, A. Huang, N. Birbilis, On the corrosion of a high solute Al-Zn-Mg alloy produced by laser powder bed fusion, Corrosion Science, 189 (2021) 109626. https://doi.org/10.1016/j.corsci.2021.109626 (Chapter 6)

Submitted journal articles:

A.P. Babu, M. Lam, J. Ma, A. Huang, N. Birbilis, Influence of second phase particles on the mechanical properties of a high solute Al-Zn-Mg alloy fabricated through laser powder bed fusion –submitted to Journal of alloys and compounds on August 2021. (Chapter 7)

Publications in collaboration:

G. Sander, A. P. Babu, X. Gao, D. Jiang, N. Birbilis, On the effect of build orientation and residual stress on the corrosion of 316L stainless steel prepared by selective laser melting, Corr. Sci. 938 (2020), 109149. https://doi.org/10.1016/j.corsci.2020.109149

List of conference presentations:

1) A. Babu, A. Huang, N. Birbilis, Development of high strength aluminium alloys in net shape by additive manufacturing, Asia Pacific International Conference on Additive Manufacturing (APICAM), Melbourne, 1-3 July 2019.

2) A. Babu, A. Huang, N. Birbilis, Fabrication of high strength aluminium alloys through selective laser melting, 14th International Aluminium conference (INALCO), The university of Tokyo, 13-15 November 2019.

3) A.P. Babu, S. Choudhary, J.C. Griffith, A. Huang, N. Birbilis, Corrosion of high solute Al-Zn-Mg alloys fabricated through LPBF, NACE Corrosion 2021 conference, April 19-30 2021.

Awards:

1) Awarded with the *Outstanding young professional award* at the International aluminium conference, Japan.

2) Won the three minute thesis competition acquiring the third place organised by the Department of Materials science on the summer conference, 2020.

3) Awarded with the ANSTO grant for attending the summer neutron school at ANSTO, Lucas heights, Sydney.

Contents

List of figures

Chapter 1

Chapter 2

Chapter 4

Chapter 5

Chapter 6

Chapter 7

List of tables

Chapter 2

Chapter 4

Chapter 5

Chapter 6

Thesis including published works declaration

I hereby declare that this thesis contains no material which has been accepted for the award of any other degree or diploma at any university or equivalent institution and that, to the best of my knowledge and belief, this thesis contains no material previously published or written by another person, except where due reference is made in the text of the thesis.

This thesis includes 3 original papers published in peer reviewed journals, and 1 submitted under the title, *Influence of second phase particles on the mechanical properties of a high solute Al-Zn-Mg alloy fabricated through laser powder bed fusion*. The core theme of the thesis is high solute Al-Zn-Mg alloys fabricated through additive manufacturing. The ideas, development and writing up of all the papers in the thesis were the principal responsibility of myself, the student, working within the Department of Materials science and Engineering, under the supervision of Prof. Nick Birbilis.

The inclusion of co-authors reflects the fact that the work came from active collaboration between researchers and acknowledges input into team-based research.

In the case of Chapter 4, 5 and 6, my contribution to the work involved the following:

Thesis Chapter	**Publication Title**	**Status** *(published, in press, accepted or returned for revision, submitted)*	**Nature and % of student contribution**	**Co-author name(s) Nature and % of Co-author's contribution***	**Co-author(s), Monash student Y/N***
Chapter 4	Laser powder bed fusion of high solute Al-Zn-Mg alloys : Processing , characterisation and properties	*Accepted*	*90%. Concept, data collection and writing first draft*	*1) Shravan K. Kairy – Methodology (2%)* *2) Aijun Huang – Supervision (3%)* *3) Nick Birbilis – Evaluation of manuscript and supervision (5%)*	*No* *No* *No*
Chapter 5	On the heat treatment and mechanical properties of a high solute Al–Zn–Mg alloy processed through laser powder bed fusion process	*Accepted*	*92%. Concept, data collection and writing first draft*	*1) Aijun Huang – Supervision (3%)* *2) Nick Birbilis – Evaluation of manuscript and supervision (5%)*	*No* *No*
Chapter 6	On the corrosion a high solute Al-Zn-Mg alloy processed through laser powder bed fusion process	*Accepted*	*88%. Concept, data collection and writing first draft*	*1) Sanjay Choudhary – Methodology (3%)* *2) James C. Griffith – Methodology (2%)* *3) Aijun Huang – Supervision (2%)* *4) Nick Birbilis – Evaluation of manuscript and supervision (5%)*	*Yes* *No* *No* *No*

I have not renumbered sections of submitted or published papers in order to generate a consistent presentation within the thesis.

Student signature: **Date: 30/08/2021**

The undersigned hereby certify that the above declaration correctly reflects the nature and extent of the student's and co-authors' contributions to this work. In instances where I am not the responsible author I have consulted with the responsible author to agree on the respective contributions of the authors.

Main Supervisor signature: **Date: 30/08/2021**

1

Introduction

Additive manufacturing (AM) has gained significant research and commercial uptake over the last two decades, and has recently emerged as an important commercial technology for manufacturing net-shape and bespoke components. In contrast to subtractive manufacturing, the fundamental principle of AM involves in manufacturing a part layer by layer from a three dimensional computer aided design (CAD) model [1]. The ongoing demand from the transportation sector for leaner supply chains and customised components has driven a significant interest for AM. Commercial entities including Airbus, Boeing and NASA are heavily engaged in the development of this technology, where a driver for advanced manufacturing is in the light weighting of flying components, increasing fuel efficiency and minimising the environmental impact [2,3]. Required light weighting is achieved through the use of low density materials such as aluminium alloys, titanium alloys, magnesium alloys or other composite materials [4].

Of those material categories, aluminium (Al) alloys are of interest in AM, because Al is relatively inexpensive, and has simple ease of use. The key factors for aluminium additive manufacturing encompasses shorter lead times, reduction of material waste, access to new alloy compositions and fabrication of complex geometries. These advantages have enabled the BMW group to utilise laser based additive manufacturing (specifically, laser powder bed fusion process) to prepare an Al-alloy component in their BMW i8 roadster vehicle. This component is 44% lighter and ten times stiffer than the original injection-mounded component [5]. In addition, the Bugatti Chiron utilises a topology optimised bracket (Figure 1.1a) made of AlSi10Mg [6]. Furthermore, a new alloy in the Al-Sc-Mg system called Scalmalloy®, has been developed and utilised by APWorks which is an Airbus subsidiary [7]. Scalmalloy® is utilised to make chassis structures (Figure 1.1b) that are 30% lighter when compared to standard predecessors.

To date, the fabrication of Al-alloys via AM has been rather widely explored (and commercially utilised) in the context of using conventional low strength cast-alloy-like compositions (such as Al-12Si and Al-10Si-Mg). These alloys result in essentially 100% dense components. On the contrary, the existing portfolio of AM prepared high strength Al-alloys is rather limited due to the formation of defects during the AM process [8]. Also, the complete benefits offered by metal additive manufacturing in the exploration of unique alloying additions through solute hyper-loading are not fully exploited. Therefore, the present work focusses on utilising the benefits offered by AM to design, develop and explore novel compositions of Al-alloys – specifically using an AM method known as laser powder bed fusion (LPBF).

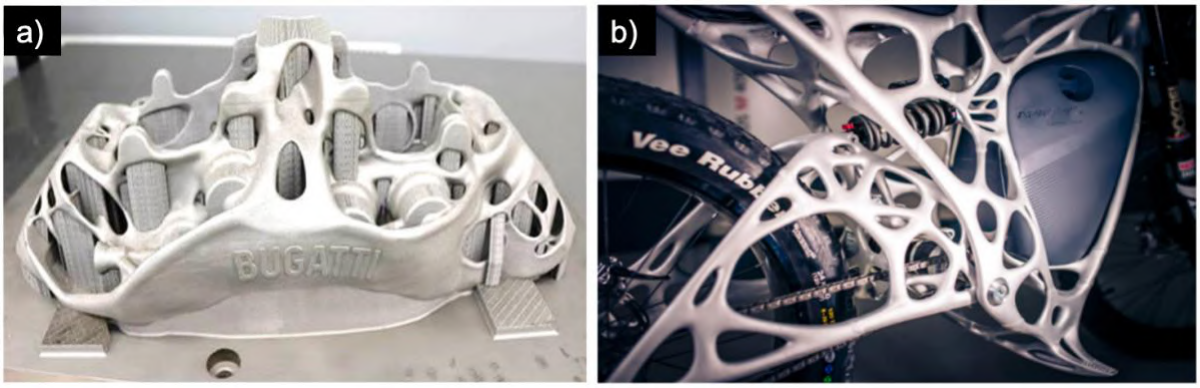

Figure 1.1: Applications of aluminium additive manufacturing through laser powder bed fusion (LPBF) technique to fabricate light weight parts such as, a) Bugatti brake calliper [6] and b) Bike frame made of Scalmalloy® [5], that were designed through topology optimisation.

References

[1] D. Herzog, V. Seyda, E. Wycisk, C. Emmelmann, Additive manufacturing of metals, Acta Mater. 117 (2016) 371–392. https://doi.org/10.1016/j.actamat.2016.07.019.

[2] A. Gisario, M. Kazarian, F. Martina, M. Mehrpouya, Metal additive manufacturing in the commercial aviation industry: A review, J. Manuf. Syst. 53 (2019) 124–149. https://doi.org/10.1016/j.jmsy.2019.08.005.

[3] R. Huang, M. Riddle, D. Graziano, J. Warren, S. Das, S. Nimbalkar, J. Cresko, E. Masanet, Energy and emissions saving potential of additive manufacturing: the case of lightweight aircraft components, J. Clean. Prod. 135 (2016) 1559–1570. https://doi.org/10.1016/j.jclepro.2015.04.109.

[4] I.J. Polmear, D. StJohn, J.-F. Nie, M. Qian, Light alloys : metallurgy of the light metals, 2017.

[5] A. Vafadar, F. Guzzomi, A. Rassau, K. Hayward, Advances in metal additive manufacturing: A review of common processes, industrial applications, and current challenges, Appl. Sci. 11 (2021) 1–33. https://doi.org/10.3390/app11031213.

[6] E. Dalpadulo, F.P. B, F. Leali, Design for Additive Manufacturing of a Topology Optimized Brake Caliper Through CAD-Platform-Based Systematic Approach Design for Additive Manufacturing of a Topology Optimized Brake Caliper Through CAD-Platform-Based Systematic Approach, Proc. XXXVII Int. Symp. 2018 Bremsen-Fachtagung, Bad Neuenahr, Ger. (2018) 181–193. https://doi.org/10.1007/978-3-030-70566-4.

[7] E. Tucker, APWorks Creates Light Rider 3D-Printed Motorcycle., (2016). https://www.dezeen.com/2016/06/06/light-rider-apworks-3d-printed-electric-motorcycle-aluminium/ (accessed May 13, 2021).

[8] S. Lathabai, Additive Manufacturing of Aluminium-Based Alloys and Composites, in: Fundam. Alum. Metall., Elsevier, 2018: pp. 47–92. https://doi.org/10.1016/b978-0-08-102063-0.00002-3.

2

Literature review

This chapter provides a review of the background and available literature on the fabrication of aluminium (Al) alloys through the laser powder bed fusion (LPBF) additive manufacturing (AM) process. Emphasis was given to the challenges faced for preparing high strength Al-alloys thorough the additive manufacturing route. Herein, the Al-Zn-Mg system comprising of the major high strength Al-alloys is discussed, and the relevance of designing new Al-alloy for AM also explored.

2.1 Additive manufacturing

Additive manufacturing (AM), as opposed to subtractive manufacturing and formative manufacturing methodologies, is described by American Society for Testing and Materials standards (ASTM 52900:2015) as a process of joining materials layer upon layer to make parts from 3D model data [1]. Typically, the commercially available AM processes can be divided into seven major types: material extrusion (ME), direct energy deposition (DED), powder bed fusion (PBF), sheet lamination (SL), vat polymerisation (VP), material jetting (MJ) and binder jetting (BJ) [2,3]. The fundamental principle behind these additive processes involves two major steps that includes slicing of a 3D computer model into multiple layers and utilising the sliced data to build a part incrementally [4].

High strength Al-alloys are widely utilised in the aerospace industry for manufacturing structural components because of their excellent strength-to-weight ratio, as well as good machinability [5]. The use of traditional subtractive manufacturing methods to produce geometrically complex aerospace components can result in fabrication complexities and high material wastage [6]. However, the ability to produce complex geometries, freedom of design and reduced material wastage render AM methods to applications in the aerospace field. In addition, AM processes enable the reduction in total number of components through part

consolidation, via advanced design of parts with complex topologies [7]. Therefore, the aerospace industry has already adopted AM on a commercial scale as a result of reduction in overall weight of the aircraft which promotes major environmental benefits [8].

The increase in requirement for economic manufacturing methods to produce light weight and dimensionally complex components results in extensive opportunities for aluminium additive manufacturing. Among the several available additive manufacturing techniques, direct energy deposition and powder bed fusion are widely applied to fabricate Al-alloys.

2.2 Direct energy deposition of Al-alloys

Direct energy deposition (DED) is a type of AM process in which a thermal energy source, such as a focussed laser, electron beam or plasma arc, is used to fuse and deposit material on top of a substrate [1]. The feedstock material for DED of Al-alloys is typically in the form of wire or powder, and protective gases such as Ar or N are used to avoid the formation of oxides. In addition, DED technologies are ideal for component repair by enabling desired features to be added on existing components [9,10]. Typically, DED processes can be classified into two major categories: wire and arc additive manufacturing (WAAM) and direct laser deposition (DLD) - of which laser engineered net shaping (LENS®) is also commercially known naming. Of these methods, considerable recent interest in the DLD approach has emerged in the past decade. The DLD method permits the production of graded materials, coatings, and has been successful in producing large-scale net-shape components; albeit principally for air stable materials [11–14]. However, specifically for Al-alloys, which are not well studied via DLD production to date; there has been particular interest in the WAAM of Al-alloys due to their ability to reduce material wastage when compared to conventional manufacturing processes [15–17].

Wire and arc additive manufacturing (WAAM) refers to the combination of an electric arc as heat source and wire as feedstock to fabricate the desired part layer-by-layer [18]. Furthermore, WAAM process is classified into three types based on the nature of heat source viz, laser-based, arc-based and electron-based [13,19]. Among these, arc-based techniques as presented in Figure 2.1, has shown promise due to improved energy efficiency and low cost of operation. Typically, a WAAM process involves 3D-model generation, setting deposition and welding parameters followed by post processing, to improve the metallurgical and mechanical properties [20].

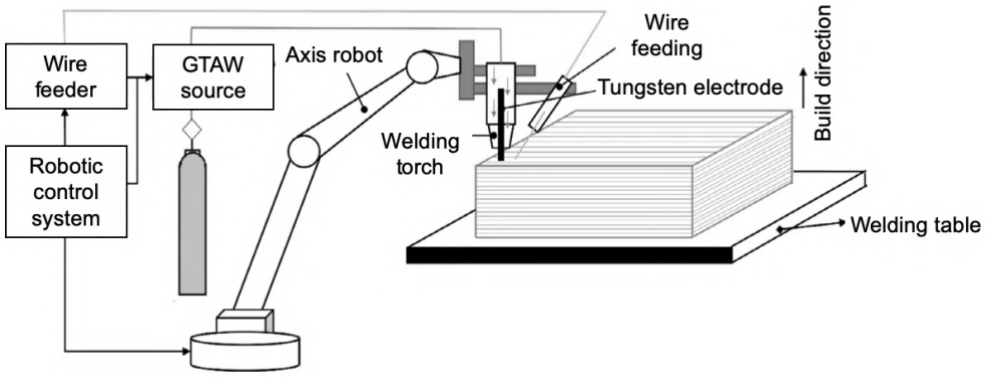

Figure 2.1: Schematic of a basic gas tungsten arc welding (GTAW) based wire and arc additive manufacturing process [17]

Extensive studies have been performed to produce different composition of aluminium alloys in the Al-Cu (2xxx) [21–24], Al-Si (4xxx) [25,26] and Al-Mg (5xxx) [27,28] alloy system through the WAAM process. However, only limited research is performed on the WAAM fabrication of Al-Mg-Si (6xxx) and Al-Zn-Mg (7xxx) alloys due to the presence of turbulent melt pool and excessive weld defects [19]. Only recently, WAAM process was used to fabricate 7055 and 7050 Al-alloy compositions where the results indicate that the mechanical properties were inferior to its wrought counterparts [29,30]. However, Klein et al. designed a novel Al-alloy with the composition of Al-3.6Zn-5.9Mg-0.5Mn-0.3Cu, through application oriented

testing of hot cracking susceptibility [31]. The applicability of the designed alloy was proven by the fabrication of a motorcycle piston with proof stresses of up to ~340 MPa and fracture strains of over 9%.

2.3 Powder bed fusion (PBF) of Al-alloys

Powder bed fusion (PBF) in AM refers to the processes in which thermal energy is used to melt and fuse selective regions of a powder bed [1]. For metal additive manufacturing through PBF, the thermal source typically used can be a laser or electron beam which further classifies PBF to: 1) Laser powder bed fusion (LPBF) and 2) Electron beam melting (EBM) processes [4,10,32]. Figure 2.2 show schematic representations of a LPBF and EBM system, respectively.

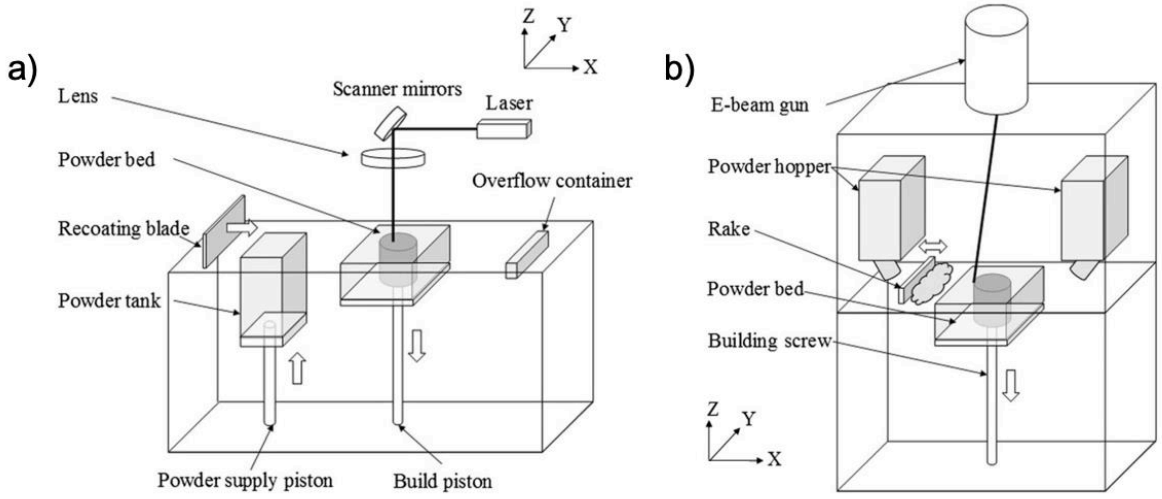

Figure 2.2: Schematic of powder bed fusion techniques – a) Selective laser melting and b) Electron beam melting [37]

EBM operates at a very high temperature (~ 650-1600°C) which is close to the melting point of Al-alloys (or their constituent elements) and the process works under vacuum conditions [33]. This results in the excess evaporation of aluminium that impacts the thermal exposure of

the alloy in an adverse manner and hence, EBM process has very limited application to Al-alloys [34–36]. In contrast, LBFP has been the dominant process that was explored for fabricating Al-alloys over the past few years and a summary of the literature on LPBF of Al-alloys will be discussed in this section.

2.3.1 Laser powder bed fusion (LPBF) of Al-alloys

Laser powder bed fusion (LPBF), commercially known as selective laser melting (SLM), is a generic powder bed additive manufacturing technique designed to melt and fuse selective regions of the metallic powders using a high intensity laser source [38]. In this process, thin layers of metal powder are fed through a powder tank with layer thickness (t) ranging between 20 μm – 100 μm and spread across the base plate using a recoating blade. Typically, the size of base plates of commercially available LPBF machines vary from 50 mm x 50 mm to 800 mm x 400 mm [32]. In addition, laser power (P) between 20W up to 1kW are available with laser scanning speed (v) ranging between 50 mm/s to 15m/s [39] . Once the laser scanning on the first layer is complete, the build plate is lowered and the next layer of powder is applied for the laser to scan in the x-y plane. The distance between scan tracks are termed as hatch spacing (h) [4,32] and this whole process is iterated until the final part is built as depicted in Figure 2.2. During this process, an inert build chamber is maintained with a continuous supply of nitrogen or argon to avoid the oxidation of the parts. Typically, the formation of oxide layers on the melt pools act as a source of porosity initiation and affects the metallurgical bonds between the aluminium powder layers [40].

Energy density (E) is an important factor in LPBF processing that directly affects the properties of the as built parts by controlling the degree of consolidation of the powder particles. The energy density function is given by [41,42]:

$$E = \frac{P}{v * h * t} \qquad \text{(Eq. 2.1)}$$

The energy density is optimised for the material under consideration and is different for different machines. Insufficient energy density is typically caused by low laser power and high scanning speed, and results in 'balling' due to the lack of wetting between subsequent layers of the melt pool [43,44]. In contrast, high laser powder and low scanning speed results in the material vaporisation and powder sputtering [45]. Therefore, a suitable combination of processing parameters is essential to obtain fully dense parts through LPBF processing.

To date, LPBF fabrication has been widespread in a variety of metal alloy systems that possess good weldability such as steels [46–51], titanium alloys [52–55] and nickel alloys [56–59]. However, the intrinsic physical properties of aluminium has limited the application of LPBF to Al-alloys [60–62] for the following reasons:

- Poor fluidity of Al-alloy powders that results in uneven layer thickness and affects layer quality.
- High laser reflectivity and thermal conductivity of Al-alloys with 91% and 237 W/(mK), respectively. This demands the use of high laser power to form dense parts through LPBF fabrication.
- The presence of stable oxide layer that results in the passivation of melt pool and causes metallurgical defects.
- High thermal expansion coefficient and the presence of wide solidification intervals generates hot cracking and large amount of residual stress that results in part deformation.

Nonetheless, the burgeoning research activity in this area has successfully implemented LPBF to Al-Si systems. However, high strength alloys in the 2xxx, 6xxx and 7xxx series that obtains

strengthening through precipitation hardening are hardly processable through LPBF due to their high solidification cracking behaviours [2,4,10,63–65].

2.3.1.1 LPBF of Al-Si alloys

Among the Al-Si system, the near eutectic alloys such as AlSi10Mg, Al-12Si, A357 and A356 alloys are the primary candidates for implementation of additive manufacturing process through LPBF. Among them, the most studied composition was the AlSi10Mg which was mainly due to low melting point and narrow solidification range [10,61,66], where the addition of 10 wt. % silicon increases the fluidity and minimises the solidification shrinkage [67].

The microstructure and mechanical properties of AlSi10Mg have been well documented in recent years [68–71] and was initially investigated by the works of Aboulkhair et al [40,72–76]. It is well known that the as-LPBF microstructure of AlSi10Mg comprises of large columnar grains that contain a fine dendritic structure due to the rapid solidification and typically results in enhanced mechanical properties [66]. Furthermore, Kim et al. revealed the extremely fine cellular structures in the melt pool and distinguished them into fine melt pool (FMP), heat affected zone (HAZ) and coarse melt pool (CMP) as shown in Figure 2.3 [77]. EDS analysis of the cells also reveal that they are mainly composed of α-Al matrix surrounded by Si-rich regions.

The Vickers hardness of as-LPBF AlSi10Mg was approximately 130-150 HV with tensile strengths and yield of 380-420 MPa and 250-350 MPa, respectively [78,79]. The obtained mechanical properties of as-LPBF AlSi10Mg were higher with respect to the heat treated cast alloy with the same composition [80]. The major strength contributions were attributed to the Hall-Petch mechanism due to eutectic cell boundaries, dislocation hardening and to the Orowan effect due to the presence of $MgSi_2$ particles [81]. Therefore, LPBF of AlSi10Mg was deeply studied in terms of post processing heat treatments, fatigue resistance, residual stress, corrosion

properties and machine learning [82–85]. Furthermore, reinforcement of TiC and TiCN to AlSi10Mg was also investigated to produce a metal matrix composite (MMC) through LPBF to further improve the mechanical properties [86–88].

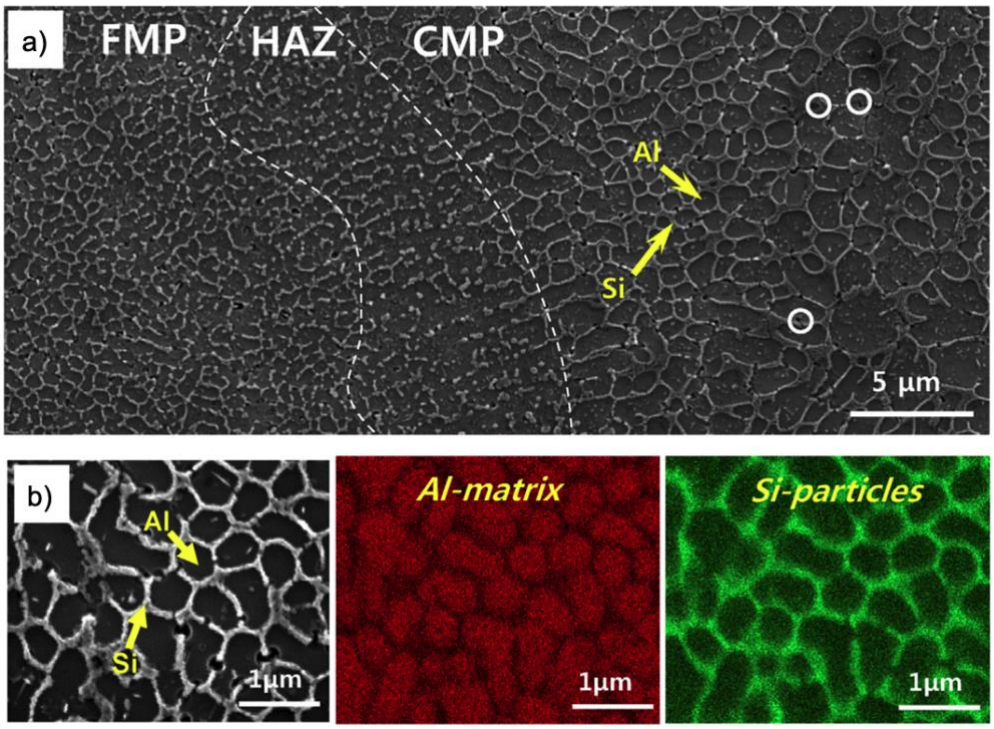

Figure 2.3: a) Microstructure of as-LPBF AlSi10Mg and b) chemical mapping using EDS, from [77]

Al-12Si is another casting alloy that was successfully processed with relative density > 99% and mechanical properties with tensile strength ranging between 380 – 400 MPa, by incorporating nano-composites [89–91]. This enabled the interest to fabricate lattice structures, analyse the tribological and corrosion properties of Al-Si12 alloys to exploit the micro- and meso-structures generated through LPBF to enhance the mechanical properties [92–95].

2.3.1.2 LPBF of Al-Cu-Mg alloys (2xxx series)

The LPBF of compositions typical of wrought aluminium alloys in the Al-Cu system, such as AA2022 (Al-5Cu-0.5Mg), AA2024 (Al-4Cu-Mg), AA2618A(Al-2Cu-1.5Mg-1.5Ni) and AA2219 (Al-6Cu-Mn) were investigated [96–99]. The preliminary works of this alloy system was done by Ahuja et al. in fabricating a nearly fully dense Al-Cu alloy (EN AW-2219 and EN AW-2618) through LPBF [97]. Following that, Zhang et al. fabricated an alloy composition close to AA2024 (Al-4.24Cu-1.97Mg-0.56Mn) with micro hardness value of 111 HV, UTS of 402 MPa and yield stress of 276 MPa through LPBF [98]. It was also reported that the mechanical properties of the LPBF prepared samples were comparable to AA2024 in the heat treated condition owing to an extremely fine supersaturated cellular-dendritic microstructure [100]. The corrosion behaviour of LPBF prepared AA2024-like composition (AM2024) was evaluated by Gharbi et al. where the corrosion rate of AM2024 was five times slower than AA2024 [96]. Furthermore, in-depth characterisation of the same Al-Cu-Mg alloy was recently reported and the summary of the findings are as depicted in Figure 2.4 [101].

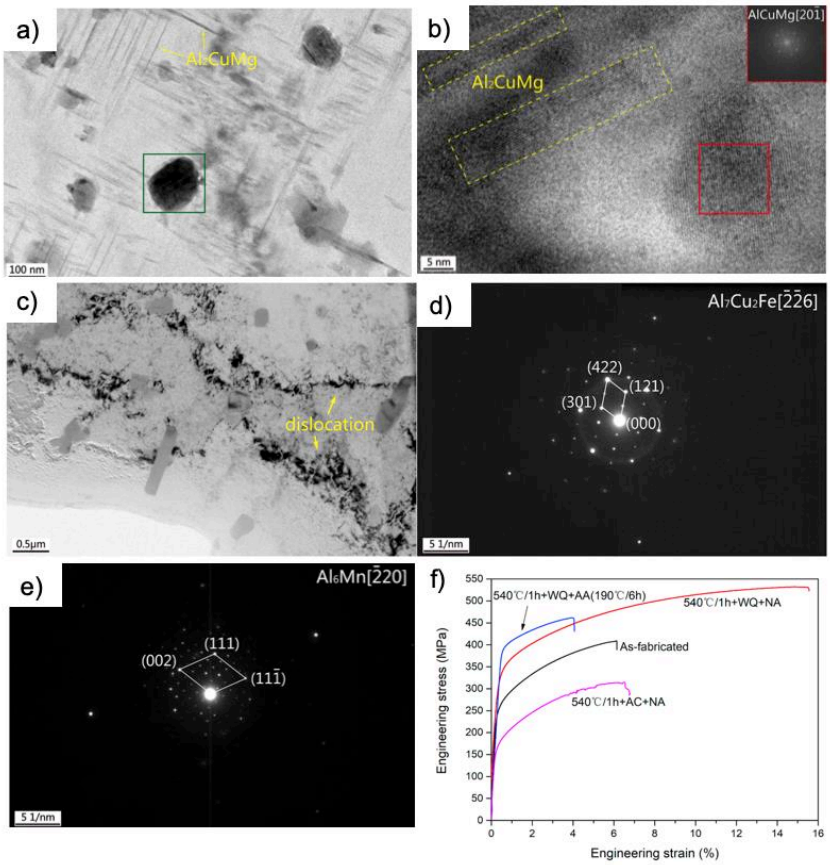

Figure 2.4: (a, c) TEM micrographs, b) High resolution TEM micrograph and (d, e) selected area diffraction patterns (SADP) of LPBF prepared Al-Cu-Mg specimen solutionised at 540 °C for 1 h, water quenched, and aged at 190 °C for 6 h. f) Tensile curves of the typical LPBF Al-Cu-Mg specimens. WQ, AC, NA, and AA refer to water quenching, air cooling, natural aging, and artificial aging. (Adapted from [101])

It was revealed that the Al-Cu-Mg alloy was strengthened through the formation of high-density acicular ultra-fine AlCuMg, Al_2CuMg and Al_7Cu_2Fe phase through appropriate heat treatment conditions, where the Al_6Mn phase was reported to be deterimental to mechanical properties. Modification of Al-Cu-Mg through the addition of Zr has also been investigated to minimise cracking through grain refinement [102].

2.3.1.3 LPBF of Al-Mg-Si alloys (6xxx series)

The initial efforts to fabricate the commercial Al-alloy composition of AA 6061 (Al-0.6Si-

1Mg-0.3Cu) through LPBF led to formation of hot cracking and excessive porosity [103]. However, one approach by Uddin et al. to minimise the defects was to heat the powder bed to 500°C to produce crack-free AA 6061 as shown in Figure 2.5 [104].

Another successful approach was through the addition of expensive nano-nucleants such as Zr or Yittrium Stabilised Zirconia (YSZ) to induce grain refinement to avoid the development of large columnar structures [105,106]. The influence of Zr in eliminating cracks and porosity are shown in Figure 2.6.

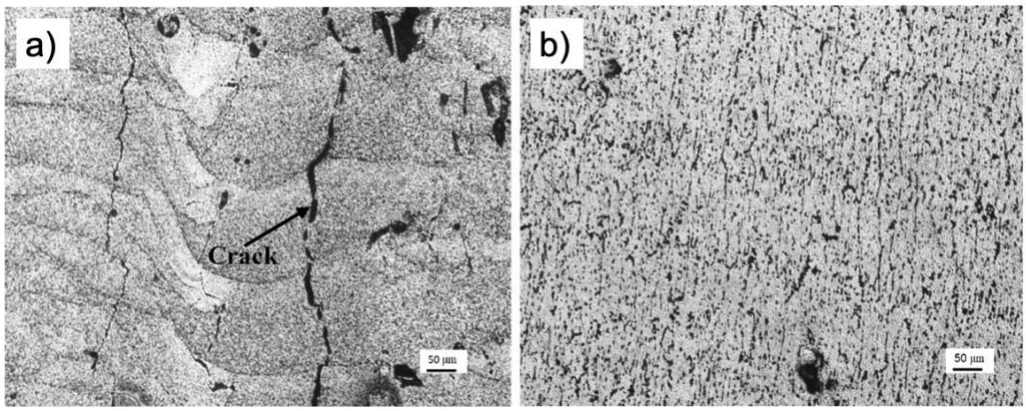

Figure 2.5:Microstructure of AA6061 specimens fabricated on a) unheated powder bed and b) powder bed heated to 500°C [104]

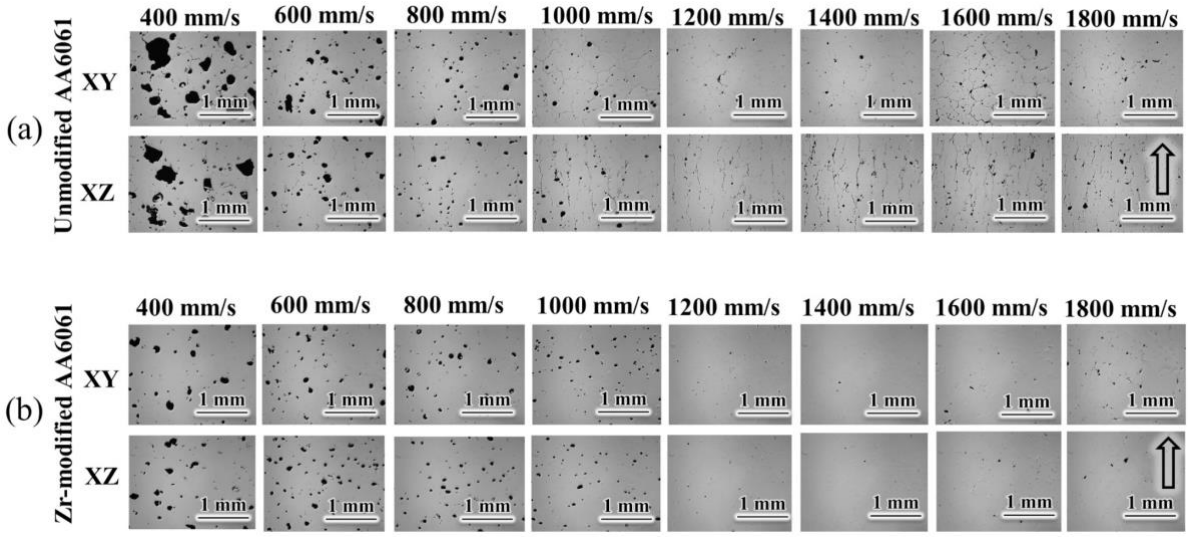

Figure 2.6: Optical micrographs of the as-built (a) unmodified AA6061 and (b) Zr-modified AA6061 from the XY and XZ cross-sections at a laser power of 350 W [106]

2.3.1.4 LPBF of Al-Mg-Sc-Zr alloys (modified 5xxx-series Al-alloys)

The benefits of adding scandium (Sc) as alloying element in Al-alloys are well documented [5,107]. However, the capability of LPBF to extend the solid solubility of Sc in aluminium was first explored by Schmidtke et al. where the concept of Scalmalloy® (Al-0.66Sc-4.5Mg-0.37Zr-0.17Si) was developed with the composition specifically designed for additive manufacturing [108]. Scalmalloy® reveals a good combination of mechanical properties, making it an ideal candidate for aerospace applications to fabricate satellite components [109,110]. A detailed investigation on the post processing heat treatment and microstructures of Scalmalloy® was performed by Spierings et al. where a maximum yield strength of 520 MPa was achieved [111]. It was seen that high laser input was required to produce dense samples that exhibited a bimodal microstructure with coarse- and fine-grained material as shown in Figure 2.7a. The microstructure was reported to be decorated with coherent nano-metre sized $Al_3(Sc_x\ Zr_{1-x})$ particles that resulted in the improved mechanical strength as shown in Figure 2.7b and c, respectively [112,113]. Such particles are unique to LPBF processing and are not observed during conventional processing of the alloy which emphasises the need for new alloy design specifically tailored for LPBF processing.

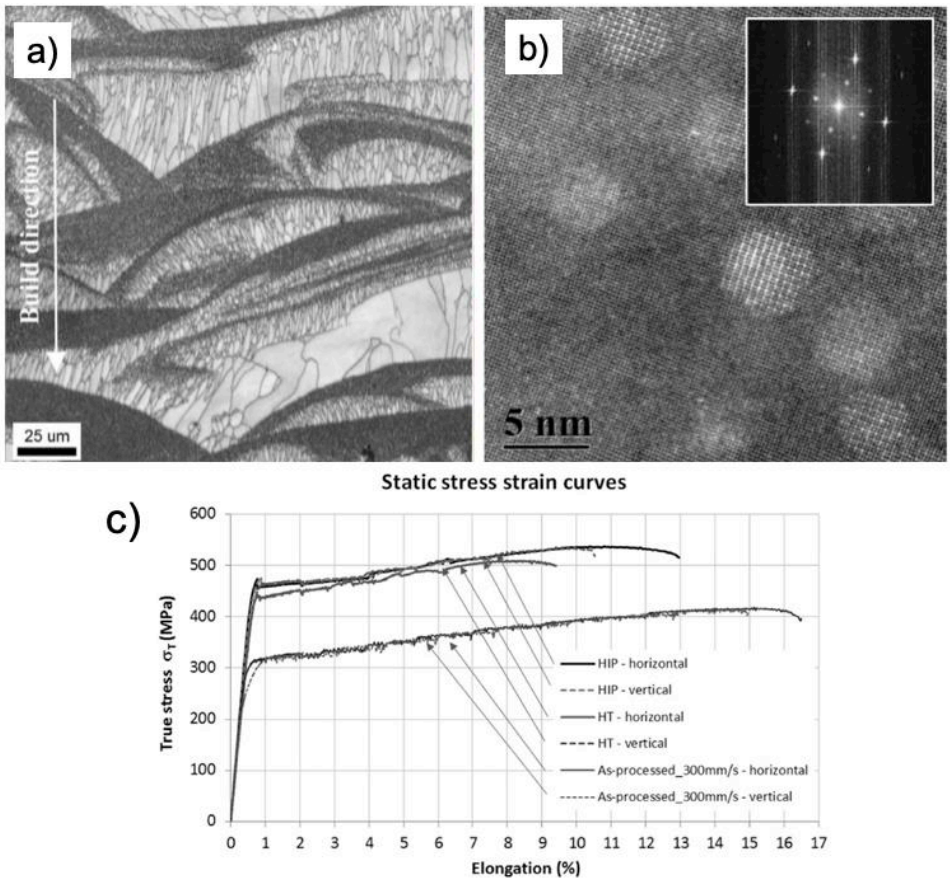

Figure 2.7: a) Bimodal microstructure showing coarse- and fine-grain distribution in Scalmalloy® [113], b) STEM micrographs showing the Al_3Sc particles within the fine-grain region [113] and c) Mechanical stress-strain curves of Scalmalloy under different conditions [111]

Following the promising results obtained from Scalmalloy®, Jia et al. designed another new alloy (Al-4.52Mn-1.32Mg-0.79Sc-0.74Zr) in the Al-Mn-Sc system that was particularly tailored for LPBF processing [114–116]. Solid solution strengthening, grain boundary strengthening and modulus hardening were proposed as the major strengthening mechanisms with a yield strength of 560 MPa and ductility of 18% after a single step heat treatment of 5h at 300°C [116]. The typical stress-strain curve of the developed Al-Mn-Sc alloy and the comparison with other high strength aluminium alloys are shown in Figure 2.8.

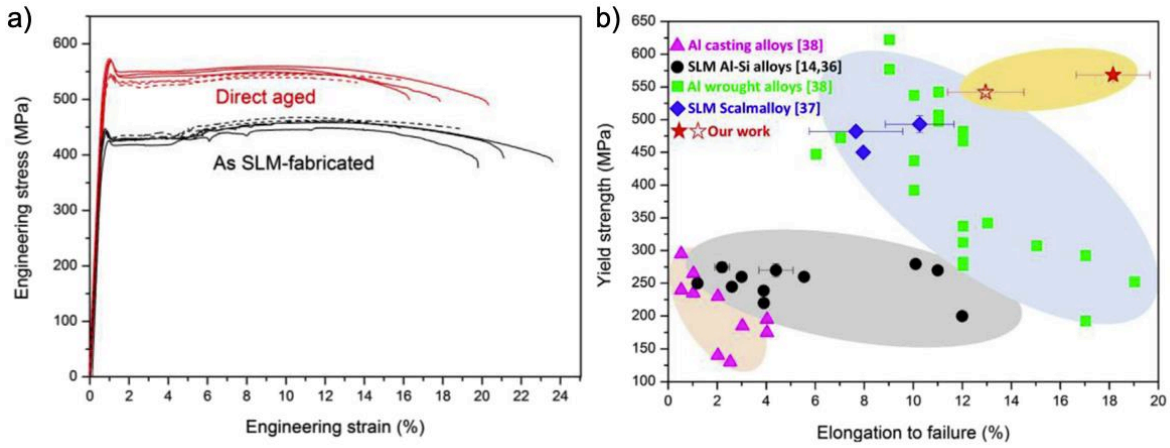

Figure 2.8: a) Stress strain curves of Al-Mn-Sc alloy in the as-fabricated and heat treated conditions and b) Comparison of properties of LPBF prepared Al-Sc-Mn alloy with other wrought Al-alloys [116]

2.3.1.5 LPBF of Al-Zn-Mg(-Cu) alloys (7xxx series)

The alloy system that offers the greatest potential for age hardening and finds extensive high strength applications is the Al-Mg-Zn(-Cu) system, where Mg and Zn contribute to precipitation strengthening while Cu promotes solid solution strengthening [117,118]. The Al-Zn-Mg(-Cu) alloys have found important applications in the aviation, automobile and transportation sector which naturally brands them as a popular selection for LPBF fabrication. Therefore, preliminary investigations were carried out by Kaufmann et al where significant efforts were made to fabricate a high strength aluminium alloy (EN AW 7075) through LPBF [119]. The same alloy system was also explored by Monteri-Sistiaga et al. by modifying the alloy composition of AA7075 with the addition of 4 wt. % Si. This aided a decrease in solidification range of the alloy while improving the fluidity, thereby leading to an increased density [120]. However, the rapid solidification through LPBF resulted in significant hot cracking and excess porosity while fabricating Al-Zn-Mg(-Cu) alloys and the resulting mechanical properties were inferior to their respective wrought counterparts [121].

Furthermore, works by Gharbi et al. and Kairy et al. revealed a new quasicrystalline phase, termed as ν-phase, that was formed in the as-LPBF 7075 Al-alloy which emphasises on the unique benefits of LPBF processing [122,123].

Recently, an approach of introducing nanoparticles of nucleants during LPBF process, that would help in controlling the solidification dynamics was successfully implemented by Martin et al. where they successfully printed crack free AA7075 with the aid of Zirconium nano-nucleants [124]. This led to the grain refinement of the material as expected, thereby producing crack-free materials with good mechanical properties as shown in Figure 2.9.

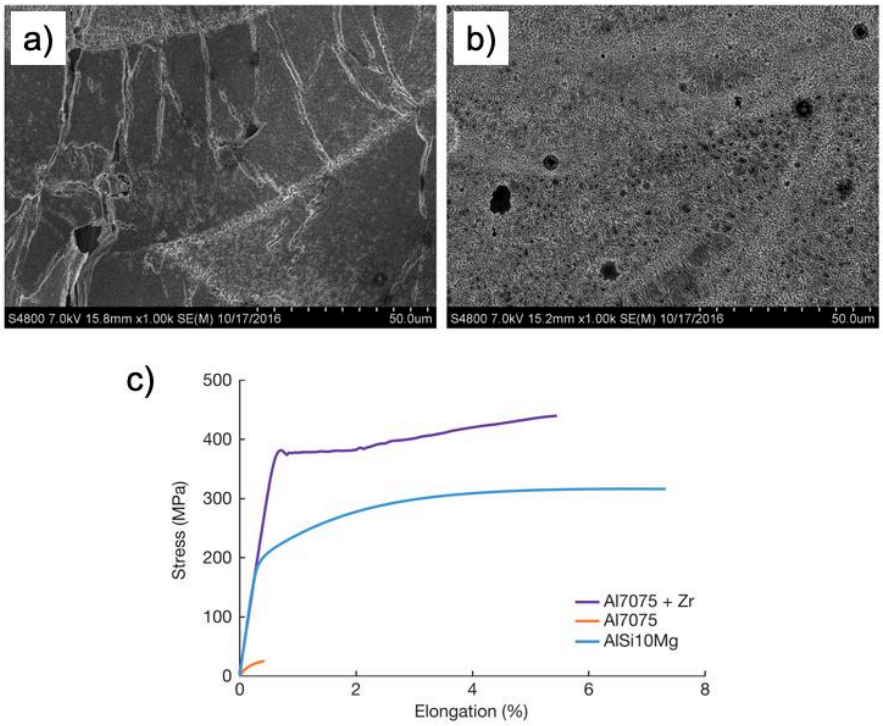

Figure 2.9: a) Large network of cracks observed in as-LPBF AA7075 without Zr, b) Absence of cracks after the addition of Zr nano-nucleant with some residual porosity and c) Mechanical properties of LPBF processed Al7075, Al7075 + Zr and AlSi10Mg [124]

A similar approach was followed on other investigations where Zr, Si and/or TiB_2 were incorporated in Al-Zn-Mg-Cu alloys to promote grain refinement and avoid the formation of defects as shown in Figure 2.10 [125,126].

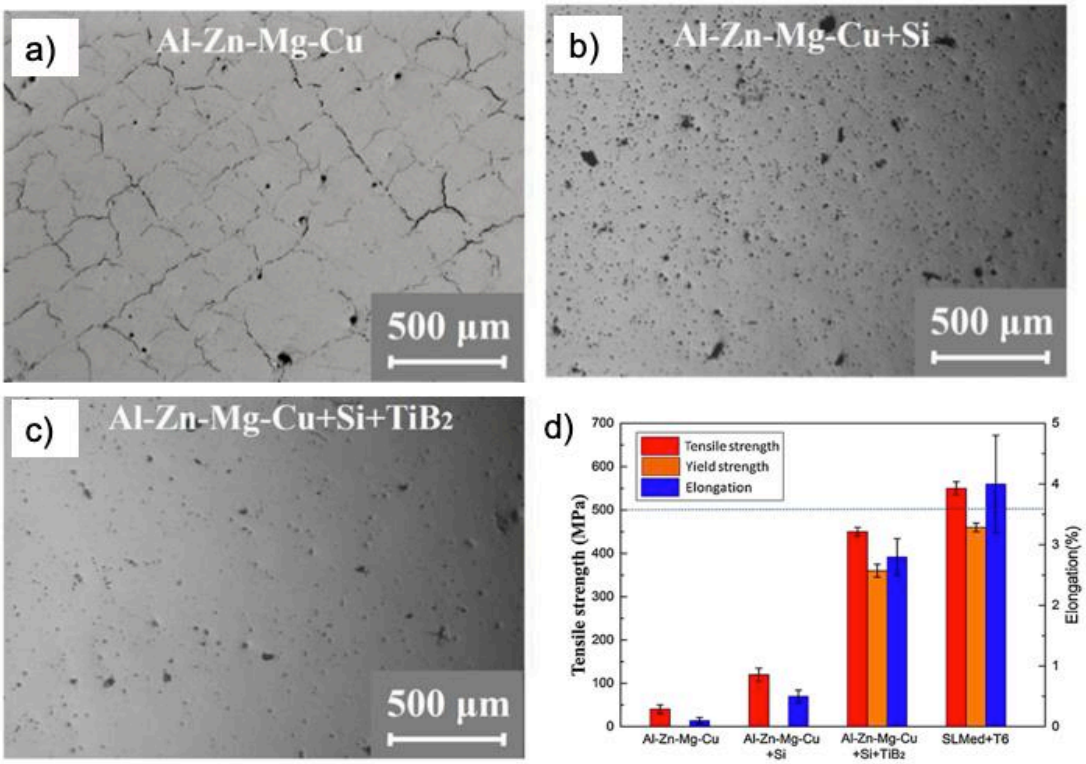

Figure 2.10: (a-c) Influence of Si and TiB^2 addition in minimising the formation of cracks in Al-Zn-Mg alloy and d) Mechanical properties of the Al-Zn-Mg with Si and TiB_2 addition [125].

2.4 Challenges faced in the AM of Al-Zn-Mg alloys

The LPBF processing of Al-Zn-Mg-(Cu) system are prone to defects due to the manufacturing conditions and the intrinsic properties of the alloys. Typically, the most common defects include the formation of porosity and hot cracking [2].

Porosity formation is the considered to be a major defect in components produced by LPBF. The cause of such defects during LPBF fabrication of Al-alloys are attributed to the following factors: metallurgical pores originating from the absorption of surrounding gases, the vaporization of alloying elements, wettability of aluminium by its successive melted layers, impurities present and the low laser absorption of aluminium [127]. Majority of these causes can be routed back to the processing parameters which can be carefully controlled to reduce

the formation of porosities to a possible extent [128]. For this reason, the porosity levels obtained from LPBF prepared components specifies the material's final performance.

Hot cracking or solidification cracking is a very common metallurgical defect in the LPBF fabrication of 2xxx and 7xxx series Al-alloys [5,107]. Typically, a large solidification range gives rise to the formation of hot cracks due to the lack of supply of liquid metal to the inter-dendritic region [129]. One method to avoid the formation of these cracks is by altering the composition of the alloy to promote the formation of eutectics which will minimise the formation of cracks [130]. Several models have been developed to define the phenomenon of hot cracking with respect to different composition of Al-alloys [129,131].

2.5 Effect of solute content on hot cracking

The relationship between the hot cracking susceptibility of Al-alloys and the percentage of alloying elements exhibits a characteristic 'lambda shape' curve as shown in Figure 2.11. Typically, high resistance to hot cracking is displayed at both low and high alloying content [132]. At low levels of alloying content, only a small amount of eutectic is formed, which on solidification results in a very thin liquid film along the grain boundaries. When the thickness of the liquid film increases as a result of increasing alloying additions, the susceptibility to hot cracking also increases [129]. However, if the percentage of alloying addition increases, the defects along the inter-dendritic region backfills due to the formation of a large amount of eutectic and thereby, minimising the crack sensitivity of the alloy [131,133].

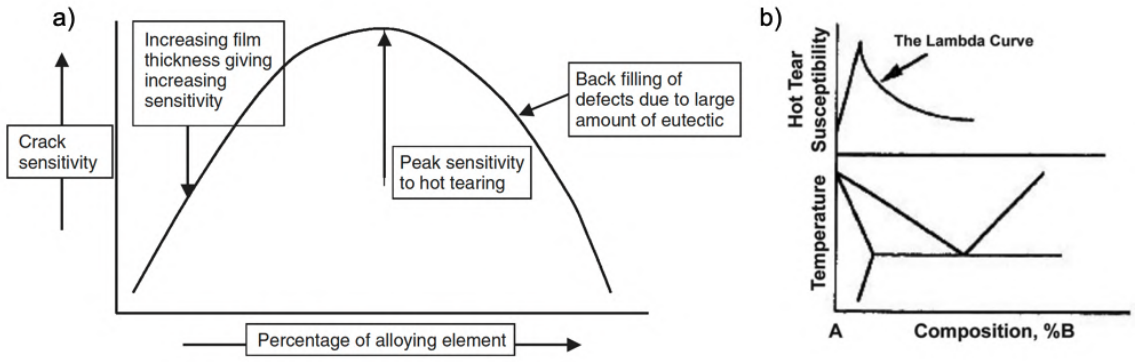

Figure 2.11: Effect of alloying elements on the hot cracking susceptibility of Al-alloys [132,134]

2.5.1 High solute alloys in the Al-Zn-Mg system

High strength alloys in the Al-Zn-Mg system are strengthened through precipitation hardening by the formation of η' and η ($MgZn_2$) phase and the precipitation sequence is as follows:

Supersaturated solid solution → Guinier Preston (GP) zones → η' metastable → η stable ($MgZn_2$) [5,118]. The aluminium rich corner of the ternary Al-Zn-Mg diagram has been thoroughly reported and an isothermal section at 200°C is shown in Figure 2.12. Depending on the solubility temperature and Zn/Mg ratio, formation of GP zones and metastable modifications of the phase, $MgZn_2$ and $Mg_{32}(Zn, Al)_{49}$ could alter the extent of strengthening. In the context of achieving high strength Al-Zn-Mg alloys, increasing the formation of η' and η ($MgZn_2$) phase during artificial ageing are of significant interest. As such, high Zn and Mg contents have been explored in the Al-Zn-Mg system through conventional ingot metallurgy, however such attempts have resulted in several processing challenges [135]. On the contrary, other powder metallurgy and rapid solidification techniques, such as the Osprey spray deposition process [136], have produced Al-Zn-Mg alloys with 12 wt. % Zn content that resulted in strengths > 600 MPa [137–139]. Such alloys are populated with high volume fraction of second phase particles that aids an improvement in mechanical properties as shown

in Figure 2.13 [140]. The commercial usage of these high solute alloys are limited due to complex processing and post-processing through these rapid solidification processes.

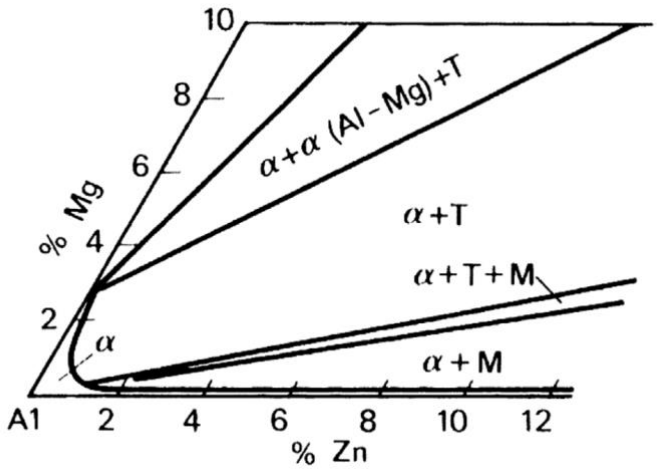

Figure 2.12: Section of ternary Al-Zn-Mg phase diagram at 200°C. M – $MgZn_2$; T – Mg_{32} $(Zn, Al)_{49}$ [5].

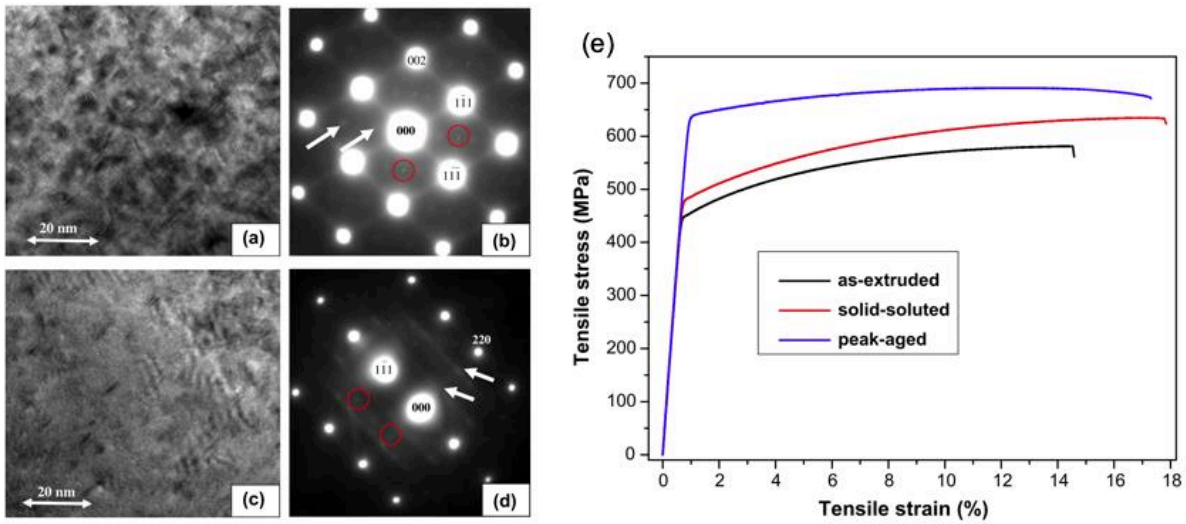

Figure 2.13: Bright field TEM micrographs and corresponding SADPs of peak aged spray deposited Al-Zn-Mg-Cu taken along $[110]_{Al}$ zone axis (a and b) and $[112]_{Al}$ zone axis (c and d), respectively and e) Stress-stain curves of spray deposited Al-Zn-Mg after different heat treatments [140].

2.6 Summary of literature review and gaps in knowledge

The high strength aluminium alloys obtained through conventional and LPBF routes are as summarised in Table 2.1. It is clear that the Al-alloys processed by conventional manufacturing processes still possess higher mechanical properties than the LPBF processed Al-alloys. It is also revealed that the fabrication of the conventional compositions through LPBF results in the formation of excessive defects as shown in Figure 2.14, due to a number of aforementioned factors. Therefore, there is a clear need to develop and design Al-alloy compositions that are specifically tailored for additive manufacturing [141], including laser based additive manufacturing specifically.

Table 2.1: Comparison of tensile properties of high strength Al alloy processed through LPBF and conventional processing

Manufacturing route	Alloy IADS designation	Ultimate tensile strength (MPa)	Elongation (%)
Wrought aluminium alloys [5]	AA2024 – T8	480	6
	AA2124 – T8	490	8
	AA6151 – T6	330	17
	AA7001 – T6	675	9
	AA7075 – T6	570	11
	AA7178 – T6	610	10
LPBF prepared Al-alloys	AlSi10Mg [73]	420	11
	AlSi10Mg+TiC [142]	482	10.8
	6061 [106]	392	3.9
	2024 [101]	532	13
	Scalmalloy® [113]	550	14

	Al-Mn-Sc [114]	573	18

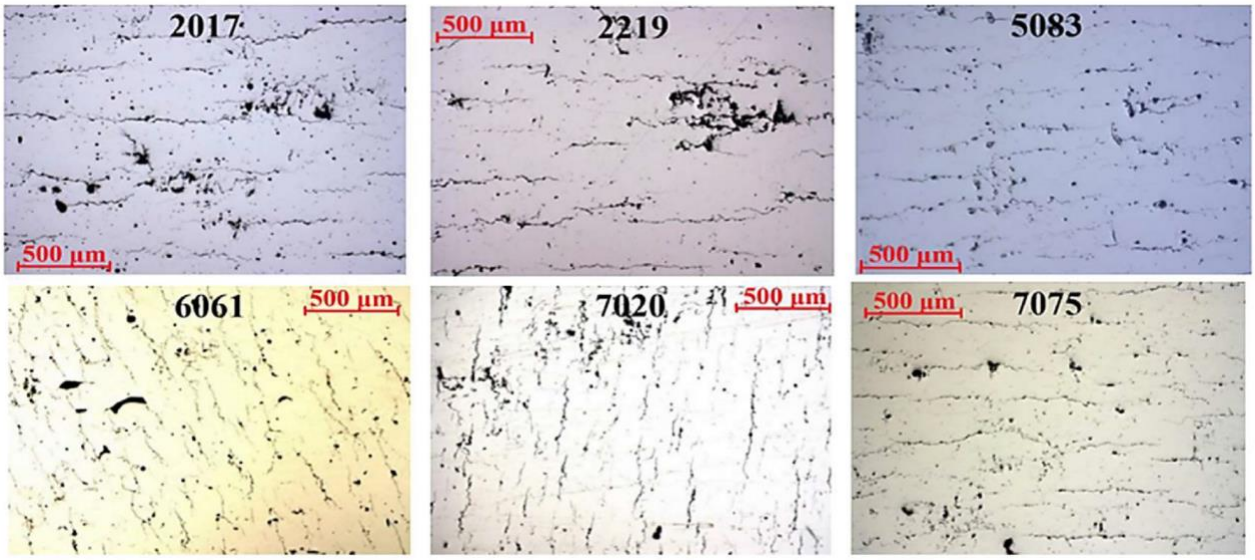

Figure 2.14: SEM micrographs of the defects in LPBF processed AA2017, AA2219, AA5083, AA6061, AA7020 and AA7075 [2]

Several studies have also revealed the unique benefits offered by additive manufacturing, and the alloys such as Scalmalloy and Al-Sc-Mn alloy exploit them through solute supersaturation [113–115]. On the contrary, LPBF of Al-alloys in the Al-Zn-Mg system are readily prone to hot cracking and demands the use of expensive alloying additions such as Sc or Zr to avoid cracking through grain refinement. However, studies also reveal that increasing the formation of eutectics by the addition of excess solute might also minimise the crack sensitivity. Furthermore, the addition of excess solute such as Zn and Mg in the Al-Zn-Mg system results in improved mechanical properties. However, the extent of solute addition is restricted due to the degree of rapid solidification and the complexity of the processing route. Nevertheless, LPBF process has the ability to overcome alloy processing complexities, as the process results in net shape (i.e. final shape) components, where rapid solidification may also be exploited to hyper load solute – offering the prospect of producing new, low cost and high strength aluminium alloys.

References

[1] A. 52900:2015, Standard Terminology for Additive Manufacturing – General Principles – Terminology, ASTM Int. i (2015) 1–9. https://doi.org/10.1520/F2792-12A.2.

[2] S.C. Altıparmak, V.A. Yardley, Z. Shi, J. Lin, Challenges in additive manufacturing of high-strength aluminium alloys and current developments in hybrid additive manufacturing, Int. J. Light. Mater. Manuf. 4 (2021) 246–261. https://doi.org/10.1016/j.ijlmm.2020.12.004.

[3] I. Gibson, D. Rosen, B. Stucker, Additive manufacturing technologies: 3D printing, rapid prototyping, and direct digital manufacturing, second edition, Springer New York, 2015. https://doi.org/10.1007/978-1-4939-2113-3.

[4] W.E. Frazier, Metal additive manufacturing: A review, J. Mater. Eng. Perform. 23 (2014) 1917–1928. https://doi.org/10.1007/s11665-014-0958-z.

[5] I.J. Polmear, D. StJohn, J.-F. Nie, M. Qian, Light alloys : metallurgy of the light metals, 2017.

[6] T. Pereira, J. V. Kennedy, J. Potgieter, A comparison of traditional manufacturing vs additive manufacturing, the best method for the job, Procedia Manuf. 30 (2019) 11–18. https://doi.org/10.1016/j.promfg.2019.02.003.

[7] S. Kim, S.K. Moon, A part consolidation design method for additive manufacturing based on product disassembly complexity, Appl. Sci. 10 (2020). https://doi.org/10.3390/app10031100.

[8] J.C. Najmon, S. Raeisi, A. Tovar, Review of additive manufacturing technologies and applications in the aerospace industry, Elsevier Inc., 2019. https://doi.org/10.1016/B978-0-12-814062-8.00002-9.

[9] R.P. Mudge, N.R. Wald, Laser engineered net shaping advances additive manufacturing and repair, Weld. J. (Miami, Fla). 86 (2007) 44–48.

[10] S. Lathabai, Additive Manufacturing of Aluminium-Based Alloys and Composites, in: Fundam. Alum. Metall., Elsevier, 2018: pp. 47–92. https://doi.org/10.1016/b978-0-08-102063-0.00002-3.

[11] D.R. Feenstra, R. Banerjee, H.L. Fraser, A. Huang, A. Molotnikov, N. Birbilis, Current Opinion in Solid State & Materials Science Critical review of the state of the art in multi-

material fabrication via directed energy deposition, Curr. Opin. Solid State Mater. Sci. 25 (2021) 100924. https://doi.org/10.1016/j.cossms.2021.100924.

[12] D.R. Feenstra, A. Molotnikov, N. Birbilis, Utilisation of artificial neural networks to rationalise processing windows in directed energy deposition applications, Mater. Des. 198 (2021) 109342. https://doi.org/10.1016/j.matdes.2020.109342.

[13] N. Shamsaei, A. Yadollahi, L. Bian, S.M. Thompson, An overview of Direct Laser Deposition for additive manufacturing; Part II: Mechanical behavior, process parameter optimization and control, Addit. Manuf. 8 (2015) 12–35. https://doi.org/10.1016/j.addma.2015.07.002.

[14] S.M. Thompson, L. Bian, N. Shamsaei, A. Yadollahi, An overview of Direct Laser Deposition for additive manufacturing; Part I: Transport phenomena, modeling and diagnostics, Addit. Manuf. 8 (2015) 36–62. https://doi.org/10.1016/j.addma.2015.07.001.

[15] K.S. Derekar, A review of wire arc additive manufacturing and advances in wire arc additive manufacturing of aluminium, Mater. Sci. Technol. (United Kingdom). 34 (2018) 895–916. https://doi.org/10.1080/02670836.2018.1455012.

[16] M.M. Tawfik, M.M. Dewidar, Enhancing the Properties of Aluminum Alloys Fabricated Using Wire + Arc Additive Manufacturing Technique - A Review M.M., J. Mater. Res. Technol. (2021). https://doi.org/10.1016/j.jmrt.2021.04.076.

[17] K.E.K. Vimal, M. Naveen Srinivas, S. Rajak, Wire arc additive manufacturing of aluminium alloys: A review, Mater. Today Proc. 41 (2021) 1139–1145. https://doi.org/10.1016/j.matpr.2020.09.153.

[18] S.W. Williams, F. Martina, A.C. Addison, J. Ding, G. Pardal, P. Colegrove, Wire + Arc additive manufacturing, Mater. Sci. Technol. (United Kingdom). 32 (2016) 641–647. https://doi.org/10.1179/1743284715Y.0000000073.

[19] B. Wu, Z. Pan, D. Ding, D. Cuiuri, H. Li, J. Xu, J. Norrish, A review of the wire arc additive manufacturing of metals: properties, defects and quality improvement, J. Manuf. Process. 35 (2018) 127–139. https://doi.org/10.1016/j.jmapro.2018.08.001.

[20] D. Ding, Z. Pan, D. Cuiuri, H. Li, A multi-bead overlapping model for robotic wire and arc additive manufacturing (WAAM), Robot. Comput. Integr. Manuf. 31 (2015) 101–110. https://doi.org/10.1016/j.rcim.2014.08.008.

[21] B. Cong, J. Ding, S. Williams, Effect of arc mode in cold metal transfer process on porosity of additively manufactured Al-6.3%Cu alloy, Int. J. Adv. Manuf. Technol. 76 (2015) 1593–1606. https://doi.org/10.1007/s00170-014-6346-x.

[22] J.Y. Bai, C.L. Yang, S.B. Lin, B.L. Dong, C.L. Fan, Mechanical properties of 2219-Al components produced by additive manufacturing with TIG, Int. J. Adv. Manuf. Technol. 86 (2016) 479–485. https://doi.org/10.1007/s00170-015-8168-x.

[23] J. Gu, J. Ding, S.W. Williams, H. Gu, P. Ma, Y. Zhai, The effect of inter-layer cold working and post-deposition heat treatment on porosity in additively manufactured aluminum alloys, J. Mater. Process. Technol. 230 (2016) 26–34. https://doi.org/10.1016/j.jmatprotec.2015.11.006.

[24] Z. Qi, B. Cong, B. Qi, G. Zhao, J. Ding, Properties of wire + arc additively manufactured 2024 aluminum alloy with different solution treatment temperature, Mater. Lett. 230 (2018) 275–278. https://doi.org/10.1016/j.matlet.2018.07.144.

[25] H. Wang, W. Jiang, J. Ouyang, R. Kovacevic, Rapid prototyping of 4043 Al-alloy parts by VP-GTAW, J. Mater. Process. Technol. 148 (2004) 93–102. https://doi.org/10.1016/j.jmatprotec.2004.01.058.

[26] Y. Wang, S. Yang, C. Xie, H. Liu, Q. Zhang, Microstructure and Ratcheting Behavior of Additive Manufactured 4043 Aluminum Alloy, J. Mater. Eng. Perform. 27 (2018) 4582–4592. https://doi.org/10.1007/s11665-018-3563-8.

[27] J. Gu, X. Wang, J. Bai, J. Ding, S. Williams, Y. Zhai, K. Liu, Deformation microstructures and strengthening mechanisms for the wire+arc additively manufactured Al-Mg4.5Mn alloy with inter-layer rolling, Mater. Sci. Eng. A. 712 (2018) 292–301. https://doi.org/10.1016/j.msea.2017.11.113.

[28] C. Zhang, Y. Li, M. Gao, X. Zeng, Wire arc additive manufacturing of Al-6Mg alloy using variable polarity cold metal transfer arc as power source, Mater. Sci. Eng. A. 711 (2018) 415–423. https://doi.org/10.1016/j.msea.2017.11.084.

[29] B. Dong, X. Cai, S. Lin, X. Li, C. Fan, C. Yang, H. Sun, Wire arc additive manufacturing of Al-Zn-Mg-Cu alloy: Microstructures and mechanical properties, Addit. Manuf. 36 (2020) 101447. https://doi.org/10.1016/j.addma.2020.101447.

[30] Z. Yu, T. Yuan, M. Xu, H. Zhang, X. Jiang, S. Chen, Microstructure and mechanical properties of Al-Zn-Mg-Cu alloy fabricated by wire + arc additive manufacturing, J.

Manuf. Process. 62 (2021) 430–439. https://doi.org/10.1016/j.jmapro.2020.12.045.

[31] T. Klein, M. Schnall, B. Gomes, P. Warczok, D. Fleischhacker, P.J. Morais, Wire-arc additive manufacturing of a novel high-performance Al-Zn-Mg-Cu alloy: Processing, characterization and feasibility demonstration, Addit. Manuf. 37 (2021) 101663. https://doi.org/10.1016/j.addma.2020.101663.

[32] D. Herzog, V. Seyda, E. Wycisk, C. Emmelmann, Additive manufacturing of metals, Acta Mater. 117 (2016) 371–392. https://doi.org/10.1016/j.actamat.2016.07.019.

[33] V. Juechter, T. Scharowsky, R.F. Singer, C. Körner, Processing window and evaporation phenomena for Ti-6Al-4V produced by selective electron beam melting, Acta Mater. 76 (2014) 252–258. https://doi.org/10.1016/j.actamat.2014.05.037.

[34] C. Körner, Additive manufacturing of metallic components by selective electron beam melting - A review, Int. Mater. Rev. 61 (2016) 361–377. https://doi.org/10.1080/09506608.2016.1176289.

[35] D. Riedlbauer, T. Scharowsky, R.F. Singer, P. Steinmann, C. Körner, J. Mergheim, Macroscopic simulation and experimental measurement of melt pool characteristics in selective electron beam melting of Ti-6Al-4V, Int. J. Adv. Manuf. Technol. 88 (2017) 1309–1317. https://doi.org/10.1007/s00170-016-8819-6.

[36] X. Gong, T. Anderson, K. Chou, Review on powder-based electron beam additive manufacturing Technology, Manuf. Rev. 1 (2014). https://doi.org/10.1051/mfreview/2014001.

[37] Y. Zhang, L. Wu, X. Guo, S. Kane, Y. Deng, Y.G. Jung, J.H. Lee, J. Zhang, Additive Manufacturing of Metallic Materials: A Review, J. Mater. Eng. Perform. 27 (2018) 1–13. https://doi.org/10.1007/s11665-017-2747-y.

[38] C.Y. Yap, C.K. Chua, Z.L. Dong, Z.H. Liu, D.Q. Zhang, L.E. Loh, S.L. Sing, Review of selective laser melting: Materials and applications, Appl. Phys. Rev. 2 (2015). https://doi.org/10.1063/1.4935926.

[39] G. Scamans, H.-T. Li, J.L. Nebreda, J. Patel, I. Stone, Y. Wang, X. Yang, Z. Fan, Advanced Casting Technologies Using High Shear Melt Conditioning, in: Fundam. Alum. Metall., Elsevier, 2018: pp. 249–277. https://doi.org/10.1016/b978-0-08-102063-0.00008-4.

[40] M. Simonelli, C. Tuck, N.T. Aboulkhair, I. Maskery, I. Ashcroft, R.D. Wildman, R.

Hague, A Study on the Laser Spatter and the Oxidation Reactions During Selective Laser Melting of 316L Stainless Steel, Al-Si10-Mg, and Ti-6Al-4V, Metall. Mater. Trans. A Phys. Metall. Mater. Sci. 46 (2015) 3842–3851. https://doi.org/10.1007/s11661-015-2882-8.

[41] L. Thijs, K. Kempen, J.P. Kruth, J. Van Humbeeck, Fine-structured aluminium products with controllable texture by selective laser melting of pre-alloyed AlSi10Mg powder, Acta Mater. 61 (2013) 1809–1819. https://doi.org/10.1016/j.actamat.2012.11.052.

[42] R. Xiao, X. Zhang, Problems and issues in laser beam welding of aluminum–lithium alloys, J. Manuf. Process. 16 (2014) 166–175. https://doi.org/10.1016/J.JMAPRO.2013.10.005.

[43] M. Islam, T. Purtonen, H. Piili, A. Salminen, O. Nyrhilä, Temperature profile and imaging analysis of laser additive manufacturing of stainless steel, in: Phys. Procedia, Elsevier, 2013: pp. 835–842. https://doi.org/10.1016/j.phpro.2013.03.156.

[44] A. Aversa, M. Moshiri, E. Librera, M. Hadi, G. Marchese, D. Manfredi, M. Lorusso, F. Calignano, S. Biamino, M. Lombardi, M. Pavese, Single scan track analyses on aluminium based powders, J. Mater. Process. Technol. 255 (2018) 17–25. https://doi.org/10.1016/j.jmatprotec.2017.11.055.

[45] T. Qi, H. Zhu, H. Zhang, J. Yin, L. Ke, X. Zeng, Selective laser melting of Al7050 powder: Melting mode transition and comparison of the characteristics between the keyhole and conduction mode, Mater. Des. 135 (2017) 257–266. https://doi.org/10.1016/j.matdes.2017.09.014.

[46] F. Bartolomeu, M. Buciumeanu, E. Pinto, N. Alves, O. Carvalho, F.S. Silva, G. Miranda, 316L stainless steel mechanical and tribological behavior—A comparison between selective laser melting, hot pressing and conventional casting, Addit. Manuf. 16 (2017) 81–89. https://doi.org/10.1016/j.addma.2017.05.007.

[47] G. Miranda, S. Faria, F. Bartolomeu, E. Pinto, S. Madeira, A. Mateus, P. Carreira, N. Alves, F.S. Silva, O. Carvalho, Predictive models for physical and mechanical properties of 316L stainless steel produced by selective laser melting, Mater. Sci. Eng. A. 657 (2016) 43–56. https://doi.org/10.1016/j.msea.2016.01.028.

[48] R. Li, Y. Shi, Z. Wang, L. Wang, J. Liu, W. Jiang, Densification behavior of gas and water atomized 316L stainless steel powder during selective laser melting, Appl. Surf.

Sci. 256 (2010) 4350–4356. https://doi.org/10.1016/j.apsusc.2010.02.030.

[49] D. Kong, X. Ni, C. Dong, X. Lei, L. Zhang, C. Man, J. Yao, X. Cheng, X. Li, Bio-functional and anti-corrosive 3D printing 316L stainless steel fabricated by selective laser melting, Mater. Des. 152 (2018) 88–101. https://doi.org/10.1016/j.matdes.2018.04.058.

[50] G. Sander, J. Tan, P. Balan, O. Gharbi, D.R. Feenstra, L. Singer, S. Thomas, R.G. Kelly, J.R. Scully, N. Birbilis, Corrosion of additively manufactured alloys: A review, Corrosion. 74 (2018) 1318–1350. https://doi.org/10.5006/2926.

[51] K. Davidson, S. Singamneni, Selective Laser Melting of Duplex Stainless Steel Powders: An Investigation, Mater. Manuf. Process. 31 (2016) 1543–1555. https://doi.org/10.1080/10426914.2015.1090605.

[52] H. Wang, B. Zhao, C. Liu, C. Wang, X. Tan, M. Hu, A comparison of biocompatibility of a titanium alloy fabricated by electron beam melting and selective laser melting, PLoS One. 11 (2016). https://doi.org/10.1371/journal.pone.0158513.

[53] L.D. Bobbio, R.A. Otis, J.P. Borgonia, R.P. Dillon, A.A. Shapiro, Z.K. Liu, A.M. Beese, Additive manufacturing of a functionally graded material from Ti-6Al-4V to Invar: Experimental characterization and thermodynamic calculations, Acta Mater. 127 (2017) 133–142. https://doi.org/10.1016/j.actamat.2016.12.070.

[54] W. Xu, M. Brandt, S. Sun, J. Elambasseril, Q. Liu, K. Latham, K. Xia, M. Qian, Additive manufacturing of strong and ductile Ti-6Al-4V by selective laser melting via in situ martensite decomposition, Acta Mater. 85 (2015) 74–84. https://doi.org/10.1016/j.actamat.2014.11.028.

[55] L.Y. Chen, J.C. Huang, C.H. Lin, C.T. Pan, S.Y. Chen, T.L. Yang, D.Y. Lin, H.K. Lin, J.S.C. Jang, Anisotropic response of Ti-6Al-4V alloy fabricated by 3D printing selective laser melting, Mater. Sci. Eng. A. 682 (2017) 389–395. https://doi.org/10.1016/j.msea.2016.11.061.

[56] G. Marchese, X. Garmendia Colera, F. Calignano, M. Lorusso, S. Biamino, P. Minetola, D. Manfredi, Characterization and Comparison of Inconel 625 Processed by Selective Laser Melting and Laser Metal Deposition, Adv. Eng. Mater. 19 (2017). https://doi.org/10.1002/adem.201600635.

[57] W. Tillmann, C. Schaak, J. Nellesen, M. Schaper, M.E. Aydinöz, K.P. Hoyer, Hot

isostatic pressing of IN718 components manufactured by selective laser melting, Addit. Manuf. 13 (2017) 93–102. https://doi.org/10.1016/j.addma.2016.11.006.

[58] J.J. Lewandowski, M. Seifi, Metal Additive Manufacturing: A Review of Mechanical Properties, Annu. Rev. Mater. Res. 46 (2016) 151–186. https://doi.org/10.1146/annurev-matsci-070115-032024.

[59] S. Li, Q. Wei, Y. Shi, C.K. Chua, Z. Zhu, D. Zhang, Microstructure Characteristics of Inconel 625 Superalloy Manufactured by Selective Laser Melting, J. Mater. Sci. Technol. 31 (2015) 946–952. https://doi.org/10.1016/j.jmst.2014.09.020.

[60] S. Gorsse, C. Hutchinson, M. Gouné, R. Banerjee, Additive manufacturing of metals: a brief review of the characteristic microstructures and properties of steels, Ti-6Al-4V and high-entropy alloys, Sci. Technol. Adv. Mater. 18 (2017) 584–610. https://doi.org/10.1080/14686996.2017.1361305.

[61] T.B. Sercombe, X. Li, Selective laser melting of aluminium and aluminium metal matrix composites: Review, Mater. Technol. 31 (2016) 77–85. https://doi.org/10.1179/1753555715Y.0000000078.

[62] T.D. Ngo, A. Kashani, G. Imbalzano, K.T.Q. Nguyen, D. Hui, Additive manufacturing (3D printing): A review of materials, methods, applications and challenges, Compos. Part B Eng. 143 (2018) 172–196. https://doi.org/10.1016/j.compositesb.2018.02.012.

[63] S.L. Sing, W.Y. Yeong, Laser powder bed fusion for metal additive manufacturing: perspectives on recent developments, Virtual Phys. Prototyp. 15 (2020) 359–370. https://doi.org/10.1080/17452759.2020.1779999.

[64] N. Li, S. Huang, G. Zhang, R. Qin, W. Liu, H. Xiong, G. Shi, J. Blackburn, Progress in additive manufacturing on new materials: A review, J. Mater. Sci. Technol. 35 (2019) 242–269. https://doi.org/10.1016/j.jmst.2018.09.002.

[65] E.O. Olakanmi, R.F. Cochrane, K.W. Dalgarno, A review on selective laser sintering/melting (SLS/SLM) of aluminium alloy powders: Processing, microstructure, and properties, Prog. Mater. Sci. 74 (2015) 401–477. https://doi.org/10.1016/j.pmatsci.2015.03.002.

[66] J. Zhang, B. Song, Q. Wei, D. Bourell, Y. Shi, A review of selective laser melting of aluminum alloys: Processing, microstructure, property and developing trends, J. Mater. Sci. Technol. 35 (2019) 270–284. https://doi.org/10.1016/j.jmst.2018.09.004.

[67] Q.G. Wang, C.. Davidson, Solidification and precipitation behaviour of Al-Si-Mg casting alloys, J. Mater. Sci. 42 (2007) 2215. https://doi.org/10.1007/s10853-006-1469-6.

[68] N. Kang, P. Coddet, C. Chen, Y. Wang, H. Liao, C. Coddet, Microstructure and wear behavior of in-situ hypereutectic Al-high Si alloys produced by selective laser melting, Mater. Des. 99 (2016) 120–126. https://doi.org/10.1016/j.matdes.2016.03.053.

[69] L. Hitzler, S. Hafenstein, F.M. Martin, H. Clemens, E. Sert, A. Öchsner, M. Merkel, E. Werner, Heat Treatments and Critical Quenching Rates in Additively Manufactured Al–Si–Mg Alloys, Materials (Basel). 13 (2020) 1–17.

[70] P. Van Cauwenbergh, V. Samaee, L. Thijs, J. Nejezchlebová, P. Sedlák, A. Iveković, D. Schryvers, B. Van Hooreweder, K. Vanmeensel, Unravelling the multi-scale structure–property relationship of laser powder bed fusion processed and heat-treated AlSi10Mg, Sci. Rep. 11 (2021) 1–15. https://doi.org/10.1038/s41598-021-85047-2.

[71] H. Hyer, L. Zhou, A. Mehta, S. Park, T. Huynh, S. Song, Y. Bai, K. Cho, B. McWilliams, Y. Sohn, Composition-dependent solidification cracking of aluminum-silicon alloys during laser powder bed fusion, Acta Mater. 208 (2021) 116698. https://doi.org/10.1016/j.actamat.2021.116698.

[72] N.T. Aboulkhair, I. Maskery, C. Tuck, I. Ashcroft, N.M. Everitt, On the formation of AlSi10Mg single tracks and layers in selective laser melting: Microstructure and nano-mechanical properties, J. Mater. Process. Technol. 230 (2016) 88–98. https://doi.org/10.1016/j.jmatprotec.2015.11.016.

[73] N.T. Aboulkhair, I. Maskery, C. Tuck, I. Ashcroft, N.M. Everitt, The microstructure and mechanical properties of selectively laser melted AlSi10Mg: The effect of a conventional T6-like heat treatment, Mater. Sci. Eng. A. 667 (2016) 139–146. https://doi.org/10.1016/j.msea.2016.04.092.

[74] I. Maskery, N.T. Aboulkhair, A.O. Aremu, C.J. Tuck, I.A. Ashcroft, R.D. Wildman, R.J.M. Hague, A mechanical property evaluation of graded density Al-Si10-Mg lattice structures manufactured by selective laser melting, Mater. Sci. Eng. A. 670 (2016) 264–274. https://doi.org/10.1016/j.msea.2016.06.013.

[75] N.T. Aboulkhair, I. Maskery, C. Tuck, I. Ashcroft, N.M. Everitt, Improving the fatigue behaviour of a selectively laser melted aluminium alloy: Influence of heat treatment and

surface quality, Mater. Des. 104 (2016) 174–182. https://doi.org/10.1016/j.matdes.2016.05.041.

[76] N.T. Aboulkhair, N.M. Everitt, I. Ashcroft, C. Tuck, Reducing porosity in AlSi10Mg parts processed by selective laser melting, Addit. Manuf. 1 (2014) 77–86. https://doi.org/10.1016/j.addma.2014.08.001.

[77] D.K. Kim, W. Woo, J.H. Hwang, K. An, S.H. Choi, Stress partitioning behavior of an AlSi10Mg alloy produced by selective laser melting during tensile deformation using in situ neutron diffraction, J. Alloys Compd. 686 (2016) 281–286. https://doi.org/10.1016/j.jallcom.2016.06.011.

[78] D. Buchbinder, W. Meiners, K. Wissenbach, R. Poprawe, Selective laser melting of aluminum die-cast alloy—Correlations between process parameters, solidification conditions, and resulting mechanical properties, J. Laser Appl. 27 (2015) S29205. https://doi.org/10.2351/1.4906389.

[79] D. Buchbinder, H. Schleifenbaum, S. Heidrich, W. Meiners, J. Bültmann, High power Selective Laser Melting (HP SLM) of aluminum parts, in: Phys. Procedia, Elsevier B.V., 2011: pp. 271–278. https://doi.org/10.1016/j.phpro.2011.03.035.

[80] U. Tradowsky, J. White, R.M. Ward, N. Read, W. Reimers, M.M. Attallah, Selective laser melting of AlSi10Mg: Influence of post-processing on the microstructural and tensile properties development, Mater. Des. 105 (2016) 212–222. https://doi.org/10.1016/j.matdes.2016.05.066.

[81] A. Hadadzadeh, B.S. Amirkhiz, M. Mohammadi, Contribution of Mg2Si precipitates to the strength of direct metal laser sintered AlSi10Mg, Mater. Sci. Eng. A. 739 (2019) 295–300. https://doi.org/10.1016/j.msea.2018.10.055.

[82] A. Leon, E. Aghion, Effect of surface roughness on corrosion fatigue performance of AlSi10Mg alloy produced by Selective Laser Melting (SLM), Mater. Charact. 131 (2017) 188–194. https://doi.org/10.1016/j.matchar.2017.06.029.

[83] M. Cabrini, S. Lorenzi, T. Pastore, S. Pellegrini, E.P. Ambrosio, F. Calignano, D. Manfredi, M. Pavese, P. Fino, Effect of heat treatment on corrosion resistance of DMLS AlSi10Mg alloy, Electrochim. Acta. 206 (2016) 346–355. https://doi.org/10.1016/j.electacta.2016.04.157.

[84] J.C. Hastie, J. Koelblin, M.E. Kartal, M.M. Attallah, R. Martinez, Evolution of internal

pores within AlSi10Mg manufactured by laser powder bed fusion under tension: As-built and heat treated conditions, Mater. Des. 204 (2021) 109645. https://doi.org/10.1016/j.matdes.2021.109645.

[85] Q. Liu, H. Wu, M.J. Paul, P. He, Z. Peng, B. Gludovatz, J.J. Kruzic, C.H. Wang, X. Li, Machine-learning assisted laser powder bed fusion process optimization for AlSi10Mg: New microstructure description indices and fracture mechanisms, Acta Mater. 201 (2020) 316–328. https://doi.org/10.1016/j.actamat.2020.10.010.

[86] X.J. Wang, L.C. Zhang, M.H. Fang, T.B. Sercombe, The effect of atmosphere on the structure and properties of a selective laser melted Al-12Si alloy, Mater. Sci. Eng. A. 597 (2014) 370–375. https://doi.org/10.1016/j.msea.2014.01.012.

[87] D. Gu, H. Wang, F. Chang, D. Dai, P. Yuan, Y.C. Hagedorn, W. Meiners, Selective laser melting additive manufacturing of TiC/AlSi10Mg bulk-form nanocomposites with tailored microstructures and properties, in: Phys. Procedia, Elsevier B.V., 2014: pp. 108–116. https://doi.org/10.1016/j.phpro.2014.08.153.

[88] P. He, H. Kong, Q. Liu, M. Ferry, J.J. Kruzic, X. Li, Elevated temperature mechanical properties of TiCN reinforced AlSi10Mg fabricated by laser powder bed fusion additive manufacturing, Mater. Sci. Eng. A. 811 (2021). https://doi.org/10.1016/j.msea.2021.141025.

[89] K.G. Prashanth, S. Scudino, H.J. Klauss, K.B. Surreddi, L. Löber, Z. Wang, A.K. Chaubey, U. Kühn, J. Eckert, Microstructure and mechanical properties of Al-12Si produced by selective laser melting: Effect of heat treatment, Mater. Sci. Eng. A. 590 (2014) 153–160. https://doi.org/10.1016/j.msea.2013.10.023.

[90] M. Liu, T. Wada, A. Suzuki, N. Takata, M. Kobashi, M. Kato, Effect of annealing on anisotropic tensile properties of al–12%si alloy fabricated by laser powder bed fusion, Crystals. 10 (2020) 1–14. https://doi.org/10.3390/cryst10111007.

[91] X.P. Li, K.M. O'Donnell, T.B. Sercombe, Selective laser melting of Al-12Si alloy: Enhanced densification via powder drying, Addit. Manuf. 10 (2016) 10–14. https://doi.org/10.1016/j.addma.2016.01.003.

[92] M. Leary, M. Mazur, J. Elambasseril, M. McMillan, T. Chirent, Y. Sun, M. Qian, M. Easton, M. Brandt, Selective laser melting (SLM) of AlSi12Mg lattice structures, Mater. Des. 98 (2016) 344–357. https://doi.org/10.1016/j.matdes.2016.02.127.

[93] J. Suryawanshi, K.G. Prashanth, S. Scudino, J. Eckert, O. Prakash, U. Ramamurty, Simultaneous enhancements of strength and toughness in an Al-12Si alloy synthesized using selective laser melting, Acta Mater. 115 (2016) 285–294. https://doi.org/10.1016/j.actamat.2016.06.009.

[94] X.P. Li, X.J. Wang, M. Saunders, A. Suvorova, L.C. Zhang, Y.J. Liu, M.H. Fang, Z.H. Huang, T.B. Sercombe, A selective laser melting and solution heat treatment refined Al-12Si alloy with a controllable ultrafine eutectic microstructure and 25% tensile ductility, Acta Mater. 95 (2015) 74–82. https://doi.org/10.1016/j.actamat.2015.05.017.

[95] K.G. Prashanth, B. Debalina, Z. Wang, P.F. Gostin, A. Gebert, M. Calin, U. Kühn, M. Kamaraj, S. Scudino, J. Eckert, Tribological and corrosion properties of Al-12Si produced by selective laser melting, J. Mater. Res. 29 (2014) 2044–2054. https://doi.org/10.1557/jmr.2014.133.

[96] O. Gharbi, D. Jiang, D.R. Feenstra, S.K. Kairy, Y. Wu, C.R. Hutchinson, N. Birbilis, On the corrosion of additively manufactured aluminium alloy AA2024 prepared by selective laser melting, Corros. Sci. 143 (2018) 93–106. https://doi.org/10.1016/j.corsci.2018.08.019.

[97] B. Ahuja, M. Karg, K.Y. Nagulin, M. Schmidt, Fabrication and characterization of high strength Al-Cu alloys processed using Laser Beam Melting in metal powder bed, in: Phys. Procedia, Elsevier B.V., 2014: pp. 135–146. https://doi.org/10.1016/j.phpro.2014.08.156.

[98] H. Zhang, H. Zhu, X. Nie, T. Qi, Z. Hu, X. Zeng, Fabrication and heat treatment of high strength Al-Cu-Mg alloy processed using selective laser melting, in: Laser 3D Manuf. III, SPIE, 2016: p. 97380X. https://doi.org/10.1117/12.2211362.

[99] R. Casati, J.N. Lemke, A.Z. Alarcon, M. Vedani, Aging Behavior of High-Strength Al Alloy 2618 Produced by Selective Laser Melting, Metall. Mater. Trans. A Phys. Metall. Mater. Sci. 48 (2017) 575–579. https://doi.org/10.1007/s11661-016-3883-y.

[100] H. Zhang, H. Zhu, T. Qi, Z. Hu, X. Zeng, Selective laser melting of high strength Al-Cu-Mg alloys: Processing, microstructure and mechanical properties, Mater. Sci. Eng. A. 656 (2016) 47–54. https://doi.org/10.1016/j.msea.2015.12.101.

[101] Y. Qi, H. Zhang, J. Zhu, X. Nie, Z. Hu, H. Zhu, X. Zeng, Mechanical behavior and microstructure evolution of Al-Cu-Mg alloy produced by laser powder bed fusion:

Effect of heat treatment, Mater. Charact. 165 (2020) 110364. https://doi.org/10.1016/j.matchar.2020.110364.

[102] H. Zhang, H. Zhu, X. Nie, J. Yin, Z. Hu, X. Zeng, Effect of Zirconium addition on crack, microstructure and mechanical behavior of selective laser melted Al-Cu-Mg alloy, Scr. Mater. 134 (2017) 6–10. https://doi.org/10.1016/j.scriptamat.2017.02.036.

[103] E. Louvis, P. Fox, C.J. Sutcliffe, Selective laser melting of aluminium components, J. Mater. Process. Technol. 211 (2011) 275–284. https://doi.org/10.1016/j.jmatprotec.2010.09.019.

[104] S.Z. Uddin, L.E. Murr, C.A. Terrazas, P. Morton, D.A. Roberson, R.B. Wicker, Processing and characterization of crack-free aluminum 6061 using high-temperature heating in laser powder bed fusion additive manufacturing, Addit. Manuf. 22 (2018) 405–415. https://doi.org/10.1016/j.addma.2018.05.047.

[105] M. Opprecht, J.P. Garandet, G. Roux, C. Flament, M. Soulier, A solution to the hot cracking problem for aluminium alloys manufactured by laser beam melting, Acta Mater. 197 (2020) 40–53. https://doi.org/10.1016/j.actamat.2020.07.015.

[106] A. Mehta, L. Zhou, T. Huynh, S. Park, H. Hyer, S. Song, Y. Bai, D.D. Imholte, N.E. Woolstenhulme, D.M. Wachs, Y. Sohn, Additive manufacturing and mechanical properties of the dense and crack free Zr-modified aluminum alloy 6061 fabricated by the laser-powder bed fusion, Addit. Manuf. 41 (2021) 101966. https://doi.org/10.1016/j.addma.2021.101966.

[107] L.F. (Lucio F.. Mondolfo, Aluminum alloys : structure and properties, Butterworths, 1976.

[108] K. Schmidtke, F. Palm, A. Hawkins, C. Emmelmann, Process and mechanical properties: Applicability of a scandium modified Al-alloy for laser additive manufacturing, in: Phys. Procedia, Elsevier B.V., 2011: pp. 369–374. https://doi.org/10.1016/j.phpro.2011.03.047.

[109] S. Begoc, F. Montredon, G. Pommatau, G. Leger, M. Gas, S. Eyrignoux, Additive manufacturing of Scalmalloy® satellite parts, Proc. 8th Eur. Conf. Aeronaut. Sp. Sci. (2019) 1–15. https://doi.org/10.13009/EUCASS2019-677.

[110] P. Jakkula, G. Ganzenmüller, F. Gutmann, A. Pfaff, J. Mermagen, S. Hiermaier, Strain Rate Sensitivity of the Additive Manufacturing Material Scalmalloy®, J. Dyn. Behav.

Mater. (2021). https://doi.org/10.1007/s40870-021-00298-4.

[111] A.B. Spierings, K. Dawson, K. Kern, F. Palm, K. Wegener, SLM-processed Sc- and Zr-modified Al-Mg alloy: Mechanical properties and microstructural effects of heat treatment, Mater. Sci. Eng. A. 701 (2017) 264–273. https://doi.org/10.1016/j.msea.2017.06.089.

[112] A.B. Spierings, K. Dawson, P.J. Uggowitzer, K. Wegener, Influence of SLM scan-speed on microstructure, precipitation of Al3Sc particles and mechanical properties in Sc- and Zr-modified Al-Mg alloys, Mater. Des. 140 (2018) 134–143. https://doi.org/10.1016/j.matdes.2017.11.053.

[113] A.B. Spierings, K. Dawson, P. Dumitraschkewitz, S. Pogatscher, K. Wegener, Microstructure characterization of SLM-processed Al-Mg-Sc-Zr alloy in the heat treated and HIPed condition, Addit. Manuf. 20 (2018) 173–181. https://doi.org/10.1016/j.addma.2017.12.011.

[114] Q. Jia, F. Zhang, P. Rometsch, J. Li, J. Mata, M. Weyland, L. Bourgeois, M. Sui, X. Wu, Precipitation kinetics, microstructure evolution and mechanical behavior of a developed Al-Mn-Sc alloy fabricated by selective laser melting, Acta Mater. 193 (2020) 239–251. https://doi.org/10.1016/j.actamat.2020.04.015.

[115] Q. Jia, P. Rometsch, S. Cao, K. Zhang, X. Wu, Towards a high strength aluminium alloy development methodology for selective laser melting, Mater. Des. 174 (2019). https://doi.org/10.1016/j.matdes.2019.107775.

[116] Q. Jia, P. Rometsch, P. Kürnsteiner, Q. Chao, A. Huang, M. Weyland, L. Bourgeois, X. Wu, Selective laser melting of a high strength Al[sbnd]Mn[sbnd]Sc alloy: Alloy design and strengthening mechanisms, Acta Mater. 171 (2019) 108–118. https://doi.org/10.1016/j.actamat.2019.04.014.

[117] J. R. Davies, Corrosion of aluminum and aluminum alloys, 1999. https://doi.org/10.1361/caaa1999p025.

[118] L.F. (Lucio F.. Mondolfo, Al-Mg-Zn alloys - A review of the literature, Res. Dev. Center, Reverse Copp. Brass Inc.,. (1967).

[119] N. Kaufmann, M. Imran, T.M. Wischeropp, C. Emmelmann, S. Siddique, F. Walther, Influence of process parameters on the quality of aluminium alloy en AW 7075 using Selective Laser Melting (SLM), in: Phys. Procedia, Elsevier B.V., 2016: pp. 918–926.

https://doi.org/10.1016/j.phpro.2016.08.096.

[120] M.L. Montero Sistiaga, R. Mertens, B. Vrancken, X. Wang, B. Van Hooreweder, J.P. Kruth, J. Van Humbeeck, Changing the alloy composition of Al7075 for better processability by selective laser melting, J. Mater. Process. Technol. 238 (2016) 437–445. https://doi.org/10.1016/j.jmatprotec.2016.08.003.

[121] R.S. Mishra, S. Thapliyal, Design approaches for printability-performance synergy in Al alloys for laser-powder bed additive manufacturing, Mater. Des. 204 (2021) 109640. https://doi.org/10.1016/j.matdes.2021.109640.

[122] S.K. Kairy, O. Gharbi, J. Nicklaus, D. Jiang, C.R. Hutchinson, N. Birbilis, On the Characterization of a Hitherto Unreported Icosahedral Quasicrystal Phase in Additively Manufactured Aluminum Alloy AA7075, Metall. Mater. Trans. A Phys. Metall. Mater. Sci. 50 (2019) 529–533. https://doi.org/10.1007/s11661-018-5025-1.

[123] O. Gharbi, S. Kumar Kairy, P.R. De Lima, D. Jiang, J. Nicklaus, N. Birbilis, Microstructure and corrosion evolution of additively manufactured aluminium alloy AA7075 as a function of ageing, Npj Mater. Degrad. 3 (2019). https://doi.org/10.1038/s41529-019-0101-6.

[124] J.H. Martin, B.D. Yahata, J.M. Hundley, J.A. Mayer, T.A. Schaedler, T.M. Pollock, 3D printing of high-strength aluminium alloys, Nature. 549 (2017) 365–369. https://doi.org/10.1038/nature23894.

[125] S.Y. Zhou, Y. Su, H. Wang, J. Enz, T. Ebel, M. Yan, Selective laser melting additive manufacturing of 7xxx series Al-Zn-Mg-Cu alloy: Cracking elimination by co-incorporation of Si and TiB2, Addit. Manuf. 36 (2020). https://doi.org/10.1016/j.addma.2020.101458.

[126] L. Li, R. Li, T. Yuan, C. Chen, Z. Zhang, X. Li, Microstructures and tensile properties of a selective laser melted Al–Zn–Mg–Cu (Al7075) alloy by Si and Zr microalloying, Mater. Sci. Eng. A. 787 (2020) 139492. https://doi.org/10.1016/j.msea.2020.139492.

[127] C. Galy, E. Le Guen, E. Lacoste, C. Arvieu, Main defects observed in aluminum alloy parts produced by SLM: From causes to consequences, Addit. Manuf. 22 (2018) 165–175. https://doi.org/10.1016/j.addma.2018.05.005.

[128] D. Dai, D. Gu, R. Poprawe, M. Xia, Influence of additive multilayer feature on thermodynamics, stress and microstructure development during laser 3D printing of

aluminum-based material, Sci. Bull. 62 (2017) 779–787. https://doi.org/10.1016/j.scib.2017.05.007.

[129] M. Rappaz, J.-M. Drezet, M. Gremaud, A New Hot-Tearing Criterion, 1999.

[130] C.E. Cross, N. Coniglio, P. Schempp, M. Mousavi, Critical Conditions for Weld Solidification Crack Growth, in: Hot Crack. Phenom. Welds III, Springer Berlin Heidelberg, 2011: pp. 25–41. https://doi.org/10.1007/978-3-642-16864-2_2.

[131] S. Kou, A criterion for cracking during solidification, Acta Mater. 88 (2015) 366–374. https://doi.org/10.1016/j.actamat.2015.01.034.

[132] G. Mathers, The welding of aluminium and its alloys, CRC Press, 2002.

[133] J. Liu, S. Kou, Susceptibility of ternary aluminum alloys to cracking during solidification, Acta Mater. 125 (2017) 513–523. https://doi.org/10.1016/j.actamat.2016.12.028.

[134] S. Li, D. Apelian, HOT TEARING OF ALUMINUM ALLOYS A CRITICAL LITERATURE REVIEW, 2011.

[135] Y.L. Wu, F.H. Froes, A. Alvarez, C.G. Li, J. Liu, Microstructure and properties of a new super-high-strength AlZnMgCu alloy C912, 1997.

[136] M. De Sanctis, Structure and properties of rapidly solidified ultrahigh strength AI-Zn-Mg-Cu alloys produced by spray deposition, 1991.

[137] H. Li, F. Cao, S. Guo, Y. Jia, D. Zhang, Z. Liu, P. Wang, S. Scudino, J. Sun, Effects of Mg and Cu on microstructures and properties of spray-deposited Al-Zn-Mg-Cu alloys, J. Alloys Compd. 719 (2017) 89–96. https://doi.org/10.1016/j.jallcom.2017.05.101.

[138] M.M. Sharma, M.F. Amateau, T.J. Eden, Mesoscopic structure control of spray formed high strength Al-Zn-Mg-Cu alloys, Acta Mater. 53 (2005) 2919–2924. https://doi.org/10.1016/j.actamat.2005.03.007.

[139] M.M. Sharma, Microstructural and mechanical characterization of various modified 7XXX series spray formed alloys, Mater. Charact. 59 (2008) 91–99. https://doi.org/10.1016/J.MATCHAR.2007.01.013.

[140] H. Yu, M. Wang, Y. Jia, Z. Xiao, C. Chen, Q. Lei, Z. Li, W. Chen, H. Zhang, Y. Wang, C. Cai, High strength and large ductility in spray-deposited Al-Zn-Mg-Cu alloys, J. Alloys Compd. 601 (2014) 120–125. https://doi.org/10.1016/j.jallcom.2014.02.126.

[141] T.G. Spears, S.A. Gold, In-process sensing in selective laser melting (SLM) additive manufacturing, Integr. Mater. Manuf. Innov. 5 (2016) 16–40. https://doi.org/10.1186/s40192-016-0045-4.

[142] D. Gu, H. Wang, D. Dai, Laser Additive Manufacturing of Novel Aluminum Based Nanocomposite Parts: Tailored Forming of Multiple Materials, J. Manuf. Sci. Eng. Trans. ASME. 138 (2016). https://doi.org/10.1115/1.4030376.

3

Research aims

A review of available literature indicates that there is not only an increasing motivation to expand the portfolio Al-alloys, but also a major deficiency in Al-alloys designed for additive manufacturing. Specifically, LPBF prepared Al-Zn-Mg alloys that may be utilised for high strength applications in the transportation sector, have not received dedicated attention from a design-directed perspective. One approach for LPBF fabrication of Al-Zn-Mg alloys is to modify the composition of existing commercial alloys. However, the key issues that hinders such a (traditional) approach, includes the need for expensive alloying additions, the possibility of hot cracking, and the development of excess porosity. Therefore, it is necessary to design novel and affordable Al-alloys in the Al-Zn-Mg system without hot cracking, that are specifically tailored to utilise the benefits of rapid solidification through LPBF.

The aim of this research is to design, produce and characterise a cost-effective and high strength Al-Zn-Mg alloy, derived from excess Zn and Mg additions afforded through LPBF, in net-shape.

A principle hypothesis for this research was that the addition of an excess of solute (namely Zn and Mg) will further promote the formation of strengthening second phase particles; aiding in the improvement of mechanical properties. This research will contribute to the field of Al-alloys prepared by AM, via providing significant insights in the exploration of an Al-alloy system capable of solute hyperloading without hot cracking.

In the approach herein, novel compositions with low hot cracking susceptibility were rationalised based on solidification modelling of a range of Al-Zn-Mg alloys, with a varying Zn:Mg ratio. The experimental workflow to achieve the objective of the present study was as follows:

1. LPBF processing of the selected Al-Zn-Mg alloy compositions:

- Design of high solute Al-Zn-Mg alloys with the aid of CALPHAD and thermodynamic databases, along with knowledge based on archival literature.
- Optimising the processing parameters of LPBF prepared Al-Zn-Mg alloys, including laser power, laser scan speed, hatch spacing and spot size, to fabricate near-dense samples in net-shape.
- Analysis of the as-LPBF microstructure using scanning electron microscopy (SEM), transmission electron microscopy (TEM) and x-ray diffraction (XRD), along with mechanical property testing including hardness measurements and uniaxial tensile testing.

2. Heat treatment of the LPBF prepared high solute Al-Zn-Mg alloy and evaluation of changes in microstructure and mechanical properties:

- Subject LPBF prepared high solute Al-Zn-Mg alloys to several heat treatment conditions such as direct heat treatment, solutionising heat treatment and ageing heat treatment.
- Evaluate the alteration of microstructural and mechanical properties as a result of heat treatment.

3. Evaluation of corrosion behaviour of high solute Al-Zn-Mg alloys:

- Perform electrochemical and exposure tests to evaluate the corrosion rate of as-LPBF and heat treated high solute Al-Zn-Mg alloys, along with their corrosion morphology.

4. *In-situ* characterisation of second phase particles to understand their effect in mechanical properties:

- Perform *in-situ* TEM and *in-situ* XRD to understand the phase transformation occurring in the high solute alloy at different heat treatment conditions.

4

LPBF fabrication of high solute Al-Zn-Mg alloys

4.1 Chapter synopsis

This chapter is focused towards the first objective of the research aim and it is a research paper with the title, "Laser powder bed fusion of high solute Al-Zn-Mg alloys: Processing, characterisation and properties" as published in Materials and design.

In this work, three high solute Al-alloys in the Al-Zn-Mg system that displayed low hot cracking susceptibility and high volume fraction of second phase particles were chosen with the following compositions (in wt. %): Al-10Zn-2Mg, Al-14Zn-3Mg and Al-18Zn-4Mg, and were successfully fabricated through laser powder bed fusion (LPBF) process. The high solute Al-Zn-Mg alloys were characterised using a number of different techniques, namely Scanning Electron Microscopy (SEM), Transmission Electron Microscopy (TEM) and X-ray Diffraction (XRD) to assess the microstructure. The microstructure of the high solute Al-alloys processed through LPBF were unique in comparison to wrought Al-alloys and were decorated with a high volume fraction of second phase particles. High resolution TEM revealed the presence of a previously unreported, icosahedral quasicrystalline phase, herein termed as the P-phase. The alloys were also subjected to mechanical testing where the hardness of the Al-Zn-Mg alloys varied between 120-160 HV_1 and the tensile properties revealed brittleness of the high solute Al-alloys in the as-LPBF condition.

Materials and Design 196 (2020) 109183

Contents lists available at ScienceDirect

Materials and Design

journal homepage: www.elsevier.com/locate/matdes

Laser powder bed fusion of high solute Al-Zn-Mg alloys: Processing, characterisation and properties

A.P. Babu [a,*], S.K. Kairy [a], A. Huang [a,b], N. Birbilis [c]

[a] Department of Materials Science and Engineering, Monash University, Clayton. VIC 3800, Australia
[b] Monash Centre for Additive Manufacturing, Monash University, Clayton, VIC 3800, Australia
[c] College of Engineering and Computer Science, The Australian National University, Acton, ACT 2601, Australia

HIGHLIGHTS

- Successful fabrication of high solute Al-Zn-Mg alloy without expensive additions such as Sc or Zr processed through SLM.
- The coexistence or clustering of particles was evidenced due to complex solidification process.
- Previously unreported, new quasicrystalline phase named as P-phase was found with a quasi-lattice constant of 0.529 nm.

GRAPHICAL ABSTRACT

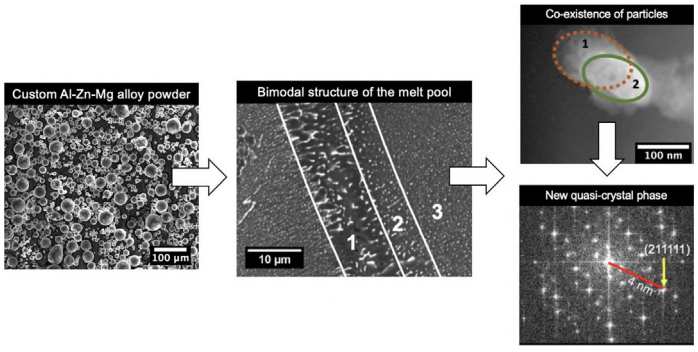

ARTICLE INFO

Article history:
Received 10 June 2020
Received in revised form 17 September 2020
Accepted 22 September 2020
Available online 26 September 2020

Keywords:
Selective laser melting
Materials design
Process optimisation
Al-Zn-Mg
TEM
Quasicrystals

ABSTRACT

Additive manufacturing of aluminium alloys by laser powder bed fusion (LPBF) has been notionally restricted to a small number of alloy compositions to avoid hot cracking and excessive porosity. In the present work, three unique alloy compositions from the Al-Zn-Mg system with high solute content (Zn > 10 wt% and Mg > 2 wt%) were designed in pursuit of attaining high strength from directly LPBF prepared Al-alloys. The high solute alloys were successfully fabricated, and in-depth microstructural characterisation and phase identification revealed the presence of a new quasicrystalline phase, which was named P-phase. The hardness of the alloys were higher than the existing as-fabricated Al-Zn-Mg alloys and comparable to conventionally fabricated high strength wrought aluminium alloys, however, the as-built tensile properties revealed brittleness. This study presents an insight into the possibilities of fabricating high strength Al-Zn-Mg alloys without expensive additions such as Sc or Zr, through selective laser melting.

1. Introduction

The production of complex components, such as those for aerospace applications, necessitates the use of intensive machining processes to achieve desired tolerance and geometry. Such traditional processes limit design freedom and component complexity [1,2]. On the possibility of producing net-shape components, the Laser Powder Bed Fusion (LPBF) process, commercially known as selective laser melting (SLM), is a form of powder bed additive manufacturing that has been demonstrated to be capable of producing complex components from a variety of alloy materials [3,4]. To date, the SLM of alloys including titanium, nickel and stainless steel has been successful, the fabrication of a portfolio of Al-alloys via the SLM process has been limited due to the formation of excessive porosity and hot cracking [3–5]. The most widely SLM prepared Al-alloys to date include the well optimised cast-alloy-

* Corresponding author.
E-mail address: abirami.babu@monash.edu (A.P. Babu).

https://doi.org/10.1016/j.matdes.2020.109183

like compositions of AlSi10 Mg (Al-10.67 Si-0.48 Mg wt%) and AlSi12 (Al—12 Si wt%), resulting in close to 100% dense components and with mechanical properties demonstrating a maximum yield strength of up to 270 MPa [6–11]. On the contrary, limited studies have been conducted on potentially high strength systems such as the Al-Zn-Cu-Mg and Al-Cu-Mg alloys, which conventionally have limited weldability (and would benefit from net-shape fabrication) and of which have a considerable interest to the aerospace and transportation industry [12].

Of the works that have pursued high strength aluminium alloys via additive manufacturing (AM) processes, only a few reported attempts have made with what are considered as traditional wrought-alloy-like compositions – largely as a result of the formation of hot cracking being observed [14,15]. However, a recent study by Zhang et al. utilised LPBF to produce a wrought alloy composition, AA2024 (Al-4.47 Cu-1.95 Mg-0.55 Mn), which resulted in successful fabrication of a high strength alloy (yield strength ~446 MPa) with the addition of 2 wt% zirconium as grain refiner [16,17]. By exploiting the rapid solidification achieved in LPBF processing - by extending the alloy solubility limits - a modified 5xxx series alloy (Scalmalloy: Al-4.5 Mg-0.66 Sc-0.37 Zr-0.17 Si) was developed by Schmidke et al., with a yield strength of 530 MPa and an elongation of 14% [18]. Considerable work on LPBF process optimisation and heat treatment was also performed, and Al_3Sc precipitates formed during artificial ageing were reported to be responsible for the increase in mechanical properties [19,20] – which represent the benchmark for a balance of strength and ductility for LPBF prepared Al-alloys. Recently, alloys in the Al-Mn-Sc system (Al-4.52 Mn-1.32 Mg-0.79 Sc-0.74 Zr-0.05 Si-0.07 Fe) were prepared by LPBF to reach yield strength of 571 MPa – in addition to Al_3Sc precipitates, Al_6Mn was also responsible for strengthening [20]. Notwithstanding the properties achieved by Scalmalloy, the pursuit of high strength LPBF prepared Al-alloys that are Sc-free (and hence cost competitive) remains an active pursuit.

In the context of Al-alloys, more generally, the Al-Zn-Mg alloy system offers significant potential for age hardening via the formation of η ($MgZn_2$) precipitates (and variants including η' and Cu-doped η'). The preliminary feasibility for producing such alloys using LPBF was studied by Montero-Sistiaga et al. where an alloy of Al-Zn-Mg system (EN AW 7075) was successfully produced by the addition of 4 wt% Si to purportedly improve fluidity and minimise hot cracking by reducing the solidification range [13]. Recently, another approach to controlling solidification dynamics was studied by Martin et al. by adding zirconium (Zr) nano-nucleants to AA7075 Al-alloy which led to grain refinement, thereby producing a crack-free and moderate strength material (yield strength ~370 MPa) [21]. In contrast, conventional wrought aluminium alloys reveal strengths of over 570 MPa in the case of AA7075 in the T6 condition [12]. Therefore, rather than seeking to fabricate existing conventional (wrought) alloy compositions, there exists an opportunity to develop new alloys commensurate with the unique processing afforded by the LPBF method [22].

In the prior pursuit of high strength Al-alloy, Al-Zn-Mg alloys with high Zn content have been explored for their improved mechanical properties, however the conventional casting processes for such alloys have resulted in macrosegregation, cracking and grain coarsening due to slow cooling [23]. To overcome such issues, rapid solidification techniques such as spray forming (Osprey process) and melt spinning techniques have pushed maximum zinc concentrations to 12 wt%, revealing yield strengths of 800 MPa [24]. The observed mechanical properties of such ultra-high strength aluminium alloys were largely dependent on the volume fraction of additional phases obtained from the control of spray parameters and heat treatment [25,26]. The ratio of solutes in rapidly solidified alloys played an important role in dictating mechanical properties, where it was demonstrated that Zn + Mg > 15 wt% was achievable [27] – however, the complexity in controlling process parameters restricted industrial usage – an aspect that can potentially be overcome with LPBF processing.

The present study presents the performance of Al-Zn-Mg alloys that were designed for additive manufacturing (namely LPBF), with the view of exploiting rapid solidification to impart high solute concentrations in achieving high strength. The rapid solidification from the LPBF process is posited to extend the solid solubility limits of Zn and Mg in the Al-Zn-Mg system, permitting the fabrication of Al-alloys with Zn > 10 wt% and Mg > 2 wt%. An added advantage of LPBF is that components may be produced in a net shape, along with detailed control of process parameters. Herein, the treatise of such alloys is presented, revealing the as-fabricated macrostructure, microstructure and mechanical properties.

2. Experimental methods

2.1. Materials

The high solute alloys considered for this study were nominally Al-10 Zn-2 Mg, Al-14 Zn-3 Mg and Al-18 Zn-4 Mg (in wt%). The selection of the compositions studied was rationalised based on solidification modelling of a range of Al-Zn-Mg alloys (with varying Mg:Zn ratio) using Thermocalc®. For instances where compositions with low hot cracking susceptibility were mapped with the aid of Rappaz's hot cracking criterion [28] and Scheil solidification model, it was deemed that empirical production (as done in this study) may be advantageous. Owing to CALPHAD calculations being based on thermodynamic database information, the translation of calculated values in the context of results from LPBF production also forms a basis for the work herein. The low boiling point and high vapour pressure of Zn and Mg have been previously reported as leading to preferential Zn and Mg vaporisation during the LPBF process [29]. Such vaporisation of Zn and Mg may lead to compositional variations that result in local hot cracking [28,29]. Therefore, additional Zn and Mg were added to the target composition in an attempt to compensate for vaporisation during LPBF. The custom pre-alloyed powders utilised herein were prepared by argon gas atomisation and supplied by TLS Technik GmbH. The as received alloy powder was passed through a 63 μm sieve to remove all oversized particles that may have formed in the manufacturing of powder using gas atomisation. The particle size distribution of the sieved powders used for LPBF fabrication was between 14 and 63 μm, and the detailed powder compositions are provided in Table 1, noting that Fe, Cu and Si present as impurities. The elemental composition of the powders and fabricated samples was determined using Inductively Coupled Plasma - Atomic Emission Spectroscopy (ICP-AES) at Spectrometer Services®, VIC, Australia to understand the difference in compositional change during the fabrication process.

The indicative powder morphology of Al-14Zn-3Mg after sieving is shown in Fig. 1. It was observed that the powder particles were predominantly spherical with very limited non-spherical or ellipsoid particles. The LPBF process involves the application of powder in repeated layers and it is known that the spherical morphology aids in improving the flowability of the powder particles [32,33]. Studies have also shown

Table 1
Chemical composition and powder size (diameter) distribution of the feedstock powder and post- LPBF fabricated alloy in wt%, measured using ICP-AES. The post-LPBF composition was measured from samples that produced maximum relative density.

Element	Al-10Zn-2Mg		Al-14Zn-3Mg		Al-18Zn-4Mg	
	Powder	Post-LPBF	Powder	Post-LPBF	Powder	Post-LPBF
Zn	10.8	8.59	14.7	10.9	19.2	11.9
Mg	2.3	2.1	3.34	2.79	4.40	3.28
Fe	0.17	0.18	0.28	0.23	0.23	0.27
Cu	0.02	0.02	0.06	0.06	0.02	0.02
Si	0.07	0.08	0.09	0.10	0.05	0.06
Al	Bal		Bal		Bal	
Powder size distribution	16–63 μm		18–63 μm		14–63 μm	

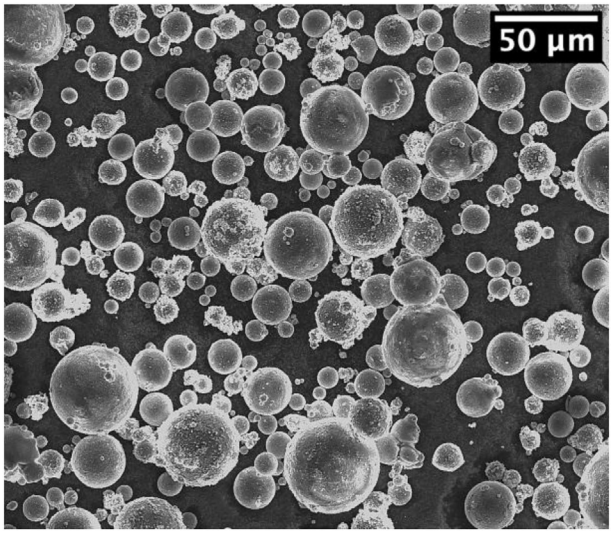

Fig. 1. Secondary electron image of Al-14Zn-3Mg powder, showing spherical morphology and size range.

that spherical shape improves the packing efficiency of the powder which aids in obtaining relatively dense parts [34].

2.2. Alloy production methods

The LPBF process was carried out using a Concept Laser Mlab Cusing-R. Several cubes that were 10 mm × 10 mm × 10 mm in dimension were fabricated in a controlled argon atmosphere upon an AA2024 base plate. Such cubes formed the basis of investigating process optimisation for attaining minimum porosity. The processing parameters explored in this study included varying the laser power and laser scan speeds, maintaining the oxygen content less than 0.2% at all times. Herein, laser powers of 90 W and 95 W were utilised, whilst laser scan speed was varied between 100 mm/s to 800 mm/s. An anti-parallel scanning strategy was adopted herein, where the subsequent layers were rotated by 90°. The hatch spacing, laser spot size and layer thickness were maintained at 0.07 mm, 50 µm and 25 µm, respectively. Square plates of 17 mm × 5 mm were fabricated for XRD samples. Specimens for tensile testing (60 mm long) were fabricated in the vertical direction in the so-called 'dog-bone' shape of 16 mm gauge length and a cross-section of 5 mm as shown in Fig. 2.

2.3. Microstructural characterisation

The specimen cubes were cut from the base plate using a Struers® Discotom-6. To avoid oxidation layers developed during fabrication, the individual cubes were cross-sectioned to a depth of 2 mm and polished perpendicular to their build direction in order to estimate their average porosity. The samples were metallographically prepared to a P2500 grit finish using silicon carbide paper, followed by polishing to a 1 µm finish using diamond suspension. The porosity of LPBF prepared samples was studied using an Olympus GX51 optical microscope. Average porosity was estimated using five representative optical micrographs which were collected at the same magnification. The fraction of surface area that was porous was analysed using the ImageJ software.

Scanning electron microscopy (SEM) was performed using a FEI® Quanta 3D FEG. Specimens for SEM were polished to a 0.01 µm surface finish using colloidal silica suspension.

Transmission electron microscopy was performed using an FEI® Tecnai G^2 T20 and FEI Tecnai G^2 F20 operating at 200 kV for imaging microstructural features and compositional analysis via energy-dispersive X-ray spectroscopy (EDXS). In addition, a double corrected FEI® Titan^3 80–300 TEM operated at 300 kV was used for atomic resolution imaging. TEM specimen preparation involved the sectioning of LPBF prepared alloys into a 500 µm slice. Such slices were mechanically thinned to ~100 µm and then punched into 3 mm discs. These discs were thinned further in order to be electron transparent using a Gatan® 691 Precision Ion Polishing System (PIPS), and plasma cleaned using a Gatan® Solarus 950 advanced plasma system before TEM imaging. A Bruker X-flash X-ray detector was utilised for collecting EDXS data, with quantitative analyses was performed using the Bruker® Esprit 1.9 X-ray software.

Phase identification via X-ray diffraction (XRD) was performed using a Bruker® D8 Advance diffractometer, with a Cu K_α radiation, operating with a Lynxeye sensitive detector. The specimens for XRD were prepared perpendicular to the LPBF build direction and were finished to a P2500 grit. Diffraction analysis was performed with a 2θ angle between 30° and 80° with a step size of 0.02°, at a generator voltage of 40 kV and an X-ray beam current of 25 mA. Bruker® EVA software was used for processing of XRD data.

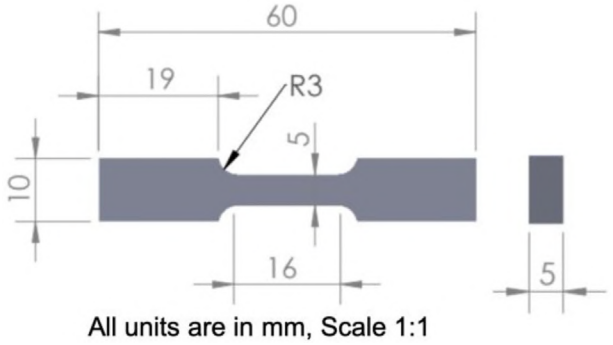

Fig. 2. Dimensions of the tensile specimens used in the present study.

2.4. Mechanical testing

Vickers hardness testing was carried out using Struers® Duramin A-300, by applying a load of 1 kg for a dwell time of 10 s, upon samples metallographically prepared to a P2400 grit finish. The average values of ten hardness measurements taken at different sites upon the samples constituted the average hardness reported.

Tensile testing was performed at an extension rate of 0.02 mm/s at room temperature using an Instron® 4050/5500R equipped with a 100 kN load cell. Two samples of every alloy composition were tested in the as-built state, to ensure the repeatability of the alloys under the given mechanical conditions.

3. Results

3.1. Optimisation of process parameters

The cubes of Al-14Zn-3Mg produced with different processing conditions upon an AA2024 base plate are shown in Fig. 3. The cubes were differentiated based on the variation of scan speed and laser power which was used for the optimisation of minimal porosity. The cube specimens underwent some form of oxidation as seen in Fig. 3 as the oxygen content maintained during printing was 0.2%.

Representative optical micrographs from the cube specimens are shown in Fig. 4. It was observed that porosity increased with scan speed. For high scan speeds, porosity was irregular in shape with dimensions up to 500–530 µm, whereas for lower scan speeds, the porosity was reduced to less <50 µm. In addition, the irregularity in porosity (shape) was also minimised at slower laser scan speed. It is believed that metallurgical pores are observed at lower scan speeds due to gas entrapment and process turbulence, confined to pores smaller than

Fig. 3. LPBF fabricated specimens of Al-14Zn-3Mg with different processing parameters (microstructures of which are presented in Fig. 4).

100 μm – whereas larger porosity is principally keyhole porosity which can be attributed to the incomplete filling of gaps with the molten metal during rapid solidification [8,30,31]. Such phenomena could be rationalised based on the alloy microstructures (as shown in Fig. 4) where small (metallurgical) pores were observed at lower scan speeds whilst keyhole pores (> 100 μm) were present for scan speeds exceeding 300 mm/s. Whilst the micrographs shown in this study are abridged in number and alloy type, it is noted that for all the alloy compositions studied herein, near dense high solute Al-Zn-Mg alloys were produced for the high laser power and slower scanning speeds studied for LPBF. This is further rationalised on the basis that aluminium has inefficient laser absorption due to its comparatively high laser reflectivity, and a higher energy density is favourable for effective melting and fusion. Similar cases have been reported in LPBF of aluminium alloys where the combination of high laser power and low scanning speeds resulted in maximum relative density [14,29].

The change in porosity of Al-14 Zn-3 Mg with respect to the laser power and scanning speeds was estimated through optical microscopy and shown in Fig. 5. It can be observed that the porosity followed a monotonic increase with scan speed, where a maximum porosity of ~18% was obtained for a scan speed of 800 mm/s. Conversely, a minimum porosity of 0.51% was achieved for a sample with laser power of 95 W and a speed of 150 mm/s.

The process parameters that resulted in the lowest observed porosity of Al-14 Zn-3 Mg was used to fabricate the remaining two alloy compositions (Al-10 Zn-2 Mg and Al-18 Zn-4 Mg), to minimise powder utilisation and to maintain a constant energy density. A laser power of 95 W was chosen with two different scan speeds of 150 mm/s and 175 mm/s, in pursuit of achieving high (viable) density. The representative optical micrographs of Al-10 Zn-2 Mg, Al-14 Zn-3 Mg and Al-18 Zn-4 Mg are shown in Fig. 6. The average porosity that was estimated from the optical micrographs of Al-10 Zn-2 Mg (Fig. 6a and b) was 0.47% and that of Al-14 Zn-3 Mg (Fig. 6c and d) was 0.38% for samples built at a laser power of 95 W and a scan speed of 175 mm/s. This corresponds to an energy density of 310 J/mm^2. However, Al-18Zn-4Mg showed signs of cracking (Fig. 6e and f) which was attributed to the appreciable loss of Zn and Mg due to vaporisation, as seen from Table 1. The post-LPBF compositions of Al-18Zn-4Mg shows that 7.3 wt% of Zn and 1.12 wt% of Mg was lost through vaporisation. In contrast, for Al-12Zn-2Mg the extent of Zn and Mg lost through vaporisation was 2.21 wt% and 0.2 wt%, respectively. Under such conditions it is possible that localised vaporisation of Zn and Mg leads to the formation of so-called vaporisation cracks. Fine cracks were evident in Al-18 Zn-4 Mg as shown in Fig. (6e and 6f). The presence of cracking has been previously reported in the welding of high solute Al-alloys, which was notionally controlled by minimising the energy density of the laser interaction process [35-38]. An increase in evaporative loss alters the overall composition of the alloys. It was observed in the present work, that the rate of vaporisation for Zn and Mg was increased with an increase in the solute content of the alloys. Although the vaporisation loss of Zn and Mg during LPBF was taken into consideration during powder production and design, in practice, it was realised that a greater extent of solute was lost from the actual (empirical) LPBF process.

3.2. Microstructural characterisation and phase analysis

The microstructural characterisation of Al-10 Zn-2 Mg, Al-14 Zn-3 Mg and Al-18 Zn-4 Mg was performed via scanning electron microscopy (SEM) using backscattered electron imaging, with the resultant micrographs shown in (Fig. 7 a, 7a' and 7a"), (7b, 7b' and 7b"), (7c, 7c' and 7c").

Results from SEM revealed a unique microstructure in comparison with conventionally (cast and wrought) processed aluminium alloys. The bright contrast of the second phase particles indicated that they were enriched with higher atomic number elements; differentiated from the Al-matrix that was lower in contrast. The microstructures imaged at lower magnification depicted U-shape melt pools of different sizes. The size of the melt pool was proportional, to the hatch spacing and laser spot size used during the LPBF process, where melt pools were approximately 27–51 μm wide. The width measured was less than the hatch spacing of 70 μm (0.07 mm) that signified overlapping of melt pool layers by ~27%. This overlapping resulted in differentiating the melt pool into three zones as shown in Fig. 7b" that are explained as follows:

(1) *Heat affected zone (HAZ)* contained elongated, plate-like particles which were comparatively large in size, ranging between 1 and 3 μm.

(2) *Coarse cellular dendrites* were present in the region between HAZ and fine cellular dendrites with reasonably coarse particles of ~1 μm. These particles were formed due to high diffusion rates from heat dissipated from the heat affected zone.

(3) *Fine cellular dendrites* contained a fine distribution of sub-micron, spherical particles and were present in the inner regions of the melt pool.

The second phase particles had high number density where their sizes varied between nanometre to sub-micrometre ranges. Therefore, characterisation of second phase particles via transmission electron microscopy (TEM) was deemed necessary, with bright field TEM images of as fabricated Al-10 Zn-2 Mg, Al-14 Zn-3 Mg and Al-18 Zn-4 Mg alloys shown in (Fig. 8 a and 8a"), (8b and 8b)" and (8c and 8c"), respectively.

The different size and distribution of the second phase particles were characterised by TEM based on their existence at different regions of the melt pool, namely the coarse cellular dendrites, heat affected zone and the fine cellular dendrites. It was observed that coarse cellular dendrites (8a, 8b and 8c) had particles with diverse morphology and size between 50 nm to ~3 μm. In contrast, the heat affected zone (Fig. 8 a', b', c') revealed a completely different microstructure that was comprised of cell-like structures. These cells varied approximately between ~600 nm – 1.3 μm in length and 900 nm – 1.3 μm in width where second phase particles appeared to nucleate preferentially at such cells. Additionally, Fig. 8 a", b", c" revealed that second phase particles were also observed at apparently random locations that comprised the region of fine cellular dendrites in the Al-matrix. The particles in this region varied in size between 30 nm to 250 nm. The difference in contrast observed in particles also suggests the coexistence of two or more phases (Fig. 8a", 8b" and 8c"). In order to understand the composition

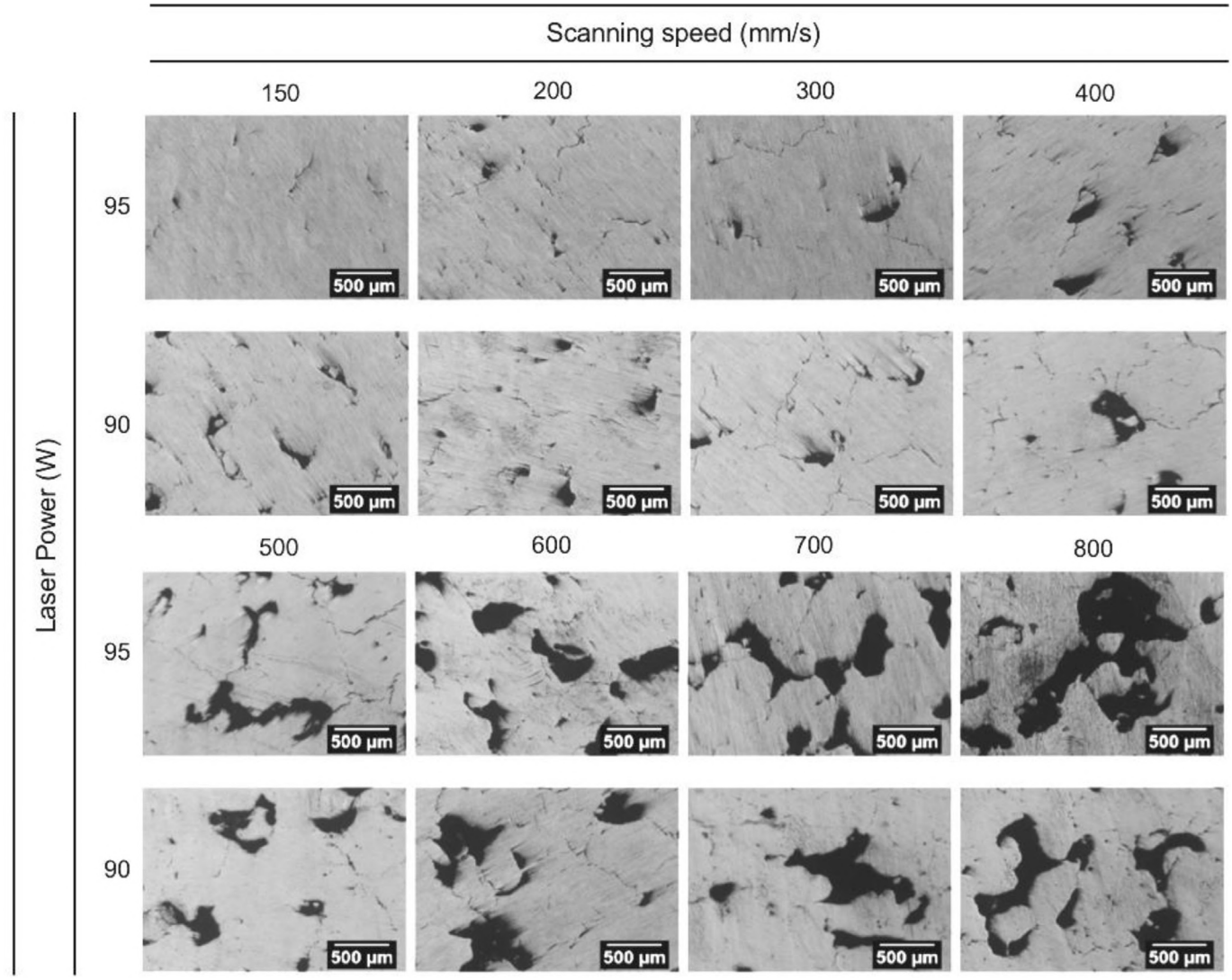

Fig. 4. (a) Optical micrographs of Al-14Zn-3Mg at different laser power and scan speed, showing variation in porosity (minimum average porosity of 0.51% was obtained at a laser power of 95 W and scan speed of 150 mm/s).

and distribution of such phases within the particles, Al-14 Zn-3 Mg was considered for further detailed characterisation. The diffraction pattern obtained from one of the second phase particles in as-built Al-14 Zn-3 Mg revealed a 3-fold symmetry (inset in Fig. 8b"). The presence of a 3-fold symmetry indicates that the particles might be of an icosahedral quasicrystalline structure. It is also known that such 3-fold symmetry does not exist in decagonal quasicrystals [39,40].

The distribution of chemical elements in the LPBF prepared Al-14 Zn-3 Mg was analysed through STEM-EDXS mapping as shown in Fig. 9. Spot analysis was performed at three different regions highlighted as features 1, 2 and 3, in Fig. 9b. The respective compositional analysis of those regions is tabulated, where Al, Zn and Mg were present as the major solutes, whereas Fe, Si and O were present as impurities. In general, second phase particles were rich in Zn and Mg. In addition, it was also observed that some particles were rich in Si, which may be evidence of Mg_2Si (Fig. 9, Point 1). It is interesting to note the appreciable difference in the solute content of the Al-matrix that exists at different locations, as determined from EDXS point analysis in Fig. 9 (Points 2 and 3). An estimate of phases (phase types) was realised through the compositional analysis from STEM-EDXS, as a description of precise phase composition was complex due to particle clustering.

In order to understand the phases within an apparent particle, high magnification BF-STEM and HAADF-STEM of a single particle is shown

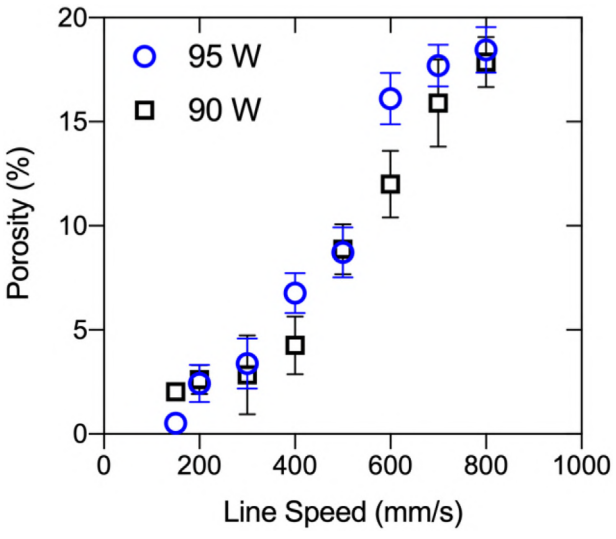

Fig. 5. Porosity of Al-14Zn-3Mg at different scan speeds for two different laser powers, namely 90 W and 95 W. The relative density of the sample with minimum porosity is 99.49%.

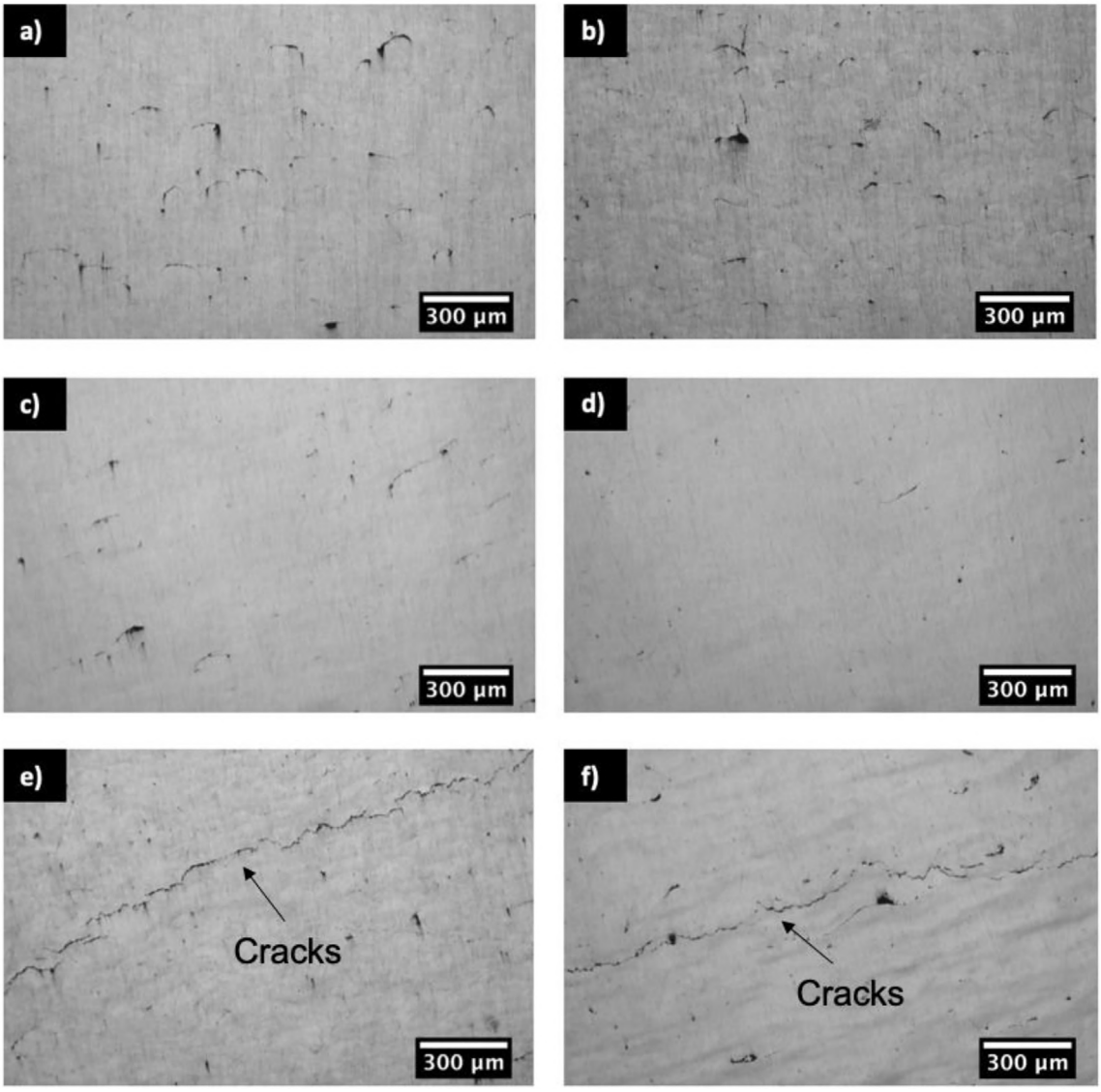

Fig. 6. Optical micrographs of Al-Zn-Mg fabricated with laser power of 95 W and at two scanning speeds, 150 mm/s and 175 mm/s, revealing the typical macro-structures. (a, b) Al-10Zn-2Mg (average porosity - 0.47%); (c, d) Al-14Zn-3Mg (average porosity - 0.38%); (e, f) Al-18Zn-4Mg (average porosity 0.76%) revealing cracking associated with localised evaporation of Mg and Zn.

in (Fig. 10 a and 10b). The features marked as 1 and 2 signified the presence of two different phases that co-exist with each other. The chemical composition of the particles was demonstrated from EDXS analysis as shown in (Fig. 10 c and 10f) with their respective elemental analysis. It can be seen that Particle 1 and Particle 2 have different compositions with the latter having a high Zn and Mg content which was confirmed by the difference in contrast. It was also noted that Particle 1 had a higher iron content with 1.6 at. % when compared to particle 2 that had an iron content of only 0.1%. It was also comprehended that a considerable amount of Mg (~3.8 at. %) and Zn (~10.2 at. %) was dissolved in the Al-matrix as highlighted in the compositional analysis acquired from Feature 3 in Fig. 10.

In order to confirm the presence of a quasicrystalline phase, high resolution STEM was performed for direct imaging. The combination of high resolution imaging coupled with the Fourier transform of STEM images permits an understanding regarding the structure of such nano-crystals present in the LPBF prepared Al-14Zn-3Mg. Characterisation revealed the unambiguous presence of a quasicrystalline phase, where lattice images of five-fold and two-fold symmetries revealed an icosahedral quasicrystal (Fig. 11). The quasi lattice parameter (a_R) was calculated by measuring the edge length of the rhombic tiles that form the building blocks in quasicrystal models by using Eq. 1 [41,42].

$$a_R = \frac{(\tau^3 . d_R)}{2} \quad (1)$$

where a_R is the quasi-lattice parameter, τ is the golden mean with the value of 1.618034 and d_R is the interplanar spacing between the brightest beam to the beam corresponding to (211111) as shown by the line that was measured as 4 nm in Fig. 11 f. The quasi-lattice parameter (a_R) was calculated for Al-14Zn-3Mg as 0.529 nm using Eq. 1. The quasicrystal phases with their respective lattice constant that are possible in the Al-Zn-Mg system are tabulated in Table 2. High solute Al-Zn-Mg alloys were previously prepared by melt spinning techniques. The expected second phase after melt spinning was $Mg_{32}(Al, Zn)_{49}$, also known as T-phase, which has an icosahedral structure and was reported to have a quasi-lattice parameter of 0.515 nm [43]. Gun quenching techniques were also used to fabricate an icosahedral quasicrystal with the composition $Mg_{32}(Al, Zn, Cu)_{49}$ that resulted in the same quasi-lattice constant of 0.515 nm [44]. Recently, LPBF fabricated AA7075 was also

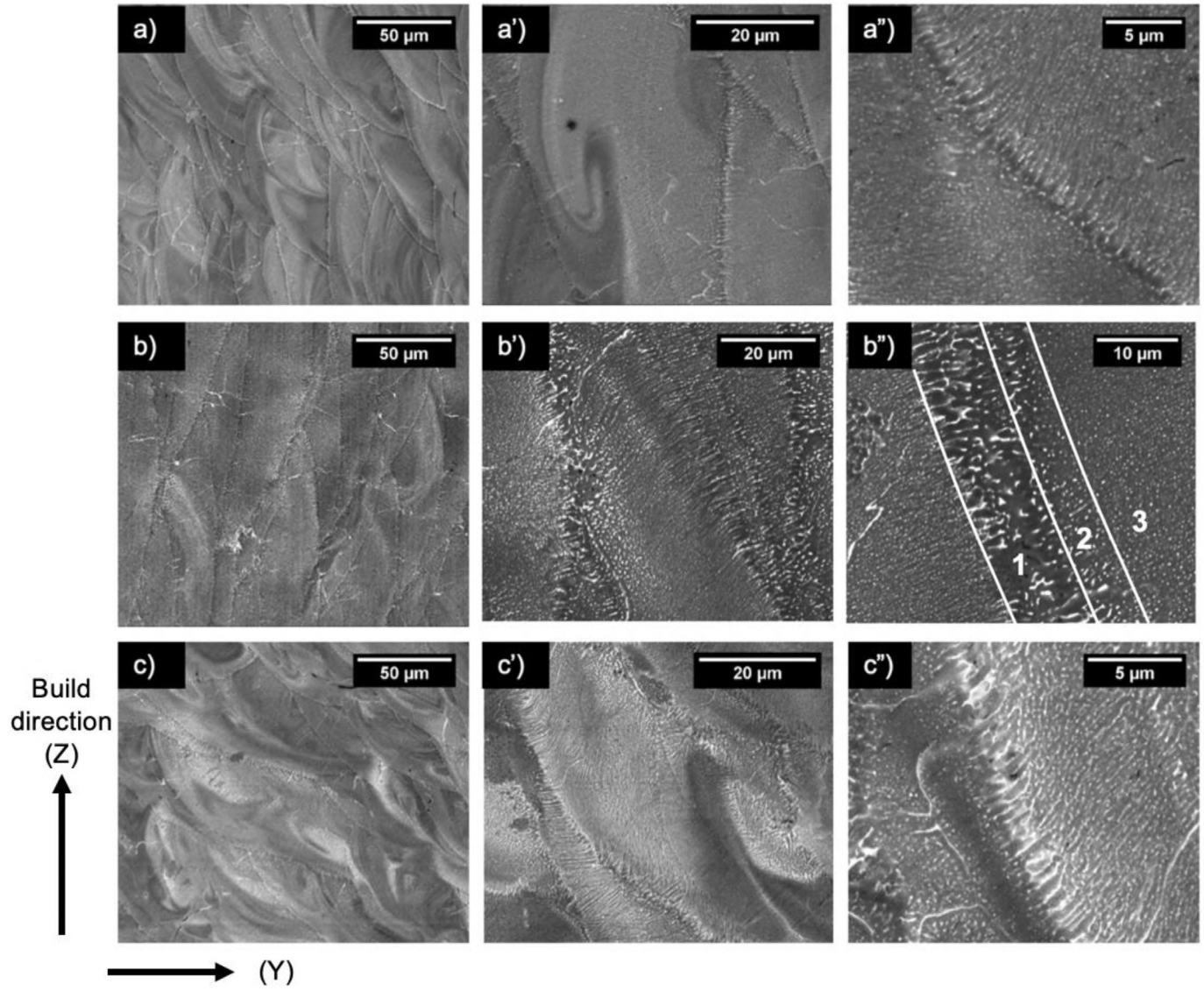

Fig. 7. Backscattered electron SEM micrographs of LPBF prepared Al-Zn-Mg at several magnifications. (a, a' and a") Al-10Zn-2Mg; (b, b' and b") Al-14Zn-3Mg; (c, c' and c") Al—18Zn— 4Mg. The low magnification of the alloys (a, b and c) show melt-pool tracks that are developed during the LPBF process. The higher magnification (a", b" and c") images reveal the presence of spherical and plate-like particles with fine cellular and coarse dendritic structures.

reported to form a quasicrystal phase, termed as ν-phase, which had a quasi-lattice parameter of 0.49 nm [45,46]. The quasi-lattice parameter of Al-14 Zn-3 Mg alloy under study was 0.529 nm which is different (in a statistically significant manner) from the previously reported values - confirming the presence of an unreported quasicrystalline phase, termed herein as P-phase.

XRD analysis (Fig. 12) was also performed to confirm the presence of this new nano-crystal phase and to assess the presence of other phases. It was identified that the Al-matrix with FCC crystal structure was present, in addition to the presence of a unique (non-FCC) phase where the peaks with complex features did not match those of T-phase or η-phase ($MgZn_2$) (Fig. 12). Therefore, the un-identified peaks reported are associated with the quasicrystalline phase particles, i.e. P-phase, which were present in high-volume fraction within the alloy. Although other phases that contain elements such as Fe and Si exist (from the TEM study), no evident peaks from such phases were noticed in X-ray diffraction, signifying the low number density and low volume fraction of Fe and Si-containing phases in the alloys.

3.3. Mechanical property evaluation

The hardness of the LPBF fabricated alloys Al-10Zn-2Mg, Al-14Zn-3Mg and Al-18Zn-4Mg were found to increase with an increase in solute content (Zn + Mg), as shown in Fig. 13. The average hardness values of Al-10 Zn-2 Mg, Al-14 Zn-3Mg and Al-18 Zn-4Mg were measured to be 124.4 ± 0.5 HV_1, 153 ± 4.7 HV_1 and 165.5 ± 2.4 HV_1, respectively. The results indicate that the hardness achieved from these alloys is higher than LPBF-AA7075, which was reported to have a hardness value of 107 HV [46]. The hardness was also comparable to the previously reported high strength aluminium alloys fabricated through selective laser melting, either through Si or Zr additions where hardness values between 100 and 160 HV have been reported [13,21,42,43]. The high hardness in the Al-Zn-Mg alloys produced herein through LPBF is attributed to the high population density of the second phase particles present in the as-build state, in addition to high solute concentration.

In order to evaluate the strength and ductility of these as-fabricated alloys with high hardness, tensile tests were performed as shown in

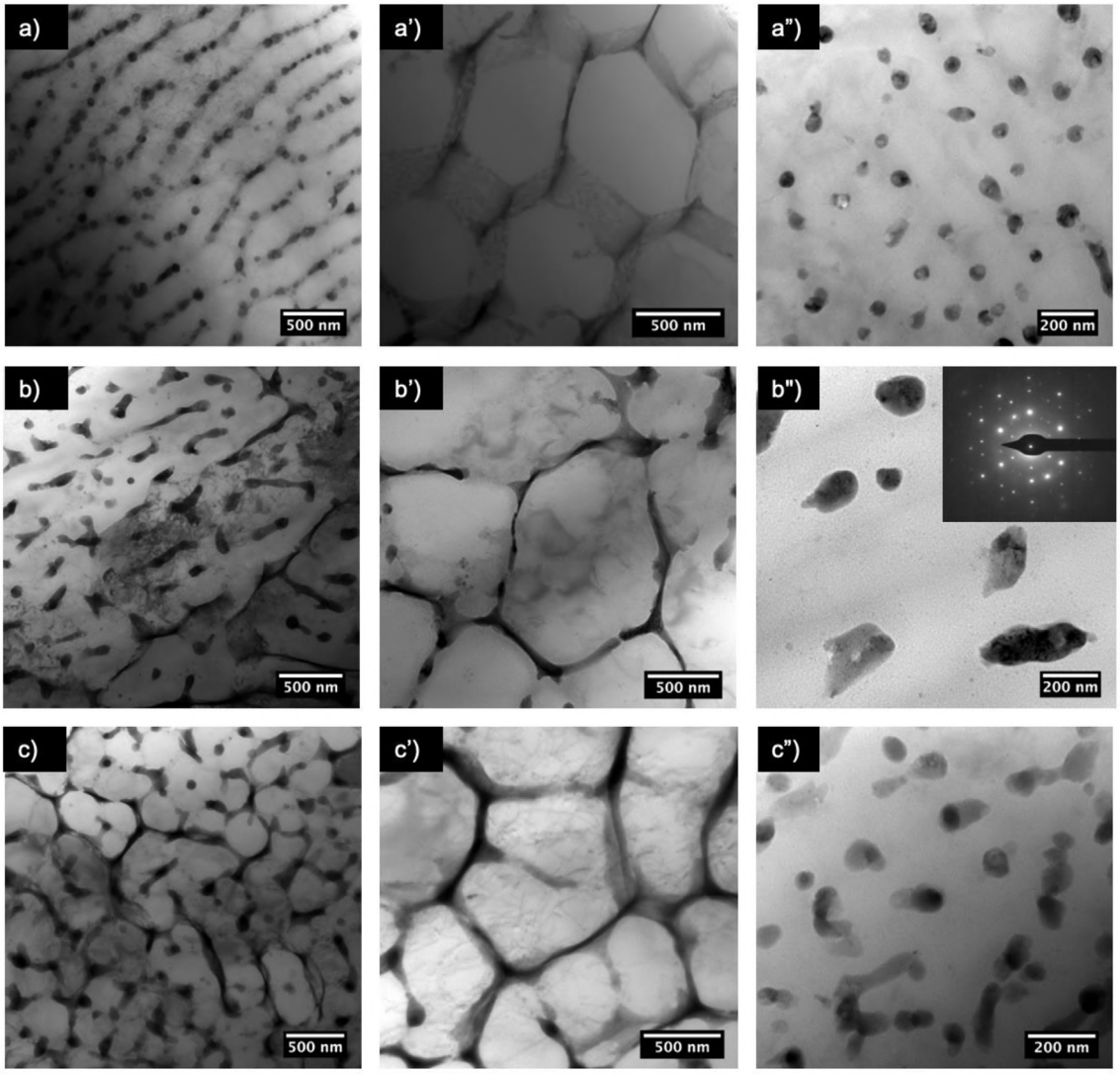

Fig. 8. TEM micrographs of Al-Zn-Mg at several magnifications - (a, a' and a") Al-10Zn-2Mg; (b, b' and b") Al-14Zn-3Mg; (c, c' and c") Al—18Zn— 4Mg. The low magnification of the alloys (a, b and c) show coarse cellular dendrites of the melt pool and (a', b', and c') shows the cell-like structures at the heat affected zone. High magnification (a", b" and c") images reveal second phase particles with different contrast with the size range of 50 to 200 nm.

Fig. 14. The results show that the samples failed well before a yield point, demonstrating the highly brittle nature of these alloys in the as-built condition- where the extent of ductility was negligible (also noted by the dashed line in Fig. 14 that would be notionally used to determine the 0.2% proof stress). The fracture morphology indicated the presence of cleavages, dimples and local occurrences of columnar grains that were exposed on the fracture surface. This denoted a mixed mode of failure between a brittle, ductile and intergranular fracture where similar fracture mechanism has been reported in the SLM of other aluminium alloys [15]. The premature samples failure may be contributed to by the high-volume fraction of second phases present in the as-built condition – although noting that the tensile properties of such alloy compositions have not previously been explored. Studies have also shown that laser spattering affects the final strength of the part which depends on several factors such as inert gas flow velocity, LPBF scanning strategy, part placement and the use of recycled powder [58,59]. The tensile samples used in the present study were carefully placed in the build plate and fresh powders were utilised to minimise the effect of spatter. The brittle nature of LPBF fabricated Al-Zn-Mg alloys may also be attributed to residual stress and high dislocation densities imparted from rapid solidification, would need further analysis.

Post- LPBF heat treatments would be essential to understand the evolution of second phase particles as a function of temperature. Heat treatment will also be essential to impart sufficient ductility to the alloys that are currently being investigated.

4. Discussion

In the present study, high solute Al-Zn-Mg alloys, without the addition of non-commodity elements such as Sc or Zr, were successfully fabricated through selective laser melting in net shape and with acceptable porosity. The macrostructure of the alloys was entirely reliant on process parameters such as the laser power and scan speed, where the size of porosity increased with increase in scan speed, similar to other aluminium alloys previously fabricated through SLM [14,15,50].

This work also indicates the microstructural features associated with production by additive manufacturing relevant to the fabrication of materials layer by layer. It was seen that U-shape melt pools (shown in Fig. 7 – a, d, g) were controlled by the laser interaction and were formed as a result of heat flow that is unique to SLM processing. The formation of such U-shaped structures could be attributed to the temperature gradient formed from the powder surface towards the build direction

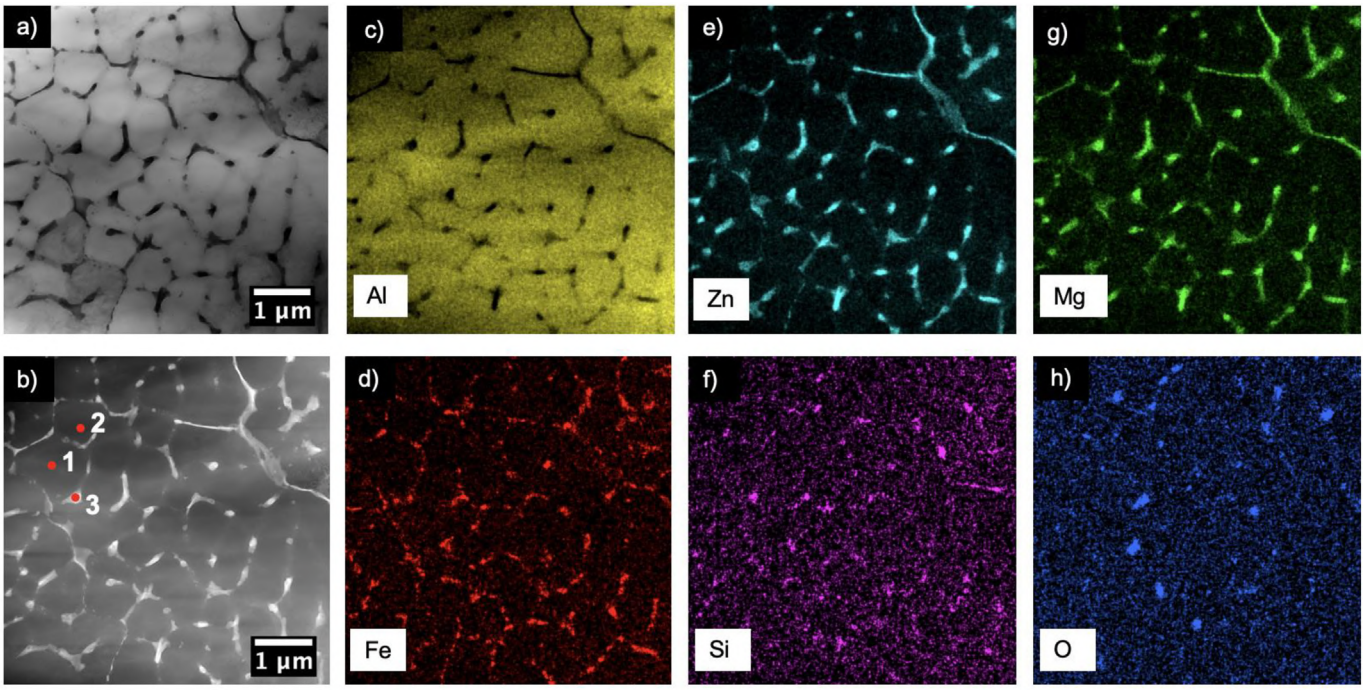

Fig. 9. BF-STEM and HAADF-STEM micrographs of Al-14Zn-3Mg are presented in (a) and (b), respectively, and the corresponding EDXS maps are presented in (c-h). The compositional variation in at. % of different elements at three different points 1, 2 and 3 are tabulated noting that Si and Fe are present as impurities.

when the heat passes from the top to bottom layer of the already sintered powder [51]. It is known that the increase in the degree of constitutional supercooling results in solidification changes from columnar dendritic mode to equiaxed dendritic mode [52]. This was realised in the present alloys where the microstructures were predominantly controlled by the complex thermal cycles existing in SLM process and had a mixture of columnar and equiaxed dendrites (bimodal) that contained second phase particles with

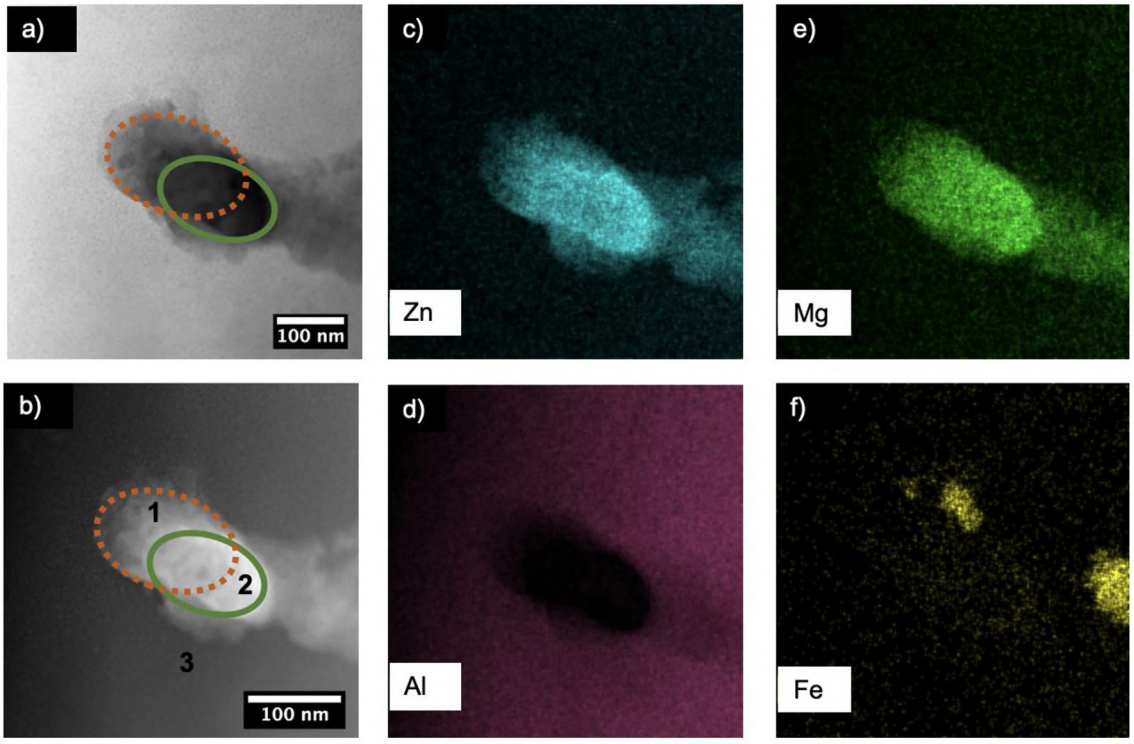

Fig. 10. High magnification BF-STEM and HAADF-STEM micrographs of Al-14Zn-3Mg are shown in (a) and (b), respectively, and their corresponding EDXS maps are presented (c-f). The features labelled as 1 and 2 indicate two individual particles that coexist and feature 3 indicates the Al-matrix. The individual compositions of those features are tabulated in at. %, showing compositional variation that existed within the mapped region.

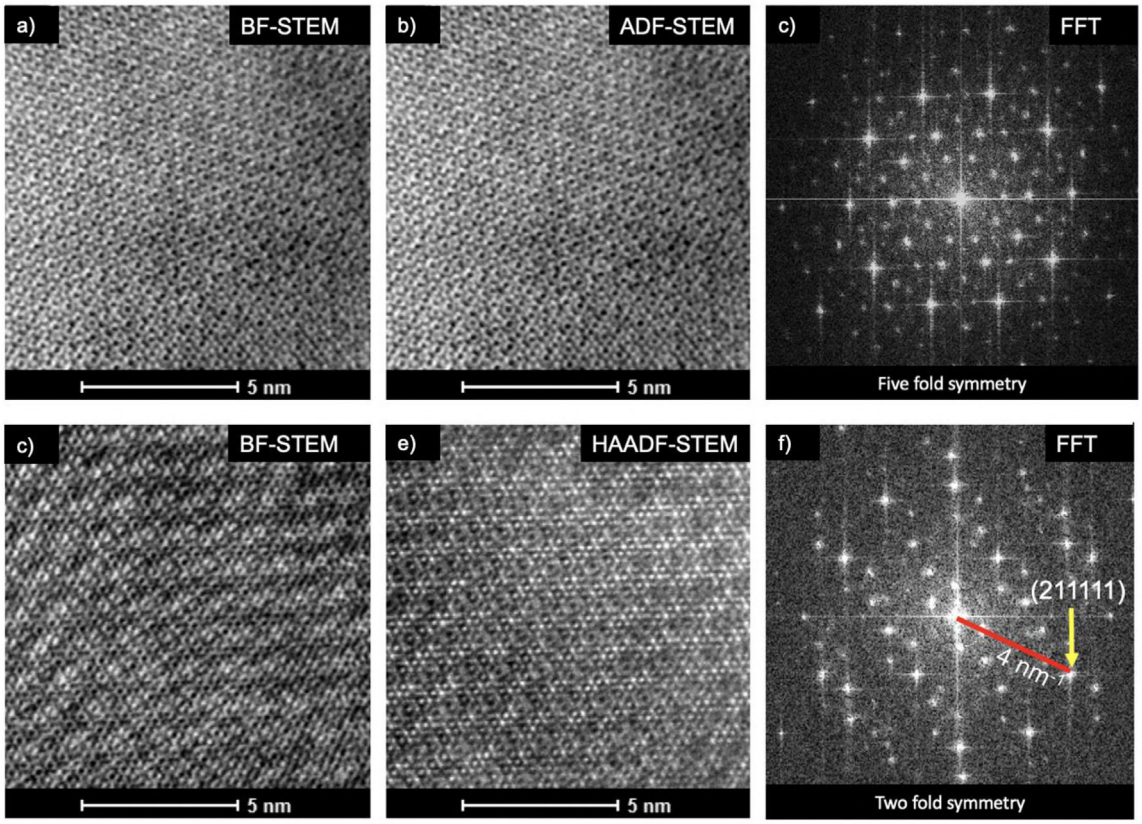

Fig. 11. (a and b) Atomic resolution BF-STEM and ADF-STEM image of a unique quasicrystal along a fivefold symmetry axis. (c) Fourier transformation of ADF-STEM image in (b). (d and e) Atomic resolution BF-STEM and HAADF-STEM image of a quasicrystal along twofold symmetrical zone axis. (f) Fourier transformation of HAADF-STEM image from (e). The distance from the diffracted spot with (211111) indices to the non-diffracted beam at the centre is denoted by the line in (f) which was measured as 4 nm^{-1}.

Table 2
Comparison of the quasi-lattice constant of different phases.

Phase	Quasi-lattice constant
ν-phase	0.49 nm
$Mg_{32}(Al, Zn)_{49}$	0.515 nm
Identified phase (P-phase)	0.526 nm

different size and morphology. The complex thermal cycles from the SLM process resulted in varied degree of constitutional supercooling and growth rate across the build surface, resulting in the formation of different zones of the melt pool. It was reported that, during rapid solidification, a large density of dislocations originate as a result of thermal contraction, arranging into honeycomb-like structures and commonly termed cellular sub-structures [53]. These cellular sub-structure boundaries provide nucleation sites for the evolution of second phase particles which resulted in unique phase

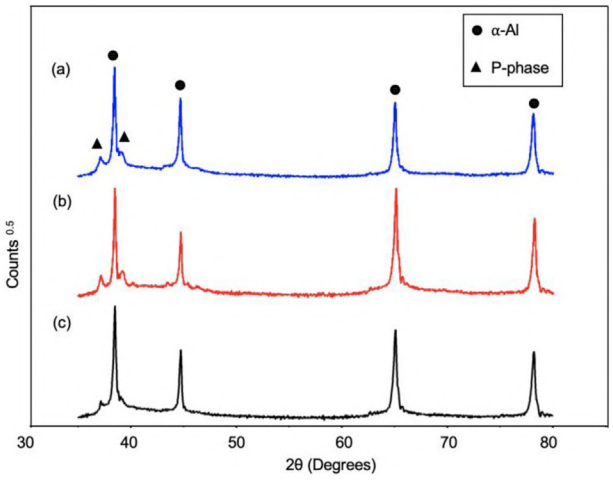

Fig. 12. X-ray diffraction pattern of as-fabricated Al-Zn-Mg through LPBF: (a) Al-10Zn-2Mg; (b) Al-14Zn-3Mg; (c) Al-18Zn-4Mg; revealing the presence of a second phase along with the Al-matrix.

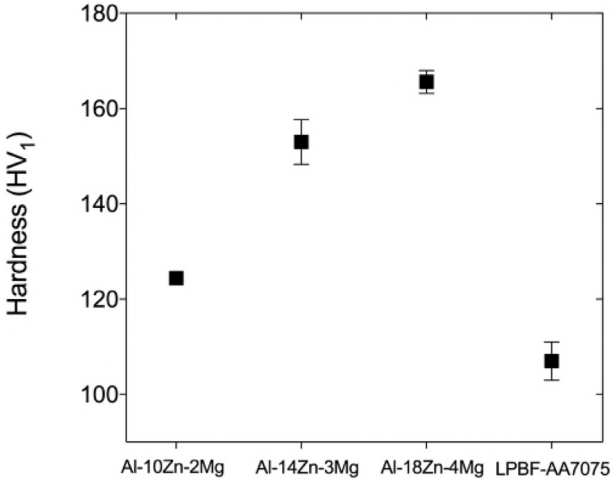

Fig. 13. Hardness of LPBF prepared Al-10Zn-2Mg, Al-14Zn-3Mg and Al-18Zn-4Mg in comparison with LPBF-AA7075 [48].

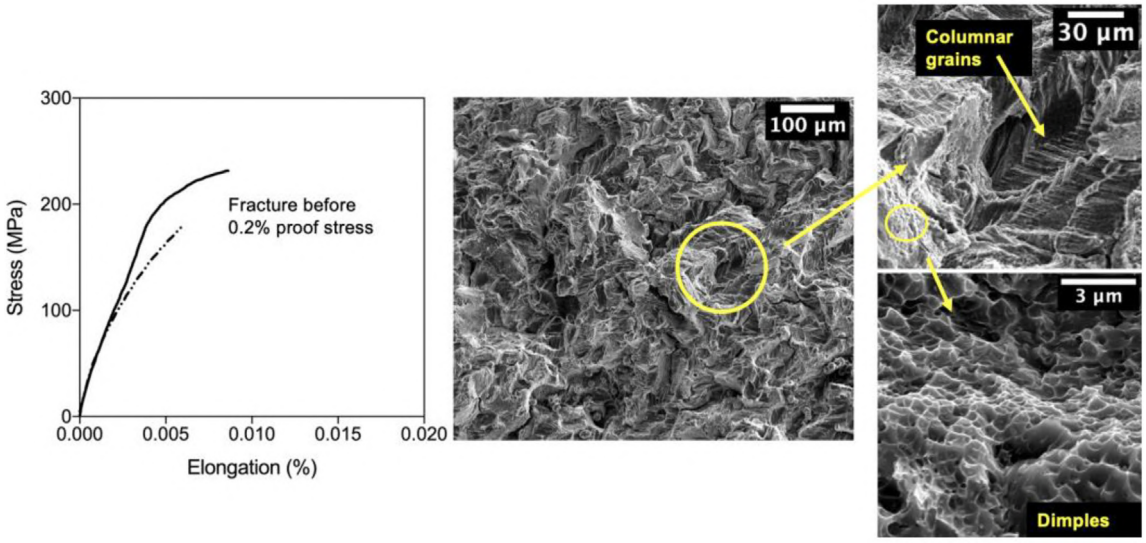

Fig. 14. Representative tensile data showing the failure before 0.2% proof stress of LPBF prepared Al-10Zn-2Mg (represented by continuous lines) and Al-14Zn-3Mg (represented by dotted lines). The representative fracture morphology shows the presence of cleavages, dimples and columnar grains that were exposed to the fracture surface denoting a mixed mode of brittle, ductile and intergranular fracture.

arrangement along the boundaries (Fig. 8 a', b', c'). Similar structures decorated with second phase particles were also reported for LPBF of AA2024, AA7075 and nickel based superalloys [46,54–57]. The coexistence of particles also implied that there was solute trapped during the rapid solidification process which – as solidification progressed, acted as sites of nucleation for the second phase to form. As the EDXS method is qualitative, the exact composition of particles formed was not possible due to particle clustering, nevertheless, the pursuit of such phenomena and phases warrants future research. It is noted that traces of Si and Fe were found in the particles, both of which Si and Fe are present as impurities. What is however noteworthy, is that the size of many-micron sized constituent particles (present from impurities in cast and wrought alloys) that are notionally rich in Fe and Si for 2xxx and 7xxx alloys, were not observed in the alloys herein – confirming that the SLM process is able to annihilate any coarse particles that are rich in transition metals. The rapid solidification of these high melting temperature elements, in combination with the Zn and Mg, however, produced complex clustering of second phase particles.

The quasicrystalline phase (P-phase) identified in the present study had a hitherto quasi-lattice constant value which is unreported in the literature [38]. The discovery of a new phase signifies a novel finding, made possible through additive manufacturing and modern advanced characterisation techniques – in spite of a century of research on the (Al-Zn-Mg) alloy system to date. Such a finding indicates that there remains significant work to be done in (re) understanding so-called conventional alloy systems in the context of SLM.

The rapid solidification through SLM facilitated the high concentration of Zn and Mg incorporated in the alloys under consideration. This was higher than the solute limits achieved through other powder metallurgy and rapid solidification processes, where the maximum Zn and Mg content was approximately 9 wt% and 3 wt% respectively [12]. Such high solute alloys resulted in high hardness that was ~30–40% higher than the additively manufactured AA7075 and Zr modified AA7075 in the as-built condition previously reported [21, 46]. However, further heat treatment is required to modify the brittleness of the alloy in order to permit sufficient alloy ductility. The research question that arises from this study is whether the presence of excess solute, or hyperloading with solute, is universally associated with deteriorated mechanical properties; Ongoing work to ascertain this question is underway.

5. Conclusions

Novel alloys based on the Al-Zn-Mg system with high solute content were successfully produced via selective laser melting (SLM), with no hot cracking and acceptably low porosity. This study revealed the possibility to develop new Al-alloys for additively manufacturing without the requirement of adding expensive alloying elements – albeit that the optimisation of property balance remains underway for the system studied. Additionally, the present study revealed new insights into the physical metallurgy of very high solute rich Al-alloys. The following conclusions may be drawn from the present work:

- Al-10Zn-2Mg and Al-14Zn-3Mg (wt%) were successfully fabricated with no visible hot cracking via SLM, with porosities of 0.47% and 0.38%, respectively. The Al-18Zn-4Mg (wt%) alloy showed potential signs of local cracking due to the localised vaporisation of Zn and Mg.
- The microstructure of the alloys investigated was unique to conventionally cast and wrought alloys, exhibiting high volume fraction of second phase particles along different regions of the melt pool in the as-built condition.
- Transmission electron microscopy revealed the presence of cell-like structures, which were developed as a result of the complex thermal cycle during SLM. In addition, several second phase particles with different composition were found to coexist in the Al-matrix.
- Previously unreported, a new icosahedral quasicrystalline phase was determined in the SLM fabricated Al-14Zn-3Mg alloy and was termed P-phase.
- The hardness of SLM fabricated Al-Zn-Mg alloys (120–160 HV_1) was determined to be higher than SLM fabricated AA7075 samples ($\approx$ 108 HV_1), in the as-built condition. However, the tensile properties of the alloys studied herein revealed brittleness and further heat treatment studies are underway to obtain optimum mechanical properties.

Data availability

The raw/processed data required to reproduce these findings cannot be shared at this time as the data also forms part of an ongoing study.

Declaration of Competing Interest

None.

Acknowledgements

The authors gratefully acknowledge the use of facilities at the Monash Centre for Electron Microscopy (MCEM), Monash X-ray Platform (MXP) and Department of Materials science and Engineering, Monash University. This work was supported by the Monash Graduate Research Scholarship.

References

[1] J.J. Lewandowski, M. Seifi, Metal additive manufacturing: A review of mechanical properties, Annu. Rev. Mater. Res. 46 (2016) 151–186, https://doi.org/10.1146/annurev-matsci-070115-032024.
[2] J. Edgar, S. Tint, "Additive manufacturing technologies: 3D printing, rapid prototyping, and direct digital manufacturing", 2nd edition, Johnson Matthey Technol. Rev. 59 (2015) 193–198, https://doi.org/10.1595/205651315x688406.
[3] D. Herzog, V. Seyda, E. Wycisk, C. Emmelmann, Additive manufacturing of metals, Acta Mater. 117 (2016) 371–392, https://doi.org/10.1016/j.actamat.2016.07.019.
[4] W.E. Frazier, Metal additive manufacturing: A review, J. Mater. Eng. Perform. 23 (2014) 1917–1928, https://doi.org/10.1007/s11665-014-0958-z.
[5] S. Lathabai, Additive Manufacturing of Aluminium-Based Alloys and Composites, in: Fundam. Alum. Metall. Elsevier, 2018 47–92, https://doi.org/10.1016/b978-0-08-102063-0.00002-3.
[6] N.T. Aboulkhair, I. Maskery, C. Tuck, I. Ashcroft, N.M. Everitt, On the formation of AlSi10Mg single tracks and layers in selective laser melting: Microstructure and nano-mechanical properties, J. Mater. Process. Technol. 230 (2016) 88–98, https://doi.org/10.1016/j.jmatprotec.2015.11.016.
[7] I. Maskery, N.T. Aboulkhair, M.R. Corfield, C. Tuck, A.T. Clare, R.K. Leach, R.D. Wildman, I.A. Ashcroft, R.J.M. Hague, Quantification and characterisation of porosity in selectively laser melted Al-Si10-Mg using X-ray computed tomography, Mater. Charact. 111 (2016) 193–204, https://doi.org/10.1016/j.matchar.2015.12.001.
[8] N.T. Aboulkhair, N.M. Everitt, I. Ashcroft, C. Tuck, Reducing porosity in AlSi10Mg parts processed by selective laser melting, Addit. Manuf. 1 (2014) 77–86, https://doi.org/10.1016/j.addma.2014.08.001.
[9] N.T. Aboulkhair, I. Maskery, C. Tuck, I. Ashcroft, N.M. Everitt, The microstructure and mechanical properties of selectively laser melted AlSi10Mg: The effect of a conventional T6-like heat treatment, Mater. Sci. Eng. A 667 (2016) 139–146, https://doi.org/10.1016/j.msea.2016.04.092.
[10] J. Suryawanshi, K.G. Prashanth, S. Scudino, J. Eckert, O. Prakash, U. Ramamurty, Simultaneous enhancements of strength and toughness in an Al-12Si alloy synthesized using selective laser melting, Acta Mater. 115 (2016) 285–294, https://doi.org/10.1016/j.actamat.2016.06.009.
[11] J. Wu, X.Q. Wang, W. Wang, M.M. Attallah, M.H. Loretto, Microstructure and strength of selectively laser melted AlSi10Mg, Acta Mater. 117 (2016) 311–320, https://doi.org/10.1016/j.actamat.2016.07.012.
[12] I.J. Polmear, D. StJohn, J.F. Nie, M. Qian, Light Alloys : Metallurgy of the Light Metals, 2017.
[13] M.L. Montero Sistiaga, R. Mertens, B. Vrancken, X. Wang, B. Van Hooreweder, J.P. Kruth, J. Van Humbeeck, Changing the alloy composition of Al7075 for better processability by selective laser melting, J. Mater. Process. Technol. 238 (2016) 437–445, https://doi.org/10.1016/j.jmatprotec.2016.08.003.
[14] N. Kaufmann, M. Imran, T.M. Wischeropp, C. Emmelmann, S. Siddique, F. Walther, Influence of Process Parameters on the Quality of Aluminium Alloy en AW 7075 Using Selective Laser Melting (SLM), in: Phys, Procedia, Elsevier B.V., 2016 918–926, https://doi.org/10.1016/j.phpro.2016.08.096.
[15] H. Zhang, H. Zhu, T. Qi, Z. Hu, X. Zeng, Selective laser melting of high strength Al-Cu-Mg alloys: Processing, microstructure and mechanical properties, Mater. Sci. Eng. A 656 (2016) 47–54, https://doi.org/10.1016/j.msea.2015.12.101.
[16] H. Zhang, H. Zhu, X. Nie, J. Yin, Z. Hu, X. Zeng, Effect of Zirconium addition on crack, microstructure and mechanical behavior of selective laser melted Al-Cu-Mg alloy, Scr. Mater. 134 (2017) 6–10, https://doi.org/10.1016/j.scriptamat.2017.02.036.
[17] K. Schmidtke, F. Palm, A. Hawkins, C. Emmelmann, Process and Mechanical Properties: Applicability of a Scandium Modified Al-alloy for Laser Additive Manufacturing, in: Phys, Procedia, Elsevier B.V., 2011 369–374, https://doi.org/10.1016/j.phpro.2011.03.047.
[18] A.B. Spierings, K. Dawson, P. Dumitraschkewitz, S. Pogatscher, K. Wegener, Microstructure characterization of SLM-processed Al-Mg-Sc-Zr alloy in the heat treated and HIPed condition, Addit. Manuf. 20 (2018) 173–181, https://doi.org/10.1016/j.addma.2017.12.011.
[19] A.B. Spierings, K. Dawson, P.J. Uggowitzer, K. Wegener, Influence of SLM scan-speed on microstructure, precipitation of Al3Sc particles and mechanical properties in Sc- and Zr-modified Al-Mg alloys, Mater. Des. 140 (2018) 134–143, https://doi.org/10.1016/j.matdes.2017.11.053.
[20] Q. Jia, F. Zhang, P. Rometsch, J. Li, J. Mata, M. Weyland, L. Bourgeois, M. Sui, X. Wu, Precipitation kinetics, microstructure evolution and mechanical behavior of a developed Al-Mn-Sc alloy fabricated by selective laser melting, Acta Mater. 193 (2020) 239–251, https://doi.org/10.1016/j.actamat.2020.04.015.
[21] J.H. Martin, B.D. Yahata, J.M. Hundley, J.A. Mayer, T.A. Schaedler, T.M. Pollock, 3D printing of high-strength aluminium alloys, Nature. 549 (2017) 365–369, https://doi.org/10.1038/nature23894.
[22] A. Aversa, G. Marchese, A. Saboori, E. Bassini, D. Manfredi, S. Biamino, D. Ugues, P. Fino, M. Lombardi, New aluminum alloys specifically designed for laser powder bed fusion: A review, Materials (2019) 12, https://doi.org/10.3390/ma12071007 Basel.
[23] M. De Sanctis, Structure and Properties of Rapidly Solidified Ultrahigh Strength Al-Zn-Mg-Cu Alloys Produced by Spray Deposition, 1991.
[24] M.M. Sharma, M.F. Amateau, T.J. Eden, Mesoscopic structure control of spray formed high strength Al-Zn-Mg-Cu alloys, Acta Mater. 53 (2005) 2919–2924, https://doi.org/10.1016/j.actamat.2005.03.007.
[25] F. Wang, B. Xiong, Y. Zhang, B. Zhu, H. Liu, X. He, Effect of heat treatment on the microstructure and mechanical properties of the spray-deposited Al–10.8Zn–2.8Mg–1.9Cu alloy, Mater. Sci. Eng. A 486 (2008) 648–652, https://doi.org/10.1016/J.MSEA.2007.09.049.
[26] M.M. Sharma, Microstructural and mechanical characterization of various modified 7XXX series spray formed alloys, Mater. Charact. 59 (2008) 91–99, https://doi.org/10.1016/J.MATCHAR.2007.01.013.
[27] H. Li, F. Cao, S. Guo, Y. Jia, D. Zhang, Z. Liu, P. Wang, S. Scudino, J. Sun, Effects of Mg and Cu on microstructures and properties of spray-deposited Al-Zn-Mg-Cu alloys, J. Alloys Compd. 719 (2017) 89–96, https://doi.org/10.1016/j.jallcom.2017.05.101.
[28] M. Rappaz, J.-M. Drezet, M. Gremaud, A New Hot-Tearing Criterion, 1999.
[29] T. DebRoy, H.L. Wei, J.S. Zuback, T. Mukherjee, J.W. Elmer, J.O. Milewski, A.M. Beese, A. Wilson-Heid, A. De, W. Zhang, Additive manufacturing of metallic components – process, structure and properties, Prog. Mater. Sci. 92 (2018) 112–224, https://doi.org/10.1016/j.pmatsci.2017.10.001.
[30] T. Mukherjee, J.S. Zuback, A. De, T. DebRoy, Printability of alloys for additive manufacturing, Sci. Rep. (2016) 6, https://doi.org/10.1038/srep19717.
[31] P. Wang, H.C. Li, K.G. Prashanth, J. Eckert, S. Scudino, Selective laser melting of Al-Zn-Mg-Cu: Heat treatment, microstructure and mechanical properties, J. Alloys Compd. 707 (2017) 287–290, https://doi.org/10.1016/j.jallcom.2016.11.210.
[32] J.A. Slotwinski, E.J. Garboczi, Metrology needs for metal additive manufacturing powders, Jom. 67 (2015) 538–543, https://doi.org/10.1007/s11837-014-1290-7.
[33] A. Strondl, O. Lyckfeldt, H. Brodin, U. Ackelid, Characterization and control of powder properties for additive manufacturing, Jom. 67 (2015) 549–554, https://doi.org/10.1007/s11837-015-1304-0.
[34] U. Ali, Y. Mahmoodkhani, S. Imani Shahabad, R. Esmaeilizadeh, F. Liravi, E. Sheydaeian, K.Y. Huang, E. Marzbanrad, M. Vlasea, E. Toyserkani, On the measurement of relative powder-bed compaction density in powder-bed additive manufacturing processes, Mater. Des. 155 (2018) 495–501, https://doi.org/10.1016/j.matdes.2018.06.030.
[35] A. Haboudou, P. Peyre, A.B. Vannes, G. Peix, Reduction of porosity content generated during Nd:YAG laser welding of A356 and AA5083 aluminium alloys, Mater. Sci. Eng. A 363 (2003) 40–52, https://doi.org/10.1016/S0921-5093(03)00637-3.
[36] R. Xiao, X. Zhang, Problems and issues in laser beam welding of aluminum–lithium alloys, J. Manuf. Process. 16 (2014) 166–175, https://doi.org/10.1016/J.JMAPRO.2013.10.005.
[37] G. Mathers, The Welding of Aluminium and its Alloys, CRC Press, 2002.
[38] L.F. Mondolfo, Al-Mg-Zn alloys - A Review of the Literature, Res. Dev. Center, Reverse Copp, Brass Inc., 1967
[39] J. Mikhael, J. Roth, L. Helden, C. Bechinger, Archimedean-like tiling on decagonal quasicrystalline surfaces, Nature. 454 (2008) 501–504, https://doi.org/10.1038/nature07074.
[40] L. Bindi, N. Yao, C. Lin, L.S. Hollister, C.L. Andronicos, V.V. Distler, M.P. Eddy, A. Kostin, V. Kryachko, G.J. MacPherson, W.M. Steinhardt, M. Yudovskaya, P.J. Steinhardt, Natural quasicrystal with decagonal symmetry, Sci. Rep. 5 (2015) 1–5, https://doi.org/10.1038/srep09111.
[41] V. Elser, Indexing problems in quasicrystal diffraction, Phys. Rev. B 32 (1985) 4892–4898, https://doi.org/10.1103/PhysRevB.32.4892.
[42] V. Elser, C.L. Henley, Crystal and quasicrystal structures in Al-Mn-Si alloys, Phys. Rev. Lett. 55 (1985) 2883–2886, https://doi.org/10.1103/PhysRevLett.55.2883.
[43] L. Bourgeois, C.L. Mendis, B.C. Muddle, J.F. Nie, Characterization of quasicrystalline primary intermetallic particles in Mg-8 wt% Zn-4 wt% Al casting alloy, Philos. Mag. Lett. 81 (2001) 709–718, https://doi.org/10.1080/09500830110073959.
[44] N.K. Mukhopadhyay, G.N. Subbanna, S. Ranganathan, K. Chattopadhyay, An electron microscopic study of quasicrystals in a quaternary alloy : Mg32(Al, Zn, Cu)49, Scr. Metall. 20 (1986) 525–528, https://doi.org/10.1016/0036-9748(86)90247-4.
[45] S.K. Kairy, O. Gharbi, J. Nicklaus, D. Jiang, C.R. Hutchinson, N. Birbilis, On the characterization of a hitherto unreported icosahedral Quasicrystal phase in additively manufactured aluminum alloy AA7075, Metall. Mater. Trans. A Phys. Metall. Mater. Sci. 50 (2019) 529–533, https://doi.org/10.1007/s11661-018-5025-1.
[46] O. Gharbi, S. Kumar Kairy, P.R. De Lima, D. Jiang, J. Nicklaus, N. Birbilis, Microstructure and corrosion evolution of additively manufactured aluminium alloy AA7075 as a function of ageing, Npj Mater. Degrad (2019) 3, https://doi.org/10.1038/s41529-019-0101-6.
[48] L. Li, R. Li, T. Yuan, C. Chen, Z. Zhang, X. Li, Microstructures and tensile properties of a selective laser melted Al–Zn–Mg–Cu (Al7075) alloy by Si and Zr microalloying, Mater. Sci. Eng. A 787 (2020) 139492, https://doi.org/10.1016/j.msea.2020.139492.
[50] B. Ahuja, M. Karg, K.Y. Nagulin, M. Schmidt, Fabrication and Characterization of High Strength Al-Cu Alloys Processed Using Laser Beam Melting in Metal Powder Bed, in: Phys. Procedia, Elsevier B.V., 2014 135–146, https://doi.org/10.1016/j.phpro.2014.08.156.
[51] L. Thijs, K. Kempen, J.P. Kruth, J. Van Humbeeck, Fine-structured aluminium products with controllable texture by selective laser melting of pre-alloyed AlSi10Mg

powder, Acta Mater. 61 (2013) 1809–1819, https://doi.org/10.1016/j.actamat.2012.11.052.
[52] S. Kou, Welding Metallurgy, Second edi John Wiley & Sons, Inc., 2003
[53] S. Gorsse, C. Hutchinson, M. Gouné, R. Banerjee, Additive manufacturing of metals: A brief review of the characteristic microstructures and properties of steels, Ti-6Al-4V and high-entropy alloys, Sci. Technol. Adv. Mater. 18 (2017) 584–610, https://doi.org/10.1080/14686996.2017.1361305.
[54] O. Gharbi, D. Jiang, D.R. Feenstra, S.K. Kairy, Y. Wu, C.R. Hutchinson, N. Birbilis, On the corrosion of additively manufactured aluminium alloy AA2024 prepared by selective laser melting, Corros. Sci. 143 (2018) 93–106, https://doi.org/10.1016/j.corsci.2018.08.019.
[55] A. Keshavarzkermani, E. Marzbanrad, R. Esmaeilizadeh, Y. Mahmoodkhani, U. Ali, P.D. Enrique, N.Y. Zhou, A. Bonakdar, E. Toyserkani, An investigation into the effect of process parameters on melt pool geometry, cell spacing, and grain refinement during laser powder bed fusion, Opt. Laser Technol. 116 (2019) 83–91, https://doi.org/10.1016/j.optlastec.2019.03.012.
[56] N.J. Harrison, I. Todd, K. Mumtaz, Reduction of micro-cracking in nickel superalloys processed by selective laser melting: A fundamental alloy design approach, Acta Mater. 94 (2015) 59–68, https://doi.org/10.1016/j.actamat.2015.04.035.
[57] X. Wang, L.N. Carter, B. Pang, M.M. Attallah, M.H. Loretto, Microstructure and yield strength of SLM-fabricated CM247LC Ni-Superalloy, Acta Mater. 128 (2017) 87–95, https://doi.org/10.1016/j.actamat.2017.02.007.
[58] A. Bin Anwar, Q.C. Pham, Study of the spatter distribution on the powder bed during selective laser melting, Addit. Manuf. 22 (2018) 86–97, https://doi.org/10.1016/j.addma.2018.04.036.
[59] M. Lutter-Günther, M. Bröker, T. Mayer, S. Lizak, C. Seidel, G. Reinhart, Spatter formation during laser beam melting of AlSi10Mg and effects on powder quality, Procedia CIRP. 74 (2018) 33–38, https://doi.org/10.1016/j.procir.2018.08.008.

5

Heat treatment and mechanical properties of a high solute Al-Zn-Mg alloy

5.1 Chapter synopsis

This chapter is focused towards heat treatment and mechanical properties of high solute Al-14Zn-3Mg and it is a research paper with the title, "On the heat treatment and mechanical properties of a high solute Al-Zn-Mg alloy processed through laser powder bed fusion process" as published in Materials science & Engineering A.

In this work, the high solute Al-14Zn-3Mg was subjected to different heat treatment conditions and the corresponding microstructure was evaluated through scanning and transmission electron microscopy (SEM and TEM). Microstructural characterisation revealed the presence of high area fraction of η' and η-$MgZn_2$ precipitates in the Al-matrix as a result of precipitation heat treatment. The formation of such hardening precipitates were expected to increase the mechanical properties of high solute Al-14Zn-3Mg, however, the results demonstrated a compromise in ductility. This behaviour was elucidated in the context of microstructure-strength relationship, where the results reveal a loss of mechanical properties in Al-alloys when the area fraction of second phase exceeds ~50%. This study provides significant insights in revealing the critical solute limits (herein, Zn and Mg) that are fundamental to achieve good mechanical properties through second phase strengthening in Al-alloys.

Materials Science & Engineering A 807 (2021) 140857

Contents lists available at ScienceDirect

Materials Science & Engineering A

journal homepage: http://www.elsevier.com/locate/msea

On the heat treatment and mechanical properties of a high solute Al–Zn–Mg alloy processed through laser powder bed fusion process

A.P. Babu [a,*], A. Huang [a,b], N. Birbilis [c]

[a] Department of Materials Science and Engineering, Monash University, Clayton, VIC, 3800, Australia
[b] Monash Centre for Additive Manufacturing, Monash University, Clayton, VIC, 3800, Australia
[c] College of Engineering and Computer Science, The Australian National University, Acton, ACT, 2601, Australia

ARTICLE INFO

Keywords:
Selective laser melting
Aluminium
Heat treatment
Al–Zn–Mg
Microstructures
Mechanical properties

ABSTRACT

High strength alloys in the Al–Zn–Mg system are primarily strengthened through artificial ageing by the formation of precipitates that are rich in Mg and Zn. In this work, a high solute Al–Zn–Mg alloy with 14 wt% Zn and 3 wt% Mg was prepared using the laser powder bed fusion process (LPBF). Heat treatment of Al–14Zn–3Mg revealed the presence of a high volume fraction of η' and η-Mg(Zn, Al)$_2$ precipitates in the Al-matrix, accompanied by a compromise of mechanical properties. This was elucidated in the context of microstructure – strength relationship, where the results demonstrate a loss of mechanical properties in aluminium alloys when the area fraction of second phases exceeds ~50%. This study is a discrete effort towards revealing the critical solute limits of Zn and Mg in aluminium that are imperative to achieve high strength through second phase particles – a fundamental concept that maybe exploited in the future design of high strength Al-alloys through additive manufacturing.

1. Introduction

Additive manufacturing has emerged over the last decade, resulting in an evolved landscape of manufacturing across diverse technological areas. Additive manufacturing techniques utilise an energy source to build products layer by layer, in contrast to conventional manufacturing techniques which involve a subtractive process [1]. Furthermore, additive manufacturing technology also addresses demand for solutions that are essential to promote value creation with minimal environmental impact. Laser powder bed fusion (LPBF), commercially known as selective laser melting (SLM), is a form of additive manufacturing which has the capability to produce bespoke net-shaped parts that cannot be fabricated through conventional manufacturing routes. The ASTM defines laser powder bed fusion as a technique that utilises thermal energy (a laser source) to selectively fuse regions of a powder in order to build the final component in a layer wise manner based on a computer model [2]. The benefits of adopting additive manufacturing coupled with the freedom of design has led to the fabrication of a portfolio of metallic materials such as aluminium alloys, stainless steels, nickel alloys and titanium alloys [3].

Of the several metallic materials fabricated through LPBF, aluminium alloys are gaining increasing interest due to their wide spread application in modern manufacturing that necessitates light weight components with complex geometry. LPBF also promotes enhanced material properties due to fine grain structures formed as a result of rapid solidification [4]. Such fine grain microstructures are attributed to the ultrafast cooling rate (10^5–10^6 K/s), resulting in increased dislocation densities that may also promote enhanced mechanical properties [5]. In the pursuit of achieving improved properties, considerable work has been reported on the LPBF fabrication of cast aluminium alloy compositions, such as AlSi10Mg [6–13] and AlSi12 [14] owing to their narrow solidification range. The strength of the aluminium alloys prepared by LPBF is demonstrably improved by ~30–50% when compared to their respective casting alloys, owing to the aforementioned factors that promote the formation of a unique microstructure [13,15]. Conversely however, complexities may also arise from the cooling rates experienced during the LPBF process, such that pursuits to further improve the mechanical properties of wrought aluminium alloys via alloying can pose challenges such as the formation of hot cracking and porosity [16]. To date, attempts have been made to directly fabricate or alter the composition of traditional wrought Al-alloys (such as the 2xxx and 7xxx series Al-alloys) by adding inoculants such as Si, Si + TiB_2, Zr or Sc to minimise hot cracking during LPBF fabrication [17–22]. The broader exploration of Al-alloy systems

* Corresponding author.
E-mail address: abirami.babu@monash.edu (A.P. Babu).

https://doi.org/10.1016/j.msea.2021.140857
Received 21 November 2020; Received in revised form 18 January 2021; Accepted 25 January 2021
Available online 31 January 2021

that are more resilient to, and exploit, the benefits of rapid solidification are yet to be widely explored.

To increase the portfolio of LPBF prepared Al-alloys and to concurrently improve their mechanical properties, there is a requirement to design alloy compositions tailored for additive manufacturing. This concept has been demonstrated with success through the development of Scalmalloy®, Al-4.5Mg-0.66Sc-0.37Zr-0.17Si (in wt. %); where a modified 5xxx series aluminium alloy with scandium additions was designed to exploit the benefits rapid solidification [23,24]. The high solidification rate existing in the molten melt pool increased the amount of solute (herein, scandium) that could be trapped in the solid solution thereby pushing the solubility limits of the alloy system [25], along with rapid solidification minimising any unwanted reaction between Sc and other alloying elements (such as Si) [26]. This resulted in improved properties where a higher Sc solute content increased the formation of nano-sized Al_3Sc precipitates [27]. Another new alloy that was designed for LPBF in the Al–Mn-Sc system is Al-4.52Mn-1.32Mg-0.79Sc-0.74Zr (in wt. %), where excess manganese was added to improve the solid solution strengthening of the alloy, in addition to second phase strengthening produced by Sc [28]. It can be comprehended that LPBF enables the addition of excess solute relative to conventional melts, that may promote the strengthening of aluminium alloys through enhanced solid solution strengthening in addition to second phase hardening.

In the pursuit of broadening the portfolio of properties of LPBF prepared Al-alloys, and to minimise alloy cost from expensive elements (such as Sc and Zr), the further development of Al-alloys for LPBF remains an active pursuit. Al–Zn–Mg alloys are widely used in the aircraft industry for their excellent strength to weight ratio in combination with good stress corrosion cracking (SCC) resistance. The main strengthening contribution in commercial Al–Zn–Mg arises from precipitation hardening, via nano-sized η' and η Mg $(Zn, Al, Cu)_2$ precipitates formed during artificial ageing. In the context of precipitation hardening – the supersaturation of solute is of critical importance, such that changes in solute solubility with temperature may be activated to stimulate fine particle precipitation [29]. As such, high Zn contents have been explored in the Al–Zn–Mg system through conventional ingot metallurgy, in order to produce cost-effective Al-alloys with high strength, however such attempts have resulted in several processing challenges due to slow cooling in conventional alloy production routes [30]. On the contrary, other powder metallurgy and rapid solidification techniques, such as the Osprey process [31,32], have set a practical limit of 12 wt % Zn that resulted in strengths >840 MPa, but restricted industrial uptake due to the complexity in processing. The LPBF process has the ability to overcome alloy processing, as the process results in net shape (i.e. final shape) components, where rapid solidification may also be exploited to hyper load solute – offering the prospect of producing low cost, high strength aluminium alloys. This was reported in a recent prior study, where high solute Al–Zn–Mg alloys were successfully fabricated through LPBF with a relative density of 99.6% and revealed a new quasicrystal phase, termed P-phase, identified for the first time [33].

Herein, a detailed study of post-process heat treatments on the resulting microstructure and mechanical properties of a high solute Al–Zn–Mg alloy fabricated using the LPBF process is presented. In particular, new insights on the effect of high Zn and Mg on the precipitation behaviour are systematically evaluated through electron characterisation techniques. The properties of commercially important aluminium alloys are also correlated with their respective area fraction of second phases, to understand the inflexion point after which the mechanical properties deteriorate.

2. Experimental methods

2.1. Material and methods

High solute Al–14Zn–3Mg powders required for LPBF were supplied by TLS Technik® GmbH. The powders were pre-alloyed and custom prepared in an argon atmosphere through the gas atomisation technique. Table 1 reveals the elemental composition of the as-received powder (pre-LPBF) and the as-LPBF prepared bulk sample. Composition was measured using Inductively Coupled Plasma – Atomic Emission Spectroscopy (ICP-AES) at Spectrometer Services® Australia. The as-received powder was passed through a 63 μm sieve and the powder size distribution was maintained between 16 and 63 μm.

A Concept laser Mlab Cusing-R with a laser spot size of 50 μm, laser power of 95W and scanning speed of 150 mm/s was used to fabricate all the samples used in this study. The hatch spacing and layer thickness were maintained at 0.07 mm and 25 μm, respectively. Cubes (with edge lengths of 10 mm) were prepared from Al–14Zn–3Mg, and sectioned perpendicular to the build direction for heat treatment studies. Rectangular 'dog-bone' shape tensile samples with the dimensions shown in Fig. 1 were also fabricated in the vertical direction and in net shape through LPBF. All samples were cut off from the build plate using a high speed saw - Struers® Discotom-6 and were directly used for analysis.

2.2. Heat treatment

Specimens heat treatment at the lower temperatures of 100 °C, 150 °C and 200 °C was carried out using an oil bath, whereas heat treatment at the higher temperatures of 300 °C, 400 °C and 500 °C was carried out using a salt bath in order to maintain a uniform temperature distribution throughout the sample. All specimens were also wrapped in aluminium foil to minimise the oil or salt contamination during respective heat treatment.

The heat treatment of Al–14Zn–3Mg was divided into two categories:

(a) Direct heat treatment of the as-LPBF samples at temperatures of 100 °C, 200 °C, 300 °C, 400 °C and 500 °C to understand the dissolution of rapidly solidified structure from LPBF.
(b) Precipitation strengthening heat treatment that involved solutionising the as-LPBF samples at 500 °C for 4 h, followed by quenching in water, after which artificial ageing was performed at 150 °C for several hours to study the evolution of precipitates.

2.3. Microstructural characterisation

Microstructural characterisation was performed using an FEI® Quanta 3D FEG focussed ion beam - scanning electron microscope (SEM) operating at 15 kV. Specimens studied were metallographically prepared using silicon carbide papers to a P2500 grit and subsequently polished using 3 μm and 1 μm diamond suspensions, followed by polishing in a colloidal silica suspension to attain 0.1 μm surface finish.

Transmission electron microscopy (TEM) was performed using an FEI® Tecnai G^2 T20 and FEI® Tecnai G^2 F20 (equipped with a high-angle annular dark field detector), both instruments operating at 200 kV. Compositional analysis via energy dispersive X-ray spectroscopy (EDXS) was performed in the FEI® Tecnai G^2 F20 equipped with a Bruker® X-flash X-ray detector and Bruker® Esprit 1.9 software. The specimen preparation for TEM involved punching of 3 mm discs from thin slices of as-LPBF Al–14Zn–3Mg samples which were then mechanically thinned to ~50 μm. These discs were ion milled using a Gatan® 691 Precision Ion Polishing System (PIPS) that operated at −100 °C. Finally, specimens were plasma cleaned using a Gatan® Solarus 950 advanced plasma system with an argon and oxygen gas mixture for ~5

Table 1
Chemical composition and powder size (diameter) distribution of the feedstock powder and post-SLM fabricated Al–14Zn–3Mg in wt. %, measured using ICP-AES.

Element (wt. %)	Zn	Mg	Fe	Cu	Si	Al
Al–14Zn–3Mg (powder)	14.7	3.34	0.28	0.06	0.09	Balance
Al–14Zn–3Mg (as-LPBF)	10.9	2.79	0.23	0.06	0.1	Balance

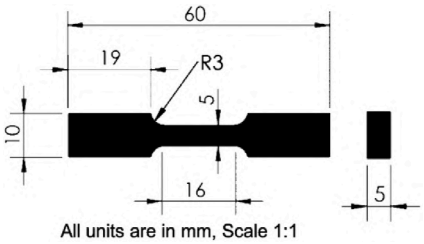

Fig. 1. Dimensions of the tensile samples used in this study.

min prior to TEM analysis.

2.4. Mechanical testing

The samples for hardness testing were metallographically prepared to a P2500 grit using silicon carbide papers. A Struers® Duramin A-300 was used for hardness measurements by applying 1 kg of load for a dwell time of 10 s where five measurements were collected for each specimen.

An Instron® 4050/5500R equipped with a 100 kN load cell and an extension rate of 0.02 mm/s was utilised for tensile testing. The stress-strain data were recorded through a 10 mm gauge extensometer where two samples for each condition were tested until fracture to ensure repeatability.

3. Results

3.1. As-LPBF Al–14Zn–3Mg microstructure prior to heat treatment

In order to understand the effects of heat treatment in altering the microstructure, it is essential to evaluate the phases present in Al–14Zn–3Mg in the as-fabricated (as-LPBF) condition. Fig. 2 (2a and 2b) reveals back scattered electron micrographs of the as-LPBF condition, where the melt pool is decorated with second phase particles of different morphology. These particles have been identified as an icosahedral quasicrystalline P-phase [33]. Due to the high solute content in Al–14Zn–3Mg, a high volume fraction of the P-phase was distributed throughout the alloy microstructure with sizes ranging from few nanometers within the melt pools to ~3 μm along the melt pool boundaries. The high angle annular dark field scanning transmission electron microscopy (HAADF-STEM) images denoting the different morphology of the P-phase are also shown in Fig. 2 (2c and 2d). It was determined that two or more particles may co-nucleate, where one particle can serve as a nucleation site for the other. The genesis of the thermodynamics behind such constituent particles formed in additive manufacturing remains unclear at this stage, noting that what is observed is a 'solidification' microstructure, that has arisen from cooling of local melt pools at a rate of $\sim 10^5$–10^6 K/s.

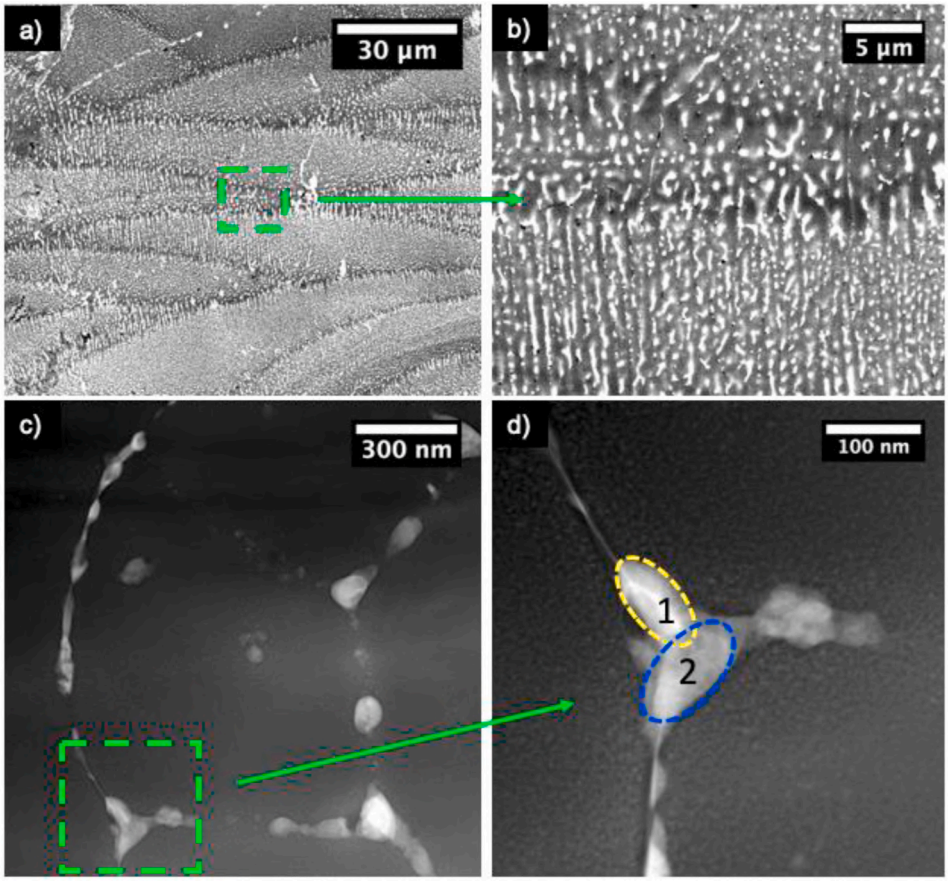

Fig. 2. (a, b) Representative back scattered electron micrographs of as fabricated (as-LPBF) Al–14Zn–3Mg taken at several magnifications showing the morphology of P-phase distributed along the melt pool region. (c, d) HAADF-STEM micrographs of as fabricated Al–14Zn–3Mg highlighting the coexistence of different particles, where a representative co-existence of particles is differentiated by numbers.

3.2. Effect of direct heat treatment on the microstructure and mechanical properties of Al–14Zn–3Mg in the as-LPBF condition

3.2.1. Microstructural characterisation of Al–14Zn–3Mg after direct heat treatment in the as-LPBF condition

Specimens of as-LPBF Al–14Zn–3Mg were subjected to direct heat treatment at 100 °C, 200 °C, 300 °C, 400 °C and 500 °C for several holding times ranging from 2 to 20 h, after which specimens were analysed using SEM. Fig. 3 shows the representative back scattered electron micrographs of Al–14Zn–3Mg in the as-LPBF condition that were directly heat treated at 100 °C, 200 °C, 300 °C, 400 °C and 500 °C, for 20 h. Even though several holding times were performed during direct heat treatment, only micrographs obtained following 20 h are presented in Fig. 3 - as a general representation of microstructure; however all the other micrographs were analysed in order to quantify particle dissolution, as reported further below. Fig. 3 (3a and 3b) confirm the persistent presence of second phase along melt pool boundaries at 100 °C and 200 °C, with such second phase having coarsened in response to heat treatment temperatures of 300 °C (Figs. 3c) and 400 °C (Fig. 3d). The microstructure obtained at 100 °C and 200 °C resembled the as-LPBF microstructure, which may indicate the thermal stability of the P-phase at temperatures up to 200 °C. At 300 °C, the change in microstructure was concomitant with the dissolution of P-phase, where inner regions of the melt pool were decorated with particles that grew in size from few nano meters (at 200 °C) to a few hundreds of nano meters. However, at 400 °C, these particles further ripened along with accompanying dissolution of smaller particles, revealing discontinuous and coarse particles along the melt pool boundary. However, at 500 °C all the particles from the as-LPBF microstructure had dissolved and there were no evidence of melt pool structures as shown in Fig. 3e. Due to the high volume of solute in the alloy, it is not readily possible to avoid rapid natural ageing of Al–14Zn–3Mg, which is manifest as sub-micron particles in Fig. 3e. This phenomena is discussed in subsequent sections. It is also noted that a

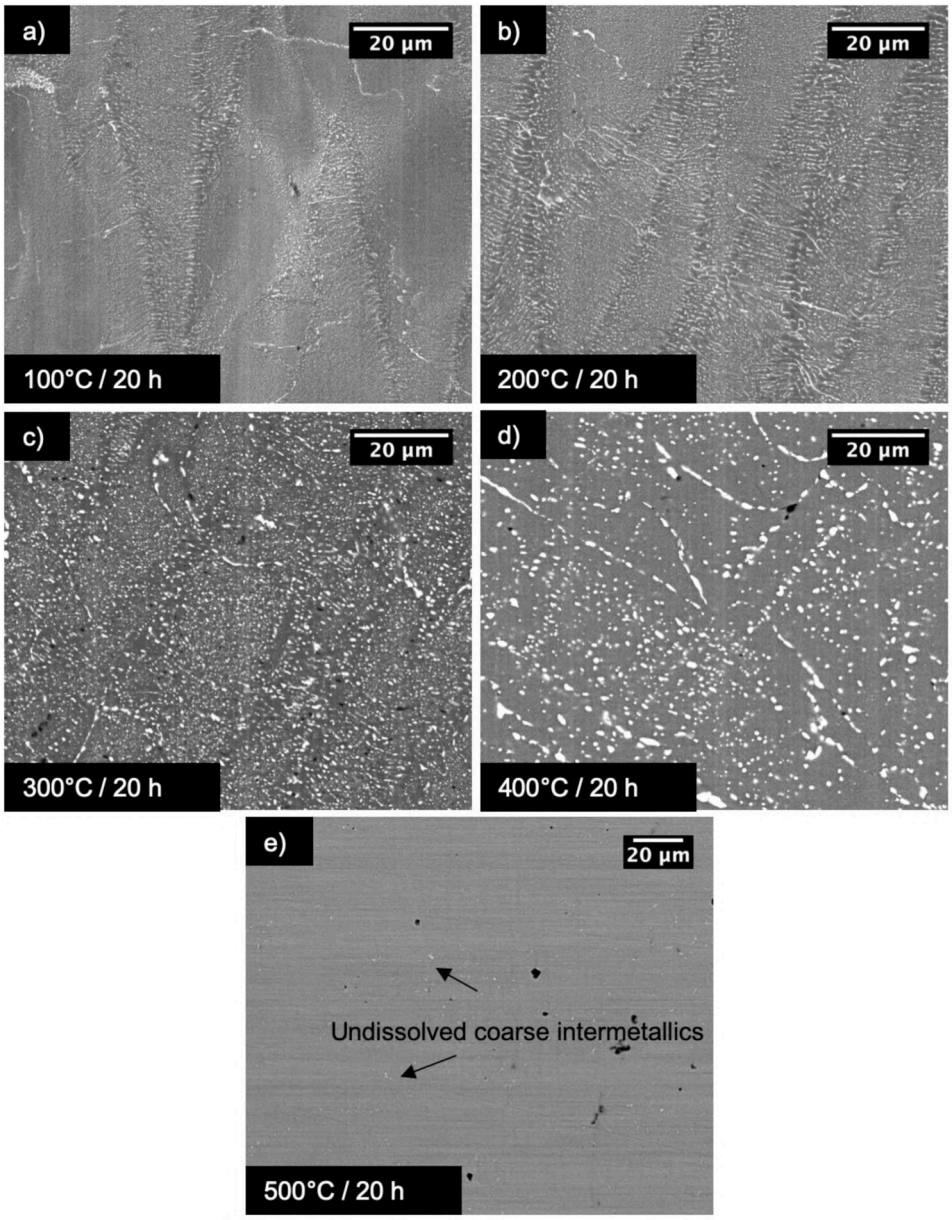

Fig. 3. Representative backscattered electron micrographs following the heat treatment of Al–14Zn–3Mg in the as-LPBF condition at (a)100 °C, (b) 200 °C, (c) 300 °C, (d) 400 °C and (e) 500 °C, for 20 h. The micrographs taken at similar magnifications reveal the changes in size and morphology of the second phase particles with increase in temperature.

small population of particles ranging between ~1 and 3 μm remain evident in the micrographs taken from as-LPBF Al–14Zn–3Mg directly heat treated at 500 °C, which are posited to be constituent intermetallics not soluble at this temperature.

3.2.2. Mechanical testing of Al–14Zn–3Mg after direct heat treatment in the as-LPBF condition

To understand the thermal stability of the quasicrystalline P-phase, Fig. 4 (a) reveals the room temperature hardness that was measured after heat treating as-LPBF Al–14Zn–3Mg at 100 °C, 200 °C, 300 °C, 400 °C and 500 °C with different holding times. It was shown that there was decrease in the hardness of Al–14Zn–3Mg up to a temperature of 300 °C after which the hardness increased. The maximum softening of the as-LPBF Al–14Zn–3Mg occurred at 300 °C between a holding time of 4–8 h, which would correspond to solubility of the P-phase. As noted from Fig. 4, the maximum variations in hardness that were noted at different temperatures along a holding time of 4 h were selected for further analysis. Fig. 4b reveals the stress-strain curves for the as-LPBF samples, which were heat treated at 100 °C, 200 °C, 300 °C and 400 °C for a holding time for 4 h to support the hardness measurements. The loss of alloy hardness is also likely to be influenced by the alteration of the rapidly solidified structures that includes fine grains and high dislocation density, along with alteration of any residual stresses formed during the LPBF process. Such alterations within the alloy microstructure also rationalise the results presented in Fig. 4b, whereby a notionally 'brittle' response is revealed following heat treatment at 100 °C and 200 °C (due to the presence of quasicrystalline P-phase) is altered towards a significant increase in ductility following heat treatment at 300 °C, due to dissolution of the P-phase. The rapid solidification imparted from LPBF and the high temperature of melt pools has the ability the ability to trap solute in the as-fabricated condition. As a result, trapped solute in the solidified alloy will contribute to precipitation with any increase in temperature (since there is a decreasing solubility of solute with increasing temperature in the Al–Zn–Mg system) with this evident at a temperature of 400 °C where the hardness and the strength increases with a loss in ductility. There exists a competition between the simultaneous dissolution of P-phase and precipitation of other phase between 100 °C and 500 °C which contributes to the decrease or increase in hardness at different temperatures. However, as demonstrated herein, the direct heat treatment of Al–14Zn–3Mg in a single step from as-LPBF condition did not yield satisfactory mechanical properties, necessitating the investigation of multi-step heat treatment.

3.3. Evaluation of solutionising temperature and time

Fig. 5 reveals the second phase volume fraction that was calculated using back scattered electron micrographs (of the nature shown in Fig. 3) from specimens heat treated between 100 and 500 °C for different holding times from the as-LPBF condition. It was revealed that the volume fraction of second phase at all the temperatures increased with longer holding times. The minimum value of volume fraction of second phase particles (~1.4%) was obtained for a holding time of 4 h at 500 °C. Owing to the high level of solute in Al–14Zn–3Mg, obtaining a single phase region with all solutes being dissolved in the alloy matrix was not possible. Consequently, the condition where minimum volume fraction of second phase was obtained was chosen as solution heat treatment (SHT) condition, which was a treatment of 500 °C for 4 h.

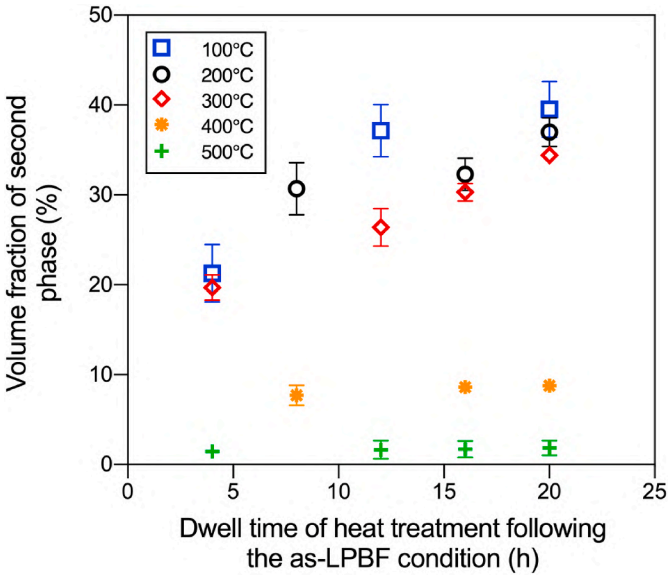

Fig. 5. Volume fraction of second phase measured at room temperature after heat treating Al–14Zn–3Mg from the as-LPBF condition at 100 °C, 200 °C, 300 °C, 400 °C and 500 °C for different times. The lowest volume fraction of second phase particles (1.4%) was obtained at 500 °C/4 h, which was subsequently chosen as the solutionising condition for this alloy.

3.4. Effect of ageing on the microstructure and mechanical properties of Al–14Zn–3Mg after solutionising at 500 °C for 4 h

3.4.1. Ageing response of Al–14Zn–3Mg following solution heat treatment

Al–14Zn–3Mg specimens were subjected to an ageing treatment at 150 °C after solutionising at 500 °C for 4 h, as shown in Fig. 6a.

The variation in Vickers hardness values obtained for the different heat treatment conditions in comparison to Al–14Zn–3Mg in the as-LPBF condition are presented in Fig. 6b.

The four different conditions represent in Fig. 6b, namely as-LPBF, solution heat treated (SHT), naturally aged (NA), and, artificially aged (AA1 and AA2) that are subsequently considered in this study are

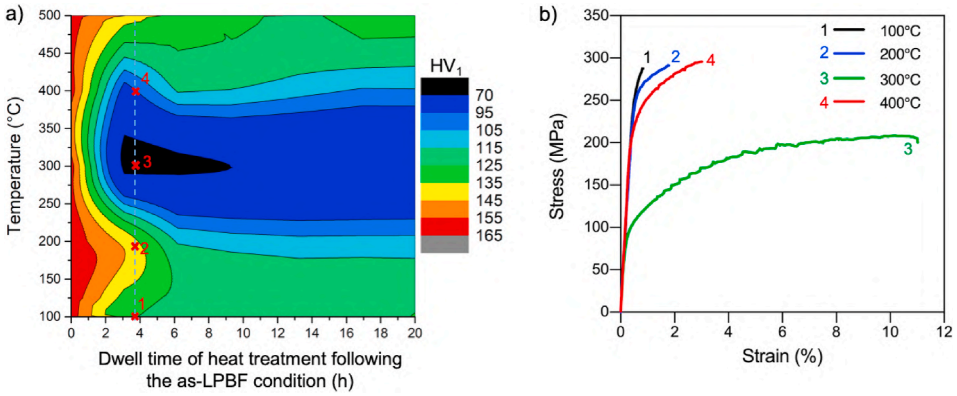

Fig. 4. (a) The hardness profiles of Al–14Zn–3Mg in the as-LPBF condition measured at room temperature after direct heat treatment at 100 °C, 200 °C, 300 °C, 400 °C and 500 °C for different dwell times. The contour plot shows that the maximum softening of Al–14Zn–3Mg occurs at ~300 °C. (b) Representative tensile data measured at room temperature showing the strength and ductility of as-LPBF Al–14Zn–3Mg directly heat treated to the corresponding temperatures of 100 °C, 200 °C, 300 °C and 400 °C for a holding time of 4 h as denoted in points 1, 2, 3 and 4 shown in (a).

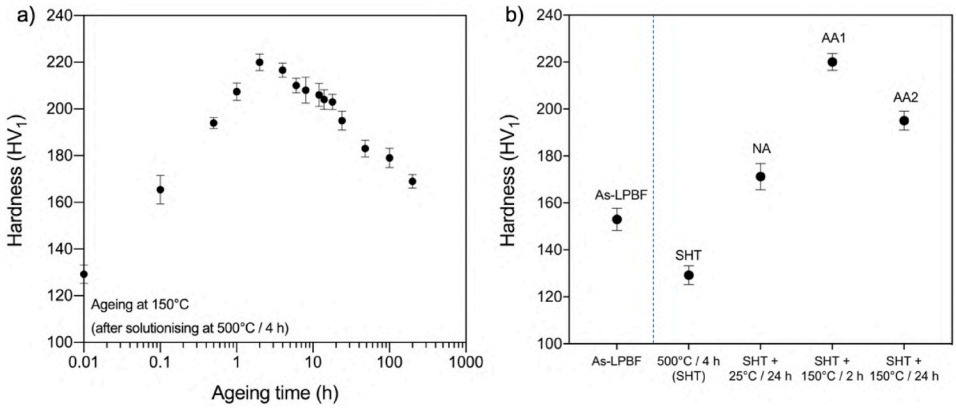

Fig. 6. (a) Ageing curve of the as-LPBF Al–14Zn–3Mg obtained after solutionising at 500 °C for 4 h and aged at 150 °C for several holding times. (b) Hardness of Al–14Zn–3Mg obtained at room temperature and following the different heat treatment conditions (described in Table 2). The peak hardness of 223 ± 2.3 HV_1 was obtained in the AA1 condition.

tabulated in Table 2.

The average hardness of as-LPBF Al–14Zn–3Mg decreased from 153 ± 4.7 to 129 ± 4 HV_1, following solution heat treatment. It was determined that ageing at 150 °C caused the hardness to rapidly increase following solutionising, to a peak hardness of 220 ± 3.6 HV_1 in approximately 2 h – revealing a rapid age hardening response for Al–14Zn–3Mg. It is noted that Al–14Zn–3Mg also has a high affinity for natural ageing following solutionising, where the hardness increased from 129 ± 4 to 171 ± 5.6 HV_1 after 24 h at room temperature. The decrease in hardness from the as-LPBF condition to the solutionised condition is principally attributed to the dissolution of the quasicrystalline P-phase, and also accompanied by the loss of the rapidly solidified structure (Fig. 2) from the LPBF process. The rapid increase in hardness after natural and artificial ageing, is synonymous with the evolution of strengthening precipitates nucleated from the super saturated solid solution.

3.4.2. Microstructural characterisation of Al–14Zn–3Mg after solutionising and ageing

The microstructures of Al–14Zn–3Mg in the as-LPBF, NA (500 °C/4 h + 25 °C/24 h), AA1 (500 °C/4 h + 150 °C/2 h) and AA2 (500 °C/4 h + 150 °C/24 h) conditions, were realised using back scattered electron imaging as shown in Fig. 7.

Specimens from as-LPBF Al–14Zn–3Mg (Fig. 7a) exhibited a distinctive melt pool arrangement, revealing a non-uniform microstructure that also revealed characteristics from the hatch of overlapping laser tracks. The microstructure included a high density of fine P-phase particles, which form during solidification of the Al–14Zn–3Mg alloy. Fig. 7b–d reveals the precipitate distribution for the NA, AA1 and AA2 conditions, where the P-phase and other rapidly solidified structures were not present. It was also discerned that there were some relatively coarse second phase particles with a size of ~1 μm distributed along the grain boundaries in the NA, AA1 and AA2 specimens (Fig. 7b–d). It was noted that there were no major discernible differences between the different heat treatment conditions (NA, AA1 and AA2) observed at the scale of Fig. 7.

To identify the composition of the coarse particles along the grain boundaries, HAADF-STEM was carried out, with the corresponding EDXS maps as shown in Fig. 8.

Table 2
Heat treatment parameters and their corresponding designation.

Heat treatment condition	500 °C/ 4 h	500 °C/4 h + 25 °C/24 h	500 °C/4 h + 150 °C/2 h	500 °C/4 h + 150 °C/24 h
Designation	SHT	NA	AA1	AA2

The composition maps reveal the presence of elements including Zn, Mg and Fe along the grain boundaries, with particles ranging between 500 nm–2 μm. Finer particles only a few nanometers in size contained Si, Zn and Mg, and distributed within the grains. It was determined that the coarse rod-shaped second phase distributed along the grain boundaries were Fe-containing intermetallics (with Fe present as an impurity in the Al–14Zn–3Mg powder).

Bright field STEM micrographs highlighting the precipitate distribution within the grains of Al–14Zn–3Mg in different heat treatment conditions (NA, AA1 and AA2) are revealed in Fig. 9.

A high density of nanoscale Zn–Mg precipitates were observed with a mixture of spherical and rod-shaped morphology (Fig. 9). Table 3 shows the edge to edge inter-precipitate spacing, average size and area fraction of the precipitates which were averaged from 100 different measurements taken from numerous TEM micrographs. The heat treated condition with a peak hardness value, AA1 (500 °C/4 h + 150 °C/2 h), contained precipitates that were ~4.1 nm in diameter. After prolonged ageing, these precipitates grew in size resulting in an average precipitate diameter of 8.8 nm in the AA2 condition (500 °C/4 h + 150 °C/24 h). It is also noted that the natural ageing of Al–14Zn–3Mg was so efficient that it resulted in precipitates with an average size of ~8.6 nm (Fig. 9 a) which is not too dissimilar to the AA2 condition. However, there was a major difference in the edge-to-edge inter-precipitate distances between the three conditions (NA, AA1 and AA2) as revealed in Table 3. It was noted that the inter-precipitate spacing in the sample in naturally aged condition (NA) was higher than the inter-precipitate spacing in the artificially aged conditions (AA1 and AA2).

Fig. 10 provides the bright field TEM micrographs for Al–14Zn–3Mg in the AA1 and conditions, along with the corresponding selected area diffraction patterns (SADPs) in the $<112>_{Al}$ and $<111>_{Al}$ projections. The strong diffraction spots arise from the face-centred cubic aluminium matrix, whilst nanoscale precipitates of semi-coherent η′ are detected at $1/3\{220\}_{Al}$ and $2/3\{220\}_{Al}$ positions (in the SADP along <112> and <111> zone axes for both the conditions). Weak and diffuse streaks along the {111} direction at {220} positions are also observed in the <112> zone axes as shown in Fig. 10 (b and e), indicating that the η′ precipitates have formed in the alloy with a platelet morphology. This correlates with observations in Fig. 9, where a mixture of precipitates with spherical and rod-shaped morphology may be confirmed as the metastable η′ precipitates. The streaks along the {111} direction in the <112> zone axis became stronger for the AA2 condition (Fig. 10e), indicating that number and size of η′ precipitates increased as confirmed from the bright field TEM images (Fig. 10a and d). Fig. 10f also revealed the presence of stable η phase in different orientations as revealed from imaging in the <111> zone axis for AA2 sample – consistent with the extensively reported transformation of η' → η with prolonged ageing

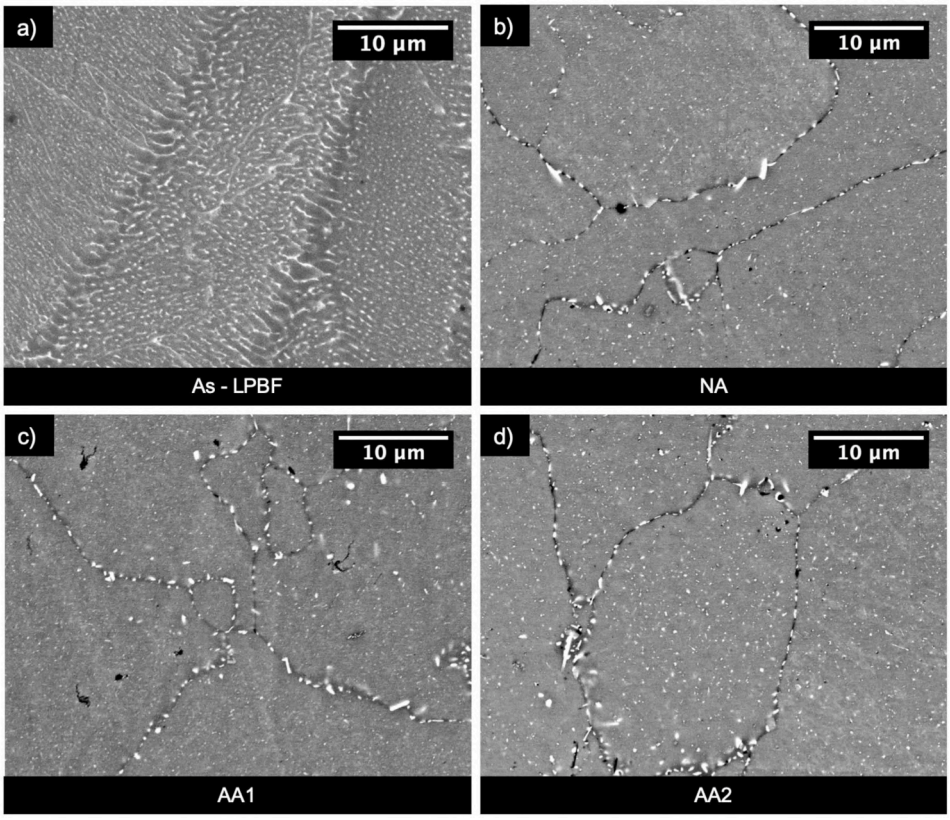

Fig. 7. Backscattered electron micrographs of Al–14Zn–3Mg at (a) as-LPBF condition, (b) NA: 500 °C/4 h + 25 °C/24 h, (c) AA1: 500 °C/4 h + 150 °C/2 h and (d) AA2: 500 °C/4 h + 150 °C/24 h. The images reveal the presence of relatively coarse particles along grain boundaries and nanoscale particles distributed within the grains for the NA, AA1 and AA2 conditions.

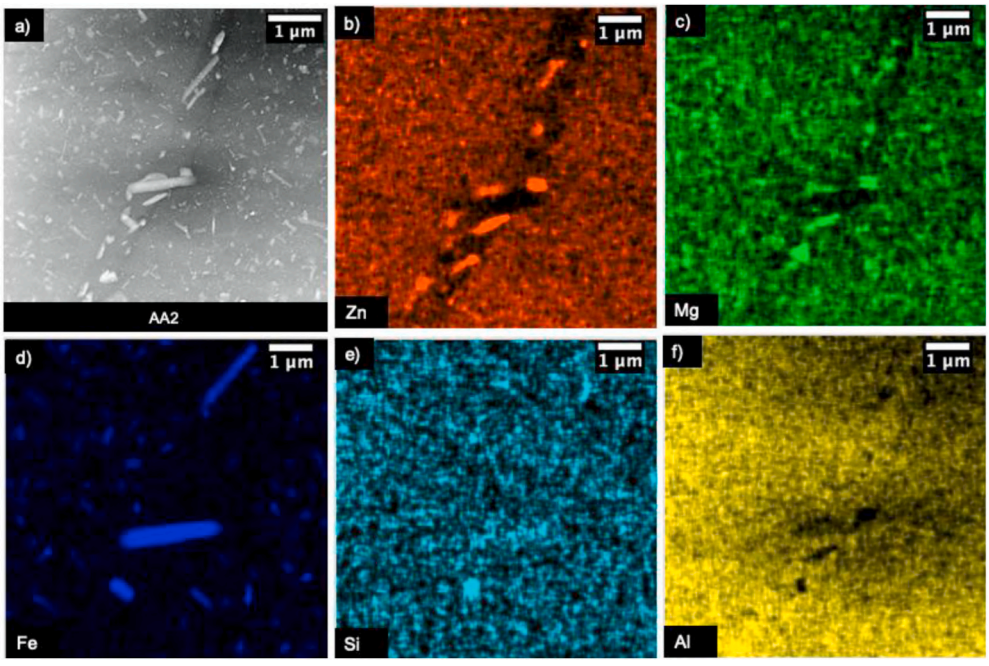

Fig. 8. (a) HAADF-STEM image of Al–14Zn–3Mg in AA2 condition: 500 °C/4 h + 150 °C/24 h, along with (b–f) corresponding EDXS maps for Zn, Mg, Fe, Si and Al.

[34–36]. Weak diffuse spots, previously reported as the GP(II) zones [37], were visible near {311}/2 on the <112> projection (Fig. 10b and e). The general precipitation sequence following SHT of the as-LPBF Al–14Zn–3Mg may be summarised as: Solid solution → GP zones → Metastable η' → Stable η. This sequence follows the expectations from conventional (i.e. lower solute rich) 7xxx series Al-alloys [38,39].

In order to calculate the orientation relationship between the matrix and η′ precipitates, electron diffraction studies were performed on a

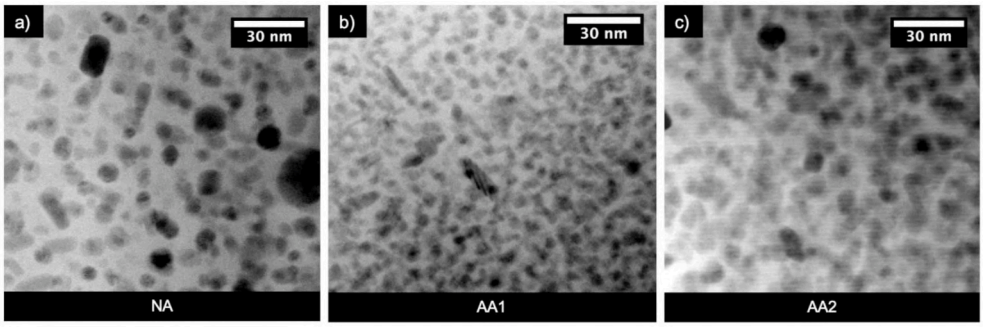

Fig. 9. Bright field STEM micrographs of Al–14Zn–3Mg revealing the variation in size and distribution of second phase particles in the (a) NA, (b) AA1 and (c) AA2 conditions.

Table 3
Average precipitate size and edge-to-edge inter-precipitate spacing of Al–14Zn–3Mg in different heat treatment conditions.

Heat treatment condition	NA: 500 °C/4 h + 25 °C/24 h	AA1: 500 °C/4 h + 150 °C/2 h	AA2: 500 °C/4 h + 150 °C/24 h
Average precipitate diameter (nm)	8.6	4.1	8.8
Edge-to-edge inter-precipitate spacing, λ (nm)	7.4 ± 3.1	3.5 ± 1.5	4.9 ± 3.6
Average area fraction of second phase (%)	39 ± 4	58 ± 3.8	55 ± 3.8

single particle as shown in Fig. 11. Selected area diffraction patterns in $<011>_{Al}$ (Fig. 11b), $<112>_{Al}$ (Fig. 11c) and $<111>_{Al}$ (Fig. 11d) projections for Al–14Zn–3Mg in AA1 condition (500 °C/4 h + 150 °C/2 h) was acquired from a single particle (Fig. 11a). The orientation relationship between the hexagonal η′ precipitate (lattice parameters of a = 0.496 nm and c = 1.402 nm) and the aluminium matrix was identified similar to other Al–Zn–Mg alloys as $<1010>_{\eta'}//<110>_{Al}$; $<1120>_{\eta'}//<112>_{Al}$; $_{Al}$ $(0001)_{\eta'}//\{111\}_{Al}$ [20,40–44]. Therefore, it can be elucidated that the high volume fraction of second phase particles present in Al–14Zn–3Mg are η' precipitate.

3.4.3. Mechanical testing of Al–14Zn–3Mg after solutionising and ageing

The mechanical properties of Al–14Zn–3Mg in both the as-LPBF and heat treated conditions are represented in Fig. 12.

The results reveal that the as-LPBF sample prematurely failed before yielding, thereby indicating the high brittle nature of the alloy, also associated with the presence of P-phase. After subjecting the as-LPBF Al–14Zn–3Mg to solutionising heat treatment at 500 °C for 4 h, the ductility increased to 9.7%, with a yield strength of 171 MPa and UTS of 261 MPa. After subjecting Al–14Zn–3Mg to natural ageing, the yield strength increased to 297 MPa and UTS to 387 MPa, with the ductility falling to a 4.2%. The sample at AA1 condition (500 °C/4 h + 150 °C/2 h) revealed failure of a brittle nature, with the yield stress, UTS and elongation at 350 MPa, 383 MPa and 1.05%, respectively. However, it was noted that the AA2 condition with a longer ageing time (500 °C/4 h + 150 °C/24 h) displayed a higher strength and ductility compared to the sample at the peak hardness (AA1) condition. This finding reinforces the well-recognised need for independent tensile testing, as hardness testing alone does not necessarily correlate closely with strength and ductility. The AA2 condition revealed an improved yield strength of 407 MPa, UTS of 447 MPa and elongation of 1.9%.

Empirical testing in the present study was unable to generate

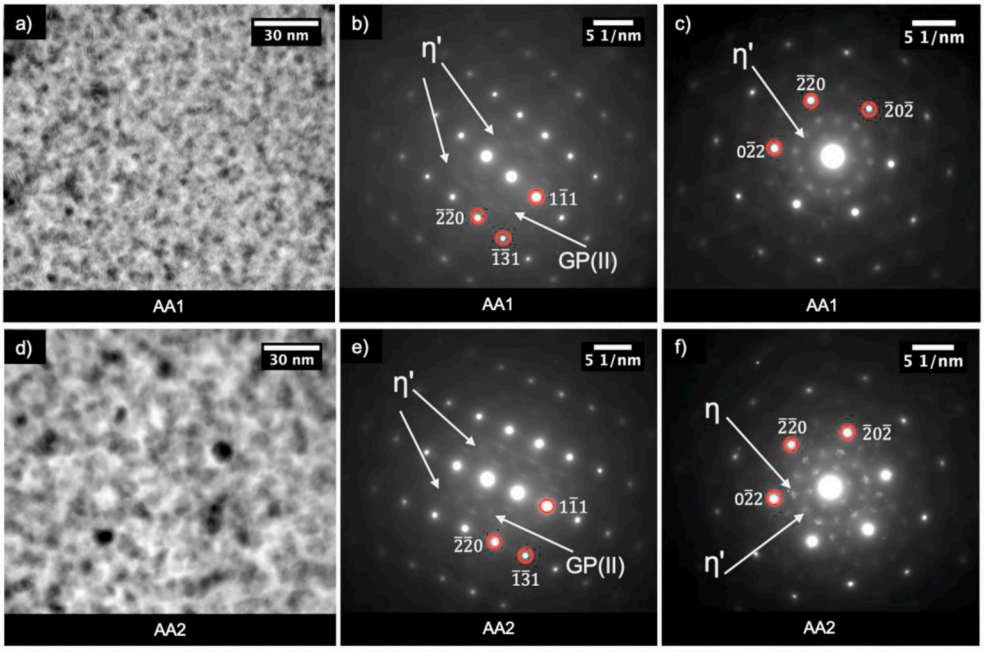

Fig. 10. Bright field TEM micrographs and selected area diffraction patterns (SADPs) obtained from Al–14Zn–3Mg in the following conditions: (a, b and c) AA1 and (d, e and f) AA2. SADP patterns corresponding to $<112>_{Al}$ projection are shown in b and e whereas spots corresponding to $<111>_{Al}$ projection are shown in c and f.

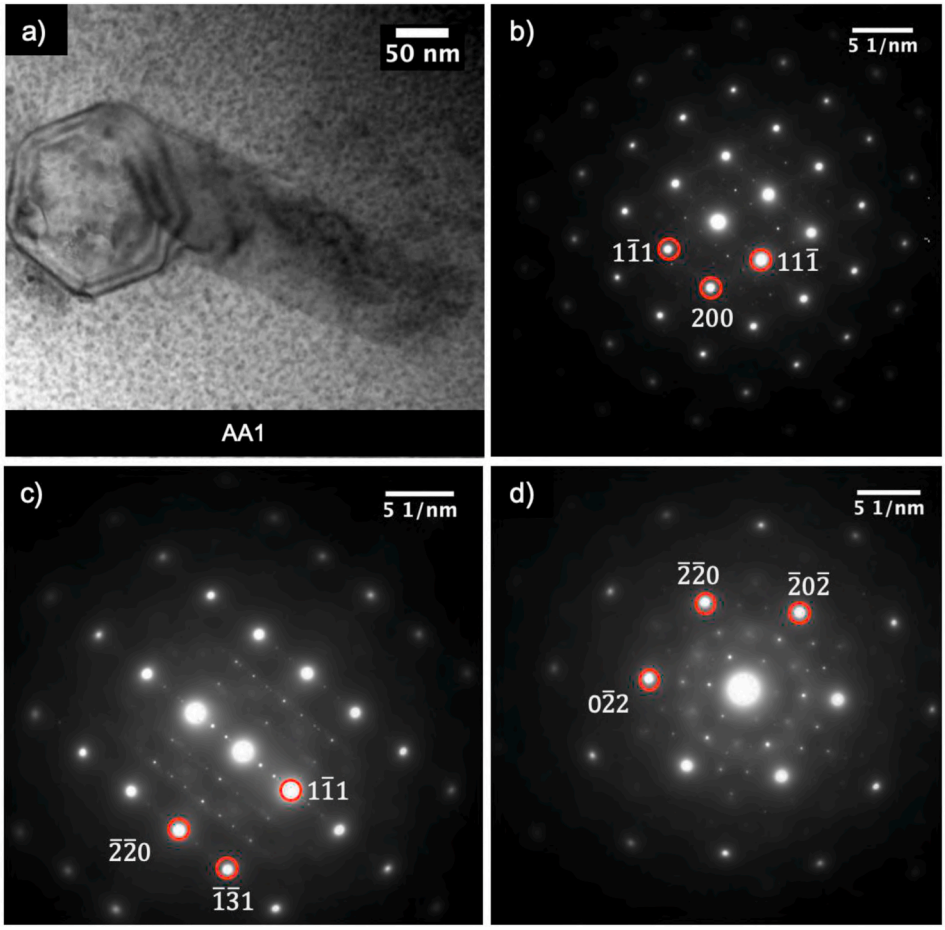

Fig. 11. (a) Bright field TEM micrograph from Al–14Zn–3Mg in the AA1 condition. The selected area diffraction patterns (SADPs) correspond to (b) $<011>_{Al}$ projection, (c) $<112>_{Al}$ projection and (d) $<111>_{Al}$ projection, confirming the presence of η′ phase.

conditions in which Al–14Zn–3Mg was capable of achieving remarkable properties as a result of possessing a high (Zn and Mg) solute content. Whilst there was expectations that Al–14Zn–3Mg could produce strengths in the realm of a gigapascal (GPa) arising from a vast population of strengthening precipitates – such a vast precipitate population in fact was responsible for little or no improvement to strength and deterioration of ductility. The rationalisation of the results are elaborated below.

4. Discussion

4.1. Microstructural characteristics

The solute rich Al–14Zn–3Mg alloy prepared by LPBF presented a unique microstructure containing a population of the brittle quasicrystalline P-phase. This P-phase is absent in the aluminium alloys prepared by ingot metallurgy, and forms during rapid solidification. Inherent in the production from the LPBF process, directional solidification coupled with rapid cooling resulted in an anisotropic microstructure in as-LPBF Al–14Zn–3Mg. Solidification particles varied from the micrometre scale at the melt pool boundaries to a finer (nanometre) scale within the melt pools regions [5,45]. The microstructural features and scale of as-LPBF Al–14Zn–3Mg was similar to other aluminium alloys processed through LPBF, such as AA7075 and AA2024 [18,20,46,47]. It is also noted that in the case of Al–14Zn–3Mg, the formation of hot cracking did not occur.

Given the poor mechanical properties of the as-LPBF Al–14Zn–3Mg, it is relevant to discuss the properties and microstructural features that were developed in Al–14Zn–3Mg following various different heat treatments. In the context of heat treated LPBF prepared Al-alloys, alloys in the Al-Sc-Mg-Mn system for LPBF revealed good mechanical properties in the as-LPBF condition after being directly exposed to a single heat treatment at 300 °C where solid solution strengthening and second phase hardening played a major role [23,24,28,48]. However, in the case of Al–14Zn–3Mg, modifying the P-phase phase through heat treatment directly applied to the as-LPBF condition did not result in benefits with regards to mechanical properties. Therefore, it is was determined herein that Al–14Zn–3Mg required a solutionising heat treatment (500 °C/4 h) in order to fully dissolve the P-phase, and to permit subsequent age hardening via additional thermal treatments.

In wrought 7xxx series Al-alloys, it is known that the main strengthening contribution to the Al–Zn–Mg system arises from the nano-sized η′ and η $Mg(Zn, Al, Cu)_2$ precipitates [29]. In the present study, a high volume fraction of such η′ and η precipitates were present in Al–14Zn–3Mg following artificial aging subsequent to solution heat treatment. Herein, it was also observed that the size of η’ precipitates that nucleated in the Al–14Zn–3Mg matrix from different heat treatment conditions ranged between 3 and 7 nm in diameter - which is similar to the precipitate size observed in wrought 7xxx series aluminium alloys [39,49].

From Table 3 and Fig. 12, it can be interpreted that the area fraction of the second phase was correlated to the alloy yield strength. The area fractions of second phase reported herein were all determined from electron microscopy, which is acknowledged as being different – and a proxy to - the second phase volume fraction. Herein, the Al–14Zn–3Mg in the NA condition had a lower area fraction of second phase, and a lower strength than in AA1 and AA2 conditions. The current

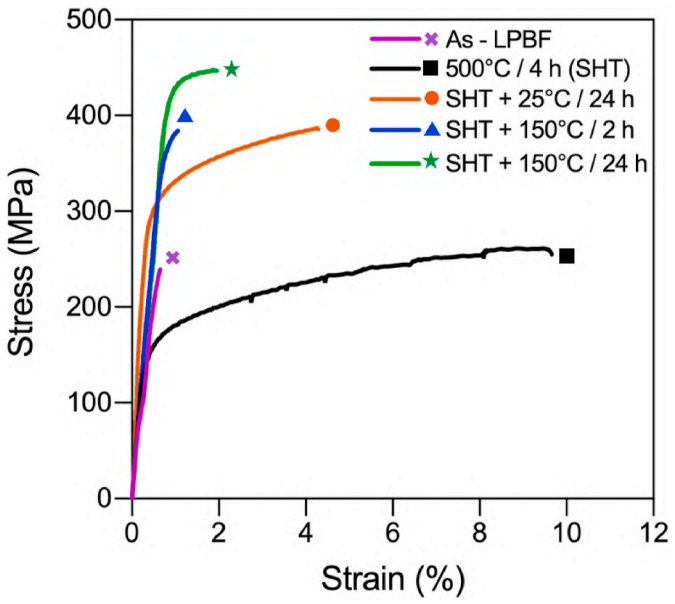

Fig. 12. Representative tensile data showing the strength and ductility of Al–14Zn–3Mg for the following conditions: As-LPBF; Solution heat treated (SHT) at 500 °C/4 h; Naturally aged (NA) at 500 °C/4 h + 25 °C/24 h; artificially aged (AA1) at 500 °C/4 h + 150 °C/2 h; and artificially aged (AA2) at 500 °C/4 h + 150 °C/24 h. It was determined that the maximum strength was attained for the AA2 condition and maximum ductility was attained in the SHT condition.

investigation demonstrates that a yield strength and ultimate tensile strength of 407 MPa and 447 MPa, respectively, are were achievable in Al–14Zn–3Mg fabricated in net shape – albeit coupled with low ductility (<1.9%).

4.2. Mechanical characteristics

To assess the correlation of mechanical properties with respect to the influence of second phase presence in aluminium alloys, it is useful to understand the effect of area fraction of second phase with their corresponding properties. The relationship between yield strength, elongation and the area fraction of second phase particles of several cast, wrought and LPBF fabricated aluminium alloys are summarised in Fig. 13. The results obtained from the present study, namely the heat treated conditions of LPBF prepared Al–14Zn–3Mg that provided mechanical properties with a balance of some ductility (namely, 300 °C/4 h, 400 °C/4 h, NA, AA1 and AA2 conditions) were also compared with the commercial aluminium alloys as shown in Fig. 13.

A general trend was revealed whereby the alloys (including Al–14Zn–3Mg) portray reduced mechanical properties following the increase of second phase area fraction beyond ~50%. It is noted that 50% is not proposed as a threshold, as the analysis herein is area fraction (and not strictly, volume fraction) and a transition at a specific area fraction is not considered in the present study to be mechanistic, but instead phenomenological from the assessment carried out. High strength aluminium alloys such as the AA7075 and AA7150 have area fraction of second phase between 40 and 50% after which the strength and ductility is seen to decrease with increasing second phase area fraction. An important caveat is also made, that conventionally processed (wrought) aluminium alloys will have strength contributions from work hardening effects that are largely absent in the alloys processed through LPBF (and always will be absent for any Al-alloys prepared by LPBF). Although, the net shape fabrication of Al–14Zn–3Mg through LPBF in the AA1 and AA2 condition possess a higher strength than most cast and wrought Al-alloys, the large population of second phase particles that dominate the Al–14Zn–3Mg microstructure results in negligible ductility – which restrict the maximum obtainable yield strength but also hinders applications that necessitate ductility. Nevertheless, this study provides two significant insights, which are (i) exploration of an Al-alloy system capable of solute hyperloading, without hot cracking, and (ii) a critical understanding of the role of second phase particles in strengthening. Both of these aspects provides new insights in the field of Al-alloy design for additive manufacturing – specifically LPBF. An open question that remains, and will form the basis of future work, is 'can there be too much solute?' in the context of developing high strength aluminium alloys. The LPBF process opens the possibility of hyper-loading solute, but also opens the possibility to unique alloying more generally (even when only confined to compositions that do not suffer hot cracking). For example, the alloy studied herein may be modified by additions of copper, or manganese, as some additional examples of future work. The exploration of previously unexplored Al-alloy compositions will undoubtedly remain a hallmark of LPBF studies in years to come.

5. Conclusions

High solute aluminium alloys can be successfully fabricated through LPBF, with opportunities for fabrication of complex components in net shape. The heat treatment and mechanical properties of such a high solute Al–14Zn–3Mg alloy were investigated herein. The main findings of the present study are summarised as follows:

1. The LPBF fabrication of a high solute Al–14Zn–3Mg revealed the presence of a unique microstructure with limited ductility, due to the presence of a quasicrystalline P-phase and the presence of a rapidly solidified microstructure. Direct heat treatment of the samples in as-LPBF condition resulted in modification of the P-phase with improvement in mechanical properties compared to the as-fabricated state.
2. Solutionising heat treatment and natural ageing (500 °C/4 h + 25 °C/24 h) of the LPBF prepared specimens revealed that Al–14Zn–3Mg had a significant affinity to age harden when precipitates with an average diameter of 8.6 nm were distributed throughout the matrix. Mechanical properties with yield strength of 297 MPa, UTS of 387 MPa and ductility of 4.2% were obtained. Such properties however, are not monotonically extrapolated from expectations of lower solute containing (and wrought) Al–Zn–Mg alloys.
3. After heat treating to the AA1 (500 °C/4 h + 15 °C/2 h) and AA2 (500 °C/4 h + 150 °C/24 h) conditions, it was noted that a previously unreported high area fraction of second phase particles (>50%) were present in the alloys studied. These second phase particles were confirmed as the strengthening η′ precipitates with sizes varying between 4 and 8 nm. Al–14Zn–3Mg in the AA2 (50 °C/4 h + 150 °C/24 h) condition demonstrated mechanical properties with yield strength of 407 MPa, UTS of 447 MPa albeit with an elongation of only 1.9%.
4. Although a high area fraction of precipitates was anticipated to be commensurate excellent mechanical properties (namely, high strength), it was realised that there was a loss in strength and ductility when the area fraction increased beyond ~50%. This presents a critical finding regarding solute limits for Al–Zn–Mg alloys being of critical relevance for future alloy design through additive manufacturing – a process where solute supersaturation is readily possible.

Data availability

The raw/processed data required to reproduce these findings cannot be shared at this time as the data also forms part of an ongoing study.

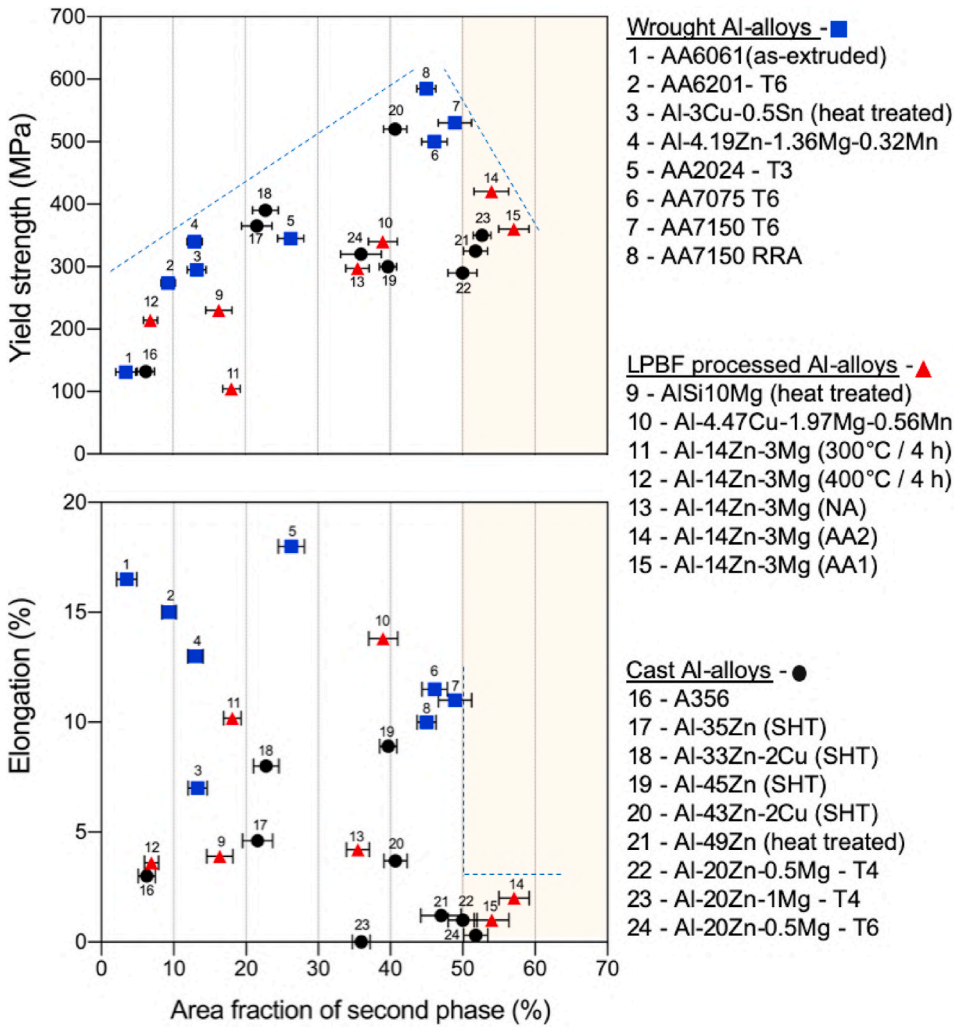

Fig. 13. Average yield strength and average elongation of several cast, wrought and LPBF processed Al- alloys plotted against the area fraction of second phase particles as determined from TEM and SEM image analysis of the alloys listed [12,50–60]. The results obtained from this study corresponds to the following data points, 11: Al–14Zn–3Mg (300 °C/4 h), 12: Al–14Zn–3Mg (400 °C/4 h), 13: Al–14Zn–3Mg (NA), 14: Al–14Zn–3Mg (AA2) and 15: Al–14Zn–3Mg (AA1).

CRediT authorship contribution statement

A.P. Babu: Conceptualization, Methodology, Investigation, Writing - original draft, Writing - review & editing. **A. Huang:** Supervision, Writing - review & editing. **N. Birbilis:** Conceptualization, Supervision, Funding acquisition, Writing - review & editing.

Declaration of competing interest

The authors declare that they have no known competing financial interests or personal relationships that could have appeared to influence the work reported in this paper.

Acknowledgements

The authors gratefully acknowledge the use of instruments, scientific and technical assistance at the Monash Centre for Electron Microscopy (MCEM), Monash X-ray Platform (MXP) and Department of Materials science and Engineering, Monash university. This research was supported by the Monash Graduate Research Scholarship and utilised infrastructure supported by Australian Research Council (LE0882821 and LE110100223).

References

[1] D. Herzog, V. Seyda, E. Wycisk, C. Emmelmann, Additive manufacturing of metals, Acta Mater. 117 (2016) 371–392, https://doi.org/10.1016/j.actamat.2016.07.019.
[2] A. 52900:2015, Standard terminology for additive manufacturing – general principles – terminology, ASTM Int (2015) 1–9, https://doi.org/10.1520/F2792-12A.2, i.
[3] W.E. Frazier, Metal additive manufacturing: a review, J. Mater. Eng. Perform. 23 (2014) 1917–1928, https://doi.org/10.1007/s11665-014-0958-z.
[4] T.B. Sercombe, X. Li, Selective laser melting of aluminium and aluminium metal matrix composites: Review, Mater. Technol. 31 (2016) 77–85, https://doi.org/10.1179/1753555715Y.0000000078.
[5] S. Gorsse, C. Hutchinson, M. Gouné, R. Banerjee, Additive manufacturing of metals: a brief review of the characteristic microstructures and properties of steels, Ti-6Al-4V and high-entropy alloys, Sci. Technol. Adv. Mater. 18 (2017) 584–610, https://doi.org/10.1080/14686996.2017.1361305.
[6] K. Bartkowiak, S. Ullrich, T. Frick, M. Schmidt, New developments of laser processing aluminium alloys via additive manufacturing technique, in: Phys. Procedia, Elsevier B.V., 2011, pp. 393–401, https://doi.org/10.1016/j.phpro.2011.03.050.
[7] D. Buchbinder, H. Schleifenbaum, S. Heidrich, W. Meiners, J. Bültmann, High power selective laser melting (HP SLM) of aluminum parts, in: Phys. Procedia, Elsevier B.V., 2011, pp. 271–278, https://doi.org/10.1016/j.phpro.2011.03.035.
[8] D. Buchbinder, W. Meiners, K. Wissenbach, R. Poprawe, Selective laser melting of aluminum die-cast alloy—correlations between process parameters, solidification conditions, and resulting mechanical properties, J. Laser Appl. 27 (2015) S29205, https://doi.org/10.2351/1.4906389.
[9] K. Kempen, L. Thijs, J. Van Humbeeck, J.P. Kruth, Mechanical properties of AlSi10Mg produced by selective laser melting, in: Phys. Procedia, Elsevier B.V., 2012, pp. 439–446, https://doi.org/10.1016/j.phpro.2012.10.059.

[10] L. Thijs, K. Kempen, J.P. Kruth, J. Van Humbeeck, Fine-structured aluminium products with controllable texture by selective laser melting of pre-alloyed AlSi10Mg powder, Acta Mater. 61 (2013) 1809–1819, https://doi.org/10.1016/j.actamat.2012.11.052.
[11] N.T. Aboulkhair, I. Maskery, C. Tuck, I. Ashcroft, N.M. Everitt, On the formation of AlSi10Mg single tracks and layers in selective laser melting: microstructure and nano-mechanical properties, J. Mater. Process. Technol. 230 (2016) 88–98, https://doi.org/10.1016/j.jmatprotec.2015.11.016.
[12] N.T. Aboulkhair, I. Maskery, C. Tuck, I. Ashcroft, N.M. Everitt, The microstructure and mechanical properties of selectively laser melted AlSi10Mg: the effect of a conventional T6-like heat treatment, Mater. Sci. Eng. 667 (2016) 139–146, https://doi.org/10.1016/j.msea.2016.04.092.
[13] J. Wu, X.Q. Wang, W. Wang, M.M. Attallah, M.H. Loretto, Microstructure and strength of selectively laser melted AlSi10Mg, Acta Mater. 117 (2016) 311–320, https://doi.org/10.1016/j.actamat.2016.07.012.
[14] E.O. Olakanmi, R.F. Cochrane, K.W. Dalgarno, Densification mechanism and microstructural evolution in selective laser sintering of Al-12Si powders, J. Mater. Process. Technol. 211 (2011) 113–121, https://doi.org/10.1016/j.jmatprotec.2010.09.003.
[15] J. Suryawanshi, K.G. Prashanth, S. Scudino, J. Eckert, O. Prakash, U. Ramamurty, Simultaneous enhancements of strength and toughness in an Al-12Si alloy synthesized using selective laser melting, Acta Mater. 115 (2016) 285–294, https://doi.org/10.1016/j.actamat.2016.06.009.
[16] N. Kaufmann, M. Imran, T.M. Wischeropp, C. Emmelmann, S. Siddique, F. Walther, Influence of process parameters on the quality of aluminium alloy en AW 7075 using Selective Laser Melting (SLM), in: Phys. Procedia, Elsevier B.V., 2016, pp. 918–926, https://doi.org/10.1016/j.phpro.2016.08.096.
[17] M.L. Montero Sistiaga, R. Mertens, B. Vrancken, X. Wang, B. Van Hooreweder, J. P. Kruth, J. Van Humbeeck, Changing the alloy composition of Al7075 for better processability by selective laser melting, J. Mater. Process. Technol. 238 (2016) 437–445, https://doi.org/10.1016/j.jmatprotec.2016.08.003.
[18] J.H. Martin, B.D. Yahata, J.M. Hundley, J.A. Mayer, T.A. Schaedler, T.M. Pollock, 3D printing of high-strength aluminium alloys, Nature 549 (2017) 365–369, https://doi.org/10.1038/nature23894.
[19] L. Lityńska-Dobrzyńska, J. Dutkiewicz, W. Maziarz, A. Góral, Microstructure of rapidly solidified Al-12Zn-3Mg-1.5Cu alloy with Zr and Sc additions, Mater. Trans. (2011) 309–314, https://doi.org/10.2320/matertrans.MB201009.
[20] O. Gharbi, S. Kumar Kairy, P.R. De Lima, D. Jiang, J. Nicklaus, N. Birbilis, Microstructure and corrosion evolution of additively manufactured aluminium alloy AA7075 as a function of ageing, Npj Mater. Degrad. 3 (2019), https://doi.org/10.1038/s41529-019-0101-6.
[21] S.K. Kairy, O. Gharbi, J. Nicklaus, D. Jiang, C.R. Hutchinson, N. Birbilis, On the characterization of a hitherto unreported icosahedral quasicrystal phase in additively manufactured aluminum alloy AA7075, Metall. Mater. Trans. A Phys. Metall. Mater. Sci. 50 (2019) 529–533, https://doi.org/10.1007/s11661-018-5025-1.
[22] S.Y. Zhou, Y. Su, H. Wang, J. Enz, T. Ebel, M. Yan, Selective laser melting additive manufacturing of 7xxx series Al-Zn-Mg-Cu alloy: cracking elimination by co-incorporation of Si and TiB2, Addit. Manuf 36 (2020), https://doi.org/10.1016/j.addma.2020.101458.
[23] K. Schmidtke, F. Palm, A. Hawkins, C. Emmelmann, Process and mechanical properties: applicability of a scandium modified Al-alloy for laser additive manufacturing, in: Phys. Procedia, Elsevier B.V., 2011, pp. 369–374, https://doi.org/10.1016/j.phpro.2011.03.047.
[24] A.B. Spierings, K. Dawson, P.J. Uggowitzer, K. Wegener, Influence of SLM scan-speed on microstructure, precipitation of Al3Sc particles and mechanical properties in Sc- and Zr-modified Al-Mg alloys, Mater. Des. 140 (2018) 134–143, https://doi.org/10.1016/j.matdes.2017.11.053.
[25] J. Zhang, B. Song, Q. Wei, D. Bourell, Y. Shi, A review of selective laser melting of aluminum alloys: processing, microstructure, property and developing trends, J. Mater. Sci. Technol. 35 (2019) 270–284, https://doi.org/10.1016/j.jmst.2018.09.004.
[26] J. Dumbre, S.K. Kairy, E. Anber, T. Langan, M.L. Taheri, T. Dorin, N. Birbilis, Understanding the formation of (Al,Si)3Sc and V-phase (AlSc2Si2) in Al-Si-Sc alloys via ex situ heat treatments and in situ transmission electron microscopy studies, J. Alloys Compd. 861 (2020) 158511, https://doi.org/10.1016/j.jallcom.2020.158511.
[27] A.B. Spierings, K. Dawson, P. Dumitraschkewitz, S. Pogatscher, K. Wegener, Microstructure characterization of SLM-processed Al-Mg-Sc-Zr alloy in the heat treated and HIPed condition, Addit. Manuf. 20 (2018) 173–181, https://doi.org/10.1016/j.addma.2017.12.011.
[28] Q. Jia, P. Rometsch, S. Cao, K. Zhang, X. Wu, Towards a high strength aluminium alloy development methodology for selective laser melting, Mater. Des. 174 (2019), https://doi.org/10.1016/j.matdes.2019.107775.
[29] I.J. Polmear, D. StJohn, J.-F. Nie, M. Qian, Light Alloys : Metallurgy of the Light Metals, 2017.
[30] Y.L. Wu, F.H. Froes, A. Alvarez, C.G. Li, J. Liu, Microstructure and Properties of a New Super-high-strength AlZnMgCu Alloy C912, 1997.
[31] M.M. Sharma, M.F. Amateau, T.J. Eden, Mesoscopic structure control of spray formed high strength Al-Zn-Mg-Cu alloys, Acta Mater. 53 (2005) 2919–2924, https://doi.org/10.1016/j.actamat.2005.03.007.
[32] H. Li, F. Cao, S. Guo, Y. Jia, D. Zhang, Z. Liu, P. Wang, S. Scudino, J. Sun, Effects of Mg and Cu on microstructures and properties of spray-deposited Al-Zn-Mg-Cu alloys, J. Alloys Compd. 719 (2017) 89–96, https://doi.org/10.1016/j.jallcom.2017.05.101.
[33] A.P. Babu, S.K. Kairy, A. Huang, N. Birbilis, Laser powder bed fusion of high solute Al-Zn-Mg alloys : processing , characterisation and properties, Mater. Des. 196 (2020) 109183, https://doi.org/10.1016/j.matdes.2020.109183.
[34] J.K. Park, A.J. Ardell, Microstructures of the commercial 7075 Al alloy in the T651 and T7 tempers, Metall. Trans. A. 14 (1983) 1957–1965, https://doi.org/10.1007/BF02662363.
[35] J. Gjønnes, C.J. Simensen, An electron microscope investigation of the microstructure in an aluminium-zinc-magnesium alloy, Acta Metall. 18 (1970) 881–890, https://doi.org/10.1016/0001-6160(70)90016-7.
[36] M. Dumont, W. Lefebvre, B. Doisneau-Cottignies, A. Deschamps, Characterisation of the composition and volume fraction of η′ and η precipitates in an Al-Zn-Mg alloy by a combination of atom probe, small-angle X-ray scattering and transmission electron microscopy, Acta Mater. 53 (2005) 2881–2892, https://doi.org/10.1016/j.actamat.2005.03.004.
[37] L.K. Berg, J. Gjøønnes, V. Hansen, X.Z. Li, M. Knutson-Wedel, G. Waterloo, D. Schryvers, L.R. Wallenberg, GP-zones in Al-Zn-Mg alloys and their role in artificial aging, Acta Mater. 49 (2001) 3443–3451, https://doi.org/10.1016/S1359-6454(01)00251-8.
[38] J. Chen, L. Zhen, S. Yang, W. Shao, S. Dai, Investigation of precipitation behavior and related hardening in AA 7055 aluminum alloy, Mater. Sci. Eng. 500 (2009) 34–42, https://doi.org/10.1016/j.msea.2008.09.065.
[39] G. Sha, R.K.W. Marceau, S.P. Ringer, Precipitation and Solute Clustering in Aluminium: Advanced Characterisation Techniques, Woodhead Publishing Limited, 2010, https://doi.org/10.1533/9780857090256.2.345.
[40] J.Z. Liu, J.H. Chen, X.B. Yang, S. Ren, C.L. Wu, H.Y. Xu, J. Zou, Revisiting the precipitation sequence in Al-Zn-Mg-based alloys by high-resolution transmission electron microscopy, Scripta Mater. 63 (2010) 1061–1064, https://doi.org/10.1016/j.scriptamat.2010.08.001.
[41] L.M. Wu, M. Seyring, M. Rettenmayr, W.H. Wang, Characterization of precipitate evolution in an artificially aged Al-Zn-Mg-Sc-Zr alloy, Mater. Sci. Eng. 527 (2010) 1068–1073, https://doi.org/10.1016/j.msea.2009.09.023.
[42] X.Z. Li, V. Hansen, J. GjØnnes, L.R. Wallenberg, HREM study and structure modeling of the η′ phase, the hardening precipitates in commercial Al–Zn–Mg alloys, Acta Mater. 47 (1999) 2651–2659, https://doi.org/10.1016/S1359-6454(99)00138-X.
[43] W. Yang, S. Ji, M. Wang, Z. Li, Precipitation behaviour of Al-Zn-Mg-Cu alloy and diffraction analysis from η′ precipitates in four variants, J. Alloys Compd. 610 (2014) 623–629, https://doi.org/10.1016/j.jallcom.2014.05.061.
[44] K. Wen, Y. Fan, G. Wang, L. Jin, X. Li, Z. Li, Y. Zhang, B. Xiong, Aging behavior and precipitate characterization of a high Zn-containing Al-Zn-Mg-Cu alloy with various tempers, Mater. Des. 101 (2016) 16–23, https://doi.org/10.1016/j.matdes.2016.03.150.
[45] C.A. Brice, N. Dennis, Cooling rate determination in additively manufactured aluminum alloy 2219, Metall. Mater. Trans. A Phys. Metall. Mater. Sci. 46 (2015) 2304–2308, https://doi.org/10.1007/s11661-015-2775-x.
[46] A. Aversa, G. Marchese, A. Saboori, E. Bassini, D. Manfredi, S. Biamino, D. Ugues, P. Fino, M. Lombardi, New aluminum alloys specifically designed for laser powder bed fusion: a review, Materials 12 (2019), https://doi.org/10.3390/ma12071007.
[47] S. Lathabai, Additive manufacturing of aluminium-based alloys and composites, in: Fundam. Alum. Metall., Elsevier, 2018, pp. 47–92, https://doi.org/10.1016/b978-0-08-102063-0.00002-3.
[48] Q. Jia, P. Rometsch, P. Kürnsteiner, Q. Chao, A. Huang, M. Weyland, L. Bourgeois, X. Wu, Selective laser melting of a high strength Al[sbnd]Mn[sbnd]Sc alloy: alloy design and strengthening mechanisms, Acta Mater. 171 (2019) 108–118, https://doi.org/10.1016/j.actamat.2019.04.014.
[49] R.K. Gupta, A. Deschamps, M.K. Cavanaugh, S.P. Lynch, N. Birbilis, Relating the early evolution of microstructure with the electrochemical response and mechanical performance of a Cu-rich and Cu-lean 7xxx aluminum alloy, J. Electrochem. Soc. 159 (2012) C492–C502, https://doi.org/10.1149/2.062211jes.
[50] A.J. Knowles, X. Jiang, M. Galano, F. Audebert, Microstructure and mechanical properties of 6061 Al alloy based composites with SiC nanoparticles, J. Alloys Compd. 615 (2015) S401–S405, https://doi.org/10.1016/j.jallcom.2014.01.134.
[51] Y. Chen, C.Y. Liu, B. Zhang, F.C. Qin, Y.F. Hou, Precipitation behavior and mechanical properties of Al–Zn–Mg alloy with high Zn concentration, J. Alloys Compd. 825 (2020) 154005, https://doi.org/10.1016/j.jallcom.2020.154005.
[52] W.B. Zhou, G.B. Teng, C.Y. Liu, H.Q. Qi, H.F. Huang, Y. Chen, H.J. Jiang, Microstructures and mechanical properties of binary Al-Zn alloys fabricated by casting and heat treatment, J. Mater. Eng. Perform. 26 (2017) 3977–3982, https://doi.org/10.1007/s11665-017-2852-y.
[53] Y. Qi, R. Lapovok, Y. Estrin, Microstructure and electrical conductivity of aluminium/steel bimetallic rods processed by severe plastic deformation, J. Mater. Sci. 51 (2016) 6860–6875, https://doi.org/10.1007/s10853-016-9973-9.
[54] J. da Costa Teixeira, D.G. Cram, L. Bourgeois, T.J. Bastow, A.J. Hill, C. R. Hutchinson, On the strengthening response of aluminum alloys containing shear-resistant plate-shaped precipitates, Acta Mater. 56 (2008) 6109–6122, https://doi.org/10.1016/j.actamat.2008.08.023.
[55] Z. Li, H. Jiang, Y. Wang, D. Zhang, D. Yan, L. Rong, Effect of minor Sc addition on microstructure and stress corrosion cracking behavior of medium strength Al–Zn–Mg alloy, J. Mater. Sci. Technol. 34 (2018) 1172–1179, https://doi.org/10.1016/j.jmst.2017.11.042.
[56] K.D. Ralston, J.G. Brunner, S. Virtanen, N. Birbilis, Effect of processing on grain size and corrosion of AA2024-T3, Corrosion 67 (2011), https://doi.org/10.5006/1.3647762.
[57] J.F. Li, N. Birbilis, C.X. Li, Z.Q. Jia, B. Cai, Z.Q. Zheng, Influence of retrogression temperature and time on the mechanical properties and exfoliation corrosion

behavior of aluminium alloy AA7150, Mater. Char. 60 (2009) 1334–1341, https://doi.org/10.1016/j.matchar.2009.06.007.
[58] H. Zhang, H. Zhu, T. Qi, Z. Hu, X. Zeng, Selective laser melting of high strength Al-Cu-Mg alloys: processing, microstructure and mechanical properties, Mater. Sci. Eng. 656 (2016) 47–54, https://doi.org/10.1016/j.msea.2015.12.101.
[59] S.Z. Han, E.A. Choi, H.W. Park, S.H. Lim, J. Lee, J.H. Ahn, N.M. Hwang, K. Kim, Simultaneous increase in strength and ductility by decreasing interface energy between Zn and Al phases in cast Al-Zn-Cu alloy, Sci. Rep. 7 (2017) 1–8, https://doi.org/10.1038/s41598-017-12286-7.
[60] Z.Y. Ma, S.R. Sharma, R.S. Mishra, Effect of friction stir processing on the microstructure of cast A356 aluminum, Mater. Sci. Eng. 433 (2006) 269–278, https://doi.org/10.1016/j.msea.2006.06.099.

6

Corrosion properties of a high solute Al-Zn-Mg alloy

6.1 Chapter synopsis

This chapter evaluates the corrosion behaviour of Al-14Zn-3Mg and it is a research paper with the title, “On the corrosion of a high solute Al-Zn-Mg alloy produced by laser powder bed fusion”, as submitted to Corrosion science.

In this work, electrochemical techniques such as potentiodynamic polarisation testing and electrochemical impedance spectroscopy were utilised to evaluate the corrosion behaviour of high solute Al-14Zn-3Mg processed through LPBF. In addition, localised corrosion response of the second phase particles were evaluated through immersion testing in 0.1M NaCl, followed by characterisation through scanning electron microscopy (SEM) and optical profilometry to evaluate the size and distribution of the pits. The findings revealed that the presence of refined microstructure and annihilation of coarse intermetallic particles in Al-14Zn-3Mg as a consequence of rapid solidification through LPBF, resulted in reduced cathodic kinetics relative to AA7075-T6. In addition, the polarisation resistance of as-LPBF Al-14Zn-3Mg was three times higher than the conventionally processed wrought Al-alloy. Therefore, this study reveals the key differences in the microstructure and its effects on the electrochemical behaviour of high solute Al-14Zn-3Mg as a function of processing, and in contrast to a wrought Al-alloy as a benchmark.

Corrosion Science 189 (2021) 109626

Contents lists available at ScienceDirect

Corrosion Science

journal homepage: www.elsevier.com/locate/corsci

On the corrosion of a high solute Al-Zn-Mg alloy produced by laser powder bed fusion

A.P. Babu [a], S. Choudhary [a], J.C. Griffith [a,b], A. Huang [a,c], N. Birbilis [d,*]

[a] Department of Materials Science and Engineering, Monash University, Clayton, VIC 3800, Australia
[b] Monash X-ray Platform, Monash University, Clayton, VIC 3800, Australia
[c] Monash Centre for Additive Manufacturing, Monash University, Clayton, VIC 3800, Australia
[d] College of Engineering and Computer Science, The Australian National University, Acton, ACT 2601, Australia

ARTICLE INFO

Keywords:
A. Aluminium
B. Polarization
C. Anodic dissolution
C. Pitting corrosion
C. Passive films

ABSTRACT

An additively manufactured aluminium alloy with very high solute content, Al-14Zn-3Mg (wt. %), was studied herein. Compared to wrought AA7075-T6 as a benchmark, Al-14Zn-3Mg revealed a lower rate of corrosion, attributed to its microstructure and solute content. Specifically, the lack of coarse intermetallic particles in the Al-14Zn-3Mg led to reduced cathodic kinetics relative to AA7075-T6. Potentiodynamic polarisation tests and electrochemical impedance spectroscopy analysis was performed, along with XPS studies of the corresponding surface films. The findings herein demonstrate the corrosion behaviour of a new high solute aluminium alloy manufactured in net shape through LPBF.

1. Introduction

The development of high strength aluminium (Al) alloys for aerospace and transportation applications has resulted in alloys in the Al-Cu, Al-Cu-Mg, Al-Cu-Li and Al-Zn-Mg-Cu systems, with tensile yield strengths reaching 570 MPa for wrought products [1,2]. Powder metallurgy and rapid solidification techniques have revealed the possibility to achieve yield strengths on the order of 800 MPa – with niche processing tailored to specific applications [3,4].

In the context of advanced and efficient manufacturing, metal additive manufacturing has emerged as critical technology to produce complex components in net shape, with minimal waste generation [5]. Laser powder bed fusion process (LPBF) - a form of metal additive manufacturing (AM) - is performed using a laser source to fabricate components in an iterative layer-by-layer manner, based on a computer model [6,7]. Advantages of metal AM for fabricating certain components for aerospace or transportation applications are evident; namely where complex part production with reduced lead times and high customisation are required. To date, the most widely studied aluminium alloys fabricated through LPBF are Al-10Si-Mg and Al-12Si owing to their excellent fluidity, which resulted in refined microstructures and better mechanical properties compared to cast Al-Si alloy counterparts [8–12]. A characteristic of LPBF is rapid solidification, and extended solubility, both of which have been demonstrated in Al-alloys [13,14]. The application of LPBF towards production of higher strength Al-alloys was also been recently explored. Gharbi et al. studied LPBF produced AA2024 (Al-Cu-Mg) and AA7075 (Al-Zn-Mg-Cu) – including the corrosion of such alloys [15,16]. The general applicability of LPBF to the range of conventional high-strength Al-alloys has gained recent research attention, particularly the Al-Zn-Mg system [17,18] which is an important alloy system for aerospace applications. It was noted that the 7xxx series (Al-Zn-Mg) alloys can suffer hot cracking or contain porosity when processed through additive manufacturing, due to their large solidification intervals [6,18]. Limited work has been performed to date to successfully fabricate AM-prepared Al-alloys in the Al-Zn-Mg system, however work to date has indicated that modification of the traditional 7xxx series alloy compositions (by the addition of Si and Zr) was important in avoiding hot cracks and processing defects [16,19–23]. However, notwithstanding the properties of AM-prepared Al-Zn-Mg alloys reported to date, it remains necessary to develop new aluminium alloys that are specifically designed for additive manufacturing in order to fully exploit the prospects offered by AM [14]. Such alloys include the aluminium alloys Al-4.5Mg-0.66Sc-0.37Zr-0.17Si (wt. %) and Al-4.52Mn-1.32Mg-0.79Sc-0.74 Zr (wt. %) that were designed with excess solute, where rapid solidification aided in solute super saturation that resulted in yield strength of 570 MPa with an elongation to fracture

* Corresponding author.
E-mail address: nick.birbilis@anu.edu.au (N. Birbilis).

https://doi.org/10.1016/j.corsci.2021.109626
Received 25 April 2021; Received in revised form 10 June 2021; Accepted 11 June 2021
Available online 17 June 2021

of 18 % [24,25]. On this basis, the work herein reports the efforts from a focused study to produce a newly designed aluminium alloy (Al-14Zn-3Mg wt. %), which can be considered a 7xxx series Al-alloy with a hyper loading Zn and Mg. Such solute hyper loading can only be rationally achieved using the LPBF process, because conventional casting (which is also a pre-requisite for wrought products) would result in ingot cracking. Furthermore, the composition of Al-14Zn-3Mg (wt. %) was also selected and optimised to not suffer hot cracking or excess porosity, based on the combination of thermodynamic modelling and experimental trials – which also revealed a new quasi-crystalline phase in the Al-Zn-Mg system that was hitherto unreported [26]. Hyper solute loaded Al-alloys can not only address target mechanical properties, but may also achieve such properties without further processing (as the AM process can produce components in net-shape).

To date, studies on the corrosion of new Al-alloys that have been specifically designed for AM are limited, and hence such studies remain critical for (i) comparison with the conventional wrought aluminium alloys that are critical to several industrial sectors, and (ii) to critically assess the corrosion of previously unexplored alloy compositions. The local composition of second phase particles that form as a result of new alloying combinations or alloying levels which is directly related to the corrosion properties of Al-alloys. [27–29].

In terms of critical background, the electrochemical behaviour and localised corrosion response of AM prepared high strength Al-alloys is limited to AA2024 [15,30] and AA7075 [16]. Even though both such alloys are not 'new' compositions specifically for AM, both such studies revealed that the processing conditions associated with LPBF process resulted in improved corrosion performance of the alloys compared to wrought counterparts. Namely, traditional micron sized (constituent) particles present in the wrought alloys were absent following AM processing conditions. Furthermore, a refined microstructure resulting in nanometre-sized particles was present following AM processing. This difference in microstructure directly improved the corrosion properties due to reduced cathodic kinetics, which was also posited to be accompanied by the formation of a more stable oxide film [15,16].

Previous work regarding the LPBF prepared Al-Zn-Mg alloy system revealed a distinct microstructure, where a new quasicrystalline phase, termed P-phase, was reported to form in the high solute Al-Zn-Mg system [26,31]. The P-phase, Al-47Zn-29Mg (in at. %), was determined to have an icosahedral structure with twofold and fivefold symmetry, and a quasi-lattice constant of 0.529 nm [26]. Evaluation of mechanical properties of Al-14Zn-3Mg in the as-LPBF and heat treated conditions, revealed that limited ductility was obtained due to the presence of high volume fraction of second phase particles [31]. Following this discovery, it is critical to understand the influence of such second phase particles in affecting the corrosion of Al-Zn-Mg aluminium alloys tailored for additive manufacturing. In the present study, the electrochemical behaviour and corrosion response of the high solute AM-prepared Al-14Zn-3Mg (wt. %) was studied in three different conditions, namely, the as-LPBF condition, the solutionised and naturally aged condition, and the solutionised and artificially aged condition.

2. Experimental methods

2.1. Material production methods and heat treatment

Pre-alloyed Al-alloy powders of the target alloy composition were developed with, and supplied by, TLS Technik GmbH. Alloy powders were prepared in an argon atmosphere through the gas atomisation technique resulting in the composition shown in Table 1.

The powder size distribution of the feedstock powders used for LPBF processing was 16–63 μm. Due to evaporation that may occur as a result of the high temperature prevailing in the LPBF melt pool, Table 1 also indicates elemental composition of the bulk specimens produced by LPBF that were measured using Inductively Coupled Plasma – Atomic Emission Spectroscopy (Spectrometer Services, Australia). This was done to reveal the composition of alloys after LPBF, quantifying the difference between the powder and final product composition after any evaporation during the LPBF process.

Table 1
Chemical composition of the feedstock powder and post-SLM fabricated Al-14Zn-3Mg in wt. %, measured using ICP-AES.

Element (wt. %)	Zn	Mg	Fe	Cu	Si	Al
Al-14Zn-3Mg (powder)	14.7	3.34	0.28	0.06	0.09	Balance
Al-14Zn-3Mg (post LPBF)	10.9	2.79	0.23	0.06	0.1	Balance

A Concept Laser® Mlab Cusing-R was utilised for LPBF, employing a constant hatch spacing and layer thickness of 70 μm and 25 μm, respectively. A laser spot size of 50 μm, laser power of 95 W and scanning speed of 150 mm/s was used to fabricate all specimens used in this study. Cube specimens with 10 mm dimensions were sectioned perpendicular to the build direction and utilised for all electrochemical and microstructural testing. The average porosity of samples used was $<$ 0.5 %, as determined by an Olympus GX51 optical microscope and ImageJ software, with optical analysis utilised to determine the fraction of surface porosity.

Heat treatment of the as-LPBF prepared Al-14Zn-3Mg samples was performed according to the following conditions: i) The as-LPBF samples were solutionised at 500 °C for 4 h, quenched in water and naturally aged at room temperature for 24 h; termed the naturally aged (NA) condition. Evaluating the high solute Al-14Zn-3Mg alloy directly in the as-solutionised state was deemed too challenging, owing to rapid natural ageing of the alloy. Therefore, a well-defined period of 24 h natural aging was selected for this work. ii) As-LPBF samples were solutionised at 500 °C for 4 h, quenched in water, then immediately aged at 150 °C for 24 h; denoting the artificially aged (AA) condition.

2.2. Microstructural characterisation and immersion testing

Microstructural characterisation using scanning electron microscopy was carried out using an FEI® Quanta 3D-FEG operating at 15 kV. Individual cube specimens of 10 mm were metallographically prepared using silicon carbide papers to a P2500 grit finish, followed by polishing with 3 μm, then 1 μm diamond suspension, and finally followed by polishing in a 0.1 μm colloidal silica suspension. Samples for immersion testing were also prepared using the aforementioned procedure, and were immersed in 0.1 M NaCl for different time periods.

2.3. Electrochemical measurements

Electrochemical test specimens were prepared to a P2500 grit finish followed by ultrasonic cleaning in ethanol. A BioLogic® VMP-3 potentiostat (under the control of EC-Lab® software, version 11.27) was utilised. All the electrochemical testing was performed using a three-electrode cell (Princeton Applied Research® K0235), and quiescent 0.1 M NaCl. A saturated calomel reference electrode (+244 mV vs. SHE), and platinum mesh counter electrode were utilised, respectively. The characteristic response of all specimens was obtained using potentiodynamic polarisation testing and electrochemical impedance spectroscopy (EIS).

2.3.1. Potentiodynamic polarisation testing

Potentiodynamic polarisation testing was performed in 0.1 M NaCl with a potential scan rate of 1 mVs^{-1}, with either following 600 s or 48 h of open circuit conditioning. Separate anodic and cathodic scans were conducted, where prior to the tests, the specimens were allowed to stabilise in the electrolyte for 600 s during which open circuit potential (OCP) was measured. In this regard, anodic polarisation was performed from −20 mV vs OCP to 1 mA/cm^2 and cathodic polarisation was performed from +20 mV vs OCP to -1.6 V_{SCE}. To ensure repeatability and consistency of the data, each scan was reproduced at least twice for all

specimens.

2.3.2. Electrochemical impedance spectroscopy testing

Electrochemical impedance spectroscopy (EIS) was performed in 0.1 M NaCl using a frequency range of 100 kHz – 0.05 Hz (measuring five points per decade), with an applied potential of ±10 mV. Data collection interval times were; 10 min, 1 h, 24 h, 48 h, 96 h, and 168 h, respectively. The acquired EIS data was fitted using the EC-Lab software® (version 11.27).

2.4. Pit analysis through optical profilometry

Optical profilometry was performed on specimens following 48 h of immersion in 0.1 M NaCl. A Veeco® WYKO NT1100 optical profilometer

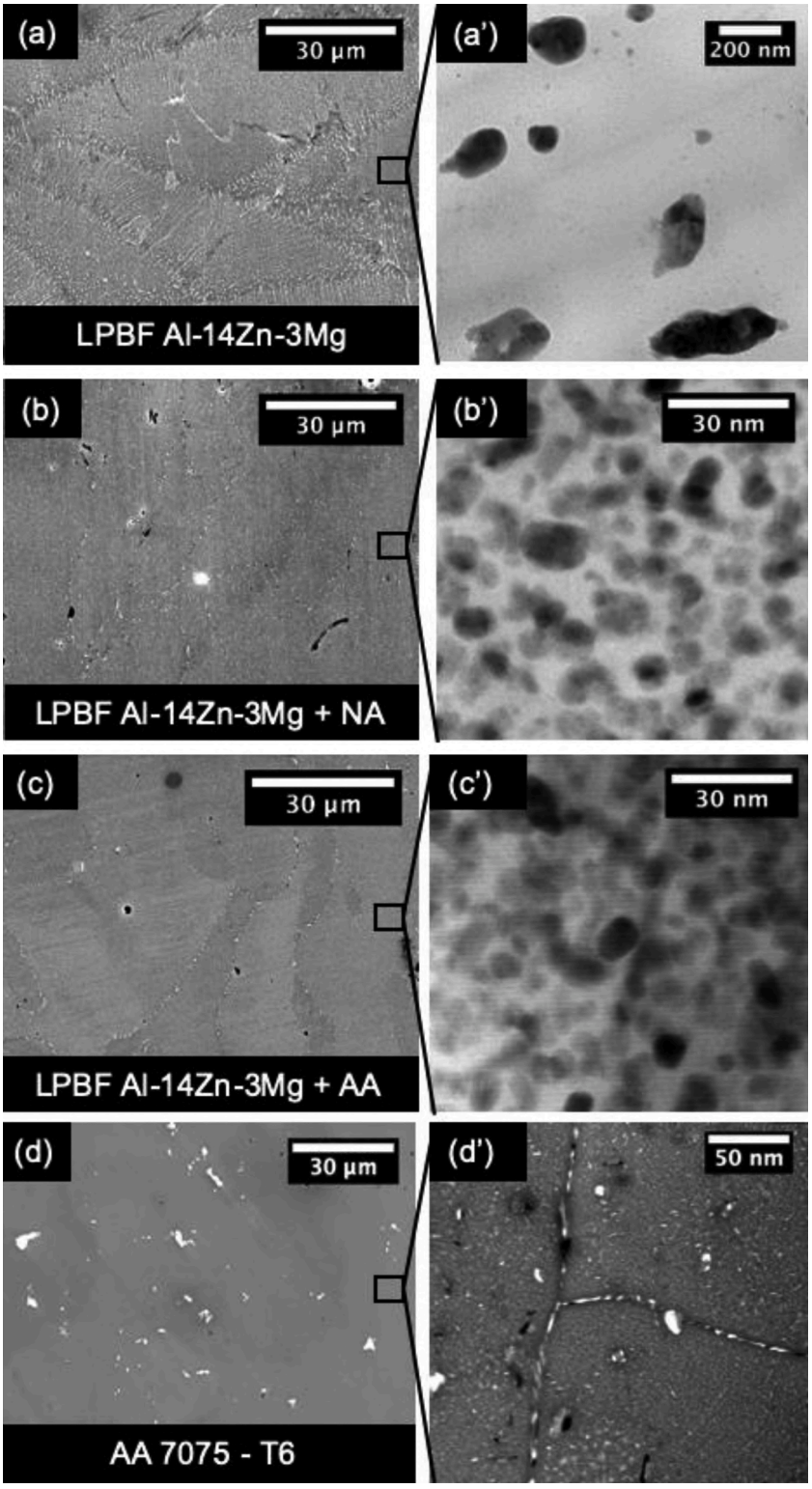

Fig. 1. Secondary electron micrographs of: (a) LPBF Al-14Zn-3Mg, (b) LPBF Al-14Zn-3Mg + NA, (c) LPBF Al-14Zn-3Mg + AA and (d) AA 7075 – T6. Their respective high magnification STEM micrographs are shown in (a', b', c' and d') (NA: 500 °C / 4 h +25 °C / 24 h and AA: 500 °C / 4 h +150 °C / 24 h).

was used to measure the depth and number of surface pits. Quantitative pit analysis was performed using Veeco Vision software® where the field of view was maintained at 300 μm x 228 μm. Prior to testing, the samples were cleaned with 10 % nitric acid for 2 min followed by ultrasonic cleaning to remove any loose products or oxides on the surface.

2.5. X-ray photoelectron spectroscopy (XPS) evaluation

X-ray photoelectron spectroscopy (XPS) was performed using Thermo Scientific® Nexsa Surface Analysis System calibrated to Au 4f and equipped with a hemispherical analyser. The incident radiation was monochromatic Al Kα X-rays (1486.6 eV) at 72 W (6 mA and 12 kV, 400 × 800 μm^2 spot). Survey (wide) and high-resolution (narrow) scans were recorded at analyser pass energies of 150 and 50 eV and step sizes of 1.0 eV and 0.1 eV, respectively. The base pressure in the analysis chamber was less than 5.0×10^{-9} mbar. A low-energy dual-beam (ion and electron) flood gun was used to compensate for surface charging. For the depth profiles, 100 levels were sputtered using a monatomic Ar^+ gas cluster ion source at 4000 eV and high current. Each level was sputtered for a single rotation lasting 30 s, with a 2 mm raster size and a 5 s delay. Optical profilometry (Veeco® WYKO NT1100 optical profilometer) was used to measure the depth of the etched region and these values were used to convert sputter time to sputter depth on the x-axis. Data processing was carried out using Avantage software® version 5.9921 and the energy calibration was referenced to the main line of C 1s at 284.8 eV. The O 1s spectra were fit using a smart background and the full width half maximum (FWHM) constrained for each species.

3. Results and discussion

3.1. Microstructural characterisation

The microstructure of AM-prepared Al-14Zn-3Mg in the as-LPBF, NA and AA conditions (along with wrought AA7075-T6 as a benchmark), are shown in Fig. 1 (a–d), respectively. The corresponding high magnification microstructures revealing nanoscale particles are presented in Fig. 1 (a'–d').

The as-LPBF Al-14Zn-3Mg revealed a distinct bimodal microstructure as revealed in Fig. 1a. The bimodal microstructure can be differentiated into three regions – namely, coarse cellular dendrites, fine cellular dendrites and the equiaxed zone, which is similar to features previously observed in other LPBF fabricated alloys [32]. Characteristic "U-shaped" melt pools were decorated with particles of differing morphology and were previously identified as P-phase, Al-47Zn-29Mg (in at. %), with an icosahedral quasicrystalline structure [26]. P-phase particles were comparatively larger in size on melt pool boundaries (at ~1−3 μm) than particles within the melt pool (at ~ 50–100 nm), as shown in Fig. 1a'.

Heat treatment of as-LPBF Al-14Zn-3Mg resulted in dissolution of the quasicrystalline P-phase during solutionising (500°C), and the subsequent precipitation of the η and η'-$MgZn_2$ phases following lower temperature (150°C) ageing heat treatment [31]. Such precipitates were observed in AM-prepared Al-14Zn-3Mg in the NA and AA conditions, as shown in Fig. 1b and c. For both such conditions, the presence of relatively coarse second phase particles (~ 1 μm) were also revealed along the grain boundaries, and precipitates less than 10 nm were distributed within the grains. It was noted that the naturally aged (NA) and artificially aged (AA) conditions revealed similar average precipitate diameter of ~ 8.6 nm (Fig. 1b') and ~ 8.8 nm (Fig. 1c'), respectively. However, the area fraction of precipitates in NA (~ 40 %) was less than that of AA (~ 55 %) condition; indicating a greater affinity for precipitation in AM-prepared Al-14Zn-3Mg following solutionising and artificial ageing, in the case where there is excess solute. In addition, the mechanical properties of Al-14Zn-3Mg in as-LPBF and heat treated conditions were evaluated in our previous work, where the hardness of Al-14Zn-3Mg in as-LPBF, NA and AA conditions was 153 ± 4.7 HV_1, 171 ± 5.6 HV_1 and 220 ± 3.6 HV_1, respectively [31].

The microstructure of AM-prepared Al-14Zn-3Mg in all the three conditions studied, was contrast to AA7075-T6, where the matrix was populated with coarse constituent particles of different morphology as shown in Fig. 1d. These particles have been previously determined to be Al_7Cu_2Fe, Al_3Fe, Al_2Cu, Mg_2Si and Al_2CuMg that were nominally formed during the casting process with over 65 % of these particles being Al_7Cu_2Fe [33,34]. For the purpose of using AA7075-T6 as a benchmark to evaluate the corrosion behaviour of AM-prepared Al-14Zn-3Mg, all the above mentioned particles present in AA7075-T6 are referred to as constituent particles throughout this work. The high magnification HAADF–STEM micrograph of AA7075-T6, as shown in Fig. 1d', reveals the hardening precipitates ($MgZn_2$) [33]. It is noted that the precipitates in AA7075–T6 were considerably finer than the precipitates in AM-prepared Al-14Zn-3Mg in the NA and AA conditions. However, coarse constituent particles were not present in AM-prepared Al-14Zn-3Mg due to the rapid solidification rates.

3.2. Electrochemical characterisation using potentiodynamic polarisation testing

The microstructural analysis of AM-prepared Al-14Zn-3Mg revealed a distinct microstructure loaded with a high area fraction of sub-micron particles, whereas, the AA7075-T6 contained coarse constituent particles. This insinuates that the localised corrosion response of AM-prepared Al-14Zn-3Mg will be distinct to the traditional wrought aluminium alloys.

Separate anodic and cathodic potentiodynamic polarisation tests of AM-prepared Al-14Zn-3Mg in the as-LPBF, NA and AA conditions, along with AA7075-T6, were conducted and results presented in Fig. 2. Results from anodic and cathodic potentiodynamic polarisation testing following a 600 s immersion and 48 h immersion in 0.1 M NaCl are shown in Fig. 2a–d, respectively. The corrosion potential (E_{corr}) and corrosion current density (i_{corr}) were obtained using Tafel linear extrapolation method on the cathodic polarisation curves, and are given in Table 2. The anodic data was avoided for the E_{corr} and i_{corr} estimation due to its pseudo-passivation tendencies which violates the ability to use it for Tafel fitting.

The as-LPBF Al-14Zn-3Mg revealed a corrosion current density (i_{corr}) value of ~1.1 μA/cm^2 and the i_{corr} value of AA7075-T6 was seven times higher with a value of ~7.85 μA/cm^2, following a 600 s immersion in 0.1 M NaCl.

The most notable feature determined from potentiodynamic polarisation testing is that the rate of the cathodic partial reaction was significantly lower on the Al-14Zn-3Mg alloy, as opposed to AA7075-T6. This lower rate of cathodic reaction upon the Al-14Zn-3Mg principally arises from two aspects, which are (i) the absence of constituent particles that are localised and rich in impurity (or alloying) elements such as Fe and Cu; which also serve as strong local cathodes, and (ii) the higher alloy Zn content, which can decrease the corrosion potential owing to the electrochemical characteristics of Zn.

A lower corrosion potential for the Al-14Zn-3Mg alloy, corresponds to less polarisation of the associated anodic partial reaction – with concomitantly lower dissolution rates(and corrosion).

The dissolution of AA7075-T6 results in a now well documented corrosion morphology that includes selective dissolution of so-called anodic constituent particles, and the trenching surrounding so-called cathodic constituent particles (which also includes dealloying type dissolution of Al-Cu-Fe(-Si) containing constituent particles). In fact, the evolution of surface corrosion upon AA7075-T6 is characterised and deduced from the time dependent polarisation response of AA7075-T6, whereby the open circuit potential drops from ~ -740 mV_{SCE} following a 600 s immersion in 0.1 M NaCl, to the lower (i.e. less noble) value of ~ -830 mV_{SCE} after 48 h immersion; suggesting that surface corrosion has resulted in the loss of some cathodic potency. In contrast, the open circuit potential of AM-prepared Al-14Zn-3Mg in the as-LPBF and heat

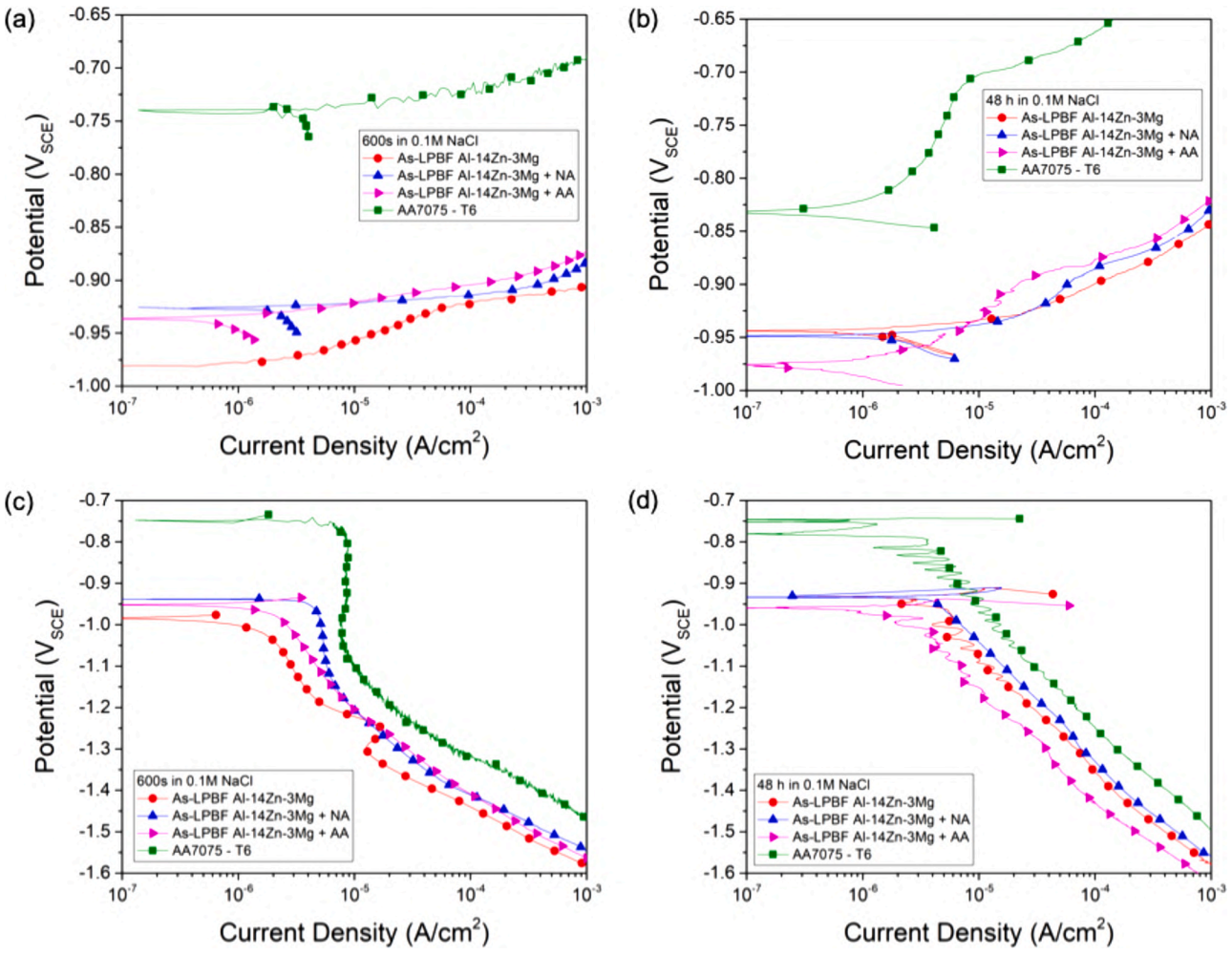

Fig. 2. Potentiodynamic polarisation response in quiescent 0.1 M NaCl for as-LPBF Al-14Zn-3Mg, LPBF Al-14Zn-3Mg in various heat treatment conditions and AA7075-T6. (a) anodic polarisation results following 5 min. of OCP conditioning, (b) anodic polarisation results following 48 h of OCP conditioning, (c) cathodic polarisation results following 5 min. of OCP conditioning, and (d) cathodic polarisation results following 48 h of OCP conditioning, respectively. (NA: 500 °C / 4 h +25 °C / 24 h and AA: 500 °C / 4 h +150 °C / 24 h).

Table 2
Tafel-type extrapolation results of potentiodynamic curves of as-LPBF Al-14Zn-3Mg, LPBF Al-14Zn-3Mg + NA, LPBF Al-14Zn-3Mg + AA and AA 7075 – T6.

Sample	i_{corr} - 600 s ($\mu A/cm^2$)	E_{corr} - 600 s (mV_{SCE})	i_{corr} - 48 h ($\mu A/cm^2$)	E_{corr} - 48 h (mV_{SCE})
As-LPBF Al-14Zn-3Mg	1.1 ± 0.11	−980 ± 9	2.26 ± 0.28	−951 ± 2
LPBF Al-14Zn-3Mg + NA	4.43 ± 0.08	−943 ± 3	3.41 ± 0.14	−936 ± 4
LPBF Al-14Zn-3Mg + AA	1.46 ± 0.17	−952 ± 6	1.59 ± 0.18	−957 ± 3
AA 7075 – T6	7.85 ± 0.15	−755 ± 5	1.21 ± 0.13	−760 ± 19

treated conditions (NA and AA) displayed little to no alteration between 600 s immersion and 48 h immersion. Table 2 shows that the AM-prepared Al-14Zn-3Mg and AA7075-T6 samples after immersion for 48 h in 0.1 M NaCl reveal a similar i_{corr}. Herein, we effectively see that the AA7075-T6 has the lowest electrochemically measured i_{corr} of ~1.21 $\mu A/cm^2$ which is analogous to the i_{corr} value of AM-prepared Al-14Zn-3Mg in AA condition (~1.59 $\mu A/cm^2$). The i_{corr} of Al-14Zn-3Mg in the as-LPBF and NA conditions present an i_{corr} of ~2.26 $\mu A/cm^2$ and ~3.41 $\mu A/cm^2$, respectively. It is noted that the i_{corr} values of all the samples are similar following a 48 h immersion and does not reveal statistically significant ranges.

3.3. Time evolution of polarisation resistance determined using EIS

To evaluate the time evolution of polarisation resistance, electrochemical impedance spectroscopy (EIS) measurements were carried out at several time intervals as follows: 10 min OCP, 1 h, 24 h, 48 h, 96 h, and 168 h, respectively. The EIS data collected after several time intervals for all the samples viz, AM-prepared Al-14Zn-3Mg in as-LPBF, NA and AA conditions, and AA7075-T6 with their corresponding Nyquist plots are shown in Fig. 3 (a–d), respectively.

The Nyquist plots of AM-prepared Al-14Zn-3Mg in the as-LPBF, NA and AA conditions after 600 s of OCP were characterised by two capacitive loops as shown in Fig. 3 (a–c). The high-frequency capacitive loop represents the characteristics of alloy-electrolyte interface and was used to determine the charge transfer resistance (R_{ct}), and double layer capacitance (Q_{dl}), whereas the film characteristics such as film resistance (R_f) and film capacitance (Q_f) were obtained from the low frequency capacitive loop [35]. For AA7075-T6, the Nyquist plot after 600 s of OCP was characterised by a low frequency inductive loop in addition to two high or moderate frequency capacitive loops. It is known that the inductive loop forms due to the weakening of the protective effectiveness of the oxide film, resulting in corrosion of the specimens during the testing process [36]. Such characteristic inductive loop was absent in the AM-prepared Al-14Zn-3Mg. This suggests that the oxide film developed upon LPBF Al-14Zn-3Mg in the as-LPBF, NA and AA

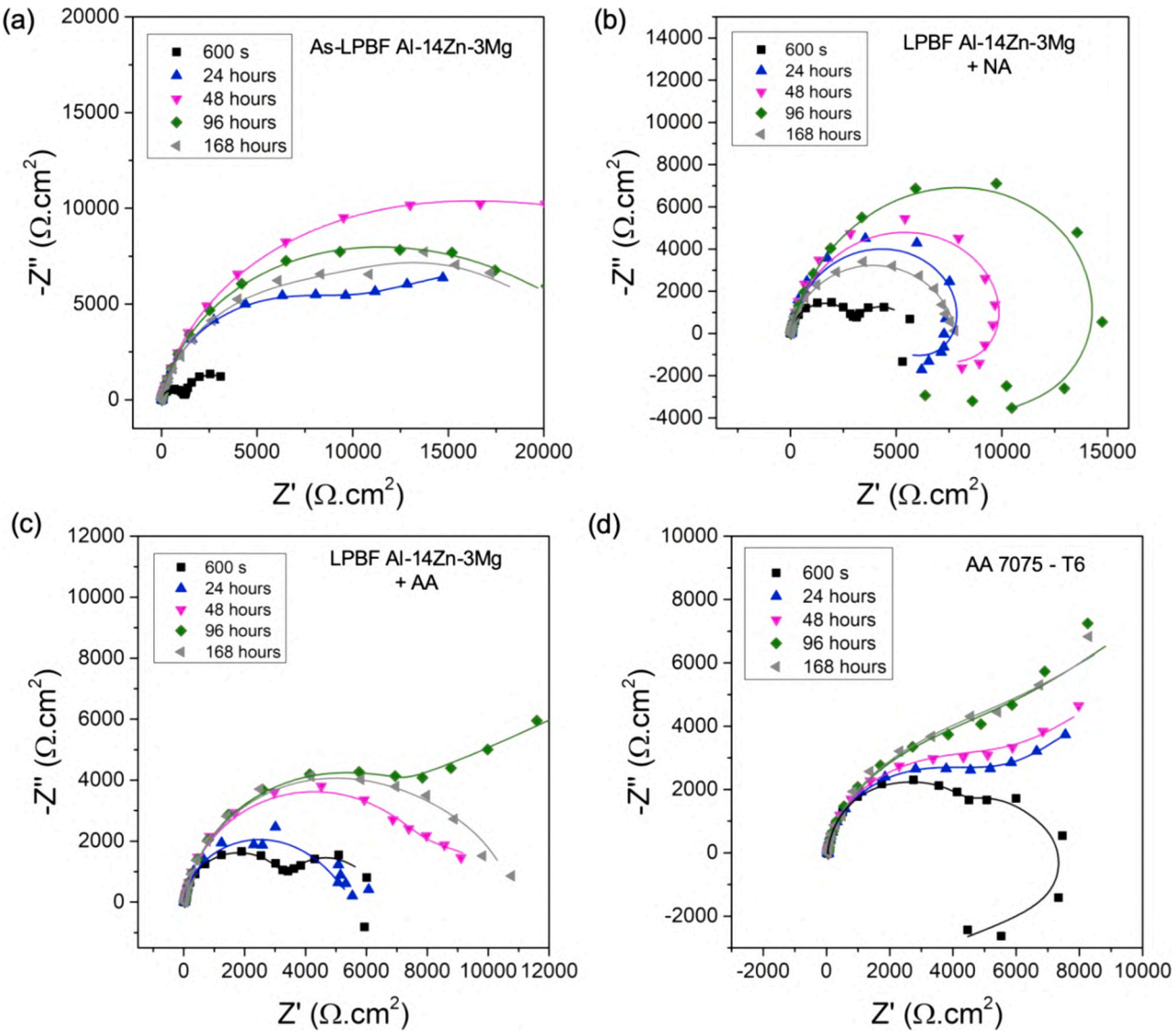

Fig. 3. Nyquist plots of (a) LPBF Al-14Zn-3Mg, (b) LPBF Al-14Zn-3Mg + NA, (c) LPBF Al-14Zn-3Mg + AA and (d) AA 7075 – T6 after various immersion times (listed in corresponding legends) in quiescent 0.1 M NaCl. The experimental data are denoted as data symbols and the solid lines are from the fitted model. (NA: 500 °C / 4 h +25 °C / 24 h and AA: 500 °C / 4 h +150 °C / 24 h).

conditions is expected to provide better corrosion protection when compared to AA7075-T6.

The Nyquist plot of AA7075-T6 was altered after 24 h of immersion. The plot was characterised by a high-frequency capacitive loop followed by a diagonal line with a slope of 45° that suggests a diffusion controlled impedance behaviour (so-called Warburg-impedance). The Warburg-impedance represents the impedance when an electrochemical reaction is under partial or complete mass transport diffusion control and is represented as 'W'. The assumptions and significance of the classical Warburg impedance model are explained in detail elsewhere [37,38]. Similarly, the Nyquist plot of AM-prepared Al-14Zn-3Mg in NA condition also changed after 24 h of immersion where the low-frequency capacitive loop was replaced by an inductive loop – indicating the free pitting of the specimen. This behaviour can be attributed to the uniform evolution of pits over the supersaturated Al-matrix that predominantly contains Mg and Zn in solid solution. In addition, the rapid natural ageing of the alloys may also result in further pitting around the periphery of the second phase particles, resulting in the free pitting of the LPBF Al-14Zn-3Mg in NA condition as seen from the EIS data (Fig. 3b). A general corrosion perspective can be obtained from the semi-circle radius of Nyquist plots where a larger radius can be directly related a reduced corrosion rate. From Fig. 3, it can be discerned that the as-LPBF Al-14Zn-3Mg displayed lower corrosion rates (Fig. 3a) when gauged to AA7075-T6 (Fig. 3d).

The equivalent circuits that was used to fit the experimental data and the associated parameters obtained as a result of fitting are highlighted in Fig. 4 and Table 3, respectively. For Nyquist plot with a single capacitive loop, the charge transfer resistance can be taken as the polarisation resistance (R_p). The polarisation resistance of the Nyquist plots with double capacitive loop (Fig. 4a), single capacitive loop with an inductive loop (Fig. 4b), and double capacitive loop with an inductive loop (Fig. 4c) were obtained by using Eq. 1, Eq. 2 and Eq. 3, respectively.

$$R_p = R_{ct} + R_f \quad (1)$$

$$1/R_p = 1/R_{ct} + 1/R_L \quad (2)$$

$$1/R_p = 1/(R_{ct} + R_f) + 1/R_L \quad (3)$$

The polarisation resistance, (R_p), was calculated for AM-prepared Al-14Zn-3Mg in as-LPBF, NA and AA conditions, and AA7075-T6 as shown in Fig. 5 with the calculated values as highlighted in Table 4.

After one week of exposure to 0.1 M NaCl, it was observed that the

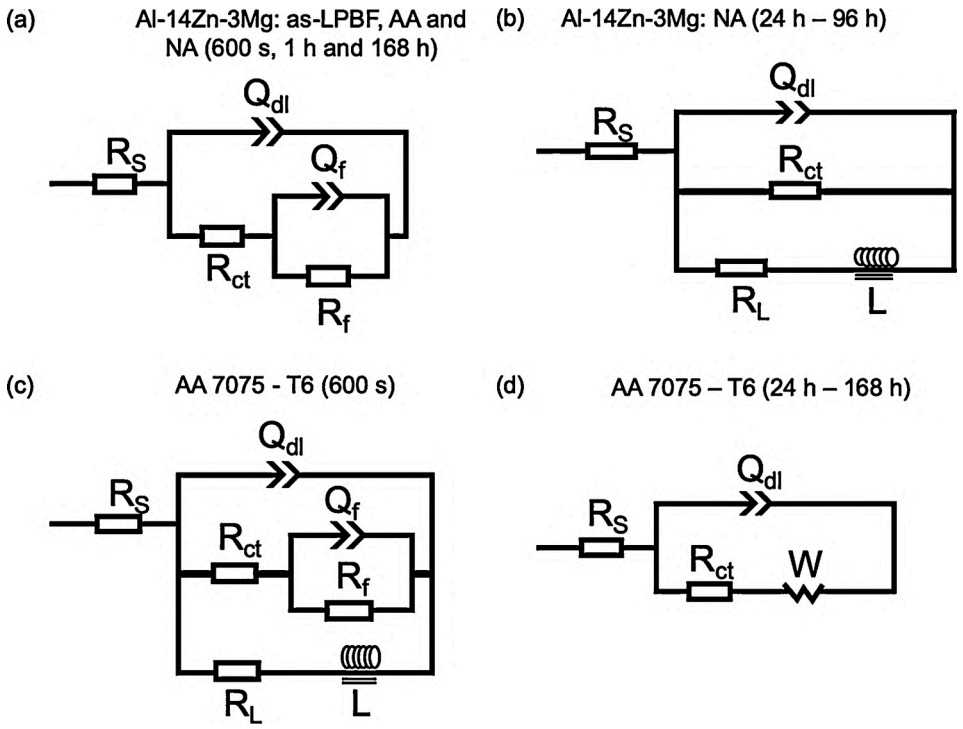

Fig. 4. Equivalent circuits used for fitting the EIS data from several immersion times of (a) Al-14Zn-3Mg in as-LPBF and AA condition for all immersion times and Al-14Zn-3Mg in NA condition for 600 s, 1 h and 168 h, (b) Al-14Zn-3Mg in NA condition for 24 h to 96 h, (c) AA 7075 – T6 for 600 s and (d) AA-7075 – T6 for 24 h to 168 h. (NA: 500 °C / 4 h +25 °C / 24 h and AA: 500 °C / 4 h +150 °C / 24 h).

polarisation resistance of AM-prepared Al-14Zn-3Mg in as-LPBF, NA and AA condition was approximately 22,000 Ω.cm^2, 11,000 Ω. cm^2 and 7800 Ω. cm^2, respectively. In addition, the polarisation resistance of all the AM-prepared Al-14Zn-3Mg increased until a certain exposure duration followed by a gradual decrease. This decrease of polarisation resistance can be attributed to the breakdown of the passive layer after prolonged exposure duration which are different for all the samples. In contrast, the AA7075-T6 revealed a polarisation resistance value of only ~6000 Ω. cm^2 after one week of exposure, suggesting the higher corrosion resistance of the additively manufactured specimens. Moreover, the difference in polarisation resistance of AM-prepared Al-14Zn-3Mg in different conditions and AA7075-T6 can be attributed to the localised corrosion behaviour of the specimens, where the absence of constituent particles and high Zn concentration plays a major role.

3.4. Evaluation of localised corrosion response by immersion testing in 0.1 M NaCl

Specimens of AM-prepared Al-14Zn-3Mg in as-LPBF, NA and AA conditions along with AA7075-T6, were immersed in quiescent 0.1 M NaCl for 48 h. To evaluate the localised corrosion response, secondary electron micrographs taken at low and high magnifications are presented in Fig. 6.

The corrosion response of as-LPBF Al-14Zn-3Mg was characterised as being localised, but not regular in its localisation. There are instances of localised corrosion predominantly associated with regions adjacent to the quasicrystalline P-phase. These localised regions of dissolution (pits) were not like circumferential trenches along the periphery of the P-phase particles – but instead, regions next to P-phase as seen in Fig. 6a. An obvious characteristic of the corrosion observed, is that localised corrosion was not associated with the entire population of P-phase, with many regions populated in P-phase remaining unaffected. The localised dissolution of individual elements (such as Zn or Mg) within the complex quasicrystalline P-phase would require further analysis to confirm. The precise mechanism regarding the localisation of corrosion adjacent to P-phase remains unknown. Whilst this work has definitively shown the phenomena, it is known that the local pH that arises across Al-alloy surfaces during corrosion, dictates the evolving corrosion morphology. For example, if P-phase (rich in Mg and Zn) begins to dissolve, increasing local pH, then the P-phase may passivate and the alkalinity dissolve the matrix. This would be a dynamic effect with regards to corrosion morphology (not studied herein). The initial tendency to consider P-phase as having a 'cathodic' nature by evidence of it being intact, may also be a result of a dynamic pH-driven process. An additional observation, is that it was noted that the pits formed in the melt pool boundaries were qualitatively larger than the pits formed within the melt pool core. Such differences in pitting behaviour are causally correlated to the microstructural variation across the specimen. Specifically, the size of P-phase is larger in the melt pool boundaries when compared to the melt pool core – a phenomenon unique to LPBF processing, as described in the previous section. A closer observation of the melt pool core further confirmed the localised dissolution of α-Al matrix adjacent to a quasicrystalline P-phase (Fig. 6a').

In the case LPBF Al-14Zn-3Mg in the NA condition, localised corrosion was related to two factors: (i) the aforementioned localised dissolution that is not regular in its location, and (ii) the dissolution of $MgZn_2$ phase. High magnification micrographs as shown in Fig. 6b' reveals an instance of $MgZn_2$ dissolution.

The localised corrosion response of Al-14Zn-3Mg in the artificially aged (AA) condition was similar to LPBF Al-14Zn-3Mg in the naturally aged (NA) condition (Fig. 6c, c'); whilst the second phase particles in AA condition were coarser due to the 24 h aging at 150°C.

In response to immersion for 48 h in 0.1 M NaCl, the benchmark wrought AA7075-T6 specimen revealed the highest extent of localised dissolution of α-Al matrix. In the case of AA7075-T6, the localised corrosion is typically associated with coarse constituent particles as seen in Fig. 6d, consistent with the well documented previous reports of localised corrosion of AA7075-T6. Fig. 6d also revealed that in Cu-containing constituent particles, a preferential dissolution of Al and Mg occurs, leaving a Cu-enriched remnant. These Cu-clusters are known

Table 3
Typical results obtained from the fitting of EIS data from as-LPBF Al-14Zn-3Mg, LPBF Al-14Zn-3Mg + NA, LPBF Al-14Zn-3Mg + AA and AA 7075-T6.

Parameters	As-LPBF Al-14Zn-3Mg					LPBF Al-14Zn-3Mg in NA					LPBF Al-14Zn-3Mg in AA					AA 7075 – T6				
	600s	24h	48 h	96h	168h	600s	24h	48 h	96h	168h	600s	24h	48 h	96h	168h	600s	24h	48 h	96h	168h
Rs (Ω)	39	39	46	42	41	72	76	75	35	83	70	66	110	114	108	35	36	36	50	52
Q_{dl} (μF cm^{-2} s$^{(n-1)}$)	11	25	24	25	26	9.1	15.8	14.2	25.7	22.7	8.4	21.5	24.4	27.0	28.0	9.7	34	43	55	66
n_{dl}	0.93	0.89	0.87	0.88	0.87	0.94	0.91	0.93	0.85	0.89	0.96	0.94	0.92	0.91	0.91	0.95	0.94	0.93	0.92	0.91
R_{ct} (Ω cm^2)	1242	11,943	16,273	16,663	14,225	3192	12,288	11,687	18,230	7755	3517	3973	8380	9765	9506	4604	4861	5233	5642	6039
Q_f (mF cm^{-2} s$^{(n-1)}$)	0.75	0.28	0.08	0.17	0.18	0.5	–	–	–	0.07	0.36	0.30	1.52	0.41	0.83	0.2	–	–	–	–
n_f	0.98	0.8	0.45	0.7	1	1	–	–	–	1	1	0.5	1	0.96	1	0.83	–	–	–	–
R_f (Ω cm^2)	2700	14,400	30,673	8079	7618	2346	–	–	–	34	2644	1632	1880	12,163	1200	7884	–	–	–	–
L (H cm^{-2})	–	–	–	–	–	–	23,929	124,368	189,265	–	–	–	–	–	–	16,114	–	–	–	–
R_L (Ω cm^2)	–	–	–	–	–	–	13,405	19,580	9990	–	–	–	–	–	–	3583	–	–	–	–
W (Ω s$^{(-1/2)}$)	–	–	–	–	–	–	–	–	–	–	–	–	–	–	–	–	1776	2029	3168	2917

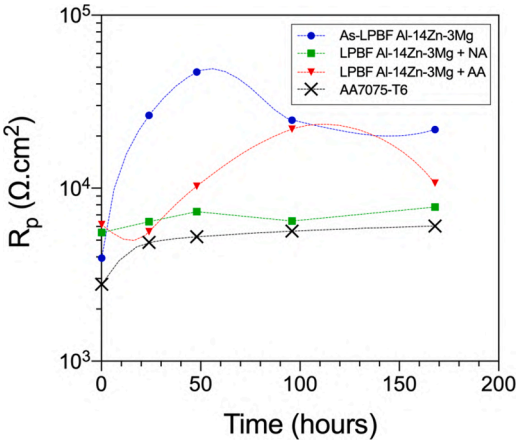

Fig. 5. EIS-determined polarisation resistance of as-LPBF Al-14Zn-3Mg, LPBF Al-14Zn-3Mg + NA, LPBF Al-14Zn-3Mg + AA and AA 7075 – T6 following 48 h immersion in quiescent 0.1 M NaCl. (NA: 500 °C / 4 h +25 °C / 24 h and AA: 500 °C / 4 h +150 °C / 24 h).

Table 4
Polarisation resistance calculated from the fitted EIS data of as-LPBF Al-14Zn-3Mg, LPBF Al-14Zn-3Mg + NA, LPBF Al-14Zn-3Mg + AA and AA 7075 – T6.

Specimen	Polarisation resistance, R_p (Ω. cm^2)				
	600 s	24 h	48 h	96 h	168 h
As- LPBF Al-14Zn-3Mg	3942	26,343	46,946	24,742	21,843
LPBF Al-14Zn-3Mg + NA	5538	6411	7318	6453	7789
LPBF Al-14Zn-3Mg + AA	6161	5605	10,260	21,928	10,706
AA-7075 T6	2784	4861	5233	5642	6039

to increase the kinetics of the oxygen reduction reaction which deteriorates the corrosion properties [39]. A closer observation (Fig. 6d') also revealed the trenches that are formed along the periphery of an Al-Cu-Fe(-Si) constituent particle.

3.5. Evaluating the onset of localised corrosion through quasi in-situ immersion testing in 0.1 M NaCl

To understand the morphology of the particle induced pitting and to understand the onset of localised corrosion, the SEM micrographs of AM-prepared Al-14Zn-3Mg in as-LPBF, NA and AA conditions were studied in comparison with AA7075-T6 before and after immersion of the specimens in quiescent 0.1 M NaCl for 5 and 10 h. A quasi in-situ like immersion was carried out where the immersion was performed ex-situ but the same region was analysed after different immersion times, herein named as quasi in-situ immersion. The secondary electron micrographs of AM-prepared Al-14Zn-3Mg in as-LPBF, NA and AA condition, and AA7075-T6 before and after quasi in-situ immersion are as shown in Fig. 7 (a–p), respectively.

The BSE and SE micrographs of the areas chosen for immersion are shown for as-LPBF Al-14Zn-3Mg (Fig. 7a, b), LPBF Al-14Zn-3Mg in NA (Fig. 7e, f), LPBF Al-14Zn-3Mg in AA (Fig. 7i, j) and wrought AA7075 – T6 (Fig. 7m, n), respectively. The BSE micrographs of as-LPBF Al-14Zn-3Mg highlights the melt pool boundary decorated with P-phase particles whereas AA7075-T6 reveals an Al-Cu-Fe(-Si) constituent particle. The second phase particles along a grain boundary were chosen for Al-14Zn-Mg in the NA and AA conditions.

Following 5 h immersion in quiescent 0.1 M NaCl, localised dissolution adjacent to second phase particles was evident in the LPBF Al-14Zn-3Mg in the NA condition (Fig. 7g) and in AA7075-T6 (Fig. 7o). These sites 'deepened' further following immersion for 10 h (Fig. 7h and p). In contrast, the as-LPBF Al-14Zn-3Mg revealed absence of deep localised where only small pits in the size ranges of sub-micron were

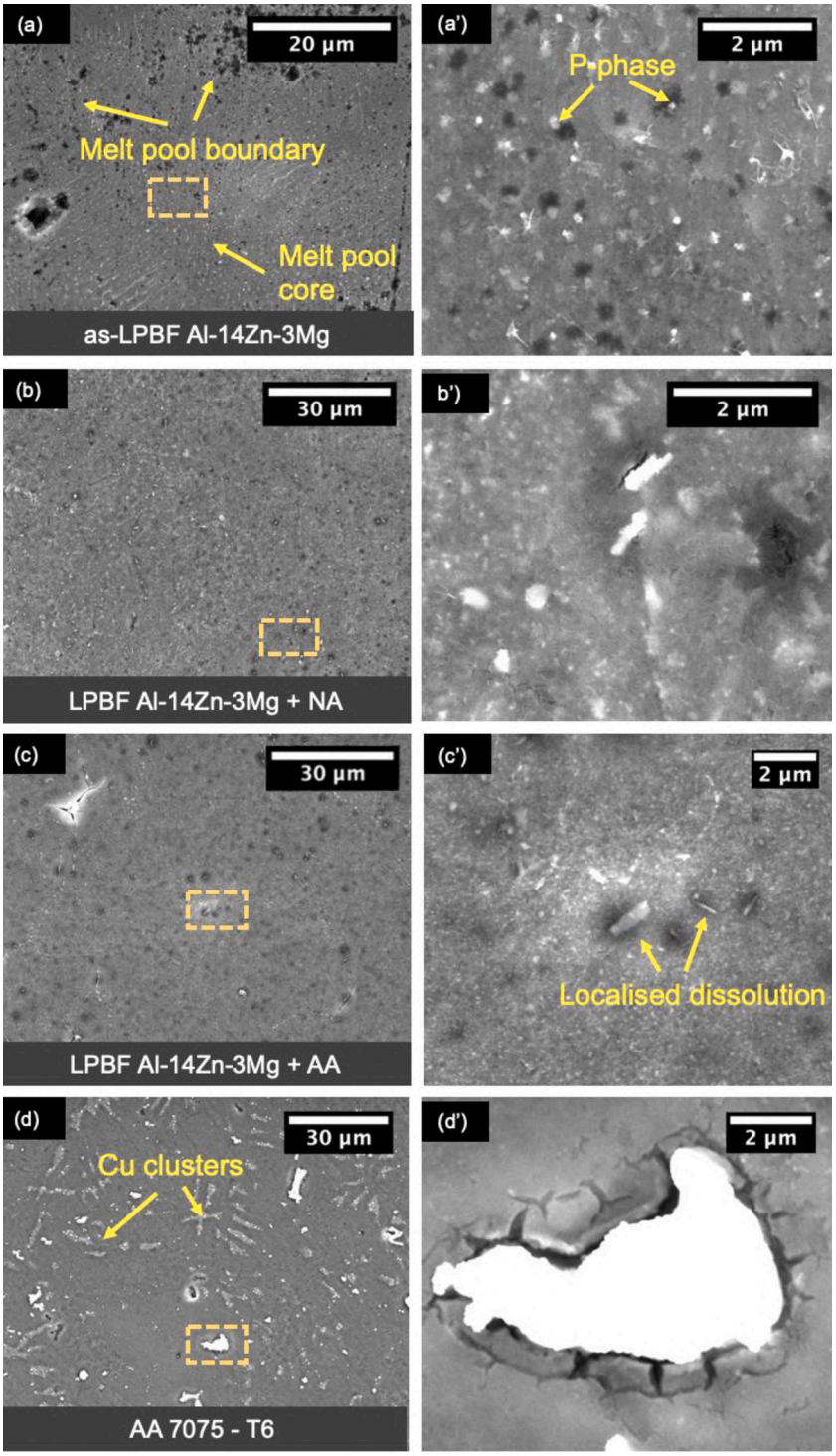

Fig. 6. Secondary electron micrographs of low and high magnification (a, a') as-LPBF Al-14Zn-3Mg, (b, b') LPBF Al-14Zn-3Mg + NA, (c, c') LPBF Al-14Zn-3Mg + AA and (d, d') AA 7075 – T6 following 48 h immersion in quiescent 0.1 M NaCl. (NA: 500 °C / 4 h +25 °C / 24 h and AA: 500 °C / 4 h +150 °C / 24 h).

present. This behaviour accentuates the importance of a fine – and fine grain - microstructure in limiting localised dissolution. It was also noticed that the number of pits in as-LPBF Al-14Zn-3Mg after 5 h of immersion was ~50 whereas after 10 h, the pit number doubled. However, the size of the pits remained in the sub-micron range, confirming the lower corrosion rates of AM-prepared Al-14Zn-3Mg when compared to the AA7075-T6, as validated through electrochemical studies. A point of interest emerging from this work, is that in conventional Al-alloys, without hyper loading of Zn solute such as herein, the self-dissolution of $MgZn_2$ phase (such as the phase in the heat treated LPBF Al-14Zn-3Mg herein), is notionally rapid. Based on results in Figs. 6 and 7, the matrix being hyper loaded in solute plays the role of not necessarily causing rapid self-dissolution of $MgZn_2$. A reason for why this is the case, is that the (slower) cathodic kinetics of LPBF Al-14Zn-3Mg result in an alloy potential that is up to 300 mV less noble than AA7075-T6. At such potentials, the driving force for rapid $MgZn_2$ dissolution is diminished. In fact, the dissolution rate of $MgZn_2$ in LPBF Al-14Zn-3Mg may even be estimated to be ~100 times slower than it

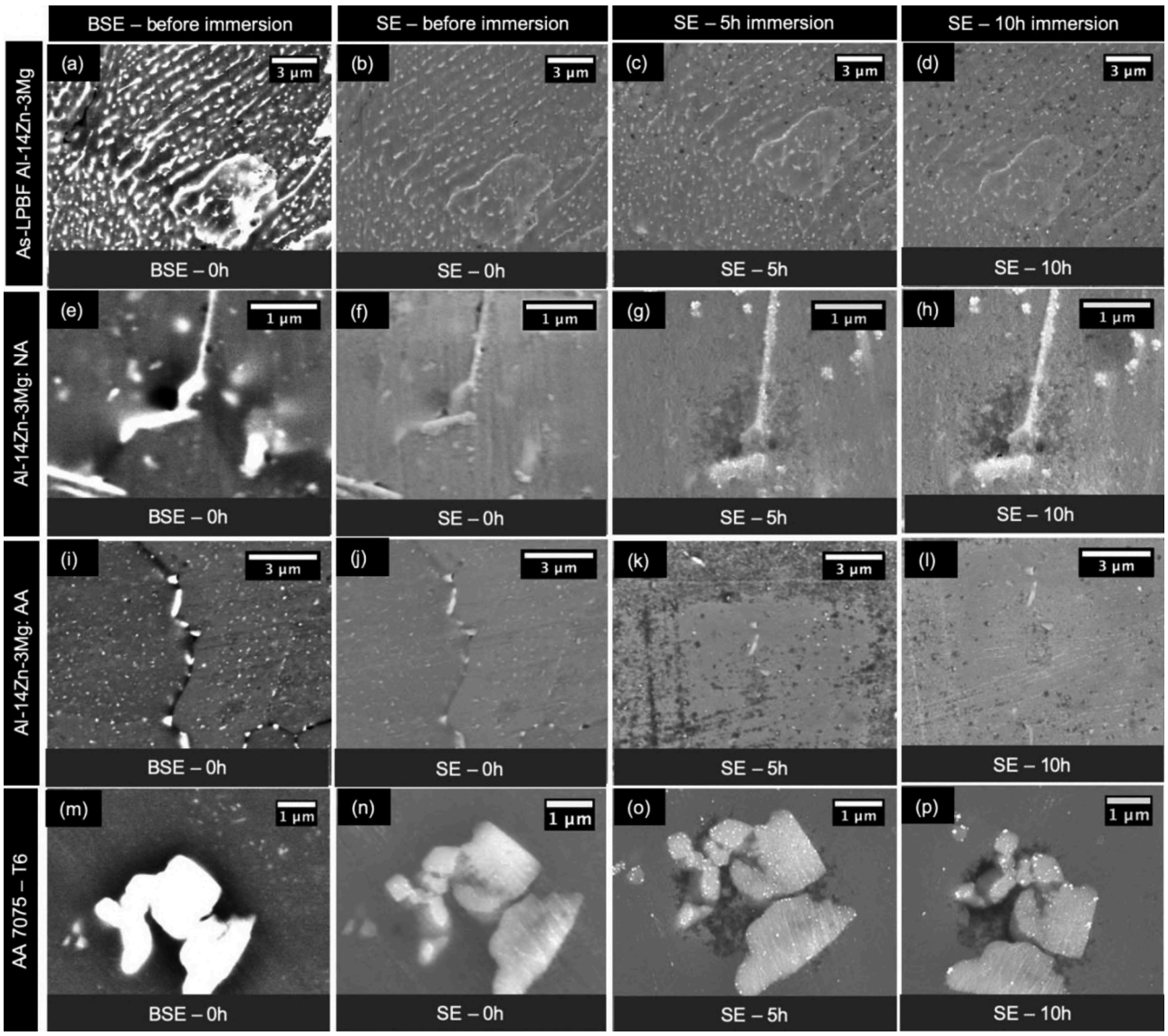

Fig. 7. Backscattered electron (BSE) and secondary electron (SE) micrographs after immersion in quiescent 0.1 M NaCl for various immersion times (as listed in the corresponding figures) of as-LPBF Al-14Zn-3Mg, (a, b, c and d), LPBF Al-14Zn-3Mg + NA, (e, f, g and h), LPBF Al-14Zn-3Mg + AA (i, j, k and l) and AA 7075-T6 (m, n, o and p). (NA: 500 °C / 4 h +25 °C / 24 h and AA: 500 °C / 4 h +150 °C / 24 h).

would be at the potentials of AA7075-T6 based on the characteristics of $MgZn_2$ as reported in [27], with any local pH increase suppressing the $MgZn_2$ dissolution even further [40]. These characteristics may, hypothetically, also be transposed to the behaviour of P-phase, although that would require further work.

3.6. Pit analysis using optical profilometry

To evaluate the differences in the size, morphology and distribution of pits, optical profilometry was utilised. Fig. 8 shows the optical profilometry analysis of the corroded surfaces after 48 h immersion in 0.1 M NaCl of AM-prepared Al-1Zn-3Mg in as-LPBF, NA and AA condition, and AA7075-T6, respectively. These three dimensional optical profilometry images demonstrate the variation in number of pits and their corresponding size ranges, over an area of 16 μm^2. The analysed results of the optical profilometry images over a ~1200 μm^2 area highlighting the key corrosion parameters are tabulated in Table 5.

The maximum pit depth of Al-14Zn-3Mg in as-LPBF, NA and AA condition, and AA7075-T6 was approximately 1.1 μm, 4.7 μm, 3.1 μm and 7.3 μm, respectively. From Table 5, it is also noticed that the number of pits in as-LPBF Al-14Zn-3Mg were almost 30 times higher than the number of pits in AA7075-T6 which had less than 70 pits over a ~1200 μm^2 area. This phenomenon of small size and high number density of pits in as-LPBF Al-14Zn-3Mg further validates the influence of a refined microstructure and absence of constituent particles in minimising the rate of corrosion. As the $MgZn_2$ precipitates that are formed after heat treatment are coarser in size than the P-phase particles, the average pit sizes of AM-prepared Al-14Zn-3Mg from as-LPBF to heat treated (NA and AA) conditions increased from approximately 400 μm–750 μm, respectively.

3.7. X-ray photoelectron spectroscopy (XPS) of surface films

The polarisation resistance of as-LPBF Al-14Zn-3Mg was distinctive with respect to AA7075-T6 and heat treated Al-14Zn-3Mg samples (in AA and NA conditions). In addition to the contrasting microstructure, which directly alters the corrosion rates, the difference in corrosion behaviour was also believed to be attributed to the variation in surface film composition and thickness - which directly inhibits corrosion by resisting the oxidation reaction of the metal [29]. After immersing the

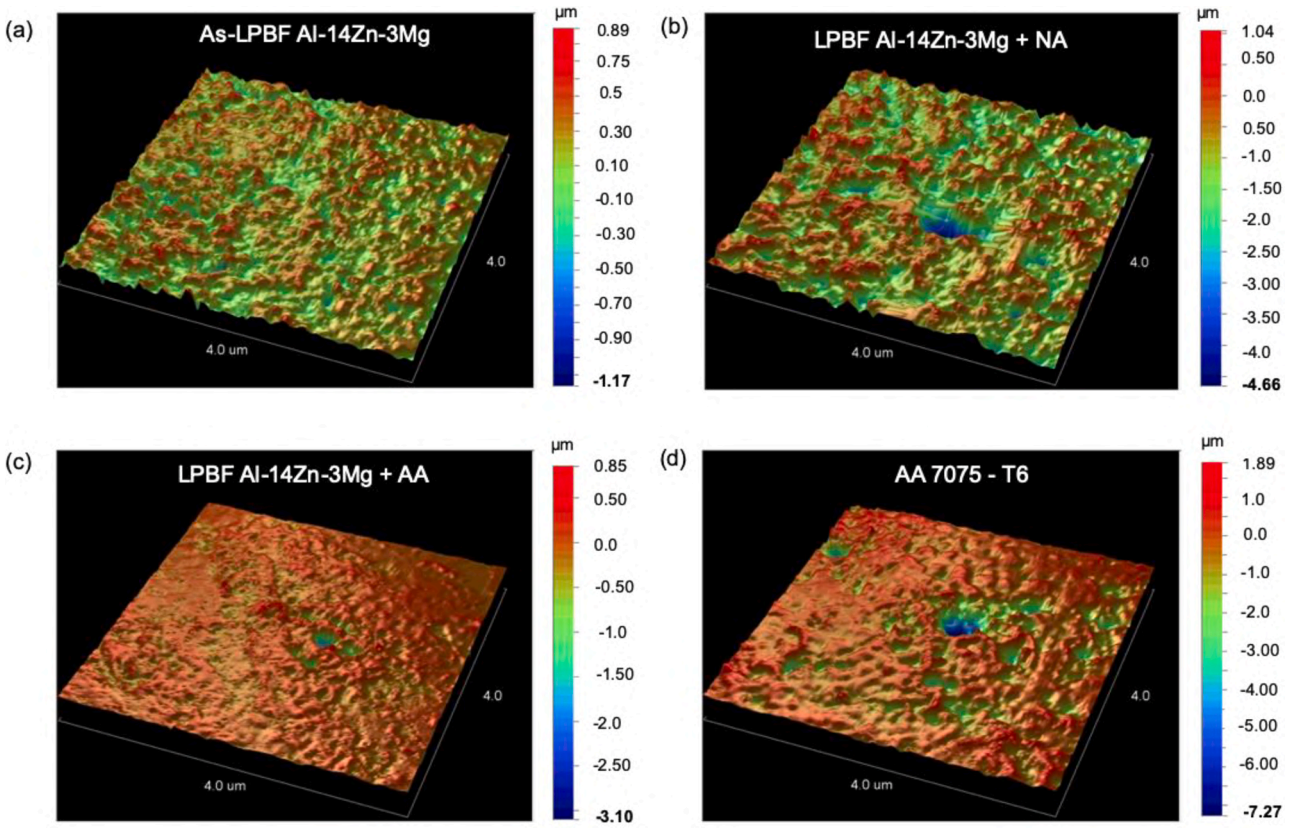

Fig. 8. Optical profilometry revealing the depth and distribution of pits in: (a) LPBF Al-14Zn-3Mg, (b) LPBF Al-14Zn-3Mg + NA, (c) LPBF Al-14Zn-3Mg + AA and (d) AA 7075 – T6, after 48 h immersion in quiescent 0.1 M NaCl. The field of view was maintained at 300 μm x 228 μm. [NA: 500 °C / 4 h +25 °C / 24 h and AA: 500 °C / 4 h +150 °C / 24 h].

Table 5
Key corrosion parameters obtained from the optical profilometry of As-LPBF Al-14Zn-3Mg, LPBF Al-14Zn-3Mg + NA, LPBF Al-14Zn-3Mg + AA and AA 7075 – T6 following 48 h immersion in quiescent 0.1 M NaCl. The total number of pits, average pit size and surface roughness were calculated from 35 μm x 35 μm field of view. (NA: 500 °C / 4 h +25 °C / 24 h and AA: 500 °C / 4 h +150 °C / 24 h).

Sample	Total number of pits over ~1200 μm^2 area	Average pit size (nm)	Surface roughness (nm)
As-LPBF Al-14Zn-3Mg	1937	375 ± 27	291
LPBF Al-14Zn-3Mg + NA	437	659 ± 48	284
LPBF Al-14Zn-3Mg + AA	396	776 ± 55	263
AA 7075 – T6	68	1154 ± 62	222

specimens in 0.1 M NaCl for 48 h, X-ray photoelectron spectroscopy (XPS) was utilised to analyse the chemical composition of the surface film of AM-prepared Al-14Zn-3Mg in as-LPBF, NA and AA condition in comparison with AA7075-T6 as tabulated in Table 6.

The results of chemical composition for AA7075-T6 and AM-prepared samples displayed similar results. The main components observed are the Al 2p, O 1s, C 1s and Zn 2p for all the samples. Minor quantities of Cl 2p, Cu 2p, Fe 2p, Mg 1s, N 1s and Si 2p were also detected. As known, aluminium readily forms a protective oxide film at room temperature which conforms to an inverse logarithmic equation [41]. From Table 6, it is evident that all the samples have developed such a surface layer that was rich in Al and O. The high resolution Al 2p scan of all four samples exhibits a single peak at around 74.2 eV which confirms the presence of oxidised aluminium species as opposed to metal. The specimen surface also revealed the presence of some

Table 6
XPS data of AA7075 – T6, as-LPBF Al-14Zn-3Mg, Al-14Zn-3Mg in NA and AA condition showing the calculated chemical composition of the surface film.

Element	Atomic percent (%)			
	Al-14Zn-3Mg (as-LPBF)	Al-14Zn-3Mg (NA)	Al-14Zn-3Mg (AA)	AA7075-T6
Al2p	24.1	20.1	17.4	22.9
OH^-	36.3	35.1	35.6	35.1
O^{2-}	20.2	20.2	18.6	23.2
H_2O/ CO_3^{2-}	3.1	2.5	0.7	1.2
C1 s	16.7	22.2	26.5	18.0
Zn2p	2.1	1.8	2.8	1.9
Cl2p	0.6	0.5	0.7	0.5
Cu2p	0.3	0.2	0.1	0.6
Fe2p	0.3	0.4	–	0.4
Mg1 s	0.2	0.1	0.3	0.2
N1 s	0.5	0.4	0.6	0.3
Si2p	0.2	0.1	0.4	0.6

adventitious carbon, due to pick up from the environment.

The high resolution oxygen spectra were deconvoluted into three peaks at ~530.4 eV, ~531.7 eV and ~533.3 eV to estimate the oxygen in aluminium oxide ($O2^-$), surface hydroxides (OH^-) and organic absorbates (H_2O/CO_3^{2-}) for all the samples, respectively as shown in Fig. 9. The intensity of the peaks shows that aluminium hydroxide is the main contribution to the formation of a surface film which is in agreement with previously reported values [42]. It can also be discerned that the ratio of hydroxide peak to the oxide peak of AA7075-T6, as-LPBF Al-14Zn-3Mg, LPBF Al-14Zn-3Mg in NA and AA conditions are 1.5, 1.8, 1.7 and 1.9, respectively. This implies that the oxide layer is more hydrated in AM-prepared Al-14Zn-3Mg when compared to the AA7075-T6.

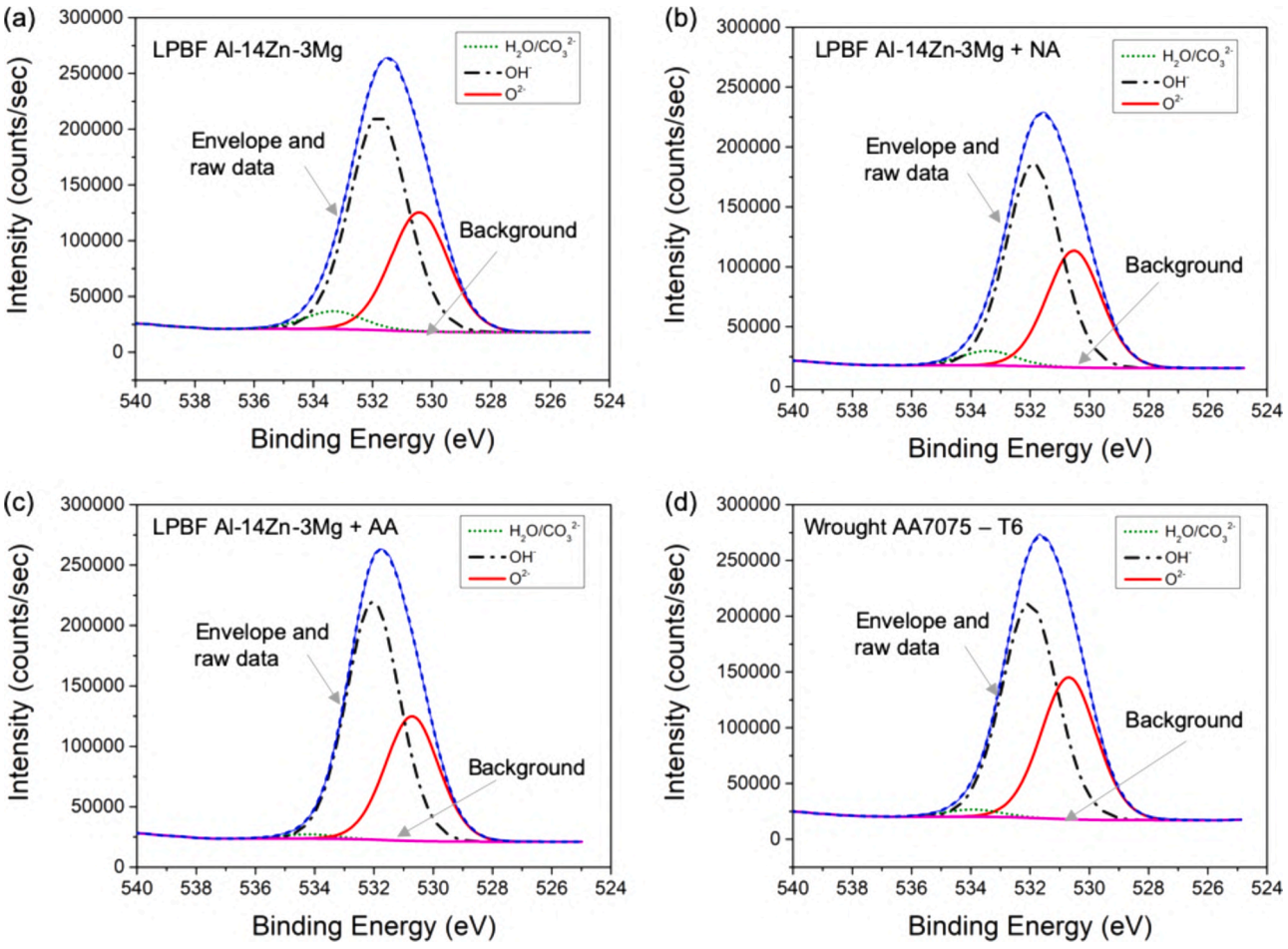

Fig. 9. Deconvolution of high resolution O1 s spectrum for (a) LPBF Al-14Zn-3Mg, (b) LPBF Al-14Zn-3Mg + NA, (c) LPBF Al-14Zn-3Mg + AA and (d) AA 7075 – T6 showing the hydroxide to oxide ratio as 1.5, 1.8, 1.7 and 1.9 respectively. The raw data and envelope are differentiated through dotted and continuous lines, respectively.

As the oxide layer of AM-prepared Al-14Zn-3Mg had a similar composition with AA7075-T6, an estimation of the comparative thickness of the oxide layer was deemed important in order to ascertain any differences that result from the large difference in alloy compositions between Al-14Zn-3Mg and AA7075-T6. Therefore, depth profiling through X-ray photoelectron spectroscopy (XPS) was carried out for three conditions after immersion in 0.1 M NaCl for 48 h, namely the as-LPBF Al-14Zn-3Mg, LPBF Al-14Zn-3Mg in AA condition and compared with AA7075-T6 as shown in Fig. 10. The concentration of oxygen reduces with increasing sputtering depth whereas the aluminium concentration increases – an indication that the oxide film is being removed as sputtering towards the bulk material progresses. This variation of concentration with respect to the sputtering depth can be used to estimate thickness of the surface oxide film [43]. As the binding energies of metallic Zn, Cu and Mg are often very close to the binding energies of their corresponding oxides, chemical state analysis can be difficult using the photoelectron peaks alone and larger chemical shifts are observed in the Auger spectra. Therefore, the sputtering progress through the surface film to the bulk material was further confirmed through observation in the change in Zn LM2, Cu LM2 and Mg KL1 as the material was removed, with the appearance of distinct metallic peaks and the gradual reduction of oxide peaks for all three elementals as depth increases. The surface oxide film thickness was estimated for AA7075-T6 as 430 nm, as-LPBF Al-14Zn-3Mg as 1100 nm and for LPBF Al-14Zn-3Mg in AA condition as 760 nm. Therefore, it is conclusive that AM-prepared Al-14Zn-3Mg forms a thicker oxide at similar electrochemical conditions when compared to AA7075-T6.

3.8. General discussion

The results herein revealed key differences in the microstructure and its effects on the electrochemical behaviour of LPBF Al-14Zn-3Mg as a function of processing, and in contrast to AA7075-T6 as a benchmark.

Whilst AA7075–T6 acquires its properties from a heterogenous microstructure through alloying and heat treatment [2,39], alloying leads to the presence of insoluble constituent particles (Fig. 1d). From a corrosion perspective, such constituent particles result in localised corrosion (Fig. 6d, d') [27]. In contrast, the presence of a refined microstructure through fine P-phase particles and absence of coarse constituent particles (Fig. 1a) in the as-LPBF Al-14Zn-3Mg, revealed a polarisation resistance value of ~22,000 Ω. cm^2 when compared to AA7075-T6 with a polarisation resistance of ~6000 Ω. cm^2. In both the cases, it is evident that so-called 'cathodic particles' support appreciable oxygen reduction cause dissolution of the adjacent material. However, the ramification of the presence of fine P-phase particles in the as-LPBF Al-14Zn-3Mg, resulted in a reduced prevalence of corrosion where the pit sizes were considerably small as seen in Fig. 6a'.

To aid in a phenomenological representation of the results herein, a schematic of the corrosion of as-LPBF Al-14Zn-3Mg in contrast to AA7075-T6 is depicted in Fig. 11.

The microstructural differences highlight the contrasting size and distribution of the second phase particles (Fig. 11); whilst the surface morphology indicates the presence of coarse constituent particles (~1−15 μm) in AA7075-T6, and all (strengthening) particles in as-LPBF Al-14Zn-3Mg being < 1 μm. The cross sectional morphology depictions

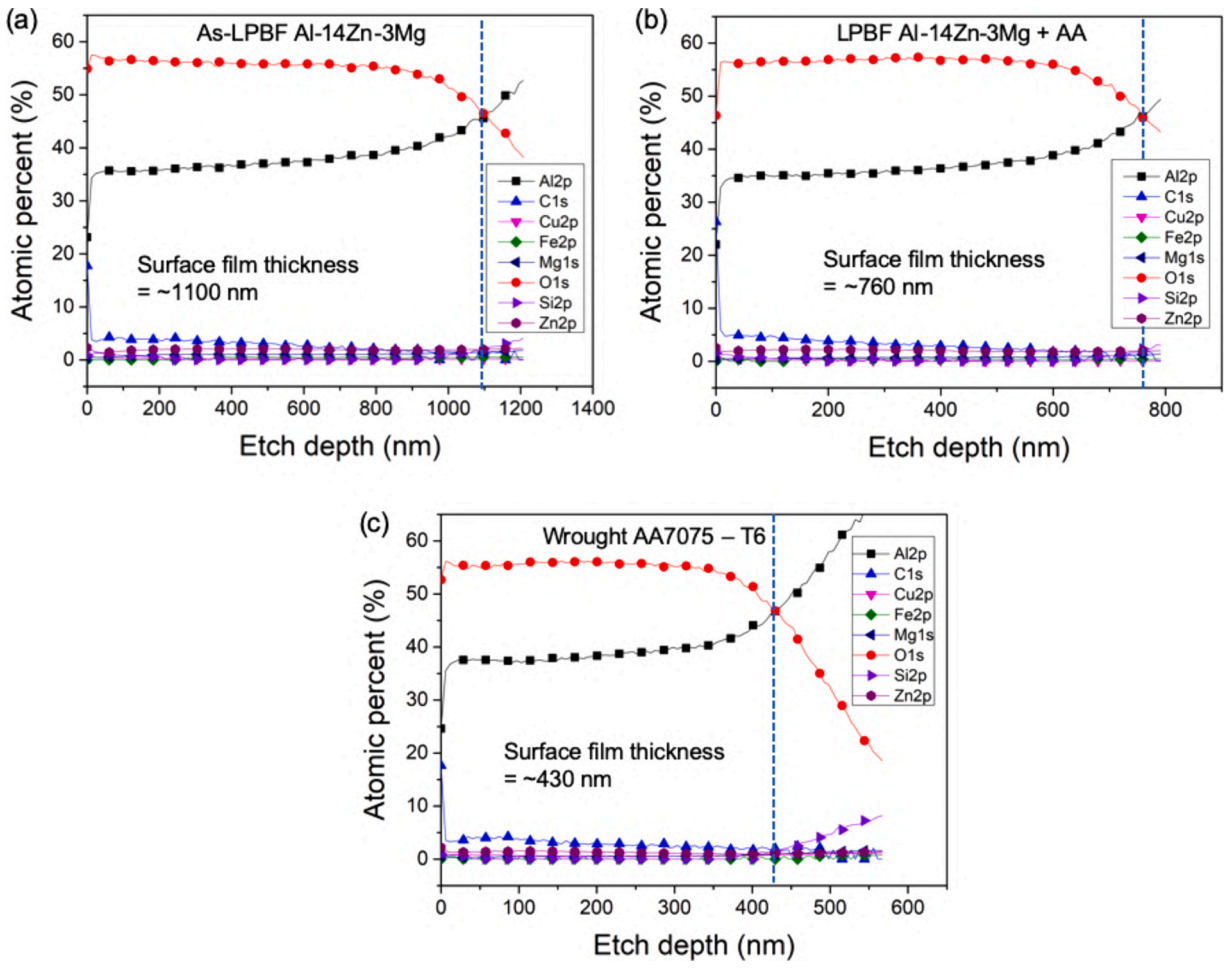

Fig. 10. XPS depth profiles showing revealing the surface film chemistry and thickness of (a) LPBF Al-14Zn-3Mg, (b) LPBF Al-14Zn-3Mg + AA, (c) AA 7075 – T6.

indicate the differences in corrosion morphology that exist, where more significant pit depths are formed in the presence of constituent particles (AA7075-T6). Conversely, several pits are formed in the as-LPBF Al-14Zn-3Mg where the pit sizes are ~ four times smaller than the pits observed in AA7075-T6. It was revealed herein from XPS analysis that the surface film upon as-LPBF Al-14Zn-3Mg (~1100 nm) was more than twice as thick as the surface film formed upon AA7075-T6 (~430 nm). Whilst the study herein raises a number of questions that are yet to be fully answered, the purpose of the study to reveal the corrosion of a comparatively (very) high solute Al-Zn-Mg alloy demonstrated that there was not a catastrophic increase in corrosion rates from hyper-alloying of Zn. In fact, the findings revealed new insights whereby the corrosion behaviour of AM-prepared high solute Al-Zn-Mg alloys are improved relative to traditional wrought high strength Al-Zn-Mg alloys for the reasons aforementioned herein – which were largely as a result of decreased cathodic kinetics in the case of LPBF prepared Al-14Zn-3Mg. The study herein has raised two questions that remain open and are the basis for future work. The first is the precise electrochemical entity of the P-phase. Such a phase is only possible to produce in a fine size, and forms from rapid solidification (and is thus, metastable in the sense that it cannot be produced at scale). Further work, focused on nano-scale quasi-in-situ methods [28,44], is one means to clarify the role – be it anodic or cathodic relative to the alloy matrix – of the P-phase. The second is to understand the origins of the thicker surface film, and if that is associated with a uniform dissolution phenomenon that is not evident from SEM analyses. The findings herein, however, reveal the possibility to explore aspects of Al-alloy corrosion that have not been previously explored. For example, the role of oxide thickness, which here was revealed to be significantly different between high-Zn alloys, and AA7075-T6; however where it was also noted that oxide film compositions remaining essentially similar. The similar oxide film compositions between alloys of vastly differing composition was unanticipated and merits future work, most likely employing methodologies such as those demonstrated by Gharbi and co-workers [15]. As is the case for understanding localised corrosion of wrought Al-alloys to date, no single study can capture all aspects, however through ongoing work it is posited that through the LPBF process and fabrication of new Al-alloy compositions, further illumination into mechanistic aspects of Al-alloy corrosion and its control by alloy design, can ensue.

4. Conclusion

The corrosion of LPBF prepared Al-14Zn-3Mg (wt. %) was studied in the as-LPBF, naturally aged (NA) and artificially aged (AA) conditions. An abridged summary of the findings are summarised below:

1 The as-LPBF Al-14Zn-3Mg revealed a distinctive microstructure populated with quasicrystalline P-phase particles of different sizes and morphology. The presence of a refined microstructure and the annihilation of coarse constituent particles due to rapid solidification resulted in lower corrosion rates of as-LPBF Al-14Zn-3Mg. The study herein indicating that the presence of a high solute content (of specifically Zn) is not detrimental to corrosion of Al-alloys, prima facie. The study also revealed that Al-14Zn-3Mg had a significantly lower corrosion potential than AA7075-T6, attributed to less Fe and Cu rich constituent particles and the absence of strong localised cathodes in

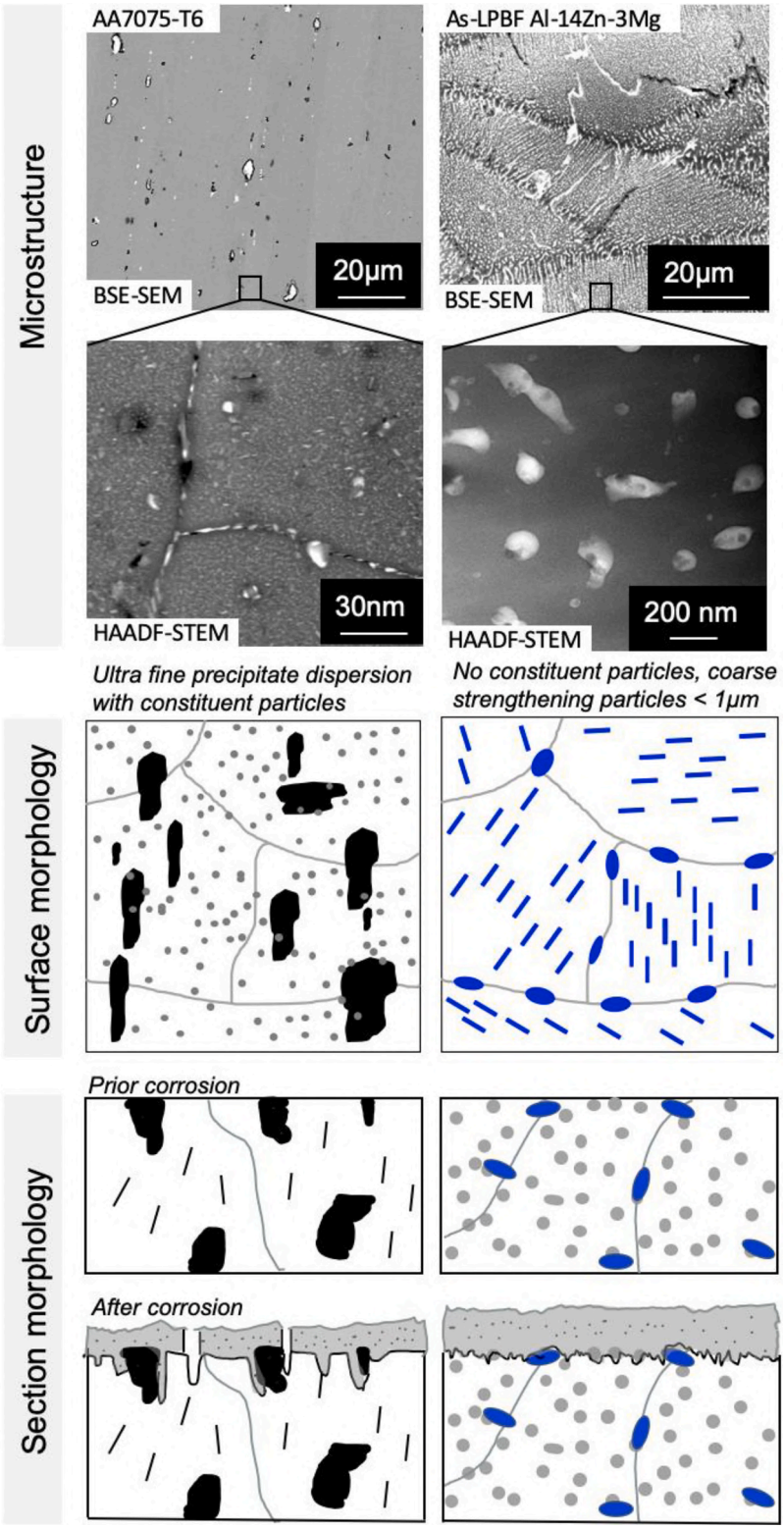

Fig. 11. Phenomenology of corrosion and surface film formation for (left) AA7075-T6 and, (right) LPBF processed Al-14Zn-3Mg.

the alloy microstructure. This lower potential of Al-14Zn-3Mg (irrespective of heat treatment) also meant that kinetics of particles rich in Zn and Mg was restricted.

2 Electrochemical impedance spectroscopy following one week in quiescent 0.1 M NaCl revealed that the as-LPBF Al-14Zn-3Mg had the highest polarisation resistance of ~ 22,000 Ω.cm^2, followed by the AA condition with a value of ~11,000 Ω. cm^2. The Al-14Zn-3Mg in the NA condition had a comparatively lower polarisation resistance of 7800 Ω. cm^2 among the AM-prepared samples, however, this value was higher than the polarisation resistance of AA7075-T6.

3 Immersion testing in quiescent 0.1 M NaCl revealed that the localised corrosion of AM-prepared Al-14Zn-3Mg was predominantly associated with discrete and non-uniformly distributed localised corrosion adjacent to second phase particles. The pits upon as-LPBF

Al-14Zn-3Mg were smaller than those of the NA and AA heat treated conditions, whilst noting that the precise mode of localised corrosion remains under further investigation. The average pit size for as-LPBF Al-14Zn-3Mg was ~375 nm whereas the AA7075 – T6 contained average pit sizes of ~1.15 μm.

4 The presence of a thicker oxide film in the AM-prepared Al-14Zn-3Mg in the as-LPBF and the AA condition was shown from XPS depth profiling; revealing a surface film thickness of ~1100 nm and ~760 nm, respectively. The presence of a thicker oxide film may influence corrosion behaviour when assessed relative to AA7075-T6 with a surface film thickness of ~430 nm; however the bulk composition (supersaturation of Zn) and the absence of coarse intermetallic particles are key factors.

Data availability

The data that support the findings of this study are available from the corresponding author, upon reasonable request.

CRediT authorship contribution statement

A.P. Babu: Conceptualization, Methodology, Investigation, Writing - original draft, Writing - review & editing. **S. Choudhary:** Investigation. **J.C. Griffith:** Investigation. **A. Huang:** Supervision. **N. Birbilis:** Conceptualization, Supervision, Funding acquisition, Writing - review & editing.

Declaration of Competing Interest

The authors report no declarations of interest.

Acknowledgements

The authors gratefully acknowledge the Monash Centre for Electron Microscopy (MCEM) and Monash X-ray Platform (MXP). This work was supported by the Monash Graduate Research Scholarship.

References

[1] E.A. Starke, J.T. Staley, Application of Modern Aluminium Alloys to Aircraft, Woodhead Publishing Limited, 2010, https://doi.org/10.1533/9780857090256.3.747.
[2] I.J. Polmear, D. StJohn, J.-F. Nie, M. Qian, Light Alloys: Metallurgy of the Light Metals, 2017.
[3] M.M. Sharma, M.F. Amateau, T.J. Eden, Mesoscopic structure control of spray formed high strength Al-Zn-Mg-Cu alloys, Acta Mater. 53 (2005) 2919–2924, https://doi.org/10.1016/j.actamat.2005.03.007.
[4] H. Li, F. Cao, S. Guo, Y. Jia, D. Zhang, Z. Liu, P. Wang, S. Scudino, J. Sun, Effects of Mg and Cu on microstructures and properties of spray-deposited Al-Zn-Mg-Cu alloys, J. Alloys Compd. 719 (2017) 89–96, https://doi.org/10.1016/j.jallcom.2017.05.101.
[5] I. Gibson, D. Rosen, B. Stucker, Additive Manufacturing Technologies: 3D Printing, Rapid Prototyping, and Direct Digital Manufacturing, second edition, Springer, New York, 2015, https://doi.org/10.1007/978-1-4939-2113-3.
[6] D. Herzog, V. Seyda, E. Wycisk, C. Emmelmann, Additive manufacturing of metals, Acta Mater. 117 (2016) 371–392, https://doi.org/10.1016/j.actamat.2016.07.019.
[7] W.E. Frazier, Metal additive manufacturing: a review, J. Mater. Eng. Perform. 23 (2014) 1917–1928, https://doi.org/10.1007/s11665-014-0958-z.
[8] N.T. Aboulkhair, N.M. Everitt, I. Ashcroft, C. Tuck, Reducing porosity in AlSi10Mg parts processed by selective laser melting, Addit. Manuf. 1 (2014) 77–86, https://doi.org/10.1016/j.addma.2014.08.001.
[9] N.T. Aboulkhair, I. Maskery, C. Tuck, I. Ashcroft, N.M. Everitt, The microstructure and mechanical properties of selectively laser melted AlSi10Mg: the effect of a conventional T6-like heat treatment, Mater. Sci. Eng. A 667 (2016) 139–146, https://doi.org/10.1016/j.msea.2016.04.092.
[10] J. Wu, X.Q. Wang, W. Wang, M.M. Attallah, M.H. Loretto, Microstructure and strength of selectively laser melted AlSi10Mg, Acta Mater. 117 (2016) 311–320, https://doi.org/10.1016/j.actamat.2016.07.012.
[11] E.O. Olakanmi, Selective laser sintering/melting (SLS/SLM) of pure Al, Al-Mg, and Al-Si powders: effect of processing conditions and powder properties, J. Mater. Process. Technol. 213 (2013) 1387–1405, https://doi.org/10.1016/j.jmatprotec.2013.03.009.
[12] J. Suryawanshi, K.G. Prashanth, S. Scudino, J. Eckert, O. Prakash, U. Ramamurty, Simultaneous enhancements of strength and toughness in an Al-12Si alloy synthesized using selective laser melting, Acta Mater. 115 (2016) 285–294, https://doi.org/10.1016/j.actamat.2016.06.009.
[13] N. Li, S. Huang, G. Zhang, R. Qin, W. Liu, H. Xiong, G. Shi, J. Blackburn, Progress in additive manufacturing on new materials: a review, J. Mater. Sci. Technol. 35 (2019) 242–269, https://doi.org/10.1016/j.jmst.2018.09.002.
[14] A. Aversa, G. Marchese, A. Saboori, E. Bassini, D. Manfredi, S. Biamino, D. Ugues, P. Fino, M. Lombardi, New aluminum alloys specifically designed for laser powder bed fusion: a review, Materials (Basel) 12 (2019), https://doi.org/10.3390/ma12071007.
[15] O. Gharbi, D. Jiang, D.R. Feenstra, S.K. Kairy, Y. Wu, C.R. Hutchinson, N. Birbilis, On the corrosion of additively manufactured aluminium alloy AA2024 prepared by selective laser melting, Corros. Sci. 143 (2018) 93–106, https://doi.org/10.1016/j.corsci.2018.08.019.
[16] O. Gharbi, S. Kumar Kairy, P.R. De Lima, D. Jiang, J. Nicklaus, N. Birbilis, Microstructure and corrosion evolution of additively manufactured aluminium alloy AA7075 as a function of ageing, Npj Mater. Degrad. 3 (2019), https://doi.org/10.1038/s41529-019-0101-6.
[17] S.C. Altıparmak, V.A. Yardley, Z. Shi, J. Lin, Challenges in additive manufacturing of high-strength aluminium alloys and current developments in hybrid additive manufacturing, Int. J. Light. Mater. Manuf. 4 (2021) 246–261, https://doi.org/10.1016/j.ijlmm.2020.12.004.
[18] S. Lathabai, Additive manufacturing of aluminium-based alloys and composites. Fundam. Alum. Metall., Elsevier, 2018, pp. 47–92, https://doi.org/10.1016/b978-0-08-102063-0.00002-3.
[19] P. Wang, H.C. Li, K.G. Prashanth, J. Eckert, S. Scudino, Selective laser melting of Al-Zn-Mg-Cu: heat treatment, microstructure and mechanical properties, J. Alloys Compd. 707 (2017) 287–290, https://doi.org/10.1016/j.jallcom.2016.11.210.
[20] S.K. Kairy, O. Gharbi, J. Nicklaus, D. Jiang, C.R. Hutchinson, N. Birbilis, On the characterization of a hitherto unreported icosahedral quasicrystal phase in additively manufactured aluminum alloy AA7075, Metall. Mater. Trans. A Phys. Metall. Mater. Sci. 50 (2019) 529–533, https://doi.org/10.1007/s11661-018-5025-1.
[21] N. Kaufmann, M. Imran, T.M. Wischeropp, C. Emmelmann, S. Siddique, F. Walther, Influence of process parameters on the quality of aluminium alloy en AW 7075 using Selective Laser Melting (SLM). Phys. Procedia, Elsevier B.V., 2016, pp. 918–926, https://doi.org/10.1016/j.phpro.2016.08.096.
[22] M.L. Montero Sistiaga, R. Mertens, B. Vrancken, X. Wang, B. Van Hooreweder, J. P. Kruth, J. Van Humbeeck, Changing the alloy composition of Al7075 for better processability by selective laser melting, J. Mater. Process. Technol. 238 (2016) 437–445, https://doi.org/10.1016/j.jmatprotec.2016.08.003.
[23] J.H. Martin, B.D. Yahata, J.M. Hundley, J.A. Mayer, T.A. Schaedler, T.M. Pollock, 3D printing of high-strength aluminium alloys, Nature 549 (2017) 365–369, https://doi.org/10.1038/nature23894.
[24] A.B. Spierings, K. Dawson, P. Dumitraschkewitz, S. Pogatscher, K. Wegener, Microstructure characterization of SLM-processed Al-Mg-Sc-Zr alloy in the heat treated and HIPed condition, Addit. Manuf. 20 (2018) 173–181, https://doi.org/10.1016/j.addma.2017.12.011.
[25] Q. Jia, P. Rometsch, S. Cao, K. Zhang, X. Wu, Towards a high strength aluminium alloy development methodology for selective laser melting, Mater. Des. 174 (2019), https://doi.org/10.1016/j.matdes.2019.107775.
[26] A.P. Babu, S.K. Kairy, A. Huang, N. Birbilis, Laser powder bed fusion of high solute Al-Zn-Mg alloys : Processing, characterisation and properties, Mater. Des. 196 (2020) 109183, https://doi.org/10.1016/j.matdes.2020.109183.
[27] N. Birbilis, R.G. Buchheit, Electrochemical characteristics of intermetallic phases in aluminum alloys: an experimental survey and discussion, J. Electrochem. Soc. 152 (2005), https://doi.org/10.1149/1.1869984.
[28] S.K. Kairy, S. Turk, N. Birbilis, A. Shekhter, The role of microstructure and microchemistry on intergranular corrosion of aluminium alloy AA7085-T7452, Corros. Sci. 143 (2018) 414–427, https://doi.org/10.1016/j.corsci.2018.08.033.
[29] S.P. Knight, K. Pohl, N.J.H. Holroyd, N. Birbilis, P.A. Rometsch, B.C. Muddle, R. Goswami, S.P. Lynch, Some effects of alloy composition on stress corrosion cracking in Al-Zn-Mg-Cu alloys, Corros. Sci. 98 (2015) 50–62, https://doi.org/10.1016/j.corsci.2015.05.016.
[30] X. Zhang, Y. Lv, S. Tan, Z. Dong, X. Zhou, Microstructure and corrosion behaviour of wire arc additive manufactured AA2024 alloy thin wall structure, Corros. Sci. 186 (2021) 109453, https://doi.org/10.1016/j.corsci.2021.109453.
[31] A.P. Babu, A. Huang, N. Birbilis, On the heat treatment and mechanical properties of a high solute Al – Zn – Mg alloy processed through laser powder bed fusion process, Mater. Sci. Eng. A. 807 (2021) 140857, https://doi.org/10.1016/j.msea.2021.140857.
[32] S. Gorsse, C. Hutchinson, M. Gouné, R. Banerjee, Additive manufacturing of metals: a brief review of the characteristic microstructures and properties of steels, Ti-6Al-4V and high-entropy alloys, Sci. Technol. Adv. Mater. 18 (2017) 584–610, https://doi.org/10.1080/14686996.2017.1361305.
[33] L.F. Lucio, F. Mondolfo, Al-Mg-Zn Alloys – A Review of the Literature, Res. Dev. Center, Reverse Copp. Brass Inc., 1967.
[34] N. Birbilis, M.K. Cavanaugh, R.G. Buchheit, Electrochemical behavior and localized corrosion associated with Al7Cu2Fe particles in aluminum alloy 7075-T651, Corros. Sci. 48 (2006) 4202–4215, https://doi.org/10.1016/J.CORSCI.2006.02.007.
[35] M. Esmaily, Z. Zeng, A.N. Mortazavi, A. Gullino, S. Choudhary, T. Derra, F. Benn, F. D'Elia, M. Müther, S. Thomas, A. Huang, A. Allanore, A. Kopp, N. Birbilis, A detailed microstructural and corrosion analysis of magnesium alloy WE43 manufactured by selective laser melting, Addit. Manuf. 35 (2020) 1–34, https://doi.org/10.1016/j.addma.2020.101321.

[36] M. Keddam, C. Kuntz, H. Takenouti, D. Schuster, D. Zuili, Exfoliation corrosion of aluminium alloys examined by electrode impedance, Electrochim. Acta 42 (1997) 87–97, https://doi.org/10.1016/0013-4686(96)00170-3.
[37] J. Huang, Diffusion impedance of electroactive materials, electrolytic solutions and porous electrodes: warburg impedance and beyond, Electrochim. Acta 281 (2018) 170–188, https://doi.org/10.1016/j.electacta.2018.05.136.
[38] V.S. Muralidharan, Warburg impedance - basics revisited, Anti-Corrosion Methods Mater. 44 (1997) 26–29, https://doi.org/10.1108/00035599710157387.
[39] J.R. Davies, Corrosion of Aluminum and Aluminum Alloys, 1999, https://doi.org/10.1361/caaa1999p025.
[40] N. Birbilis, R.G. Buchheit, Investigation and discussion of characteristics for intermetallic phases common to aluminum alloys as a function of solution pH, J. Electrochem. Soc. 155 (2008) C117, https://doi.org/10.1149/1.2829897.
[41] F.P. Fehlner, M.J. Graham, Thin oxide film formation on metals. Corros. Mech. Theory Pract., third ed., 2011, pp. 217–234, https://doi.org/10.1201/b11020-5.
[42] C.M. Abreu, M.J. Cristóbal, R. Figueroa, G. Pena, M.C. Pérez, An XPS study on the influence of nitrogen implantation on the passive layers developed on different tempers of AA7075 aluminum alloy, Surf. Interface Anal. 42 (2010) 592–596, https://doi.org/10.1002/sia.3498.
[43] J.O.M. Bockris, Y. Kang, The protectivity of aluminum and its alloys with transition metals, J. Solid State Electrochem. 1 (1997) 17–35, https://doi.org/10.1007/s100080050019.
[44] S.K. Kairy, P.A. Rometsch, C.H.J. Davies, N. Birbilis, On the electrochemical and quasi in situ corrosion response of the Q-phase (AlxCuyMgzSiw) intermetallic particle in 6xxx series aluminum alloys, Corrosion 73 (2017) 87–99, https://doi.org/10.5006/2249.

7

Effect of second phase particles on mechanical properties of a high solute Al-Zn-Mg alloy

7.1 Chapter synopsis

This chapter evaluates the second phase particles formed during heat treatment of Al-14Zn-3Mg and it is a research paper with the title, "Influence of second phase particles on the mechanical properties of a high solute Al-Zn-Mg alloy fabricated through laser powder bed fusion", and will be submitted to the Intermetallics journal.

From previous works, the loss of mechanical properties during direct heat treatment of the as-LPBF high solute Al-14Zn-3Mg (in wt. %) was unclear. In contrast, Al-alloys in the Al-Sc-Mg and Al-Sc-Mn benefitted from a one-step heat treatment where the solute supersaturation through LPBF was adequate to promote direct precipitation (absence of solutionising) of strengthening second phase particles. However, in Al-14Zn-3Mg, direct ageing resulted in the loss of mechanical properties. Therefore, this work aims to understand the phase transformation that occurs in high solute Al-14Zn-3Mg at different temperatures through *in-situ* TEM and *in-situ* XRD characterisation. It is noted that the temperatures existing in the thin TEM specimen may not directly correlate to the bulk heat treatment, however, the phase changes are necessary to understand the variation in mechanical properties. *In-situ* TEM revealed the dissolution of the quasicrystalline P-phase and the formation of T-phase ($Mg_{32}(Zn, Al)_{49}$) between 300°C and 400°C, respectively. The correlation between the mechanical properties and formation of different second phase particles at different temperatures were rationalised based on CALPHAD modelling of volume fraction, interprecipitate spacing and mean radius of the second phase particles.

7.2 Abstract

A high solute 7xxx series aluminium alloy, Al-14Zn-3Mg (in wt. %), was prepared using laser powder bed fusion (LPBF). To provide an insight into the correlation of second phase particles and mechanical properties, several heat treatment conditions were modelled with CALPHAD, and phase transformations were realised through in-situ characterisation techniques. It was revealed that the formation of T-phase ($Mg_{32}(Zn, Al)_{49}$) at 400°C contributed to loss of ductility from the direct heat treatment of as-LPBF Al-14Zn-3Mg. However, the improvement in hardness of solutionised and peak aged Al-14Zn-3Mg was attributed to the formation of high volume fraction of η' and η ($MgZn_2$) precipitates with low inter-precipitate spacing.

7.3 Introduction

The 7xxx series (Al-Zn-Mg) aluminium (Al) alloy system achieves strengthening that is developed via careful heat treatments resulting in η' and η ($MgZn_2$) precipitates [1–4]. Typically, optimising the formation (i.e. number density of volume fraction) of such precipitates has been associated with achieving enhanced mechanical properties [5–7]. Demonstrations of achieving optimised precipitation in Al-alloys have been attained by exploring solute supersaturation, by rapid solidification techniques such as Osprey spray forming process and other powder metallurgical routes [8–10]. More recently, laser powder bed fusion (LPBF), a form of additive manufacturing, has been shown to be capable of producing Al-alloys with solute supersaturation by exploiting metallurgical solubility limits by the non-equilibrium nature of the LPBF process itself [11–13].

The fabrication of Al-Mn-Sc alloys (Scalmalloy®) by LPBF was benefitted by permitting a higher level of alloyed Sc through solute supersaturation - where only a single step post heat

treatment was required for strengthening [14–16]. The direct heat treatment of as-LPBF Al-Mn-Sc alloys to 300°C /5h resulted in the formation of Al_3Sc precipitates, resulting in enhanced strength without requiring solutionising heat treatment [14]. However, the cost of Sc restricts industrial usage. In the pursuit of cost effective high strength alloys, a novel high solute Al-Zn-Mg alloy with 14 wt. % Zn and 3 wt. % Mg was fabricated through LPBF in our previous works. The second phase in as-LPBF Al-14Zn-3Mg comprised of an icosahedral quasicrystalline P-phase [17]. In contrast to Al-Sc-Mn alloys, direct heat treatment of as-LPBF Al-14Zn-3Mg resulted in loss of ductility, demanding the need for solutionising heat treatment. Heat treatment of Al-14Zn-3Mg resulted in the dissolution of P-phase during solutionising and artificial ageing was accompanied by a high area fraction (> 50%) of η and η' ($MgZn_2$) precipitates, which further altered the mechanical properties [18].

The influence of second phase particles on the mechanical properties of high solute Al-14Zn-3Mg was not comprehended owing to the complexity of microstructural formation. Herein, *in-situ* transmission electron microscopy and *in-situ* XRD studies were performed with the aid of CALPHAD simulations to understand the influence of second phase particles in altering the mechanical properties of high solute aluminium alloys.

7.4 Materials and methods

The as-received powders with composition, Al-14.7Zn-3.34Mg-0.28Fe-0.06Cu-0.09Si (in wt. %) was obtained from TLS Technik GmbH. The as-received powders were passed through a 63 μm sieve where the powder size distribution was maintained between 16 – 63 μm.

A Concept laser Mlab Cusing-R with the following parameters were used to fabricate all the samples: hatch spacing of 0.07 mm, layer thickness of 25 μm, laser spot size of 50 μm, laser power of 95W, scanning speed of 150 mm/s was used to fabricate all the samples used in this

study. 10 mm cubes were sectioned perpendicular to the build direction and were used for heat treatment studies. The heat treatment of the as-LPBF samples were performed by solutionising at 500°C for 4 h, quenched in water and aged at 150°C for 2 h which was indicated as the peak aged condition.

Transmission electron microscopy was performed using an FEI® Tecnai G^2 T20 and FEI® Tecnai G^2 F20 operating at 200 kV for *in-situ* studies and imaging microstructural features, respectively. A Gatan® model 652 Tantalum cup heating stage equipped with alpha/beta tilting was used with a Gatan® model 1905 Temperature Controller. The specimen preparation for TEM involved punching of 3 mm discs from thin slices of LPBF prepared Al-14Zn-3Mg samples which were then mechanically thinned to ~50 μm using a Gatan® 691 Precision Ion Polishing System (PIPS) that operated at –100°C. The samples were plasma cleaned using a Gatan® Solarus 950 advanced plasma system for ~5 minutes with an argon and oxygen gas mixture prior to TEM analysis.

In situ XRD experiments were performed using a Bruker® D8 Advance diffractometer with a Bruker® LynxEye XE position sensitive detector. The Cu tube was operated at 40 kV and 40 mA. A Bruker® MTC wide range temperature chamber was used for temperature and vacuum environment control. Heating rate of 5°C/min was used to heat the sample up to 400°C and XRD data was collected from 5° to 105° with a step size of 0.05°. Quantitative phase analysis was done through TOPAS® academic v7 Rietveld refinement software, with careful estimation of environmental chamber contribution to the XRD pattern, and correcting the apparent preferred orientation of matrix Al phase using March-Dollase model.

CALPHAD simulations were performed using the Thermocalc® 2020b software with TCAL4 and MOBAL4 databases. The kinetic and strength simulations utilised the Morral-Purdy and Zander model (Zander pre-factor, $K_p = 6.2 \times 10^{-6}$), respectively.

7.5 Results and discussion

7.5.1. Mechanical property evaluation of Al-14Zn-3Mg in as-LPBF and at different heat treatment condition

The hardness, yield strength and elongation of Al-14Zn-3Mg in as-LPBF and in different heat treatment conditions are shown in Figure 1. It was revealed that the as-LPBF Al-14Zn-3Mg failed prematurely with 0% elongation which can be due to the presence of a brittle icosahedral quasicrystalline P-phase [17]. In addition, direct heat treatment of as-LPBF Al-14Zn-3Mg to 100°C / 4h and 200°C / 4h resulted in a slight increase in elongation accompanied by the decrease in strength. This can be due to the loss of dislocations and rapidly solidified structures at elevated temperatures that results in improved elongation when compared to the as-LPBF Al-14Zn-3Mg. Herein, it was noticed that the maximum softening of Al-14Zn-3Mg occurs at 300°C / 4h where the elongation reached ~10%. However, at 400°C / 4h, the elongation decreases significantly to ~2% and further increased to ~9.5% when solutionising at 500°C / 4h. Following solutionising, the peak aged Al-14Zn-3Mg microstructure was populated with a high number density of η, η' – $MgZn_2$ precipitates and shows the highest hardness of 220 HV_1 (350 MPa). The area fraction of precipitates was reported to be > 50% due to the excess addition of solute, and the detailed characterisation of Al-14Zn-3Mg in all the heat treated conditions is explained in our previous work [18].

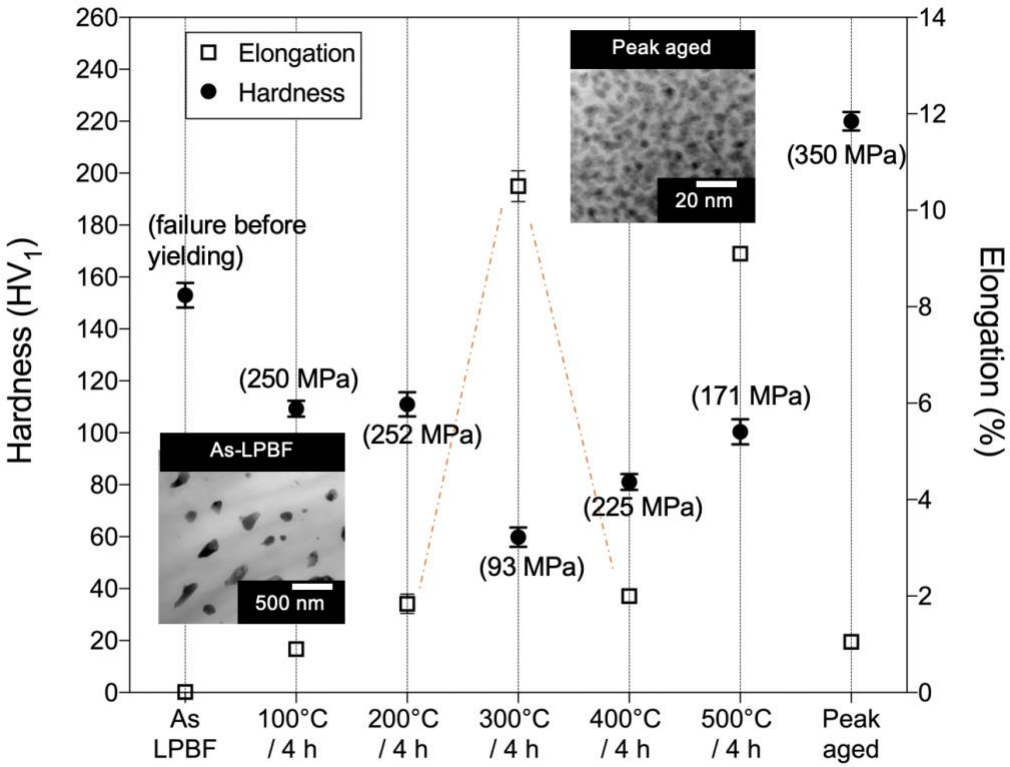

Figure 1: (a) Hardness and elongation variation from as-LPBF Al-14Zn-3Mg to different heat treatment conditions with BF-STEM micrographs of as-LPBF and peak aged Al-14Zn-3Mg.

7.5.2. In-situ TEM characterisation and CALPHAD modelling of the different phases formed during the heating of as-LPBF Al-14Zn-3Mg

To understand the sharp fall in elongation when heat treating to 400°C / 4h, *in-situ* TEM micrographs were acquired with the heating rate, holding time and temperature cycle, as shown in Figure 2a. The volume fraction of second phase particles formed under equilibrium conditions are modelled using CALPHAD as shown in Figure 2b. The respective TEM micrographs obtained with the conditions as shown in Figure 2a are presented in Figure 3(a-j).

From CALPHAD simulations, it can be noticed that the T-phase $Mg_{32}(Zn, Al)_{49}$ can form between 350°C - 450°C and are known to form via a degraded peritectic reaction [19].

However, it should also be noted that phase transformation might occur at different temperatures in the thin specimen used for TEM and may not exactly represent bulk behaviour.

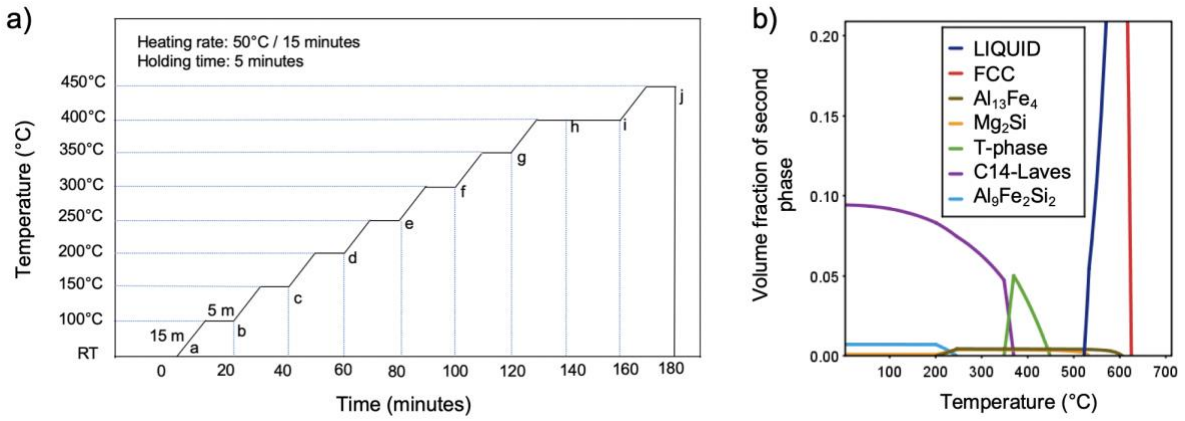

Figure 2: (a) Different temperatures and holding times followed during in-situ TEM with the alphabets (a-j) corresponding to the in-situ TEM micrographs acquired at the respective conditions, (b) CALPHAD simulation showing the formation of T-phase between 350°C and 450°C.

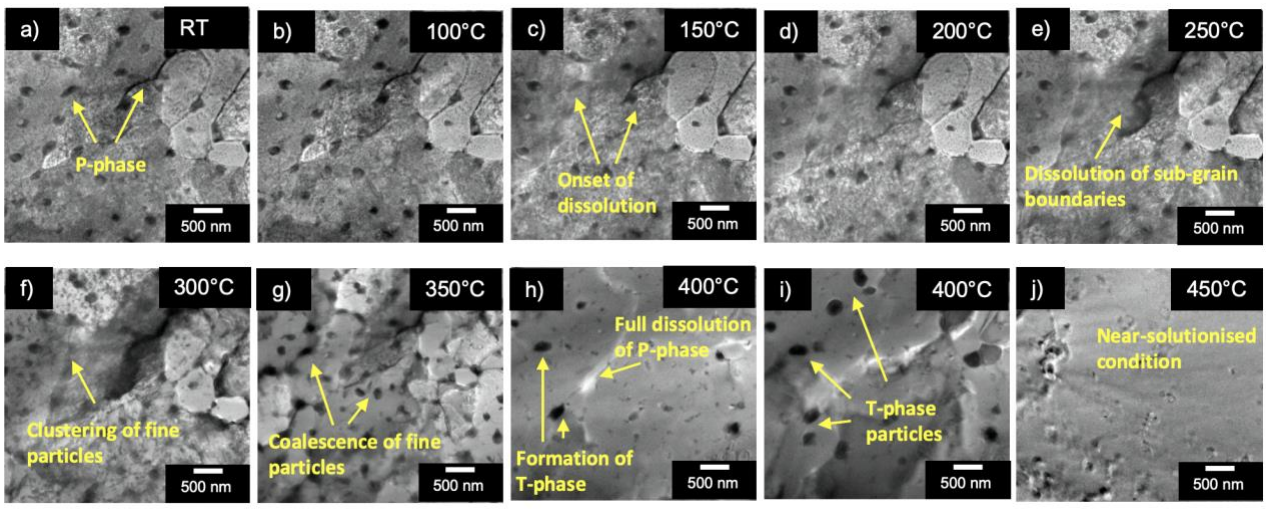

Figure 3 (a-j): In-situ TEM micrographs obtained at different temperatures and holding times denoting the solubility of the icosahedral P-phase and formation of T-phase.

From Figure 3a-3e, it can be seen that the quasicrystalline P-phase was stable at 100°C. However, at 150°C the onset of dissolution was noticed, As the temperature increased, the

microstructure revealed the dissolution of sub-grain boundaries up to 250°C. Furthermore, the increase in temperature to 300-350°C resulted in the clustering and coalescence of fine P-phase particles followed by complete dissolution. The dissolution of P-phase at these temperature intervals (300-400°C) might have resulted in maximum softening of Al-14Zn-3Mg as suggested from Figure 1. At 400°C, the P-phase has completely dissolved and the presence of new particles are evidenced which might have contributed to the reduction in elongation. These particles further coarsen at longer holding times (Figure 3i) and are suggested to be the T-phase particles from CALPHAD modelling of volume fraction of second phase formed in Al-14Zn-3Mg as shown in Figure 2b. The model also suggests that T-phase particles possess rapid kinetics where they completely dissolve at 450°C. This behaviour can be evidenced in the TEM micrograph shown in Figure 2j, which confirms that the formation of T-phase was restricted to a short temperature interval.

7.5.3. In-situ XRD characterisation and CALPHAD modelling of T-phase formed when heat treating as-LPBF Al-14Zn-3Mg to 400°C

To confirm the formation of T-phase in high solute Al-14Zn-3Mg, in-situ XRD was performed at 400°C with the corresponding peaks as shown in Figure 4a. The respective CALPHAD modelling that highlights the mean radius and volume fraction of T-phase particles formed at different temperature are highlighted in Figure 4b.

The in-situ XRD results from Figure 4a confirm the formation of T-phase particles at 400°C and the Rietveld analysis of the peaks indicate that the volume fraction of T-phase particles formed at 400°C was 4.55% with minor quantities of Al-Cu phase particles. This finding was in agreement with the CALPHAD modelling (Figure 4b) which denotes that the volume

fraction of T-phase particles at 400°C was ~ 4.9%. In addition, the model also predicts that the mean radius T-phase particles at 400°C was ~ 75 nm.

T-phase particles are reported to form in high Zn and Mg containing Al-alloys in the Al-Zn-Mg system and possess a cubic structure with lattice parameter value of 14.16 Å [20,21]. Typically, the formation of T-phase particles are utilised for the hardening characteristics in designing novel high strength Al-Zn-Mg alloys [20,22–24]. However, in the current high solute Al-14Zn-3Mg, the formation of T-phase at 400°C does not yield satisfactory mechanical properties and hence necessitates the need for solutionising heat treatment, unlike other Al-Mn-Sc alloys which can be strengthened through direct ageing.

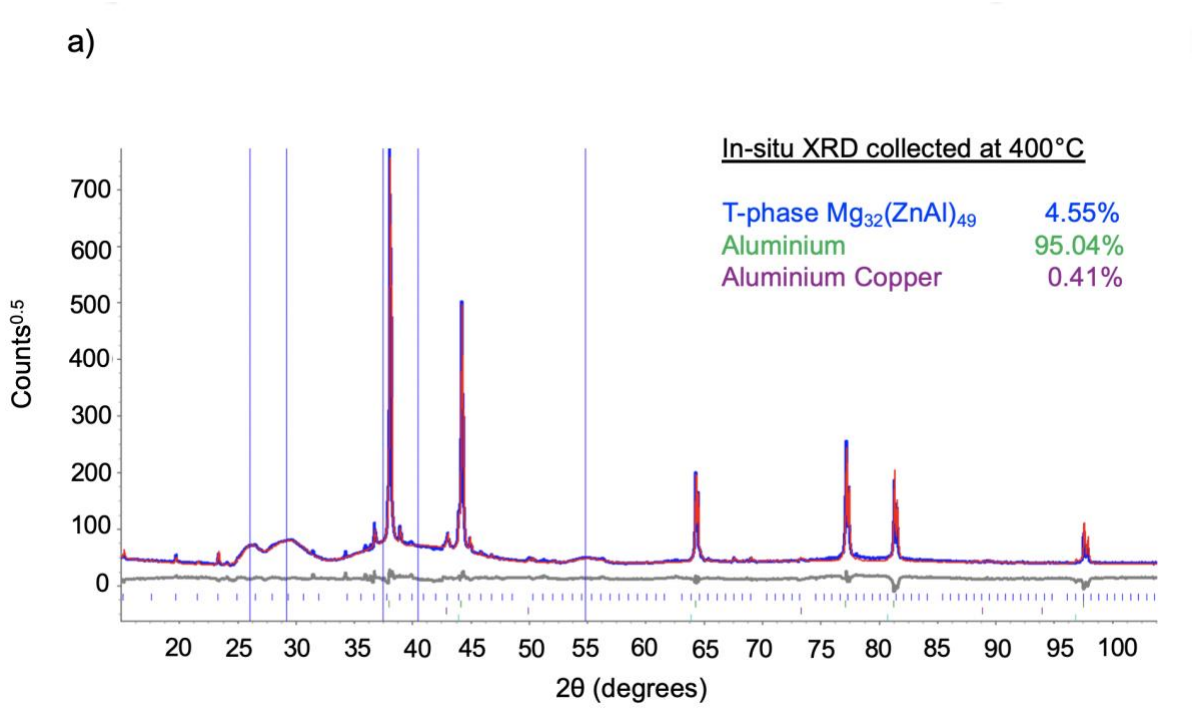

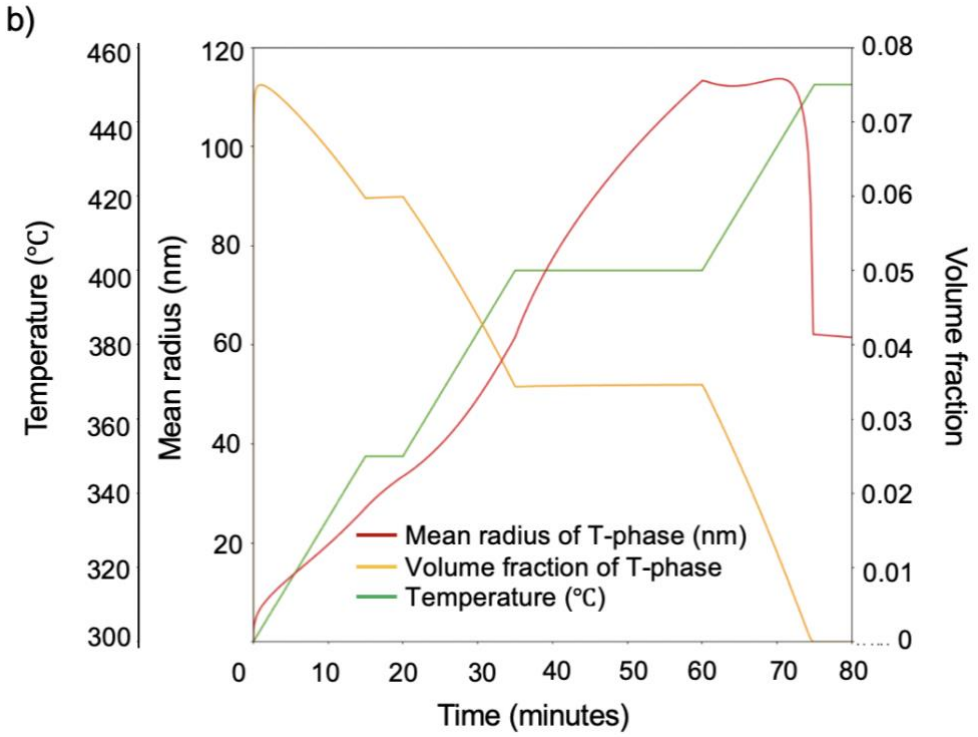

Figure 4: Quantification of T-phase formed at 400°C through (a) in-situ XRD and (b) CALPHAD modelling showing the volume fraction and mean radius of the T-phase

7.5.4. CALPHAD modelling of second phase particles formed after solutionising heat treatment at 500°C and precipitation heat treatment at 150°C

It is widely accepted that the alloys in the Al-Zn-Mg system are strengthened via the formation of hardening η, η'-$MgZn_2$ precipitates through precipitation hardening with the following transformation scheme, namely, solid solution(α) → GP-zones → η'→ η-$MgZn_2$ [25–27]. In the case of LPBF prepared Al-14Zn-3Mg, the precipitation heat treatment at 150°C following solutionising resulted in the rapid precipitation of η, η'-$MgZn_2$. The hardness, yield strength and elongation of the peak aged Al-14Zn-3Mg was 220 HV_1, 350MPa and 1%, respectively. The reduced elongation can be attributed to excess solute (herein, Zn and Mg) resulting in the formation of high area fraction of second phase particles (> 50%) [18]. To comprehend this

behaviour with respect to wrought Al-alloys, the ageing curve of the experimental and calculated values of Al-14Zn-3Mg, AA7075-T6 [11] and AA7046-T6 [12] are shown in Figure 5a. Their respective mean radius and the volume fraction of precipitates calculated through the precipitation module in Thermocalc® are shown in Figure 5b. The experimental and calculated hardness values rationally correspond and it was interesting to note that the calculated interprecipitate spacing in the peak aged condition of Al-14Zn-3Mg was only 2.7 nm when compared to AA7075-T6 and AA7046-T6 which have interprecipitate spacings of 9 nm and 5.4 nm, respectively. The experimental interprecipitate spacing of Al-14Zn-3Mg are reported to be ~3.5 nm [18]. In addition, the volume fraction of precipitates in peak aged Al-14Zn-3Mg were twice higher than the volume fraction of precipitates in peak aged AA7075-T6 and AA7046-T6. The kinetics of precipitation to attain the peak aged conditions to form precipitates with similar mean radius in Al-14Zn-3Mg, AA7075-T6 and AA7046-T6 were 2h, 3h and 17h, respectively. Although the nature of processing of Al-14Zn-3Mg, AA7075-T6 and AA7046-T6 was different, it is essential to understand the extent of second phase formation in high solute Al-Zn-Mg alloys processed through LPBF, with other wrought Al-alloys as a benchmark. In addition, evidences of high volume fraction and smaller interprecipitate distance compliments the previous findings [18] where too much solute might result in the deterioration of mechanical properties.

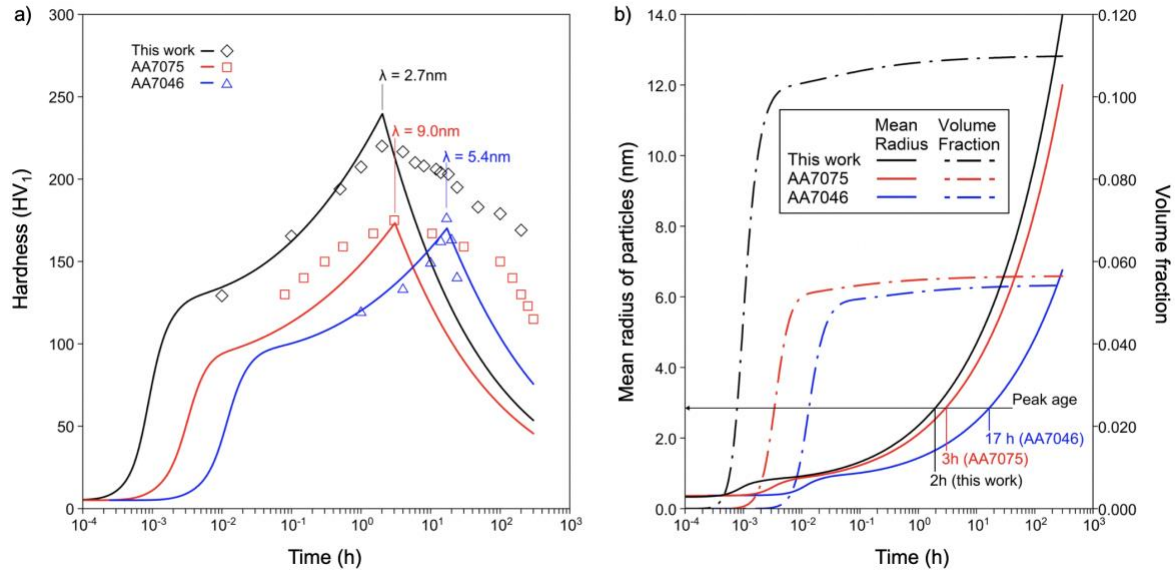

Figure 5: Comparison of Al-14Zn-3Mg with AA7075 and AA7046 denoting the (a) agreement of experimental and modelled values of the peak hardness and interprecipitate spacing of precipitates, (b) Volume fraction and mean radius of second phase particles

7.6 Conclusion

The combined studies of CALPHAD and in-situ characterisation have revealed the behaviour of second phase particles in a solute supersaturated Al-Zn-Mg alloy fabricated through LPBF. Herein, the following conclusion can be drawn:

1) From the in-situ TEM observations on Al-14Zn-3Mg at 400°C, the formation of T-phase, $Mg_{32}(Zn, Al)_{49}$ and dissolution of P-phase was observed. In-situ XRD further confirms the volume fraction of T-phase at 400°C as 4.55%. The formation of T-phase was suggested to contribute to the loss of ductility during direct heat treatment to 400°C.

2) The peak aged Al-14Zn-3Mg has low inter-precipitate spacing (2.7 nm) and high volume fraction of precipitates (0.11) when compared to AA7075-T6 and AA7046-T6 in peak aged condition – which was due to the presence of excess solute.

The LPBF process opens the possibility of hyper-loading solute, resulting in the design and fabrication new alloys with unique alloying. This study demonstrates the insights and

possibilities for fabrication of high strength and high solute aluminium alloys through additive manufacturing where solute supersaturation plays a major role. In addition, this study also provides significant insights in highlighting the importance of CALPHAD modelling in exploration of previously unexplored Al-alloy compositions and their potential heat treatment pathways through LPBF processing.

References

[1] L.F. (Lucio F.. Mondolfo, Aluminum alloys : structure and properties, Butterworths, 1976.

[2] I.J. Polmear, Solute partitioning to enhance mechanical properties of aged aluminium alloys, Woodhead Publishing Limited, 2010. https://doi.org/10.1533/9780857090256.2.367.

[3] J. R. Davies, Corrosion of aluminum and aluminum alloys, 1999. https://doi.org/10.1361/caaa1999p025.

[4] M. Dumont, W. Lefebvre, B. Doisneau-Cottignies, A. Deschamps, Characterisation of the composition and volume fraction of η′ and η precipitates in an Al-Zn-Mg alloy by a combination of atom probe, small-angle X-ray scattering and transmission electron microscopy, Acta Mater. 53 (2005) 2881–2892. https://doi.org/10.1016/j.actamat.2005.03.004.

[5] A. Deschamps, Y. Brechet, Influence of predeformation and ageing of an Al-Zn-Mg Alloy-II. Modeling of precipitation kinetics and yield stress, Acta Mater. 47 (1998) 293–305. https://doi.org/10.1016/S1359-6454(98)00296-1.

[6] G.P.M. Leyson, L.G. Hector, W.A. Curtin, Solute strengthening from first principles and application to aluminum alloys, Acta Mater. 60 (2012) 3873–3884. https://doi.org/10.1016/j.actamat.2012.03.037.

[7] J. Wang, Physical Metallurgy of Aluminum Alloys, Alum. Sci. Technol. 2 (2018) 44–79. https://doi.org/10.31399/asm.hb.v02a.a0006503.

[8] M.M. Sharma, M.F. Amateau, T.J. Eden, Mesoscopic structure control of spray formed high strength Al-Zn-Mg-Cu alloys, Acta Mater. 53 (2005) 2919–2924. https://doi.org/10.1016/j.actamat.2005.03.007.

[9] Y. Chen, C.Y. Liu, B. Zhang, F.C. Qin, Y.F. Hou, Precipitation behavior and mechanical properties of Al–Zn–Mg alloy with high Zn concentration, J. Alloys Compd. 825 (2020) 154005. https://doi.org/10.1016/j.jallcom.2020.154005.

[10] H. Yu, M. Wang, Y. Jia, Z. Xiao, C. Chen, Q. Lei, Z. Li, W. Chen, H. Zhang, Y. Wang, C. Cai, High strength and large ductility in spray-deposited Al-Zn-Mg-Cu alloys, J. Alloys Compd. 601 (2014) 120–125. https://doi.org/10.1016/j.jallcom.2014.02.126.

[11] A.B. Spierings, K. Dawson, P. Dumitraschkewitz, S. Pogatscher, K. Wegener, Microstructure characterization of SLM-processed Al-Mg-Sc-Zr alloy in the heat treated and HIPed condition, Addit. Manuf. 20 (2018) 173–181. https://doi.org/10.1016/j.addma.2017.12.011.

[12] Q. Jia, F. Zhang, P. Rometsch, J. Li, J. Mata, M. Weyland, L. Bourgeois, M. Sui, X. Wu, Precipitation kinetics, microstructure evolution and mechanical behavior of a developed Al-Mn-Sc alloy fabricated by selective laser melting, Acta Mater. 193 (2020) 239–251. https://doi.org/10.1016/j.actamat.2020.04.015.

[13] J. Bi, Z. Lei, Y. Chen, X. Chen, Z. Tian, N. Lu, X. Qin, J. Liang, Microstructure, tensile properties and thermal stability of AlMgSiScZr alloy printed by laser powder bed fusion, J. Mater. Sci. Technol. 69 (2021) 200–211. https://doi.org/10.1016/j.jmst.2020.08.033.

[14] Q. Jia, P. Rometsch, S. Cao, K. Zhang, X. Wu, Towards a high strength aluminium alloy development methodology for selective laser melting, Mater. Des. 174 (2019). https://doi.org/10.1016/j.matdes.2019.107775.

[15] Q. Jia, P. Rometsch, P. Kürnsteiner, Q. Chao, A. Huang, M. Weyland, L. Bourgeois, X. Wu, Selective laser melting of a high strength Al[sbnd]Mn[sbnd]Sc alloy: Alloy design and strengthening mechanisms, Acta Mater. 171 (2019) 108–118. https://doi.org/10.1016/j.actamat.2019.04.014.

[16] P. Rometsch, Q. Jia, K. V. Yang, X. Wu, Aluminum alloys for selective laser melting - towards improved performance, Elsevier Inc., 2019. https://doi.org/10.1016/B978-0-12-814062-8.00016-9.

[17] A.P. Babu, S.K. Kairy, A. Huang, N. Birbilis, Laser powder bed fusion of high solute Al-Zn-Mg alloys: Processing, characterisation and properties, Mater. Des. 196 (2020). https://doi.org/10.1016/j.matdes.2020.109183.

[18] A.P. Babu, A. Huang, N. Birbilis, On the heat treatment and mechanical properties of a high solute Al–Zn–Mg alloy processed through laser powder bed fusion process, Mater. Sci. Eng. A. 807 (2021). https://doi.org/10.1016/j.msea.2021.140857.

[19] M. Feuerbacher, C. Thomas, S. Roitsch, Single-crystal growth of the complex metallic alloy phase Mg32(Al,Zn)49, Intermetallics. 16 (2008) 943–947. https://doi.org/10.1016/j.intermet.2008.04.012.

[20] N. Takata, M. Ishihara, A. Suzuki, M. Kobashi, Microstructure and strength of a novel heat-resistant aluminum alloy strengthened by T-Al6Mg11Zn11 phase at elevated temperatures, Mater. Sci. Eng. A. 739 (2019) 62–70. https://doi.org/10.1016/j.msea.2018.10.034.

[21] N. Takata, T. Okano, M. Aikawa, A. Suzuki, M. Kobashi, K. Hagihara, Morphology and mechanical properties of the T-Al6Mg11Zn11 phase in the eutectic microstructure of Al–Zn–Mg ternary alloys, Intermetallics. 124 (2020) 106881. https://doi.org/10.1016/j.intermet.2020.106881.

[22] D. Zhang, X. Wang, Y. Pan, S. Hou, J. Zhang, L. Zhuang, L. Zhou, Friction stir welding of novel T-phase strengthened Zn-modified Al–Mg alloy, J. Mater. Sci. 56 (2021) 5283–5295. https://doi.org/10.1007/s10853-020-05609-z.

[23] X.B. Yang, J.H. Chen, J.Z. Liu, F. Qin, J. Xie, C.L. Wu, A high-strength AlZnMg alloy hardened by the T-phase precipitates, J. Alloys Compd. 610 (2014) 69–73. https://doi.org/10.1016/j.jallcom.2014.04.185.

[24] Y. Deng, Z. Yin, F. Cong, Intermetallic phase evolution of 7050 aluminum alloy during homogenization, Intermetallics. 26 (2012) 114–121. https://doi.org/10.1016/j.intermet.2012.03.006.

[25] L.F. (Lucio F.. Mondolfo, Al-Mg-Zn alloys - A review of the literature, Res. Dev. Center, Reverse Copp. Brass Inc.,. (1967).

[26] J. Gjønnes, C.J. Simensen, An electron microscope investigation of the microstructure in an aluminium-zinc-magnesium alloy, Acta Metall. 18 (1970) 881–890. https://doi.org/10.1016/0001-6160(70)90016-7.

[27] L.K. Berg, J. Gjoønnes, V. Hansen, X.Z. Li, M. Knutson-Wedel, G. Waterloo, D. Schryvers, L.R. Wallenberg, GP-zones in Al-Zn-Mg alloys and their role in artificial aging, Acta Mater. 49 (2001) 3443–3451. https://doi.org/10.1016/S1359-6454(01)00251-8.

8

Summary and Future work

8.1 Summary

The survey of available literature regarding additive manufacturing of Al-alloys revealed that laser powder bed fusion (LPBF) of alloys in the Al-Zn-Mg system were prone to hot cracking and excessive porosity. In addition, fabrication of the existing (conventional) wrought Al-alloy compositions through LPBF was ineffective; demanded the addition of grain refiners such as Sc or Zr. However, new alloys that were specifically tailored for LPBF, such as alloys in the Al-Sc-Mg and Al-Sc-Mn system, resulted in improved mechanical properties from unique microstructures. Therefore, the present research work was aimed in the design, fabrication and characterisation of new, high solute Al-alloys, in the Al-Zn-Mg system prepared through LPBF. Herein, the summary of the key findings during the fabrication, heat treatment, microstructural evaluation and corrosion behaviour assessment of the alloys are discussed below:

8.1.1 LPBF processing of the chosen Al-Zn-Mg alloy compositions

- Novel alloys in the Al-Zn-Mg system with compositions Al-10Zn-2Mg, Al-14Zn-3Mg and Al-18Zn-4Mg (wt. %) were successfully fabricated through the LPBF process with no cracking and acceptably low porosity, without the addition of non-commodity elements such as Sc or Zr. Specifically, Al-10Zn-2Mg and Al-14Zn-3Mg were fabricated with no cracking and with a porosity of 0.47% and 0.38%, respectively. However, Al-18Zn-4Mg showed potential signs of cracking which was due to the localised vaporisation of Zn and Mg.
- Microstructural characterisation revealed the presence of a unique microstructure with cell-like structures and several second-phase particles that co-exist in the Al-matrix.

- A new icosahedral quasicrystalline phase, herein termed as the P-phase, was identified to form in Al-14Zn-3Mg in the as-LPBF condition. Such findings reveal the unique characteristics of LPBF processing and the benefits of new alloy design.
- The hardness of the high solute Al-Zn-Mg alloys was within the range of 120 – 160 HV_1, depending on the solute content, and were determined to be higher in hardness than LPBF prepared AA7075 (108 HV_1). The increase in hardness was attributed to the excess solute and elimination of defects arising from fabrication.

8.1.2 Heat treatment of the chosen high solute Al-Zn-Mg alloy and evaluation of mechanical properties

- High solute Al-14Zn-3Mg was selected for further characterisation due to the existence of low porosity (0.38%). The presence of a unique and rapidly solidified microstructure that was decorated with P-phase particles resulted in limited ductility in the as-LPBF condition, however, direct heat treatment of Al-14Zn-3Mg resulted in an improvement in mechanical properties.
- Notwithstanding the mechanical properties obtained through direct heat treatment, solutionising heat treatment was performed at 500°C for 4 hours, which resulted in the effective dissolution of P-phase.
- Following solutionising, it was revealed that the high solute Al-14Zn-3Mg had a massive affinity to age harden at room temperature where precipitates of 8.6 nm were formed after 24 hours of natural ageing. In addition, it was noted that a previously unreported high area fraction of second phase particles (>50%) were present in Al-14Zn-3Mg in the artificial aged conditions (500°C for 4 hours followed by 150°C for 2 hours and 24 hours, respectively).

- The second phase particles in the artificial aged condition (500°C for 4 hours followed by 150°C for 24 hours) were confirmed as the strengthening η′ precipitates, with sizes varying between ~4 and 8 nm, and demonstrated mechanical properties with yield strength of 407 MPa, UTS of 447 MPa - albeit with an elongation of only 1.9%.
- Critical solute limits in designing high solute Al-alloys were revealed with a loss in mechanical properties such as strength and ductility when the area fraction of second phase particles increased beyond 50%.

8.1.3 Evaluation of corrosion behaviour of high solute Al-Zn-Mg alloy:

- Electrochemical characterisation of the as-LPBF Al-14Zn-3Mg revealed that quasicrystalline P-phase was 'cathodic' to the α-Al matrix. In addition, the annihilation of coarse Fe and Cu rich constituent particles in LPBF prepared Al-14Zn-3Mg resulted in lower corrosion rates when compared to AA7075-T6.
- The polarisation resistance calculated through electrochemical impedance spectroscopy (EIS) of Al-14Zn-3Mg in as-LPBF, naturally aged and artificial aged condition was ~ 22,000 $\Omega.cm^2$, 7800 $\Omega.cm^2$ and 11,000 $\Omega.cm^2$, respectively. Herein, the polarisation resistance of LPBF prepared Al-14Zn-3Mg were superior to the polarisation resistance of a wrought high strength Al-alloy (AA7075-T6).
- The corrosion pits upon Al-14Zn-3Mg in the as-LPBF condition were considerably smaller than those of the naturally aged and artificially aged conditions, which was associated wit finer feature sizes of second-phases in LPBF prepared Al-Zn-Mg alloys (compared to conventional wrought Al-alloys) and the absence of constituent-type particles. Also, the average pit size for as-LPBF Al-14Zn-3Mg was ~375 nm whereas the AA7075-T6 used as a benchmark, contained average pit sizes of ~1.15 μm
- In addition to the supersaturation of solute and the annihilation of coarse constituent, the surface oxide upon as-LPBF Al-14Zn-3Mg revealed the presence of a thicker oxide

film with a surface film thickness of ~1100 nm which may contribute to an improved corrosion resistance when assessed relative to AA7075-T6 which had a surface film thickness on only ~430 nm.

8.1.4 *In-situ* characterisation of second phase particles to understand their effect in mechanical properties:

- *In-situ* TEM characterisation of the evolution of second phase particles under increased temperature revealed the dissolution temperature of the quasicrystalline P-phase which was ranging between 350°C and 400°C.
- The formation of T-phase ($Mg_{32}(Zn, Al)_{49}$) was evidenced at ~400°C which was attributed as one of the factors for the loss of ductility during direct heat treatment of Al-14Zn-3Mg.
- The excess volume fraction of second phase particles in solute rich Al-Zn-Mg was modelled using CALPHAD where improved hardness and low interprecipitate spacing were reported when assessed with other high strength wrought Al-alloys.

8.2 Future work

The research herein revealed a critical understanding of the role of second phase particles in strengthening and the capability of solute hyperloading in Al-Zn-Mg alloys through additive manufacturing. This study serves as a benchmark for exploration of new Al-alloys without the formation of hot cracking through design-directed alloying. It also reveals the notion of critical solute limits which are essential for designing new Al-alloys through laser-based AM, where solute supersaturation is readily available. In order to expand the portfolio of LPBF fabricated Al-alloys with favourable mechanical properties, the following future works are recommended:

i. The present study revealed that there was a loss in mechanical property when the area fraction of second phase increased beyond 50%. Therefore, future research is required to alter the solute content (herein, Zn and Mg) to control the volume fraction of second phase particles to less than 50% which might result in high strength and high solute Al-alloys that could be potentially fabricated through LPBF.

ii. The investigated high solute Al-alloys possess exceptional hardness due to the presence of a new P-phase which also contributes to the brittle nature of the alloy. The wear properties of such high solute and high hardness Al-alloys are unknown and will be of interest for surface modification applications.

iii. The alloy studied herein may be modified with Cu or Mn to explore new Al-alloy compositions through LPBF, and it would be interesting – and fundamentally important - to note the changes in microstructural, mechanical and corrosion properties.

iv. The high solute Al-alloy compositions established in this study be fabricated through direct energy deposition (DED), which will provide critical understanding in the applicability of newly designed Al-alloys for different additive manufacturing techniques.

v. The investigations in the present research also revealed the improved corrosion resistance of high solute Al-alloys prepared through LPBF when compared to traditional wrought Al-alloys. This behaviour can be explored, or exploited in a number of ways, for example (i) by the production of corrosion resistant net-shape components that are served by the portfolio of mechanical properties described herein, or (ii) by utilising the high solute alloy compositions as coatings or DED for corrosion protection of other less corrosion-resistant Al-alloys.